

**AFRL-ML-WP-TR-2001-4007**



## **LIFE PREDICTION METHODOLOGIES FOR AEROSPACE MATERIALS**

**N.E. ASHBAUGH, D.J. BUCHANAN, A.L. HUTSON, R. JOHN, K. LI, W.J. PORTER,  
AND D.A. STUBBS**

**UNIVERSITY OF DAYTON RESEARCH INSTITUTE  
STRUCTURAL INTEGRITY DIVISION  
300 COLLEGE PARK  
DAYTON, OHIO 45469-0128**

**AUGUST 2000**

**INTERIM REPORT FOR PERIOD 25 MAY 1998 - 24 MAY 1999**

Approved for public release; distribution unlimited.

**MATERIALS AND MANUFACTURING DIRECTORATE  
AIR FORCE RESEARCH LABORATORY  
AIR FORCE MATERIEL COMMAND  
WRIGHT-PATTERSON AFB, OHIO 45433-7750**

## REPORT DOCUMENTATION PAGE

<b>1. REPORT DATE (DD-MM-YYYY)</b> 01-08-2000	<b>2. REPORT TYPE</b> Interim Report	<b>3. DATES COVERED (FROM - TO)</b> 25-05-1998 to 24-05-1999
<b>4. TITLE AND SUBTITLE</b> Life Prediction Methodologies for Aerospace Materials  Unclassified		<b>5a. CONTRACT NUMBER</b>
		<b>5b. GRANT NUMBER</b>
		<b>5c. PROGRAM ELEMENT NUMBER</b>
<b>6. AUTHOR(S)</b> Ashbaugh, N. E. ; Buchanan, D. J. ; Hutson, A. L. ; Li, John K. ; Porter, W. J. ;		<b>5d. PROJECT NUMBER</b>
		<b>5e. TASK NUMBER</b>
		<b>5f. WORK UNIT NUMBER</b>
<b>7. PERFORMING ORGANIZATION NAME AND ADDRESS</b> UNIVERSITY OF DAYTON RESEARCH INSTITUTE STRUCTURAL INTEGRITY DIVISION 300 COLLEGE PARK Dayton , OH 45469-0218		<b>8. PERFORMING ORGANIZATION REPORT NUMBER</b>
<b>9. SPONSORING/MONITORING AGENCY NAME AND ADDRESS</b> Materials and Manufacturing Directorate Air Force Research Laboratory Air Force Materiel Command Wright-Patterson AFB , OH 45433-7750		<b>10. SPONSOR/MONITOR'S ACRONYM(S)</b>
		<b>11. SPONSOR/MONITOR'S REPORT NUMBER(S)</b>
<b>12. DISTRIBUTION/AVAILABILITY STATEMENT</b> A PUBLIC RELEASE  Materials and Manufacturing Directorate Air Force Research Laboratory Air Force Materiel Command		

Wright-Patterson AFB , OH 45433-7750

### 13. SUPPLEMENTARY NOTES

#### 14. ABSTRACT

The effect of microstructure, environment, and coatings on mechanisms of fatigue and fatigue crack initiation and growth in TiAl intermetallic alloys has been investigated. For a gamma titanium aluminide alloy, the coarse and refined lamellar materials with colony sizes equal to 700 and 280  $\mu\text{m}$ , respectively, have substantially greater crack growth resistance than does the fine duplex material with approximately 20  $\mu\text{m}$  grain size. The influence of laboratory air on a wrought gamma TiAl alloy produces crack growth rates more than an order of magnitude higher than those observed in ultra high vacuum environment at temperature ranging from ambient to 800 °C. A two-phase glass coating that exhibits a reduction in oxidation rate of an orthorhombic titanium aluminide, which was used as the matrix in a composite, fails to produce any enhancement in fatigue like. An extensive investigation involving fatigue, fatigue crack growth, mechanisms, modeling, and metallurgy of titanium matrix composites (TMC) is being conducted. Life models for isothermal and thermomechanical fatigue and crack propagation have been developed using concepts based on the maximum fiber stress, life fraction for time and cycle dependent response, matrix stress-life behavior, and fiber bridging. A model was developed for deformation, damage evolution, and failure of unidirectional TMC under sustained load. Effects of heat treatments on tensile and creep behavior of an orthorhombic neat matrix and on several continuous SiC fibers have been evaluations. Thermally induced stresses and damage progression in ceramic matrix composites due to fatigue and fracture are being studied. In monolithic materials, effects of stress ratio on FCG in an Al-alloy in the absence of closure and prediction of residual stress in Ti-6Al-4V generated by laser shock peening have been investigated.

#### 15. SUBJECT TERMS

Titanium aluminides, gamma, orthorhombic, titanium matrix composites; SiC fibers; ceramic matrix composites; nickel-base superalloys; turbine blade materials; high cycle fatigue; fatigue crack growth; elevated temperatures, creep, thermal fatigue; thermomechanical fatigue; fretting fatigue, load interactions; mixed-mode; stress intensity factors; finite element analysis; nondestructive evaluation

#### 16. SECURITY CLASSIFICATION OF:

17. LIMITATION OF ABSTRACT  
Public Release

18. NUMBER OF PAGES  
168

19a. NAME OF RESPONSIBLE PERSON  
Fenster, Lynn  
lfenster@dtic.mil

<b>a. REPORT</b> Unclassified	<b>b. ABSTRACT</b> Unclassified	<b>c. THIS PAGE</b> Unclassified			<b>19b. TELEPHONE NUMBER</b> International Area Code  Area Code Telephone Number 703 767-9007 DSN 427-9007
----------------------------------	------------------------------------	-------------------------------------	--	--	---

## NOTICE

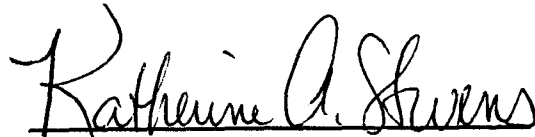
USING GOVERNMENT DRAWINGS, SPECIFICATIONS, OR OTHER DATA INCLUDED IN THIS DOCUMENT FOR ANY PURPOSE OTHER THAN GOVERNMENT PROCUREMENT DOES NOT IN ANY WAY OBLIGATE THE US GOVERNMENT. THE FACT THAT THE GOVERNMENT FORMULATED OR SUPPLIED THE DRAWINGS, SPECIFICATIONS, OR OTHER DATA DOES NOT LICENSE THE HOLDER OR ANY OTHER PERSON OR CORPORATION; OR CONVEY ANY RIGHTS OR PERMISSION TO MANUFACTURE, USE, OR SELL ANY PATENTED INVENTION THAT MAY RELATE TO THEM.

THIS REPORT IS RELEASABLE TO THE NATIONAL TECHNICAL INFORMATION SERVICE (NTIS). AT NTIS, IT WILL BE AVAILABLE TO THE GENERAL PUBLIC, INCLUDING FOREIGN NATIONS.

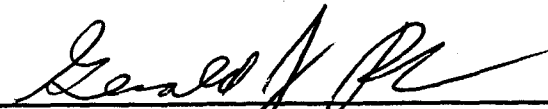
THIS TECHNICAL REPORT HAS BEEN REVIEWED AND IS APPROVED FOR PUBLICATION.



BRETT P. CONNER, 1LT, USAF  
Metals Branch, Life Prediction Section  
Metals, Ceramics & NDE Division



KATHERINE A. STEVENS, Chief  
Metals Branch  
Metals, Ceramics & NDE Division



GERALD J. PETRAZZ, Asst Chief  
Metals, Ceramics & NDE Division  
Materials & Manufacturing Directorate

Do not return copies of this report unless contractual obligations or notice on a specific document requires its return.

REPORT DOCUMENTATION PAGE			Form Approved OMB No. 0704-0188	
Public reporting burden for this collection of information is estimated to average 1 hour per response, including the time for reviewing instructions, searching existing data sources, gathering and maintaining the data needed, and completing and reviewing the collection of information. Send comments regarding this burden estimate or any other aspect of the collection of information, including suggestions for reducing this burden, to Washington Headquarters Services, Directorate for Information Operations and Reports, 1215 Jefferson Davis Highway, Suite 1204, Arlington, VA 22202-4302, and to the Office of Management and Budget, Paperwork Reduction Project (0704-0188), Washington, DC 20503.				
1. AGENCY USE ONLY (LEAVE BLANK)		2. REPORT DATE August 2000		3. REPORT TYPE AND DATES COVERED Interim, 25 May 1998 – 24 May 1999
4. TITLE AND SUBTITLE Life Prediction Methodologies for Aerospace Materials			5. FUNDING NUMBERS C: F33615-98-C-5214 PE: 62102F PR: 4347 TA: 52 WU: 01	
6. AUTHOR(S) N.E. Ashbaugh, D.J. Buchanan, A.L. Hutson, R. John, K. Li, W.J. Porter, and D.A. Stubbs				
7. PERFORMING ORGANIZATION NAME(S) AND ADDRESS(ES) UNIVERSITY OF DAYTON RESEARCH INSTITUTE STRUCTURAL INTEGRITY DIVISION 300 COLLEGE PARK DAYTON, OHIO 45469-0128			8. PERFORMING ORGANIZATION REPORT NUMBER	
9. SPONSORING/MONITORING AGENCY NAME(S) AND ADDRESS(ES) Materials and Manufacturing Directorate Air Force Research Laboratory Air Force Materiel Command Wright-Patterson AFB, OH 45433-7750 POC: Lt. Brett Conner, AFRL/MLLMN (937) 255-1348			10. SPONSORING/MONITORING AGENCY REPORT NUMBER  AFRL-ML-WP-TR-2001-4007	
11. SUPPLEMENTARY NOTES				
12a. DISTRIBUTION AVAILABILITY STATEMENT Approved for public release; distribution unlimited.			12b. DISTRIBUTION CODE	
13. ABSTRACT (Maximum 200 words) <p>The effect of microstructure, environment, and coatings on mechanisms of fatigue and fatigue crack initiation and growth in TiAl intermetallic alloys has been investigated. For a gamma titanium aluminide alloy, the coarse and refined lamellar materials with colony sizes equal to 700 and 280 <math>\mu\text{m}</math>, respectively, have substantially greater crack growth resistance than does the fine duplex material with approximately 20 <math>\mu\text{m}</math> grain size. The influence of laboratory air on a wrought gamma TiAl alloy produces crack growth rates more than an order of magnitude higher than those observed in ultra high vacuum environment at temperature ranging from ambient to 800 °C. A two-phase glass coating that exhibits a reduction in oxidation rate of an orthorhombic titanium aluminide, which was used as the matrix in a composite, fails to produce any enhancement in fatigue like.</p> <p>An extensive investigation involving fatigue, fatigue crack growth, mechanisms, modeling, and metallurgy of titanium matrix composites (TMC) is being conducted. Life models for isothermal and thermomechanical fatigue and crack propagation have been developed using concepts based on the maximum fiber stress, life fraction for time and cycle dependent response, matrix stress-life behavior, and fiber bridging. A model was developed for deformation, damage evolution, and failure of unidirectional TMC under sustained load. Effects of heat treatments on tensile and creep behavior of an orthorhombic neat matrix and on several continuous SiC fibers have been evaluations.</p> <p>Thermally induced stresses and damage progression in ceramic matrix composites due to fatigue and fracture are being studied. In monolithic materials, effects of stress ratio on FCG in an Al-alloy in the absence of closure and prediction of residual stress in Ti-6Al-4V generated by laser shock peening have been investigated.</p>				
14. SUBJECT TERMS Titanium aluminides, gamma, orthorhombic, titanium matrix composites, SiC fibers, ceramic matrix composites, nickel-base superalloys, turbine blade materials, high cycle fatigue, fatigue crack growth, elevated temperatures, creep, thermal fatigue, thermomechanical fatigue, fretting fatigue, load interactions, mixed-mode, stress intensity factors, finite element analysis, nondestructive evaluation			15. NUMBER OF PAGES 168	
			16. PRICE CODE	
17. SECURITY CLASSIFICATION OF REPORT Unclassified	18. SECURITY CLASSIFICATION OF THIS PAGE Unclassified	19. SECURITY CLASSIFICATION OF ABSTRACT Unclassified	20. LIMITATION OF ABSTRACT SAR	

## **TABLE OF CONTENTS**

<b>SECTION</b>	<b>PAGE</b>
List of Figures.....	vii
List of Tables.....	viii
Foreword.....	ix
<b>1.0 EXECUTIVE SUMMARY .....</b>	<b>1</b>
1.1 $\gamma$ TiAl-BASE ALUMINIDES.....	1
1.2 Ti-MATRIX AND Ti-ALUMINIDE COMPOSITES .....	1
1.3 CERAMIC MATRIX COMPOSITES.....	1
1.4 INITIATION AND GROWTH OF FATIGUE CRACKS IN AEROSPACE MATERIALS.....	2
1.5 DEVELOPMENT OF EXPERIMENTAL PROCEDURES, METHODOLOGIES AND LABORATORY ENHANCEMENTS .....	3
<b>2.0 INTRODUCTION .....</b>	<b>4</b>
2.1 BACKGROUND .....	4
2.2 PROGRAM OBJECTIVES .....	4
2.3 REPORT ORGANIZATION.....	4
<b>3.0 DAMAGE TOLERANCE STUDIES OF <math>\gamma</math> TiAl-BASE TITANIUM ALUMINIDES.....</b>	<b>6</b>
3.1 LIFE PREDICTION METHODOLOGY FOR TiAl-BASE TITANIUM ALUMINIDES .....	6
3.1.1 Assuring Reliability of Gamma Titanium Aluminides in Long-Term Service <b>[C1]</b> .....	6
3.1.2 Tailoring TiAl Intermetallic Alloys to Satisfy Damage Tolerance Requirements for High Performance Turbine Engines <b>[C2]</b> .....	6
3.2 MECHANISMS OF FATIGUE CRACK INITIATION IN TiAl INTERMETALLIC ALLOYS 6	
3.2.1 The Role of Near-Threshold Small-Crack Behavior of Titanium Alloys for Use in Advanced Turbine Engines <b>[C3]</b> .....	6
3.2.2 Mixed Mode Crack Growth in a Gamma Ti-Al <b>[C4]</b> .....	7
3.2.3 Mixed Mode Crack Growth in a Gamma Ti-Al Alloy <b>[C5]</b> .....	7

3.2.4	Processing Issues in Gamma Ti-Al [C6].....	7
3.2.5	Defects in Wrought Gamma Ti-Al [C7] .....	7
3.2.6	High-Cycle Fatigue Behavior and Life Estimates of a Gamma Ti-Al [C8].....	7
3.2.7	Initiation and Creep (Small) Crack Growth Behavior in a Gamma Ti-Al Alloy.....	8
3.3	MODELING EFFORTS: ANALYSIS OF STRESS CONDITIONS LEADING TO INITIATION.....	8
<b>4.0</b>	<b>DAMAGE ACCUMULATION AND FAILURE OF Ti-MATRIX COMPOSITES (TMC)</b>	<b>10</b>
4.1	BRIDGING STRESS DISTRIBUTIONS DURING FATIGUE CRACK GROWTH IN CONTINUOUSLY REINFORCED [0] METAL MATRIX COMPOSITES [C9] .....	10
4.2	TENSILE AND CREEP BEHAVIOR.....	10
4.2.1	Tensile Behavior of Ti-22Al-26Nb Wire.....	10
4.2.2	Damage and Deformation Prediction of [0] Titanium Matrix Composites Under Fatigue-Dwell Loading.....	10
4.3	A POWER LAW CREEP MODEL FOR Ti-6Al-4V .....	11
<b>5.0</b>	<b>DAMAGE ACCUMULATION AND FAILURE OF CERAMIC MATRIX COMPOSITES (CMC)</b> .....	<b>12</b>
5.1	IN SITU NONDESTRUCTIVE CHARACTERIZATION OF DAMAGE PROGRESSION IN CERAMIC MATRIX COMPOSITES AT ROOM AND ELEVATED TEMPERATURES.....	12
5.2	FRACTURE BEHAVIOR OF NEXTEL610/ALUMINOSILICATE .....	12
5.3	HIGH TEMPERATURE STRAIN GAGES FOR CMC TESTING .....	13
5.4	HIGH TEMPERATURE EXTENSOMETER FOR MEASURING CENTER HOLE DISPLACEMENTS .....	13
5.5	FATIGUE CRACK GROWTH BEHAVIOR OF NEXTEL610/ ALUMINOSILICATE .....	13
5.6	STRESSES DUE TO TEMPERATURES IN CMC AEROSPACE COMPONENTS .....	14
5.7	NOTCH SENSITIVITY OF NEXTEL720/ALUMINOSILICATE.....	14
5.8	HEAT TRANSFER AND STRESS ANALYSIS OF CMC COMBUSTOR DESIGN CONCEPTS .....	14



5.9	DEVELOPMENT OF CREEP DAMAGE MODEL FOR OXIDE/OXIDE CMC .....	15
5.10	DEVELOPMENT OF FINITE ELEMENT MESH GENERATOR FOR UNIT CELL MODELING OF WOVEN CMC .....	15
<b>6.0</b>	<b>HIGH CYCLE FATIGUE AND FATIGUE CRACK GROWTH IN AEROSPACE MATERIALS .....</b>	<b>16</b>
6.1	FRETTING FATIGUE .....	16
6.1.1	Effect of Flat-on-Flat Contact Fretting Fatigue on the Fatigue Life of Ti-6Al-4V [C10].....	16
6.1.2	Fretting Fatigue Behavior of Ti-6Al-4V Against Ti-6Al-4V Under Flat-on-Flat Contact with Blending Radii [C11] .....	16
6.1.3	Effect of Specimen Thickness on Fretting Fatigue Behavior .....	16
6.2	HIGH CYCLE FATIGUE STUDIES.....	17
6.2.1	The Effect of LCF Cracks and Loading History on HCF Threshold .....	17
6.2.2	Investigation of PRDA V Ti-6Al-4V S-N and Micro Foreign Object Damage (FOD) Behavior Under High Cycle Loading.....	17
6.2.3	Micro FOD (Foreign Object Damage) Effects on the HCF Life of Ti-6Al-4V.....	17
6.3	EVOLUTION AND EFFECTS OF DAMAGE IN TI-6AL-4V UNDER HIGH CYCLE FATIGUE [C12].....	18
6.4	HCF SYSTEM ENHANCEMENTS .....	18
6.5	CPLM FOR TI ALLOYS.....	18
6.6	CRACK INITIATION AND FATIGUE LIFE OF Ti-6Al-4V UNDER TORSION.....	19
<b>7.0</b>	<b>DEVELOPMENT OF EXPERIMENTAL PROCEDURES, METHODOLOGIES, AND LABORATORY ENHANCEMENTS.....</b>	<b>20</b>
7.1	IMPROVEMENTS TO THERMAL GRADIENT TESTING APPARATUS.....	21
7.2	DEVELOPMENT/IMPLEMENTATION OF A TORSION TESTING SYSTEM.....	21
7.3	LVDT EXTENSOMETER USE IN ELEVATED TEMPERATURE TESTING .....	21
7.4	MODIFIED SPECIMEN DESIGN FOR STRAIN CONTROLLED TESTING.....	22

7.5	IMPROVEMENT TO DIRECT CURRENT POTENTIAL DROP CRACK DETECTION SYSTEM.....	22
7.6	EXPERIMENTAL METHODOLOGIES TO DETERMINE BASIC FATIGUE CRACK-GROWTH DATA.....	23
7.7	IMPROVEMENTS IN ACOUSTIC EMISSION DETECTION OF FIBER CRACKING IN MMC DURING CREEP TESTING.....	23
7.8	RESULTS FROM USING THE DRY COUPLANT ULTRASONIC SCANNING ON CMC .....	24
7.9	LABVIEW® CONTROL OF HIGH FREQUENCY TEST SYSTEM.....	25
7.10	DEVELOPMENT OF SHEAR WAVE ULTRASONIC SYSTEM FOR DETECTING FATIGUE CRACKS IN FRETTING TESTS.....	25
7.11	BIAXIAL FATIGUE FRETTING APPARATUS DESIGN .....	26
7.12	DATA ARCHIVAL AND STATUS OF KEYSERVER® .....	26
<b>8.0</b>	<b>REFERENCES .....</b>	<b>28</b>
	Appendix A: Compendium of Manuscripts .....	29
	List of Manuscripts .....	30
	List of Symbols, Abbreviations, and Acronyms .....	154

## ***LIST OF FIGURES***

<b>FIGURE</b>		<b>PAGE</b>
1.	Schematic Drawing of Open Center Hole Specimen Showing the Location of Hole Endpoint Displacement Measurements.....	13
2.	Ultrasonic Shear Waves Propagate Within the Specimen and Scatter From Fretting Fatigue Cracks Growing Beneath Fretting Pads.....	26

***LIST OF TABLES***

---

<b>TABLE</b>	
1.	Test Matrix.....17

## FOREWORD

The work described in this report was performed at the Ceramic Development & Materials Behavior Branch in the Metals, Ceramics & Nondestructive Evaluation Division of the Materials & Manufacturing Directorate, Air Force Research Laboratory (AFRL/MLLN) under Contract No. F33615-98-C-5214, "Life Prediction Methodologies for Aerospace Materials." The contract is administered under the direction of AFRL by Mr. Jay R. Jira. The program is being conducted by the Structural Integrity Division, University of Dayton Research Institute, Dayton, Ohio with Dr. Noel E. Ashbaugh and Mr. Robert J. Andrews acting as the Principal Investigator and Program Manager, respectively. This report is an interim report on the progress of the 5-year contract effort.

In the first year of the contract, the investigations were developed and directed by Drs., Robert Brockman, Geoffrey Frank, Reji John, Nathan Klingbeil, and Kezhong Li and Messrs. Dennis Buchanan, David Johnson, Richard Goodman, George Hartman, David Maxwell, W. John Porter, and David Stubbs and Mrs. Alisha Hutson and graduate student Ms. Victoria Kramb. Mrs. Jacqui Hawkins was responsible for coordinating the input and typing of this document. This interim report covers the work performed during the period of 25 May 1998 to 24 May 1999.

## **SECTION 1**

### **EXECUTIVE SUMMARY**

---

#### **1.1   g TiAl-BASE ALUMINIDES**

As our understanding of the mechanical behavior of gamma titanium aluminides (TiAl) continues to mature, the transitioning of these materials from the laboratory to application in USAF systems still must overcome a few significant hurdles. For example, a general lack of experience in applying materials with such limited ductility and damage tolerance is apparent in the design community. Also, life prediction methodologies and models still require significant refinement to further compel designers into including these types of materials in their systems. The focus of our work over the past year was to further improve our understanding of the mechanical behavior, concentrating on fatigue properties, and to incorporate these advancements into robust models and improved life prediction techniques that will increase the likelihood of widespread application.

Significant progress was made in a number of areas over the past year including: 1) increased understanding of the effect of material defects, i.e., inclusions and grain size variances on tensile and fatigue behavior specifically initiation in wrought material, 2) significant use of analytical tools, such as orientation imaging microscopy (OIM), to aid in determining microstructural situations favorable for initiation of fatigue cracks, 3) continued refinement of models to predict elastic and plastic behavior of fully lamellar microstructures under static loading, and 4) characterization of mixed-mode crack growth to determine the effect of grain orientation on crack growth rates and threshold behavior.

#### **1.2   Ti-MATRIX AND Ti-ALUMINIDE COMPOSITES**

Various mechanical properties of titanium matrix composites (TMC) must be understood to provide a robust life prediction model under service conditions. The following studies have provided important steps in improving this understanding. Fiber bridging of cracks that grow in TMC is critical for extended life of the material. The bridging stress distribution during fatigue crack growth in a unidirectional reinforced metal matrix composite (SCS-6/TIMETAL®21S) was experimentally determined and compared to various available models in the literature.

In other activities, a testing procedure was developed to determine the mechanical tensile properties of Ti-22Al-26Nb wire that is used as a matrix material in the processing of TMC. An existing deformation and failure model for a unidirectional continuously reinforced titanium matrix composite, SCS-6/Ti-6Al-4V, has been extended for application to fatigue spectrum loading for the temperature range 260 to 538 °C. A model that conforms to both the primary and secondary tensile creep response more accurately over a range of temperatures (260 to 538 °C) and stress levels than a more sophisticated constitutive model has been used successfully to simulate both relaxation (stepped strain) tests and cyclic low cycle fatigue (LCF) tests of neat titanium material.

#### **1.3   CERAMIC MATRIX COMPOSITES**

Ceramic matrix composites (CMC) are currently being considered for replacement materials in high temperature environments such as gas turbine engines. Some of the applications include exhaust wash structures, exhaust nozzle flaps, and seals and combustor liners. Many of the

available CMC materials suffer from oxidation. Hence oxide/oxide CMC systems are being considered for their inherent resistance to oxidation. Several experimental projects were conducted on oxide/oxide systems as well as some model materials to support the development of damage initiation and accumulation models. To understand the development of matrix cracks under monotonic loading in unidirectionally reinforced [0]16 Nicalon/MAS-5, surface replication and photography were correlated with *in situ* surface wave ultrasonics. Extensometry and strain gages at notches and holes in woven oxide/oxide CMC demonstrated that the deformation at the notch tip in the loading direction remained linear up to the onset of fiber breakage and nonlinear for off-axis deformation due to the nonlinear shear behavior. An existing thermal gradient test system was upgraded to provide more flexibility and repeatability in producing temperature gradients at temperatures up to 1000°C that produce thermal stresses in excess of the ultimate strength of the materials.

In support of the ER Combustor program, finite element models for heat transfer and stress analysis of the combustor cavities were used with the Nextel720/AS material properties to evaluate the feasibility of oxide/oxide materials for the trapped vortex combustor walls. In addition to the homogeneous material models of Nextel720/AS, a 3-D model of the eight harness satin weave composite has been developed based on the unit cell, or representative volume element. This approach allows for separate material models for the fiber and the matrix. A creep damage model with a Weibull distribution for fiber failure has been implemented into a user-supplied subroutine into the ABAQUS finite element code. These models will allow the designer to evaluate different candidate CMC materials for high temperature gas turbine environments where ultimate strength, time dependent behavior and damage tolerance are critical.

#### **1.4 INITIATION AND GROWTH OF FATIGUE CRACKS IN AEROSPACE MATERIALS**

Failures in rotating components of gas turbine engines have created a major problem in maintaining the readiness of the Air Force Fleet. Generally, the fatigue failures are associated with either large amplitude loads leading to LCF failures or low amplitude loads leading to high cycle fatigue (HCF) failures. The research efforts described below are associated with both types of failures.

Most HCF failures have been accompanied by or initiated by other in-service damage associated with fretting, LCF, or foreign object damage (FOD). The effect of fretting on unfretted specimen life is being quantified by conducting interrupted fretting tests for different contact radii, applied normal stresses, and stress ratios followed by residual strength uniaxial fatigue tests. Also, the influence of a Cu-Ni plasma spray deposited coating is being evaluated. In another study, LCF loading at two stress ratios,  $R=0.1$  and  $R=-1.0$ , was used to initiate surface cracks in notched tension specimens. After the LCF damage was documented, the HCF behavior was investigated at two stress ratios,  $R=0.1$  and  $R=0.5$ .

The effect of various types of FOD on the high cycle fatigue behavior was investigated. Two methods were used to generate the FOD sites: firing small projectiles (5 mm or less) and pushing a wedge into specimens. Projectiles of both glass and steel were used in conjunction with two specimen geometries. Initially, specimens designed to simulate typical blade airfoil shapes were used to quantify how well the bulk of the data, generated using a straight-sided specimen, would represent real components.

In some test results dealing with the effects of various types of in-service damage such as LCF, FOD, and fretting, and dealing with regions where the S-N curve is relatively flat, the limit stresses were much higher than expected. This phenomenon was presumed to be caused by a

coaxing effect. However, the variability in the limit stresses appeared to be an effect of experimental scatter that was greater for FOD and fretting fatigue testing.

For characterization of threshold crack growth determination, a test technique was employed to determine the load above which crack extension occurred. A parameter that is denoted as the crack propagation stress intensity factor,  $K_{PR}$ , was computed to characterize three load interaction cases typical of in-service loading.  $K_{PR}$  was an effective correlating parameter for the three cases.

## **1.5 DEVELOPMENT OF EXPERIMENTAL PROCEDURES, METHODOLOGIES, AND LABORATORY ENHANCEMENTS**

Several new test systems, equipment, and experimental procedures were developed to support the studies of damage initiation and propagation in the different alloys and composites evaluated during this time period. Improvements were made to existing thermal and mechanical test systems as well as specimen designs and testing procedures. The University of Dayton Research Institute (UDRI) also continued its maintenance of the digital, electronic data archive of all specimens and test results produced in the Air Force Research Laboratory, Materials & Manufacturing Directorate (AFRL/MLLN) laboratories.

Two of the new test systems developed this year were a torsion testing system and a high resolution extensometer. The torsion testing system, operating at a frequency of 5 Hz, was successfully demonstrated using Ti-6Al-4V cylindrical dogbone specimens. Testing of the high-resolution extensometer demonstrated strain measurement resolution of 20 microstrain at specimen temperatures exceeding 800 °C.

Several new damage measurement methods were developed and/or enhanced including two ultrasonic nondestructive evaluation (NDE) methods for measuring cyclic loading damage in CMCs and detecting fretting fatigue cracks in Ti-6Al-4V specimens. A new methodology for determining the onset of crack growth during mechanical fatigue testing was developed. The methodology called crack propagation load measurement (CPLM) was successfully demonstrated through several fatigue crack growth tests.

Design and development work also was directed at modification of existing specimen designs. One of the design modifications was made to a 1-mm thick, Ti-22Al-26Nb specimen that allowed strain-controlled fatigue tests to attain fully reversed stress conditions without buckling the specimen. Another design effort produced a specimen geometry that will allow biaxial loading tests that simulate fretting conditions within turbine engine blade slots.

Improvements to existing test systems, an ongoing necessity in the AFRL/MLLN laboratories, were conducted on four different systems this year. The systems include a thermal gradient test system, the Direct Current Potential Drop (DCPD) crack detection system, the acoustic emission system used to detect and locate fiber breaks in metal matrix composite (MMC) materials, and one of the high frequency test systems. Maintenance and improvements of the data archival system and continued support of the Keyserver® software also were done during the year.



## **SECTION 2**

### **INTRODUCTION**

---

#### **2.1 BACKGROUND**

The U.S. Air Force has various programs in place directed towards the advancement of new gas turbine engines and aerospace vehicle technology and the support of current gas turbine engines. These programs include Integrated High Performance Turbine Engine Technology (IHPTET), Titanium Matrix Composite Turbine Engine Component Consortium (TMCTECC), National Turbine Engine Durability (NTED), Engine Rotor Life Extension (ERLE), etc. The primary goals are: (1) improved performance, i.e., maintain properties at higher service temperatures, and (2) reduction in weight, i.e., use of lightweight materials with high temperature capability. Advanced materials such as  $\gamma$ -TiAl alloys, high temperature intermetallics, TMC, and CMC are leading candidates to satisfy these needs for various engine components. In addition, the need to extend the life of a wide range of current aerospace components has resulted in programs such as the High Cycle Fatigue (HCF) Initiative, Aging Aircraft, and Propulsion Life Extension (anticipated). These programs are directed towards conventional materials, such as aluminum alloys, Ni-base superalloys and titanium (Ti) alloys (near  $\alpha$  and  $\alpha+\beta$ ). To apply the advanced materials effectively, a thorough understanding of the material behavior must be obtained and a methodology for life prediction of these materials must be developed.

#### **2.2 PROGRAM OBJECTIVES**

The primary objectives of the proposed program are listed below:

- (a) To evaluate the performance of advanced and conventional materials under simulated service conditions.
- (b) To develop and/or adapt experimental techniques for characterization of deformation, damage evolution, and failure of advanced and conventional materials under typical service conditions.
- (c) To develop an understanding of the mechanisms leading to deformation, damage accumulation and failure of advanced and conventional materials under a variety of test conditions including simulated mission cycles.
- (d) To develop physically-based deformation and life prediction models necessary to ensure in-service reliability and maintainability of advanced and conventional materials subjected to aerospace usage loading conditions.
- (e) To transition the new technology to U.S. Air Force suppliers and customers.
- (f) To use and update the data for various aerospace materials in the current archival system and enhance the materials data archival procedure.

#### **2.3 REPORT ORGANIZATION**

This first interim report presents the research conducted on the material behavior and modeling of aerospace materials within the Ceramics Development & Materials Behavior Branch (MLLN) in the Metals, Ceramics & Nondestructive Evaluation Division of the Materials Directorate at

Wright-Patterson Air Force Base, OH. This effort was conducted over the period from 25 May 1998 to 24 May 1999. The investigations that have been completed and were in progress during the first year of the contract will be discussed in this report.

In Sections 3, 4, 5, and 6, the material properties and damage assessment for  $\gamma$ -titanium aluminides, TMC, CMC, and other engine materials, respectively, are discussed. The development of experimental procedures and test techniques, methodologies, and laboratory enhancements are presented in Section 7. Extended discussions of the work-in-progress are presented to provide as much information as possible about the current investigations. Copies of the manuscripts which have been written on the completed efforts are provided in the Compendium for the convenience of readers who wish to have more detailed information of the investigations readily available.

## **SECTION 3**

### **DAMAGE TOLERANCE STUDIES OF $\gamma$ TiAl-BASE TITANIUM ALUMINIDES**

---

#### **3.1 LIFE PREDICTION METHODOLOGY FOR TiAl-BASE TITANIUM ALUMINIDES**

##### **3.1.1 Assuring Reliability of Gamma TiAl in Long-Term Service [C1]**

Gamma TiAl alloys offer the potential for major reductions in the weight of turbine engine components, if higher-density materials can be replaced without sacrificing long-term reliability in service. To assess this potential, an overview is presented of the structural capabilities available from gamma TiAl alloys. Emphasis is given to effects of material defects, mechanistic aspects of fatigue damage evolution, and the roles of high temperature, time-dependent deformation, and environment. Although gamma alloys exhibit excellent fatigue strengths, in many applications the material's resistance to service-induced damage is a critical concern. In turbine engines, such damage may result from impacts by foreign objects in the flow path. In addition, numerous components in turbine engines are subject to both LCF and HCF. To predict the range of behavior that may be expected for gamma TiAl requires consideration of damage tolerance, specifically addressing the potential for growth of small fatigue cracks that may form under a variety of circumstances. Approaches for life prediction in these materials are discussed, emphasizing the roles of fatigue crack initiation and growth. In addition, an attempt is made to assess the strengths and limitations of these materials with respect to application requirements and to suggest avenues for improvements in the balance of mechanical properties.

##### **3.1.2 Tailoring TiAl Intermetallic Alloys to Satisfy Damage Tolerance Requirements for High Performance Turbine Engines [C2]**

Gamma TiAl intermetallic alloys offer major weight savings as replacement materials for the more conventional alloys used in today's advanced turbine engines. However, to fully utilize the potential of gamma alloys in fracture critical structural applications, an unprecedented capability for life prediction under demanding service conditions is required. Key issues in fatigue crack nucleation and growth are discussed, emphasizing the role of relevant microstructural features on crack-size effects in this class of alloys.

#### **3.2 MECHANISMS OF FATIGUE CRACK INITIATION IN TiAl INTERMETALLIC ALLOYS**

##### **3.2.1 The Role of Near-Threshold Small-Crack Behavior of Titanium Alloys for Use in Advanced Turbine Engines [C3]**

Increasingly accurate life prediction models are required to utilize safely the full capability of current and future structural materials in advanced gas turbine engines. As an aid to understanding the role of crack size and threshold crack growth in these life predictions, two classes of material are examined: a conventional high strength titanium alloy and a gamma TiAl intermetallic alloy. Residual life calculations and fatigue life maps are used to illustrate the significance of crack size under realistic loading. Using weight function analyses, it is shown that surface residual stresses can greatly increase the threshold crack size for propagation of surface cracks. In the conventional titanium alloy, large-crack fracture mechanics data appear to be applicable to small fatigue cracks of practical or inspectable sizes. However, in a coarse microstructure of the gamma alloy, the scale of small cracks and initial damage can be of the order of microstructural dimensions, leading to rapid crack propagation. Local anisotropy in this

material is shown to explain this behavior, leading to guidance for optimizing microstructure to improve durability and useful lifetime under realistic loading conditions.

### **3.2.2 Mixed Mode Crack Growth in a Gamma TiAl [C4]**

This paper describes the results of an investigation of mixed mode (mode I and mode II) loading on the crack growth behavior of a gamma TiAl alloy. A centrally notched disk specimen was used, and the tests were conducted at room temperature. Mixed mode loading conditions were achieved by orienting the machined flaw at different angles to the loading axis. A specimen with large ( $\approx 5$  mm) grains was used to characterize the interlamellar growth under mixed mode loading conditions. Preliminary results indicate that the interlamellar mixed mode crack-growth rate is  $\approx 10$ -100 times faster than the transgranular mode I crack-growth rate in a gamma TiAl and is also associated with a significantly lower  $\Delta K_{th}$ .

### **3.2.3 Mixed Mode Crack Growth in a Gamma TiAl Alloy [C5]**

The results of an investigation of mixed mode (mode I and mode II) loading on the crack-growth behavior of a gamma TiAl alloy are discussed. A centrally notched disk specimen was used, and the tests were conducted at room temperature. Mixed mode loading conditions were achieved by orienting the machined flaw at different angles to the loading axis. A specimen with large ( $\approx 5$  mm) grains was used to characterize the interlamellar growth under mixed mode loading conditions. Preliminary results indicate that interlamellar mixed mode crack-growth rate is  $\approx 10$ -100 times faster than the transgranular mode I long crack growth rate and up to  $\approx 10$  times faster than small crack-growth rate

### **3.2.4 Processing Issues in Gamma Titanium Aluminides [C6]**

Processing issues regarding two wrought and one cast alloy based on TiAl are discussed. Various analytical techniques were used to investigate the microstructural anomalies. In the wrought alloys, chemical segregation issues were the primary finding. Significant variances in grain size and local inhomogeneities in the microstructures due to insufficient distribution of alloying elements are discussed. The primary issues for the cast material were the formation of a thick columnar microstructure at the investment mold/metal interface and the presence of a large inclusion, which had been liberated from the investment shell. Suggestions are given for improving the processing methods.

### **3.2.5 Defects in Wrought Gamma Titanium Aluminides [C7]**

Various defects were observed in several wrought gamma TiAl. Most of the defects are believed to originate from melting and casting processes and have survived through the subsequent forging and homogeneous heat treatment processes. The defects in these materials include serious compositional segregation, porosity, and oxides. While the presence of defects is an obvious concern, fatigue initiation is not always associated with defects of this type and primarily occurs in colonies with lamellae oriented normal to the loading direction. The nature of the defects observed, their effects on fatigue, and the relationship between the anisotropic behavior of the lamellar microstructure and fatigue initiation will be discussed.

### **3.2.6 High-Cycle Fatigue Behavior and Life Estimates of a Gamma Titanium Aluminides [C8]**

The isothermal high-cycle fatigue behavior of the Ti-47Al-3Nb-2Cr-0.2W (at%) gamma TiAl is strongly influenced by temperature and microstructure. The high-cycle fatigue behavior beyond 10<sup>8</sup> cycles is characterized by performing high-frequency, high-cycle-fatigue testing at 23, 600,

and 800 °C on nearly-lamellar and duplex microstructures at a test frequency of 350Hz and a stress ratio of 0.1.

The duplex microstructure has slightly better fatigue strength at 23 °C and considerable higher fatigue strength at 600 °C for lives up to 108 cycles when compared to the nearly-lamellar microstructure. The fatigue strengths of the duplex and nearly-lamellar microstructures are about the same at 800 °C for lives up to 108 cycles.

Crack initiation sites are identified at 23, 600, and 800 °C along with the damage mechanisms associated with these initiation sites for the duplex and nearly-lamellar microstructures. Initial and final crack sizes are determined and used to estimate fatigue crack growth life. Defects, such as porosity that were found in this forged alloy, shorten the fatigue life of the duplex microstructure considerably.

A comparison of the predicted fatigue crack growth life to the experimental fatigue life suggest that the majority of nearly-lamellar fatigue life at 600 and 800 °C consists of crack propagation at high stresses and crack initiation at low stresses. The majority of duplex fatigue life at 800 °C consists of crack propagation at high and low stresses.

### **3.2.7 Initiation and Creep (Small) Crack Growth Behavior in a Gamma TiAl Alloy**

A preliminary investigation is being conducted on initiation and growth of small cracks under constant applied load in a gamma TiAl alloy. The selected model material that is also being evaluated for aerospace applications is 3-95 gamma TiAl, Ti-47Al-2Cr-1Mo-0.2B. The natural initiation sites are being induced at notches/stress concentrations in modified (keyhole) C(T) specimens. Two temperatures, 540 °C and 760 °C, and two notch radii, 5.1 and 1.5 mm (0.2 and 0.06 in) are being considered for a gamma TiAl alloy. The development of test methodology involving the application of direct current potential drop for crack length detection is being used.

## **3.3 MODELING EFFORTS: ANALYSIS OF STRESS CONDITIONS LEADING TO INITIATION**

The goal of the on-going efforts is to explain the influence of material anisotropy on the fatigue and fracture behavior of gamma TiAl. Numeric simulations have been performed to determine the magnitude of localized stress concentrations that arise in near-lamellar gamma materials due to differences in orientation of the lamellar colonies. The simulations have used finite element analyses of representative volume elements that include sufficient numbers of randomly oriented lamellar colonies and  $\gamma$ -TiAl grains to reproduce the effects that would be observed in a large sample. Both 2-D (plane stress/plane strain) models and 3-D models have been developed. The 2-D models have been used to assess the effects of grain size distribution and geometry. The 3-D models have been used to evaluate how stresses are distributed in a 3-D structure. Results obtained from the 2-D and 3-D models have been compared to illustrate the inaccuracies that arise from the assumptions inherent in plane stress or plane strain analyses of grain structures.

The models show that localized stress concentrations are induced by the elastic anisotropy of the lamellar colonies. In on-going work, the models are being employed to understand the influence of the stress concentration arising from elastic anisotropy on the development of plasticity, which is well known to be highly anisotropic. Fatigue loading does not include bulk plasticity, especially in the long life regime; however, highly anisotropic materials may develop areas of local plasticity that could dictate fatigue and fracture behavior. A plasticity model is being developed along the lines of conventional single-crystal plasticity models for representing

multiple slip modes. This plasticity model is being implemented in the form of a user-supplied material model (UMAT) subroutine for the ABAQUS finite element code.

## **SECTION 4**

### **DAMAGE ACCUMULATION AND FAILURE OF Ti-MATRIX COMPOSITES (TMC)**

---

#### **4.1 BRIDGING STRESS DISTRIBUTIONS DURING FATIGUE CRACK GROWTH IN CONTINUOUSLY REINFORCED [0] METAL MATRIX COMPOSITES [C9]**

An optimization procedure was developed to deduce the fiber bridging stresses from crack opening displacements measured *in situ* during crack growth. This procedure was used to determine the bridging stress distribution during fatigue crack growth in a unidirectionally reinforced metal matrix composite (SCS-6/TIMETAL®21S). The bridging stress was non-zero at the crack tip contrary to predictions from conventionally used shear lag models. The bridging stress at the crack tip was proportional to the applied far-field stress. The deduced bridging law was similar to the new shear lag models with non-zero bridging stresses at the crack tip. The results showed that: (1) the bridging stress intensity factor was independent of the fiber bridging models, and (2) the magnitude of the fiber stresses exhibited significant dependence on the fiber bridging model.

#### **4.2 TENSILE AND CREEP BEHAVIOR**

##### **4.2.1 Tensile Behavior of Ti-22Al-26Nb Wire**

Mechanical tensile properties of Ti-22Al-26Nb wire were determined. The wire is used as a matrix material in the processing of composite materials. The testing procedure that had been used for straight SiC fibers was to be applied to the wire tests. However, the wire was supplied in small coils or wrapped around a spool; it was not available in straight form. The wire had to be straightened to achieve appropriate alignment before it could be tested. Even if the as-received wire had no residual stresses, unknown values of residual stresses would be created in straightening process that could confound the determination of modulus and, possibly, other tensile properties. As a check on modulus, ultrasonic measurements were made on relatively straight pieces of wire that were subsequently tested in the fiber tester.

The procedure that was adapted for the wire tested in the fiber tester was the following: straighten as best as possible by hand the section of wire to be tested, mount it in the fiber tester with reasonable alignment, strain it  $\approx 1\text{-}2\%$  to minimize the residual stress and to straighten the test section, remove it from tester and remeasure the diameter, now mount it with good alignment in the fiber tester, and conduct the tensile test. The modulus values obtained from ultrasonic measurements and from the fiber tester were in good agreement at 91-94 GPa. Ultimate stress and strain-to-failure values were  $\approx 1300$  MPa and  $\approx 10\%$ , respectively. The modulus is lower than expected but processing the wire could create a highly textured microstructure.

##### **4.2.2 Damage and Deformation Prediction of [0] Titanium Matrix Composites Under Fatigue-Dwell Loading**

An existing deformation and failure model for a unidirectional continuously reinforced titanium matrix composite, SCS-6/Ti-6Al-4V, has been extended for application to fatigue spectrum loading for the temperature range 260 to 538°C. A constitutive model for the Ti-6Al-4V matrix, with primary and secondary creep rate terms, has been shown to be more accurate than the Bodner-Partom model for predicting creep and relaxation behaviors. The constitutive model,

which was calibrated using monotonic tensile and creep data, accurately predicts the cyclic fatigue behavior of the neat matrix. The deformation model incorporates a two-parameter Weibull distribution to characterize the SCS-6 fiber strengths. Acoustic emission data were collected during the tests and provided the history of the fiber breaks for comparison with the predicted fiber failures from the model. The predictions accurately captured the deformation and fiber damage during step-loading tests.

### **4.3 A POWER LAW CREEP MODEL FOR TI-6AL-4V**

Recent efforts at modeling the creep behavior of titanium-matrix MMCs have employed the Bodner-Partom unified constitutive model, which was originally developed for cyclic viscoplastic analysis. The UDRI has performed an evaluation of the Bodner-Partom creep model for predicting a number of experimental results obtained at AFRL/MLLN. Although some features of the Bodner predictions are accurate, an accurate prediction of both the primary and secondary creep responses is generally impossible using the Bodner model. Capturing both of these features precisely seems to require either multiple terms in the material model, or a model which incorporates “memory” effects on multiple time scales, as opposed to a state-variable approach.

The UDRI has developed a more conventional creep model for neat titanium based upon a stress power law representation of the primary creep response and a hyperbolic sine model of the secondary (steady) creep behavior. The model conforms to the tensile creep response more accurately over a range of temperatures (260 to 538°C) and stress levels, and has been used successfully to simulate both relaxation (stepped strain) tests and cyclic (LCF) tests of neat titanium material. Currently we are refining the primary creep model to improve accuracy in stepped loading tests, which involve a strong primary creep component.



## **SECTION 5**

### **DAMAGE ACCUMULATION AND FAILURE OF CERAMIC MATRIX COMPOSITES (CMC)**

---

#### **5.1 IN SITU NONDESTRUCTIVE CHARACTERIZATION OF DAMAGE PROGRESSION IN CERAMIC MATRIX COMPOSITES AT ROOM AND ELEVATED TEMPERATURES**

This investigation used an integrated NDE/mechanical test system to characterize damage initiation and accumulation in  $[0]_{16}$  Nicalon/MAS-5 and  $[0/90]_{3S}$  SiC/BMAS CMC systems at room and elevated (up to 900 °C) temperatures [Gural, 1998]. Extensive surface replication and photography were used to correlate changes in ultrasonic surface and longitudinal wave characteristics to damage mechanisms.

The sudden decrease in the peak-to-peak amplitude of the surface wave signal coincided with the onset of matrix cracking at room and elevated temperatures. The amplitude of the surface wave signal decreased with increasing crack density. Matrix cracking first occurred in matrix rich regions where the fiber spacing was the widest. In both  $[0]_{16}$  and  $[0/90]_{3S}$  materials, testing at elevated temperatures delayed the onset of matrix cracking. Testing at elevated temperatures resulted in an overall reduction in the number of matrix cracks for both  $[0]$  and  $[0/90]$  materials.

A shear lag model was used to deduce the changes in the interfacial sliding stress as a function of temperature for the  $[0]_{16}$  and  $[0/90]_{3S}$  material. The sliding stress decreased with increasing temperature for both materials. Predictions for the composite unloading modulus are not influenced by changes in the sliding stress. Predictions for the permanent strain indicated that the  $[0]_{16}$  material possessed a very low debond energy.

#### **5.2 FRACTURE BEHAVIOR OF NEXTEL610/ALUMINOSILICATE**

The notched fracture behavior of a woven oxide/oxide ceramic matrix composite, Nextel610/Alumina-Silica (Nextel610/AS), was investigated at 23 °C and 950 °C [Kramb et al., 1999]. Fracture tests showed that notch sensitivity was temperature and geometry dependent. At 23 °C, open center hole specimens were notch insensitive. In contrast, edge-notched specimens were notch sensitive, with failure stresses corresponding to a peak stress intensity factor  $\approx 14.6 \text{ MPa}\sqrt{\text{m}}$ . Local strain measurements ahead of the notches showed that deformation in the fiber directions remained linear up to the onset of fiber breakage. Off-axis deformation was nonlinear, due to the nonlinear shear behavior at 23 °C. At 950 °C, failure stresses decreased by 30% and 50% for the center hole and edge notched specimens respectively. The reduction in notch strength with temperature was associated with a change in damage mode. At 23 °C, distributed matrix cracking resulted in stress redistribution around the notch. At 950 °C, crack growth resulted in longitudinal fiber breakage and growth of a dominant crack. Finite element modeling of the deformation behavior was conducted for both test temperatures. The results of the analysis showed that at 23 °C deformation in the fiber directions was linear elastic, off-axis deformation was dominated by the nonlinear shear behavior. At 950 °C, deformation was nearly linear elastic up to the point of dominant crack initiation.

### 5.3 HIGH TEMPERATURE STRAIN GAGES FOR CMC TESTING

The use of high temperature strain gages for measuring local strains was investigated using an oxide/oxide CMC at 950 °C. The free filament strain gages consisted of platinum-rhodium looped wires (gage size 1.6 mm by 1.6 mm) bonded to the specimen using a high temperature ceramic adhesive. During the preliminary testing, the gages remained bonded to the specimen surface, lead wires remained intact and output from the strain gage could be monitored. The output exhibited excessive electrical noise at temperature however, and useful strain measurements could not be obtained. Further investigations are required to examine the source of the electrical noise, and optimum adhesive for attaching the gages to the specimen surface.

### 5.4 HIGH TEMPERATURE EXTENSOMETER FOR MEASURING CENTER HOLE DISPLACEMENTS

Fracture tests conducted on open center hole specimens at elevated temperatures required a method for measuring displacements on the specimen surface, at the hole endpoints ( $\Delta$ ) (Fig. 1). A high temperature extensometer was developed which incorporated components and mounting hardware from existing high temperature extensometers. The resulting extensometer, with gage length  $\approx$  6 mm, measured surface displacements with a resolution  $\approx$  0.002 mm. Noise in the displacement measurements at 950 °C currently limits the resolution. Further improvements in the extensometer design may reduce the resolution and allow for high temperature measurements of crack opening displacements.

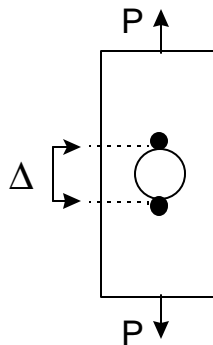


Figure 1. Schematic Drawing of Open Center Hole Specimen Showing the Location of Hole Endpoint Displacement Measurements.

### 5.5 FATIGUE CRACK GROWTH BEHAVIOR OF NEXTEL610/ALUMINOSILICATE

Fatigue crack growth tests were conducted at 950 °C on single edge notched specimens with clamped ends. Extended fatigue cycling ( $> 10^6$  cycles) at an applied stress = 82 percent of the monotonic notch strength showed that crack mouth opening displacements (CMOD) increased continuously. Destructive evaluation of the interrupted test specimens showed that damage evolution was associated with dominant crack growth and longitudinal fiber breakage. The results of the fatigue test were correlated with those of a sustained load test conducted at the same applied stress level. Good correlation between the observed deformation from the fatigue and sustained load test showed that the observed increases in CMOD were due primarily to creep of the composite. The results of the sustained load tests also confirmed that the reduction in notch strength at 950 °C was not due time at temperature.

## **5.6 STRESSES DUE TO TEMPERATURES IN CMC AEROSPACE COMPONENTS**

The CMC are targeted for use in advanced aerospace turbine engine components that are exposed to exhaust gas temperatures  $\geq 1000$  °C. Under the direction of the Defense Advanced Research Projects Agency (DARPA), various CMC systems are under consideration as replacement materials for divergent flaps and seals in engines. The typical flaps and seals currently in use are made of Rene '41 (a nickel-base superalloy). During various stages of engine operation, the effective diameter of the nozzle can be expanded or contracted by moving the flaps and seals. Under these conditions, the seals cover significant areas of the flaps ranging from  $\approx 10$  to  $\approx 50$  percent of the flap area. The overlapped region of the flaps can be up to 700 °C cooler than the central one-third of the flap. Consequently, severe temperature gradients occur in the flaps during service. The temperature gradients are associated with temperatures as high as 800 to 1000 °C and temperature gradients of 20 °C/mm across 40 mm near the back ends of the flap.

## **5.7 NOTCH SENSITIVITY OF NEXTEL720/ALUMINOSILICATE**

Oxide/oxide CMC are currently being considered for aerospace applications for elevated temperature environments by virtue of their resistance to oxidation. Many of these applications require notches to enable cooling and attachments. Hence, a study was undertaken to investigate the fracture behavior the notched oxide/oxide CMC at 23 °C and 1000 °C. Fracture tests were conducted on notched Nextel 720/AS with eight harness satin weave fiber architecture manufactured by Composite Optics, Inc. The CMOD was measured using high temperature extensometry during testing. The effect of notches on the ultimate strength and deformation were studied and compared with results from unnotched tensile tests. Single notched specimens, MSE(T), exhibited as much as a 50 percent drop in net-section strength when compared with unnotched tensile results. The decrease in net-section strength is attributed to the additional bending stresses at the notch. Double notched specimens, DE(T), exhibited no reduction in net-section strength up to temperatures of 1000 °C.

## **5.8 HEAT TRANSFER AND STRESS ANALYSIS OF CMC COMBUSTOR DESIGN CONCEPTS**

The UDRI is supporting the AFOSR-funded CMC Entrepreneurial Research Program, a joint venture of the Materials and Manufacturing Directorate and the Propulsion Directorate, by providing heat transfer and stress analysis of conceptual designs of a trapped-vortex combustion system. The combustor achieves high efficiency by allowing air and fuel to recirculate in the primary combustion zone, achieving higher temperatures and more complete combustion. The program is intended to address material issues associated with the higher heating loads in parallel with the combustor system design.

We have performed heat transfer and stress analysis of axisymmetric cavities with thick and thin walls, to determine temperature levels, temperature gradients, and approximate thermal stresses. All analytical predictions performed so far are based on the Nextel 720/AS oxide/oxide material system. Stress analysis results based on nominal macroscopic properties have been provided to the Mechanics group for micromechanical stress analysis. We also have developed a simple spreadsheet-based analysis of the temperature distribution through the cavity wall. This simplified model can be used to investigate the effect of cavity heat flux, back-wall radiation, wall thickness, and film coefficients on the temperature field.

Results of the preliminary combustor cavity analyses suggest that oxide/oxide CMCs may be a feasible choice for the trapped vortex combustor, provided the wall thickness is relatively small and adequate active cooling is integrated into the system.

## **5.9 DEVELOPMENT OF CREEP DAMAGE MODEL FOR OXIDE/OXIDE CMC**

The UDRI is developing improved analytical modeling techniques for woven oxide/oxide CMCs, with particular emphasis on the Nextel 720/AS material system. One avenue of investigation is the development of creep and damage models for the constituent materials. A Weibull model of damage in Nextel 720 fiber tows has been developed based on experimental data available in the literature [Wilson, 1997]. The model is quite simple, but predicts the tensile behavior of the fiber tow very accurately. Such a damage model is important in the analysis of CMC creep, in which damage caused by thermal degradation is thought to be an important mechanism. The completed damage and creep models will be implemented as user-supplied material subroutines for the ABAQUS finite element analysis code.

## **5.10 DEVELOPMENT OF FINITE ELEMENT MESH GENERATOR FOR UNIT CELL MODELING OF WOVEN CMC**

The UDRI also has developed software tools to improve the efficiency of modeling CMC weaves in detail. Typically a local stress model of a woven composite is based on a unit cell, or representative volume element, which is the smallest repeating geometric pattern in the composite. For complicated weaves (such as eight harness satin), the mere construction of a suitable geometric model for analysis can consume weeks of engineering time. We have developed an automated mesh geometry generator that allows the weave to be specified in terms of fiber paths and dimensions, and then generates a detailed finite element mesh automatically. As a result, a unit cell model can be constructed literally in minutes. The finite element data are output in a form compatible with the MSC/PATRAN modeling package, which provides a path to the most common finite element software for various types of mechanical analysis.

## **SECTION 6**

### **HIGH CYCLE FATIGUE AND FATIGUE CRACK GROWTH IN AEROSPACE MATERIALS**

---

#### **6.1 FRETTING FATIGUE**

##### **6.1.1 Effect of Flat-on-Flat Contact Fretting Fatigue on the Fatigue Life of Ti-6Al-4V [C10]**

The effect of fretting fatigue on the fatigue life of Ti-6Al-4V at room temperature has been evaluated as part of an ongoing multiphase study. A flat-on-flat contact with blending radii was employed to simulate the geometry used in dovetail blade attachments. Results from two independent test matrices are presented. The first involved interrupted fretting tests followed by residual strength uniaxial fatigue tests. Two stress ratios,  $R=0.5$  and  $R=0.8$ , and two average clamping stresses, 140 MPa and 420 MPa, were investigated. For each combination of average clamping stress and stress ratio, specimens were tested to one of three different percentages (0.1%, 1%, and 10%) of fretting fatigue life to evaluate the rate of damage accumulation. The second involved an investigation of fretting fatigue behavior in the presence of Cu-Ni plasma spray deposited coating, common to many turbine engine components, on the fretting pads. All tests in this part of the investigation were conducted with a constant normal stress of 420 MPa at 300 Hz. Two initial baseline tests were axially loaded using a step loading procedure to obtain a limit stress at a  $10^7$  cycle life. The expense of the plasma spray process prompted the remaining tests to be conducted using a standard S-N approach with an axial stress of 300 MPa. All tests were performed at  $R=0.5$  under lab air conditions. Comparisons were made of the tests incorporating the Cu-Ni coating to those with typical as received pads, and with grit-blasted and stress-relieved pads designed to simulate the roughness inherent to the plasma-sprayed surface. Fractography in a scanning electron microscope (SEM) was used to qualitatively analyze fretting damage in both phases of the investigation.

##### **6.1.2 Fretting Fatigue Behavior of Ti-6Al-4V Against Ti-6Al-4V Under Flat-on-Flat Contact with Blending Radii [C11]**

A two-phase study was conducted to evaluate fretting fatigue damage in a flat on flat contact at room temperature. First, the axial stresses necessary to fail specimens at 10 million cycles for different contact radii, applied normal stresses, and stress ratios were evaluated. Then, the effect of fretting on unfretted specimen life was quantified by conducting interrupted fretting tests for various load ratios and normal stresses followed by residual strength uniaxial fatigue tests. Ti-6Al-4V was used throughout the study. Fractography was used to qualitatively analyze fretting damage.

##### **6.1.3 Effect of Specimen Thickness on Fretting Fatigue Behavior**

The applicability of laboratory fretting fatigue results to the modeling of behavior in dovetail components is debatable because of differences between the geometries in lab and service applications. Lab samples are usually thin specimens with fretting imposed on either one or both faces of the specimen, while service components such as dovetail blade attachments are relatively thick with appreciable distance between adjacent contacts. The University has developed a study to investigate the effect of lab specimen thickness on fretting fatigue behavior in an effort to link lab results and real component behavior, and to provide information on the effect of imposed shear force on fretting fatigue. The test matrix for this study, as shown below (Table 1), will be completed for three different specimen thicknesses: 1, 2, and 4 mm. The tests

have already been completed for 2 mm thick specimens under a different study. Four 4 mm thick samples have been tested, but continued testing is delayed due to machine repairs.

**Table 1. Test Matrix**

<b>10,000,000 cycles</b>	<b>140 MPa Contact stress</b>	<b>420 MPa Contact stress</b>
10%	1 test @ R=0.5	1 test @ R=0.5
10%	1 test @ R=0.5	1 test @ R=0.5
10%	1 test @ R=0.8	1 test @ R=0.8
N%	1 test @ R=0.5	1 test @ R=0.5
N%	1 test @ R=0.5	1 test @ R=0.5
N%	1 test @ R=0.8	1 test @ R=0.8
100%	1 test @ R=0.5	1 test @ R=0.5
100%	1 test @ R=0.5	1 test @ R=0.5
100%	1 test @ R=0.8	1 test @ R=0.8

## **6.2 HIGH CYCLE FATIGUE STUDIES**

### **6.2.1 The Effect of LCF Cracks and Loading History on HCF Threshold**

The influence of LCF initiated cracks HCF threshold of Ti-6Al-4V plate is being investigated. The LCF loading at two stress ratios,  $R=0.1$  and  $R=-1.0$ , was used to initiate surface cracks in notched tension specimens. DCPD was used to detect crack initiation. The surface crack sizes were measured via SEM prior to failure and via heat-tint marking on the fracture surface examined after failure. After the LCF damage was documented, the HCF behavior was investigated at two stress ratios,  $R=0.1$  and  $R=0.5$ . The HCF tests were conducted at 600 Hz using a step loading procedure. Both the LCF loading history and LCF crack size effect were analyzed to determine the loading history effect on the HCF threshold. Comparisons were made with long crack threshold data obtained using compact tension [C(T)] and single edge notched tension [SE(T)] specimens.

### **6.2.2 Investigation of PRDA V Ti-6Al-4V S-N and Micro Foreign Object Damage (FOD) Behavior Under High Cycle Loading**

The influence of specimen geometry and size on the limit stresses for a  $10^7$  fatigue life, as determined by the step loading approach employed throughout these HCF studies (see Section 6.3), is being studied. The stress ratios used in this study are 0.1, 0.5, 0.8, and 0.9. The test frequencies are 400 and 1800 Hz. The tests are conducted at laboratory air temperature on flat dogbone, cylindrical dogbone and cylindrical hourglass specimens. After the armature of the shaker in the test system was replaced and dynamic calibrations were performed to ensure accurate load levels, ten tests in the study have been completed on flat dogbone specimens with a 3.5-mm wide by 1.8-mm thick gage section.

### **6.2.3 Micro FOD Effects on the HCF Life of TI-6Al-4V**

The effect of various types of FOD on the HCF behavior of the Ti-6Al-4V plate material, incorporated in the above study, were investigated. Two methods were used to generate the FOD damage sites: firing small projectiles (5 mm or less) and pushing a wedge into specimens. Projectiles of both glass and steel were used in conjunction with the two specimen geometries employed. Initially, specimens designed to simulate typical blade airfoil shapes were used to quantify how well the bulk of the data, generated using a straight-sided specimen, would represent real components. The UDRI provided both test system support and technician time to conduct many of the tests, including dynamic system calibrations for each specimen geometry.

### 6.3 EVOLUTION AND EFFECTS OF DAMAGE IN Ti-6Al-4V UNDER HCF [C12]

The development of an accelerated test procedure for the determination of material fatigue limits is important when investigating baseline material properties and the effects of in-service damage on HCF resistance. Such a procedure, called the step loading procedure, has been developed and its validity proven here and in previous papers for pristine materials. However, in testing designed to investigate the effects of various types of in-service damage such as LCF, FOD, and fretting, and in the investigation where the S-N curve is relatively flat, some tests result in limit stresses much higher than expected, presumably due to the coxing effect. Limit stresses determined using an S-N approach provide a much better statistical average of the material behavior because more specimens are tested to achieve the desired result, as compared to accelerated test procedures where material variability can have a greater impact on the end product. The limit stress data presented do not indicate a dependence on the number of steps used in the step loading procedure, either for pristine or LCF damaged material. The specimens subjected to prior LCF damage did result in a linear increase in limit stress as a function of the number of steps, but this appears to be related to the step size, since all of the tests began at nearly the same stress. When the limit stresses were plotted as a function of LCF damage, no decrease in HCF resistance was observed, regardless of step size or number of steps used. In addition, data presented on a Haigh diagram indicated no dependence on step size, initial stress, or number of steps used, and showed remarkably little scatter over a wide range of stress ratios. While the data presented do not represent a systematic study of coxing, they do support previous work in showing no evidence of coxing for Ti-6Al-4V. Variability in the results appears to be an effect of experimental scatter, which is expected to be greater for FOD and fretting fatigue testing.

### 6.4 HCF SYSTEM ENHANCEMENTS

Some modification of HCF System #4 was required to correct an alignment drift problem. Although a woods metal device was in place, the machine's vertical alignment continued to drift because the shaker was allowed to move relative to the test frame. This problem was corrected by bolting and welding braces between the frame and the shaker unit, and similarly attaching bracing between the frame columns for added frame stiffness. Many tests have been conducted since these modifications were implemented.

### 6.5 CPLM FOR TI ALLOYS

Titanium alloy Ti-6Al-2Sn-4Zr-2Mo was used to generate fatigue crack-growth rate data. For this study, a test technique, CPLM used to determine the load above which crack extension occurs, allows determination of a parameter that is denoted as the *crack propagation stress intensity factor*,  $K_{PR}$ , was used [Lang, M. and Marci, G., 1999]. Three test methods utilizing the CPLM test technique were used for this study. The first method consisted of constant amplitude loading to extend a crack 0.75 mm. An overload(s) was then applied and the CPLM technique was started. The second method extended the crack 0.75 mm with constant amplitude loading. An unloading below the minimum load value was then applied and the CPLM technique was started. In the third method, spectrum loading was used to extend the crack 0.75 mm and was stopped at a predetermined endpoint in the spectrum. The CPLM technique started at that endpoint to evaluate the effect that variable amplitude loading has on  $K_{PR}$ . All tests were conducted using compact tension specimens with a 40 mm width. The tests for the first and second methods conducted at room temperature and 316 °C. For the third method, the tests were conducted at room temperature.

## **6.6 CRACK INITIATION AND FATIGUE LIFE OF Ti-6Al-4V UNDER TORSION**

The primary objective of this investigation is to determine the interaction between damage introduced by a torsion fatigue load and a uniaxial fatigue load. Initially, a stress-life diagram needs to be determined under torsion fatigue loading. Then, fractions of a selected life would be applied under torsion load followed by uniaxially fatigue load to failure. If the uniaxially fatigue life is significantly influenced, a more representative test matrix would be developed to explore the interactions and mechanisms. Five tests have been conducted to develop the torsional stress-life curve. Some inconsistencies have occurred in the data. Measurements of residual stresses are being evaluated to determine if the interaction between the applied torsion and the residual stresses can explain these inconsistencies.



## **SECTION 7**

### **DEVELOPMENT OF EXPERIMENTAL PROCEDURES, METHODOLOGIES, AND LABORATORY ENHANCEMENTS**

---

Several new test systems, equipment, and experimental procedures were developed to support the studies of damage initiation and propagation in the different alloys and composites evaluated during this time period. Improvements were made to existing thermal and mechanical test systems as well as specimen designs and testing procedures. The UDRI also continued its maintenance of the digital and electronic data archive of all specimens and test results produced in the AFRL/MLLN laboratories. The details of the new systems, procedures, and enhancements are contained in the subsections that follow. A brief review of the subsections is given below.

A new torsion testing system was designed and constructed that expanded the mechanical testing capability in AFRL/MLLN laboratories. Successful implementation of the torsion testing system, described in Section 7.2, was demonstrated using Ti-6Al-4V cylindrical dogbone specimens.

Several mechanical tests required high-resolution strain measurements that were beyond the capability of commercial gages. Section 7.3 describes a new type of extensometer that measures strain with 20-microstrain resolution at specimen temperatures exceeding 800 °C.

Sections 7.8 and 7.10 describe the adaptation of existing ultrasonic NDE methods for measuring cyclic loading damage in CMCs and detecting fretting fatigue cracks in Ti-6Al-4V specimens.

Section 7.6 briefly describes a new methodology for determining the onset of crack growth during mechanical fatigue testing. The methodology, called crack propagation load measurement, was developed by visiting scientist Marcus Lang, and demonstrated through many fatigue crack-growth tests conducted in AFRL/MLLN laboratories.

Some of the advanced tests conducted in the laboratories required modification of existing specimen designs. Section 7.4 describes the design modifications made to a 1 mm thick, Ti-22Al-26Nb specimen that allowed strain-controlled fatigue tests to attain fully reversed stress conditions without buckling the specimen. Section 7.11 contains a brief description of a specimen geometry that will allow biaxial loading tests to occur in the AFRL/MLLN laboratories that simulate fretting conditions within turbine engine blade slots.

Improvements to existing test systems, an ongoing necessity in the AFRL/MLLN laboratories, was conducted on four different systems this year. Section 7.1 describes the improvements made to a thermal gradient test system. Section 7.5 contains information on the hardware, software, and algorithm upgrades made to the DCPD crack detection system. Improvements to the acoustic emission system used to detect and locate fiber breaks in MMC materials are described in Section 7.7. A commercial programming package was evaluated and implemented to control one of the high frequency test systems and a brief summary of the software testing is included in Section 7.9. An update on the ongoing maintenance and improvements of the data archival system is presented in Section 7.12 along with a brief status report on the Keyserver® software.

## **7.1 IMPROVEMENTS TO THERMAL GRADIENT TESTING APPARATUS**

A substantially improved thermal gradient test system was designed, assembled and tested. The heat lamps are now mounted to screw-driven slides with quick disconnects that allow precise control of the lamp elevation with respect to the test sample. The slides also have a calibrated angular displacement mount that provides repeatable orientation of the lamps incident angle with respect to the test sample. The new system reduces the variation in lamp placement and allows for more repeatable test conditions between successive tests.

## **7.2 DEVELOPMENT/IMPLEMENTATION OF A TORSION TESTING SYSTEM**

The UDRI developed a torsion testing system for evaluating monolithic and composite materials in torsional fatigue. The system consists of a servo-hydraulic rotary actuator and a reaction plate mounted on a 0.38 by 1.22 by 0.13 m (15 by 48 by 5 inch) steel T-slot table. The rotary actuator is rated at 226 N-m (2000 in-lbf) torque and has a maximum dynamic displacement of  $\pm 45^\circ$ . The reaction plate attaches securely to the T-slot table and provides a mounting surface for the torque cell. A torque cell provides a precise,  $\pm 10$  V, feedback signal that is proportional to the torque applied to the specimen. An angular displacement transducer connected to the rear shaft of the actuator produces a dc electrical signal that is proportional to the angular position of the actuator. An axial/torsional extensometer simultaneously measures the axial deflection and torsional rotation on the specimen. A computer controlled servo-controller provides the capability to control torque, angular displacement or torsional strain.

The test system was aligned using a cylindrical dogbone specimen instrumented with 12 strain gages for determining concentric and angular misalignments. The operation of the torsional test system was tested using Ti-6Al-4V cylindrical dogbone specimens. Tests were conducted under torque control at a frequency of 5 Hz. Both torque and angular displacement data were collected specimens tested to failure. The onset of torsional fatigue cracks was identified by an increase in angular displacement.

## **7.3 LVDT EXTENSOMETER USE IN ELEVATED TEMPERATURE TESTING**

Several mechanical tests required extensometers with very high strain resolution and low drift over time. Testing confirmed that commercially available glass rod extensometers did not have the required strain resolution and drifted considerably during typical test durations of several days. The mechanical tests being conducted required strain information over a range of several hundred microstrain so an extensometer was needed with a resolution of better than 20 microstrain. Also, the extensometer needed to be stable over time; drifts in the output due to environmental changes (temperature for example) also had to be approximately 20 microstrain. Commercially available extensometers could not meet these requirements so UDRI decided to design and build an extensometer useful for low strain measurements at elevated temperatures.

The UDRI's design incorporated a sensitive, miniature, Linear Variable Differential Transformer (LVDT) and a one-piece extensometer body designed using a material with a near-zero coefficient of thermal expansion. The final design was tested for stability at room temperature under both static and dynamic loading conditions, and elevated temperature with static loading conditions.

The amount of drift measured at room temperature under static conditions was typically less than 25 microstrain over a 36-hour test. This drift could be made negligible by allowing the extensometer a warm up period of roughly 8 hours. The LVDT extensometer also was tested under dynamic loading conditions, demonstrating good stability with a change in strain less than 10 microstrain during 550,000 mechanical cycles. These tests demonstrated the LVDT

extensometer's high strain resolution and low sensitivity to environmental influences such as temperature or humidity.

At elevated temperature the LVDT extensometer was used to measure the Coefficient of Thermal Expansion (CTE) of a nickel-based superalloy, MA754, and a CMC, Nextel720/AS. The tests were conducted using a clam shell furnace for the heat source. The test conducted on MA754 imposed a three thermal cycle test from room temperature to 825 °C to determine the repeatability of the LVDT extensometer. The results showed excellent repeatability and very little hysteresis. The CTE determined from this test compared very favorably to that quoted by the material's manufacturer. The test conducted on the CMC was to determine the stability of the LVDT extensometer with a heat source applied to the rods. The test lasted over 17 hours and showed a mean drift of less than 50 microstrain, indicating good thermal stability.

#### **7.4 MODIFIED SPECIMEN DESIGN FOR STRAIN CONTROLLED TESTING**

The strain controlled fatigue test matrix on neat Ti-22Al-26Nb could not be completed due to specimen buckling at the elevated temperature test conditions. The requested strain limits at the elevated temperatures produced rapid mean stress relaxation that drove the tests to nearly fully reversed stress conditions which could not be supported by the 1-mm thick test specimens. Tabs made from 2-mm thick TMC were welded to the test specimens to increase the moment of inertia. The tabs extended past the front face of the friction grips to the outside edge of the gage section. The tabs provided enough bending stiffness resistance to support the compressive stress reached during the fatigue testing. Finite difference calculations predicted approximately a 25% increase in the elastic buckling stress due to the welded tabs.

#### **7.5 IMPROVEMENT TO DIRECT CURRENT POTENTIAL DROP CRACK DETECTION SYSTEM**

Several different measurement techniques are used in the AFRL/MLLN laboratories to measure crack length during crack growth testing. The techniques include optical observations, back face strain (BFS), crack mouth opening displacement (CMOD), laser interferometric displacement gage (LIDG), and DCPD.

During the past year, significant efforts have been made to improve the equipment implementing the DCPD technique. Specifically, both the system software and hardware have been modified in order to increase DCPD measurement accuracy and incorporate its use in other test modules. The modifications included:

- 1) Several new analog-to-digital (A-D) computer boards were evaluated for use in crack growth tests using the new WinMATE software. Simulated crack growth tests over 100 hours were conducted and the boards were evaluated for signal amplitude resolution, signal-to-noise levels, and thermal stability. A 26-bit A-D board manufactured by Thaler, Inc. (model ADC180C) was chosen as the best available board for AFRL/MLLN applications and is currently undergoing evaluation for potential use in the DOS-based MATE DCPD creep crack growth testing modules.
- 2) A standard geometry for C(T) specimens was specified and four different sets of DCPD power and pickup lead placement positions were written into the DOS-based MATE crack-growth test software. The new WinMATE testing software will allow lead placement at any position.
- 3) Numerous improvements were made to the standard DOS-based MATE DCPD crack-growth software to improve data acquisition, upgrade the display of data, and print out data.

## 7.6 EXPERIMENTAL METHODOLOGIES TO DETERMINE BASIC FATIGUE CRACK-GROWTH DATA

A new experimental technique was developed to determine the onset of crack growth during mechanical fatigue. The technique, CPLM, allows the calculation of a unique parameter called the *crack propagation stress intensity factor* ( $K_{pr}$ ). To calculate  $K_{pr}$  the specimen is loaded with a relatively small cyclic load creating a stress intensity factor far below the expected  $K_{pr}$  value. The fatigue loads applied to the specimen create a stress intensity factor that is greater than the intrinsic threshold value ( $\Delta K_T$ ) in order to cause a very small amount of crack propagation in the specimen. If during the fatigue cycles the crack does not start to grow, the mean load of the fatigue cycles is increased by a small amount while maintaining the same cyclic amplitude. The mean load is incrementally increased until the crack “propagates” which determines the value of  $K_{pr}$ . “Propagation” is defined as a crack-growth rate larger than  $10^{-7}$  mm/cycle (which also is the value used to define the traditional threshold crack-growth rate.) When the mean load is increased to the point that crack propagation occurs,  $K_{pr}$  is calculated from the cyclic loads at that mean load.

## 7.7 IMPROVEMENTS IN ACOUSTIC EMISSION DETECTION OF FIBER CRACKING IN MMC DURING CREEP TESTING

An acoustic emission NDE technique, incorporating broad band transducers and modal analysis, was applied to a unidirectional continuously reinforced titanium matrix composite (SCS-6/Ti-6Al-4V) to detect and locate fiber breaks during elevated temperature creep tests. Earlier work at AFRL has resulted in reasonable success at locating fiber breaks in the composite. The work during the past year concentrated on refining the location capability and improving the ability to discriminate between actual fiber break signals and other electronic and/or material-generated signals.

To improve the locating of fiber breaks, it was necessary to have a better understanding of the mode of propagation of the acoustic energy in the composite. Our hypothesis was that the fiber break creates a bulk wave, which propagates throughout the composite in all directions. The presence of the specimen surface causes some of the energy to propagate as a surface wave, which then excites the waveguides placed on the specimen surface. The waveguides convert the surface wave energy into a bulk wave, which propagates up the waveguide to the ultrasonic sensor. To test this assumption, surface wave transducers were attached to a specimen during creep testing. The surface wave transducers detected the energy correlating with fiber breaks as determined by other sensors attached to the specimen. Further experimentation showed that the surface wave sensors would not detect bulk wave energy inserted into the end of the specimen. Using pencil lead breaks a surface wave velocity of approximately 3,800 m/s was calculated which is close to theoretically calculated values. The velocity value of 3,800 m/s also produces accurate locations when used on fiber break data (as compared with destructive fiber break measurements). While not completely conclusive, these tests provided evidence that fiber breaks are detected by the waveguides via surface wave propagation.

During many of the tests described above, bulk wave ultrasonic sensors were attached to the ends of the specimen. Tests were conducted to measure the bulk wave velocity and understand the effect of gripping pressure on the acoustic propagation. (The grip pressure effect occurs because the energy from fiber breaks must pass through the gripped region of the specimen to reach the bulk wave sensors.) The tests also showed that the amplitude of the received bulk wave signal decreased as the grip pressure increased. At grip pressures of 10,000 psi (test conditions) very little bulk wave energy was detected. This led to the use of Surfalloy® grip inserts instead of smooth inserts, which significantly lessened the negative effects of grip pressure on the bulk wave signal amplitude. The bulk wave velocity calculated from the test data

was approximately 7,300 m/s, which is very close to theoretical rod wave velocity for the composite specimen.

Several tests were conducted on the composite specimen using pencil lead breaks as the acoustic energy source. The waveguide sensor signals were examined to see if the waveguides themselves were creating specific frequencies in the signals due to harmonic vibration. It was found that harmonics of the fundamental longitudinal vibration of the waveguide were present in the signals. Future analysis of the acoustic emission signals, especially if the details of the break event itself are studied, may require the removal of the waveguide harmonics.

The lead break tests also showed that the acoustic emission system's cross correlation algorithm for locating events was less accurate than the system's threshold crossing algorithm. Analyzing the data from both sensors showed that, in general, the bulk wave sensors provided signals that were easier to use with the threshold crossing algorithm than the waveguide sensors. Based on these results, it was decided to conduct future experiments with both bulk wave sensors and waveguide sensors to determine event location.

The result of the acoustic emission tests conducted during the past year have resulted in a better understanding of how the energy from a fiber break propagates through the composite specimen. Understanding the acoustic energy propagation resulted in more accurate velocity values in the event location algorithms, and more efficient sensing mechanisms to detect the fiber break energy. In future tests both bulk wave and the waveguide sensors will be used to capture the fiber break events. The combination of sensors should provide more accurate event location and improve discrimination of actual fiber breaks from extraneous electronic noise and other acoustic events within the composite.

## **7.8 RESULTS FROM USING THE DRY COUPLANT ULTRASONIC SCANNING ON CMC**

The dry couplant ultrasonic C-scan system was used to characterize damage in six Si<sub>3</sub>N<sub>4</sub>-BN fibrous monolith specimens. The specimens were subjected to cyclic loading at different load levels creating damage near a notch cut into one edge of each specimen. Earlier experience with this material indicated that when notched specimens were loaded in tension, damage occurred ahead of the notch tip in the form of delaminations and multiple cracks. Single, well-defined cracks propagating from the notch tip did not develop.

The dry couplant C-scan system was selected for characterizing damage in the CMC because the boron nitride interphase was thought to be moisture sensitive. Although exposure to liquid couplants was acceptable for some of the testing, dry couplant techniques were desired for interrupted tests (where additional mechanical testing would occur after the damage characterization) and for evaluation for future laboratory and field applications.

The dry couplant C-scan system was mounted directly to the mechanical load frame and scanned specimens *in situ*, while the specimens were still in the grips. The C-scan system collected and stored ultrasonic A-scans at 1-mm intervals as the transducer was raster-scanned across the specimen. A 5 MHz, 6-mm diameter transducer was used incorporating a special polymer tip to couple the ultrasonic energy into the CMC specimen. Data were acquired over a 19 by 51 mm section of the specimen. Standard commercial ultrasonic pulser-receivers and A-D converters were used to acquire the data. The mechanical system that moved the transducer across the specimen, and periodically pressed the transducer to the specimen, was designed and built by UDRI. Typical data acquisition times were one hour.

The images produced by the dry couplant C-scan system correlated very well with images produced by other NDE techniques including thermal imaging, reflector plate immersion ultrasonics, and through-transmission immersion ultrasonics. The low resolution (1 mm) was evident in the dry couplant images, however, simple modifications and automation of the dry couplant system could easily improve the image resolution. Good correlation between the dry couplant technique and the other NDE techniques was achieved for all six specimens. The comparative results for one of the specimens is included in the paper "Damage Characterization of a Si<sub>3</sub>N<sub>4</sub>-BN Fibrous Monolith Using NDE Techniques", by J.L. Finch, et. al., published in the *Proceedings of the 23<sup>rd</sup> Annual Conference of the American Ceramic Society at Cocoa Beach On Composites, Advanced Ceramics, Materials, and Structures; January 25-29, 1999*.

The feasibility of using a dry couplant, ultrasonic, C-scan technique to detect damage in moisture-sensitive CMCs was demonstrated. Simple engineering modifications and automation of the transducer movement will result in an *in situ* NDE system suitable for characterizing damage in materials where the use of NDE techniques requiring liquid couplants is undesirable.

## **7.9 LABVIEW® CONTROL OF HIGH FREQUENCY TEST SYSTEM**

LabView®, a graphical programming package, was evaluated to determine its ease of use in creating Windows-based control software for the HCF fatigue test systems. A working program was generated that successfully demonstrated control and data acquisition functions of the magnetostrictive system operating at 2-kHz loading frequencies. The load waveform was generated directly from the D/A channel of a standard National Instruments board, eliminating the need for a separate waveform generator and expansion chassis. Based on the success of the trial software, a version of the LabView® software/hardware configuration is planned for the other HCF systems. Benefits will include upgrading to Windows environment, intranet test monitoring, and elimination of some custom built hardware required for HCF/LCF operation of the shakers. The need for the 12-bit WavTek function generators (two per system) will be eliminated by the waveform generating capabilities of the 16-bit boards (one per system). Software written in LabView® can be easily customized for future researcher needs.

## **7.10 DEVELOPMENT OF SHEAR WAVE ULTRASONIC SYSTEM FOR DETECTING FATIGUE CRACKS IN FRETTING TESTS**

A means of detecting small (< 0.500 mm long) fatigue cracks caused by fretting fatigue was needed that could "look inside" the fatigue specimen. The need to "look inside" the specimen arose because the cracks occurred in the specimen underneath the metallic pads used to create the fretting conditions. Thus, no portion of the crack was visible via optical inspection. Removing the specimen from the testing machine was inconvenient for several reasons including the increased risk of specimen misalignment relative to the fretting pads and the fact that the cracks exhibit very short crack propagation lives. The fatigue loading frequency was typically several hundred cycles per second. Thus, for a specimen expected to have a 10-million cycle fatigue life, of which crack propagation was expected to be 10% of life, the experimenter must choose the correct 15 - 20 minute time window to remove the specimen. The short time window carried with it an uncertainty of one hour or more due to variations in fatigue life from specimen to specimen. Consequently, trying to guess when a crack was present often resulted in either "no crack" or a "broken specimen".

The use of an ultrasonic NDE technique called “angle beam shear wave” was proposed to detect the fatigue cracks. The technique works by creating shear waves in the specimen traveling at a 45-degree angle. The shear waves reflect off the internal faces of the specimen as the energy propagates from the transducer towards the suspected crack (see Figure 2). Upon reaching the crack, some portion of the shear waves scatter from the crack surface and return to the transducer. If the crack is relatively smooth it forms a 90-degree reflector with the specimen surface and a large portion of the energy returns to the transducer.

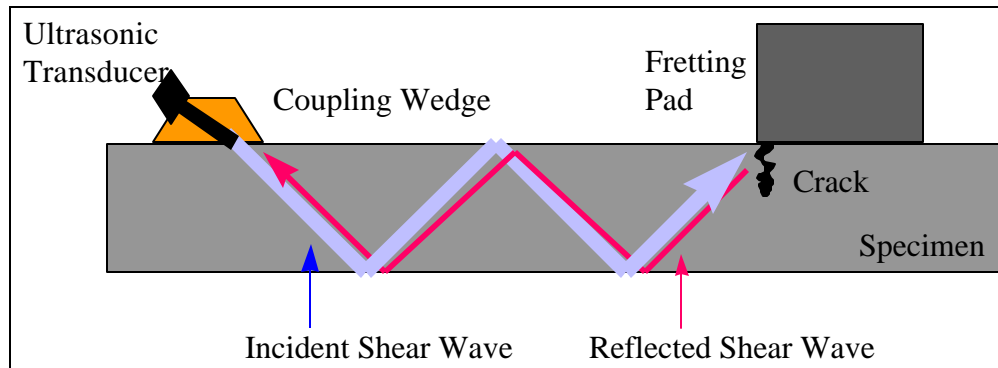


Figure 2. Ultrasonic Shear Waves Propagate within the Specimen and Scatter from Fretting Fatigue Cracks Growing Beneath the Fretting Pads

Preliminary tests have shown that the technique is feasible for detecting fretting cracks. In one test, a crack approximately 1 mm long was found in the specimen after the test was stopped due to changes seen in the ultrasonic signals. Future work is planned to optimize the ultrasonic transducers and incorporate multiple transducers to monitor all of the fretting regions in the specimen.

## 7.11 BIAxIAL FATIGUE FRETTING APPARATUS DESIGN

Results from the fretting fatigue data collected to date on flat samples have lead engineers to conclude that testing of a dovetail geometry is necessary to fully understand the fretting fatigue conditions in real hardware. In response to this need, a fretting fatigue apparatus has been developed to fit existing MTS and electromagnetic shaker systems. The gripping apparatus, test specimens, and fretting pads have been designed and manufactured, and the ability of the apparatus to simulate the damage observed in engine hardware is under investigation.

## 7.12 DATA ARCHIVAL AND STATUS OF KEYSERVER®

The Data Archive is a central computer on which test data generated by WUD 1 is stored and indexed. Its purpose is to prevent the loss of valuable test data and provide independent user access within WUD 1. Few fundamental changes have been implemented since the archive was established; however, one addendum to accommodate fiber test data has been made. Reference to single fibers was impractical, so the data was arranged by fiber groups according to the fiber source and heat treatment condition. A single number is assigned to each fiber batch. All tests for each batch are stored according to the assigned number. A results summary sheet is included, which indicates the strength and modulus results of each fiber test cross referenced with the test file name, as well as the type of failure for each fiber and any notes recorded by the technician. A large volume of test data was added to the archive for both fibers and coupons. Computer system support for the server was transferred to MLOC as a

result of changes in Air Force computer administrator regulations. The UDRI still supports local administration of file access privileges and works with MLOC on global system administration. The Keyserver® system, which was put in place in 1996 to provide hands-off control of commercial software licenses, has also been maintained. The system that houses the Keyserver® was upgraded to a faster machine to keep pace with current computer technology.



## **SECTION 8**

### **REFERENCES**

---

Gural, R.J., "In Situ Nondestructive Characterization of Damage Progression in Ceramic Matrix Composites at Room and Elevated Temperatures," M.S. Thesis, Department of Mechanical Engineering, University of Dayton, September 1998.

Kramb, V.A., R. John and L.P. Zawada, "Notched Fracture Behavior of an Oxide/Oxide Ceramic-Matrix Composite," *J. Am. Ceram. Soc.*, Vol. 82, No. 11, pp. 3087-3096, 1999.

Lang, M. and Marci, G., "Reflecting on the Mechanical Driving Force of Fatigue Crack Propagation," Standard Technical Publication 1332, American Society for Testing and Materials, West Conshohocken, PA, 1999

Wilson, D.M., "Statistical Tensile Strength of Nextel<sup>TM</sup> 610 and Nextel<sup>TM</sup> 720 Fibres," *J. Mat. Sci.* **32**, pp. 2535-2542, 1997.

**Appendix A**  
**Compendium of Manuscripts**

## ASSURING RELIABILITY OF GAMMA TITANIUM ALUMINIDES IN LONG-TERM SERVICE

James M. Larsen, Andrew H. Rosenberger, Brian D. Worth<sup>†</sup>, Kezhong Li<sup>\*</sup>, David C. Maxwell<sup>\*</sup>, and W. John Porter<sup>\*</sup>

Air Force Research Laboratory, Materials and Manufacturing Directorate, (AFRL/MLLN)  
Wright-Patterson Air Force Base, Ohio 45433-7817, USA

<sup>†</sup> Previously with the University of Dayton Research Institute; now deceased.

<sup>\*</sup>The University of Dayton Research Institute  
Dayton, Ohio 45419-0128, USA

### Abstract

Gamma TiAl alloys offer the potential for major reductions in the weight of turbine engine components, if higher-density materials can be replaced without sacrificing long-term reliability in service. To assess this potential, an overview is presented of the structural capabilities available from gamma titanium aluminide alloys. Emphasis is given to effects of material defects, mechanistic aspects of fatigue damage evolution, and the roles of high temperature, time-dependent deformation and environment. Although gamma alloys exhibit excellent fatigue strengths, in many applications the material's resistance to service-induced damage is a critical concern. In turbine engines, such damage may result from impacts by foreign objects in the flow path. In addition, numerous components in turbine engines are subject to both low- and high-cycle fatigue. To predict the range of behavior that may be expected for gamma titanium aluminides requires consideration of damage tolerance, specifically addressing the potential for growth of small fatigue cracks that may form under a variety of circumstances. Approaches for life prediction in these materials are discussed, emphasizing the roles of fatigue crack initiation and growth. In addition, an attempt is made to assess the strengths and limitations of these materials with respect to application requirements and to suggest avenues for improvements in the balance of mechanical properties.

### Introduction

Gamma titanium aluminides have been under examination for aerospace applications for more than 20 years. Significant progress has been made in understanding their mechanical behavior, in developing improvements in their balance of properties, and in reexamining barriers to utilizing limited-ductility alloys in structural applications. Thus far, however, the application of these materials has been limited to a few low-risk components. This is due largely to a long-standing caution associated with using new materials in fracture-critical structures. In fact, the US Air Force requires all fracture-critical engine components be designed based on a damage tolerance philosophy, which is detailed in the Engine Structural Integrity Program, ENSIP [1]. To overcome current design and life-management concerns will require advances in life prediction techniques that lead to reliable and durable, *full life* components.

This paper describes some efforts aimed at developing the scientific basis for a damage tolerant design philosophy tailored for

intermetallics in general and specifically the gamma titanium aluminide class of materials. The general fatigue behavior of several gamma alloys and microstructures is discussed, along with the influence of intrinsic material defects on the fatigue life and the associated scatter in fatigue properties. A simple life integration is used to illustrate the influence of large-crack growth rates and crack-growth thresholds on component life. The fatigue crack growth behavior found for gamma alloys is compared with the behavior of a conventional,  $\alpha+\beta$  titanium alloy to illustrate the opportunities and obstacles presented by gamma alloys. The intermediate temperature behavior of these materials is discussed as one area of particular design concern. Also highlighted is the likely influence of small-crack growth behavior, which is inferred from the fatigue performance of notched specimens. This paper concludes with a discussion of progress and work remaining in the development of damage tolerant design tools for gamma alloys.

### Materials and Experimental

A number of gamma alloys have been, and continue to be, under examination for Air Force applications. Among these are the alloys and microstructures used in the current study, which are shown as back-scattered SEM images in Figure 1. Figures 1a through 1c, show the K5 alloy (Ti-46.5Al-2Cr-3Nb-0.2W) in three different microstructural conditions: duplex, refined-fully lamellar, and coarse lamellar, respectively. Figure 1d presents the microstructure of a similar carbon-boron-silicon-modified K5 alloy (Ti-46Al-2Cr-2.7Nb-0.1B-0.2W-0.15Si-0.2C), known as KD-CBS. Figure 1e shows the scaled-up alloy 3-95 (Ti-46Al-2Cr-2Nb-1Mo-0.2B) [2], and the cast alloy 47XD<sup>TM</sup> (Ti-47Al-2Nb-2Mn-0.8B) from Howmet is presented in Fig. 1f. Compositions of all alloys are given in atomic percent. Additional processing and mechanical property information on these alloys can be found in Refs. [3] and [4]. In general, the duplex microstructure composed of a mixture of single-phase  $\gamma$  grains and lamellar  $\alpha_2 + \gamma$  grains (Fig. 1a) produces the best balance of tensile properties, including strength and elongation when compared to nearly lamellar microstructures (Fig. 1b-f). However, materials with lamellar microstructures are superior in creep, toughness, and fatigue crack growth resistance. Improvements in the tensile properties of lamellar material, through reductions in colony size, also have been demonstrated [5].

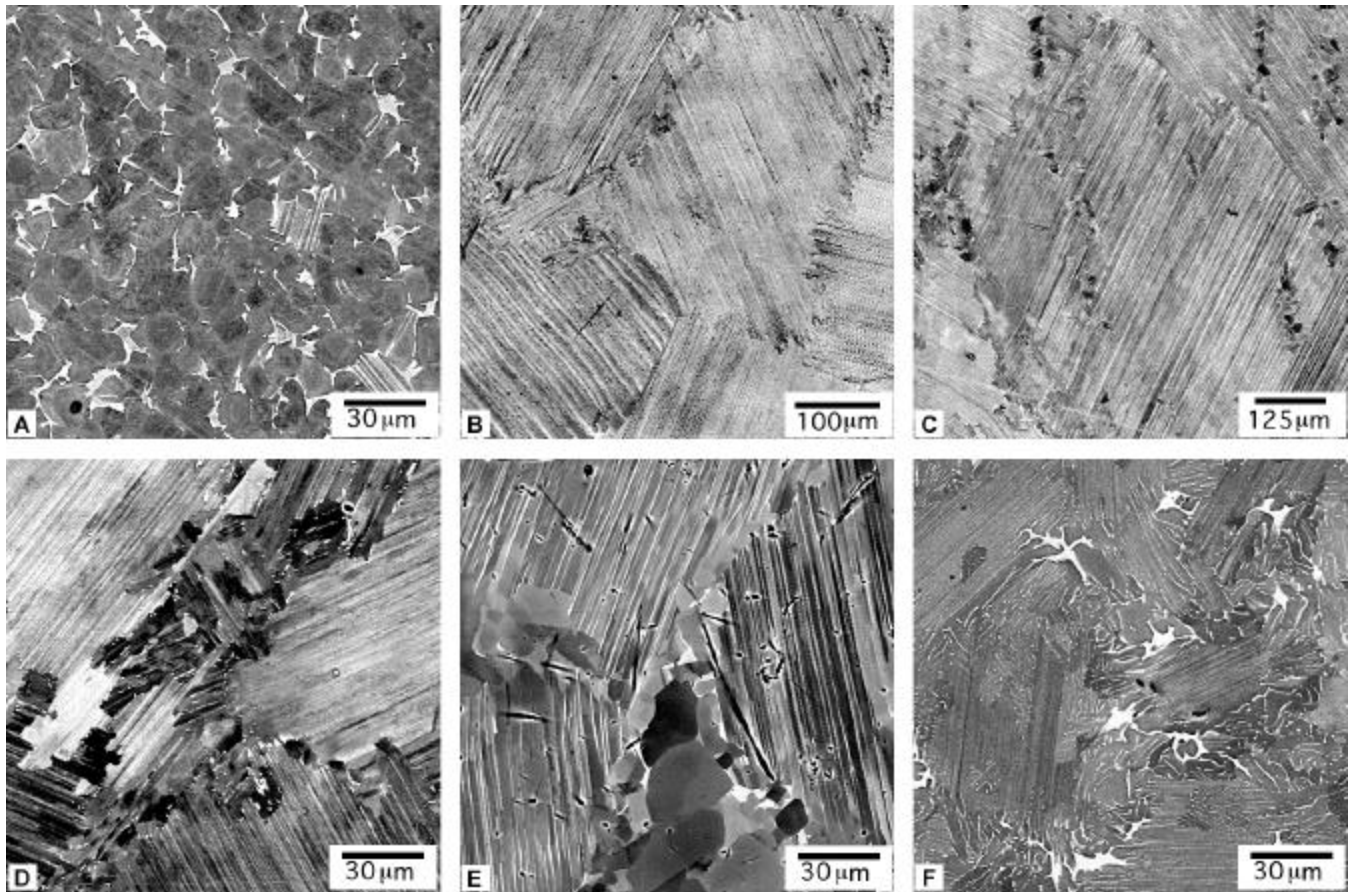


Figure 1: Six gamma alloys and microstructures under consideration for aerospace components (compositions in at%): (a) K5 (Ti-46.5Al-3Nb-2Cr-0.2W) duplex, (b) K5 refined fully lamellar, (c) K5 coarse lamellar, (d) KD-CBS (Ti-46Al-2Cr-2.7Nb-0.2W-0.15Si-0.1B-0.2C), (e) 47XD™ (Ti-47Al-2Nb-2Mn-0.8B), and (f) alloy 3-95 (Ti-46Al-2Nb-2Cr-1Mo-0.2B).

## Results

### Fatigue Resistance

The smooth-bar fatigue performance of the six materials is shown in Fig. 2. In the K5 alloy, it is apparent that a refinement of the lamellar colony size significantly improves the fatigue performance, such that it mimics that of the fine-gained duplex material. The CBS derivative of K5 exhibits similar fatigue performance, while the weaker 47XD™ alloy demonstrates fatigue resistance similar to that of the coarse lamellar K5. Alloy 3-95 exhibits tremendous variability in fatigue life at a given stress (up to five orders of magnitude), and no reasonable best-fit curve was possible for this material. In the specific heat of this alloy that was examined, inherent variations in microstructure and material processing defects were responsible for the high fatigue scatter, as discussed later in this paper and in more detail by [4,6].

A comparison of the fatigue performance of the six microstructures as a function of the maximum cyclic stress normalized by ultimate tensile strength is shown in Figure 3. All materials fall in a tight band having  $10^7$ -cycle endurance limits greater than 75% of their UTS. Another comparison of these materials shows that all have endurance limits greater than 90% of their respective yield strengths. This indicates that gamma alloys have impressive smooth-bar fatigue resistance, in spite of the fact that they exhibit *open*  $\sigma$ - $\epsilon$  hysteresis loops throughout their fatigue lives. Although the high smooth-bar fatigue properties of gamma alloys may make a safe-life design

philosophy attractive, such an approach fails to take into account the debit in fatigue resistance that occurs due to effects of realistic material defects or damage produced during processing, use, or maintenance.

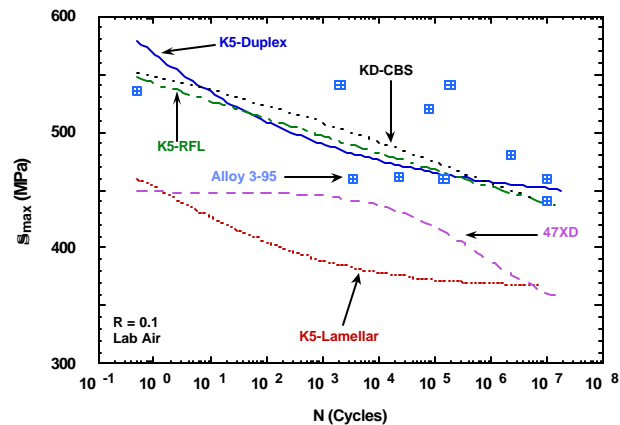


Figure 2: Smooth-bar fatigue performance of the six alloys at room temperature and  $R = 0.1$ .

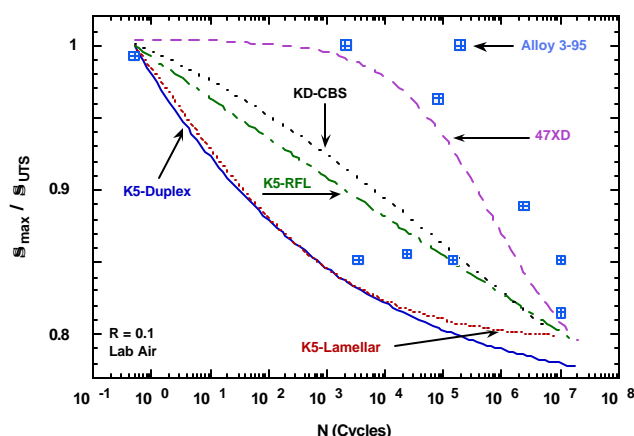


Figure 3: Smooth-bar fatigue performance of the six alloys normalized by their ultimate tensile strength.

### Defects in Cast and Wrought Gamma Alloys

The fatigue resistance of gamma alloys is significantly degraded by defects [6]. These can include material defects (porosity, inclusions, non-homogeneous microstructure), service-induced damage (foreign object damage, domestic object damage, surface embrittlement, and LCF or HCF crack initiation), and defects or damage produced during manufacturing and maintenance (tool nicks or over straining). Considerable efforts have been, and are being, devoted to understanding the influence of defects and damage. The location of defects with respect to the orientations of the surrounding microstructure has been shown to be important [3]. Notch fatigue tests by Worth, et al in coarse lamellar material often resulted in cracks initiating at locations well away from the notches, highlighting the anisotropic nature of the microstructure.

Alloy 3-95, being a single-hearth plasma-arc-melted ingot, contained a number of inclusions, pores, and melt inhomogeneities that are believed to have led to the tremendous scatter in fatigue properties of this material. This Mo-containing alloy also has a propensity for forming a cellular B2 +  $\gamma$  phase, which may reduce resistance to fatigue crack initiation. Shown in Fig. 4 is a micrograph of a series of alumina inclusions found in alloy 3-95. Although the individual particles are small, when they are aligned they can severely degrade the fatigue resistance. A more complete discussion of the various microstructural defects observed in gamma alloys can be found in [4,6]. Harding, et al., [7,8] are examining the effects of foreign object damage and simulated tool nicks on the fatigue behavior of several gamma alloys. This damage also reduces the fatigue strength – again indicating that the design philosophy for gamma alloys must incorporate a damage tolerant approach for fracture critical components.

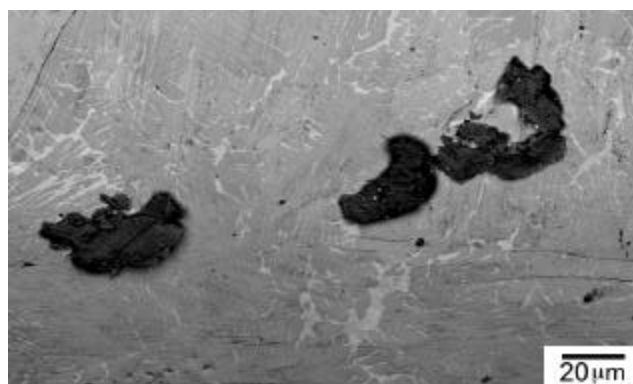


Figure 4: Alumina particles in alloy 3-95 which, when aligned, represent a serious microstructural defect in this alloy.

### Effect of High Temperature Exposure

Usage conditions for gamma alloys in turbine engines will include long exposures at elevated temperatures, which could be viewed as producing another form of structural defect in the material. Elevated temperature exposure has been shown to produce a detrimental effect on the room temperature ductility [9-11]; however, it was found that the ductility debit occurs only if the subsequent test temperature is below 200°C [10]. The influence of high temperature exposure on the fatigue properties of alloy 3-95 has been examined [12], and it was found that a debit in fatigue resistance also exists. Additionally, as discussed below, the fatigue behavior is affected differently than the tensile behavior, and this has a direct influence on the service performance of gamma alloys.

**Tensile Effects** As shown in Fig. 5, an exposure to air at 760°C results in a significant reduction in ductility at room temperature for exposures as short as 50 hrs, while at 540° and 760°C, there is no noticeable ductility reduction – consistent with other investigations [10,11]. The concomitant reduction in tensile strength at room temperature was ~75 MPa. There was also, however, a reduction in the tensile strength at 540°C, by ~40-50 MPa, that was partly due to cracking in the embrittled annulus of the affected surface material. For example, cracks were found that extended 20 to 30  $\mu$ m into the material. This type of strength reduction is previously undocumented and should be taken into account for reliable long-term design. Post-exposure removal of the affected surface restored the as-received properties.

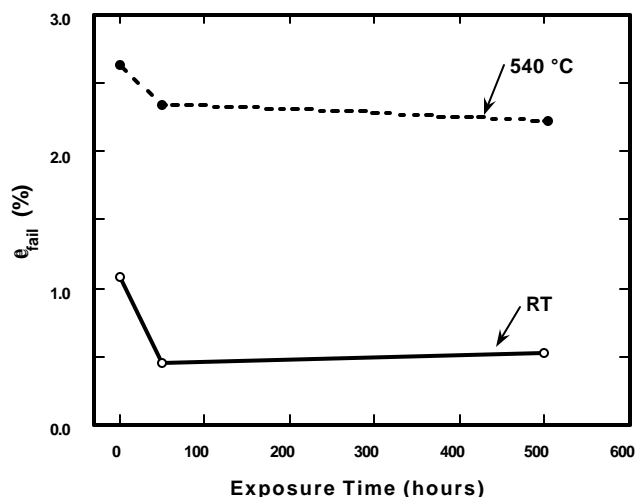


Figure 5: Failure strain versus exposure time for room temperature and 540°C tensile tests. All tests at 760°C resulted in strains to failure in excess of 30 percent.

**Fatigue Effects** The effect of identical high temperature exposures on the fatigue endurance limit was examined for alloy 3-95. Specimens were exposed in air at 760°C and subsequently fatigue tested using the step-stress method [13]. A plot of the  $10^7$ -cycle fatigue strength as a function of temperature is shown in Fig. 6 for unexposed specimens and specimens exposed at 760°C for 500 hours. The unexposed specimens appear to exhibit a slight increase in fatigue resistance between room temperature and 540°C, with a 25% drop in fatigue capability at 760°C. After exposure at 760°C, the most severe reduction in fatigue strength occurs at 540°C (~80 MPa), with a lesser decrease at 760°C and almost no reduction at room temperature. This type of fatigue-strength reduction is also previously undocumented and must be taken into account for reliable long-term design. The fatigue properties of the unexposed material were largely restored after low-stress grinding to remove the embrittled layer.

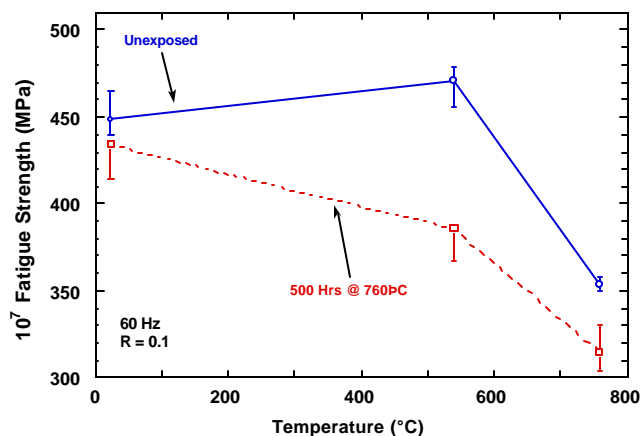


Figure 6:  $10^7$ -cycle fatigue strength versus temperature for as-received specimens and specimens subject to 760°C for 500 hrs.

#### Fatigue Crack Growth

It is well known that microstructure and temperature have a pronounced effect on the fatigue crack growth resistance of gamma alloys [e.g., 14-17]. This behavior is exemplified by the data shown in Fig. 7 for the duplex and coarse lamellar K5 materials, whose microstructures were presented in Figs. 1a and 1c, respectively. As shown in Fig. 7, at a given temperature, the lamellar microstructure

exhibits much greater fatigue crack growth resistance than does the duplex material. The lamellar material also holds a substantial advantage over the duplex microstructure in terms of threshold stress intensity factor range,  $\Delta K_{th}$ , and the apparent fracture toughness,  $K_{Ic}$ .

For both of these microstructures, the crack growth rate data exhibit the steepest slope at room temperature. The power-law exponent of the K5-D material is approximately 23, while the similar exponent for K5-FL is about 7. As shown in the figure, increasing the temperature to 600°C results in a significant increase in growth rates at the lower  $\Delta K$  values, coupled with a decline in  $\Delta K_{th}$  and an apparent increase in  $K_{Ic}$ , at least in the duplex material. Further increasing the temperature to 800°C reverses this trend, and  $\Delta K_{th}$  increase again. Thus, the intermediate temperature represents a worst case in terms of crack growth resistance. This unusual behavior at intermediate temperatures is well documented for various alloys [18,19], although as discussed below, the cause of the behavior remains in debate.

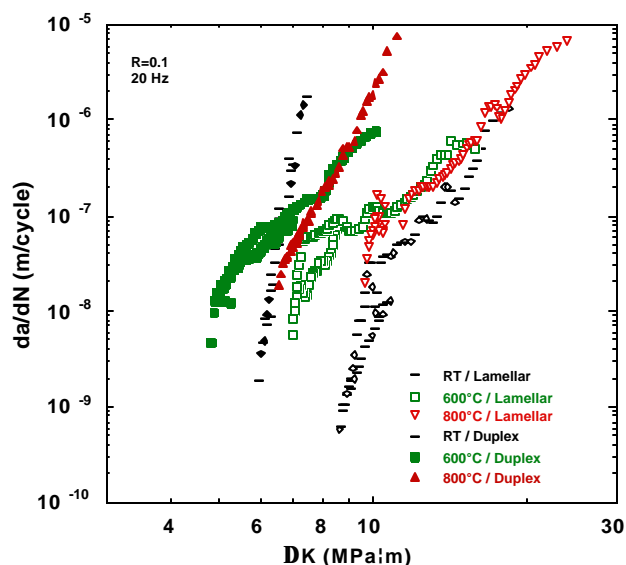


Figure 7: Effect of temperature on fatigue crack growth rate behavior for the duplex and coarse lamellar microstructures.

#### Fatigue Crack Growth at an Intermediate Temperature

The effect of temperature on  $\Delta K_{th}$  is illustrated in Fig. 8 for five of the materials shown in Fig. 1. It is apparent that all these materials and microstructural variants exhibit a similar temperature dependence on threshold. That is, the lowest threshold occurs within the temperature range of 540° to 650°C, with higher thresholds above and below this range.

This “anomalous” temperature dependence has been attributed to oxide induced crack closure [20], whereby the effective crack driving force at the highest temperatures is reduced as the result of an oxide wedging action known as oxide-induced crack closure. These findings were supported by crack-flank oxide thickness measurements, however no attempt to measure crack closure was reported. Alternatively, Rosenberger, et al., [18] proposed that the minimum in  $\Delta K_{th}$  at the intermediate temperature is due to environmental embrittlement that is especially virulent at temperatures slightly below the brittle-to-ductile transition temperature. Careful measurement of crack closure at elevated temperature revealed that there was no increase in crack closure at the highest temperatures, in



contrast to what would be expected based on the mechanism of oxide-induced closure. In fact, it was found that crack closure decreased at the highest temperatures. Complementary tests conducted in an ultra-high vacuum environment ( $3 \times 10^{-7}$  Pa) revealed that fatigue crack growth rates were reduced by as much as two orders of magnitude, *and* the intermediate-temperature anomaly was absent.

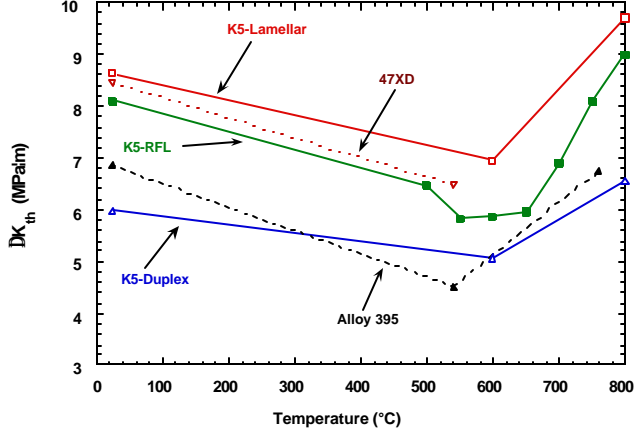


Figure 8:  $DK_{th}$  as a function of test temperature for five of the materials shown in Figure 1.

Additional analysis of crack-mouth-opening-displacement (CMOD) as a function of temperature was conducted on a number of the materials in this paper. The normalized CMOD as a function of cycles is shown in Fig. 9 for alloy 3-95, which typified results from the other alloys. In this figure, the measured CMOD is normalized by a prediction from Newman [21] based on time-independent linear elastic fracture mechanics. At lower temperatures, CMOD is reasonably well predicted by Newman's formulation, i.e., normalized CMOD  $\approx 1$ . At the highest temperature, 760°C, the measured CMOD increases as a function of cycles, relative to the prediction. This indicates that there is a monotonic increase in crack opening displacement, or that the region of the crack tip is accumulating creep strain. Under this condition of accumulated crack opening strain, it is unlikely that oxide induced crack closure has a significant effect. The more probable cause for the increase in  $DK_{th}$  at high temperatures is a local reduction of the stress intensity factor due to crack tip blunting and an associated redistribution of the crack tip stress field.

#### Residual Crack Propagation Lifetime

As an aid to quantify the significance of the unusual temperature dependence of crack growth rate behavior in the gamma alloys, one may consider its influence on the crack propagation lifetime. A simple estimate was performed by calculating the number of cycles required to propagate a crack from an initial size,  $a_i$ , to failure under realistic loading conditions. Assuming that the

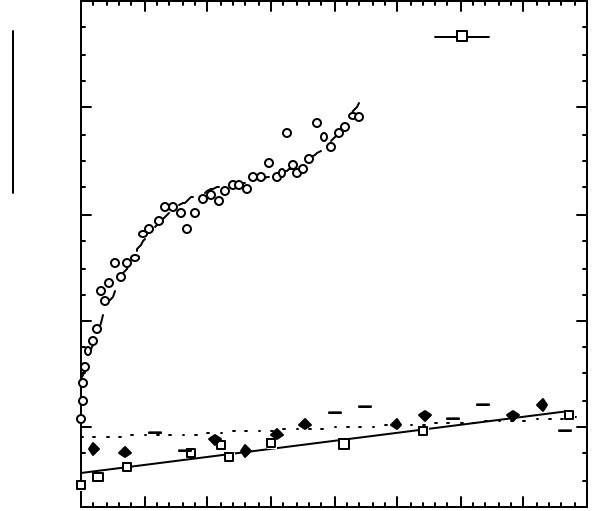


Figure 9: Mean CMOD normalized by predictions of Newman [21] as a function of cycles for alloy 3-95 at RT, 540°C and 760°C.

large-crack behavior depicted in Fig. 7 applies to the small cracks that grow in actual components, the crack propagation lifetime is given by

$$N_p = \int_{a_i}^{a_c} \frac{da}{f(\Delta K)} \quad (1)$$

where  $a_c$  is the critical crack length corresponding to the material's effective fracture toughness in fatigue ( $K_Q$ ),  $f(\Delta K)$  is a crack-growth-rate function representing the data, and  $DK$  is defined for a specific crack geometry and loading history. In the example calculations to follow, the crack was assumed to be a semicircular surface flaw of depth  $a$ , which is a typical crack geometry observed in actual components.

To examine the effect of the assumed initial crack size,  $a_i$ , on the calculated crack propagation lifetime,  $N_p$ , based on the large-crack data, Eq. 1 was solved numerically to construct the remaining-life plot shown in Fig. 10. For a given  $a_i$ , and a set of loading and temperature conditions,  $N_p$  is given by the ordinate on the plot. For purposes of comparison and discussion later, the figure also shows results of calculations for a conventional titanium alloy, Ti-6Al-2Sn-4Zr-6Mo, under the same loading conditions at room temperature. The six gamma curves shown have features common to all life calculations performed using the crack growth data of Fig. 7. For combinations of  $a_i$  and loading conditions that result in  $DK$  less than  $DK_{th}$ ,  $N_p$  in Fig. 10 is infinite. When  $DK_{th}$  is exceeded, however, there is a sharp transition from infinite predicted lifetime to finite lifetime. Based on the large-crack data, and an assumed maximum stress of  $S_{max} = 325$  MPa, the threshold crack depths,  $a_{th}$ , corresponding to  $DK_{th}$  were 0.27, 0.21, and 0.33 mm for the duplex materials at room temperature, 600°C, and 800°C, respectively. For the lamellar material at the same three temperatures these values were 0.64, 0.37, and 0.77 mm. As shown in the figure, for crack sizes exceeding these threshold values, the total remaining life in fatigue crack growth in each case was less than about  $10^6$  cycles, and most similarly-estimated lives were substantially less than  $10^5$  cycles. In the duplex

material at 600°C, this transition occurred at less than  $10^4$  cycles. Thus, assuming that large-crack behavior applies to the physically small cracks of interest in actual engine components, for cyclic lives greater than about  $10^5$  cycles for most usage conditions,  $\Delta K_{th}$  must not be exceeded if failure is to be avoided.

Since major rotating components in turbine engines are commonly life-limited by low-cycle fatigue, the overall crack-growth resistance of a material is also of major importance. For example, turbine engine components in fighter aircraft are commonly designed for a full life of approximately 8,000 total accumulated cycles (TACs), and the engine overhaul and inspection intervals are typically half the full life. This condition places great importance on crack growth resistance, which, as shown in Fig. 7, can vary significantly as a function of microstructure and temperature. For all three temperatures, the remaining life curves for the duplex material terminate at relatively small crack sizes, as shown in Fig. 10, particularly at the intermediate temperature. Under the same loading conditions, the lamellar material can tolerate much larger cracks without failure. The implications of this difference will be discussed later.

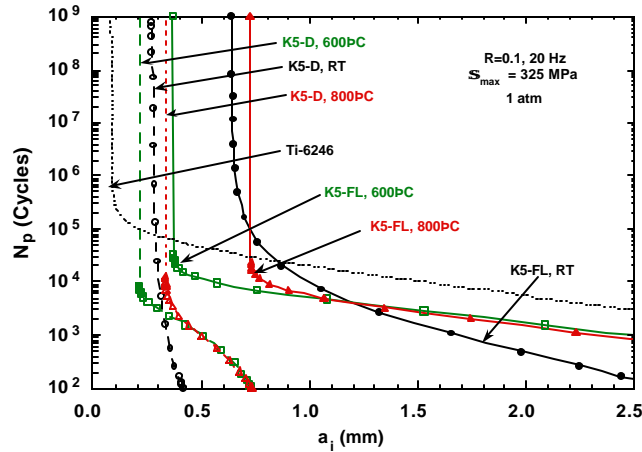


Figure 10: Effect of temperature on remaining fatigue crack propagation lifetime for the duplex and coarse lamellar microstructures of alloy K5 and for Ti-6246.

#### Fatigue Life Maps

To help visualize the role of crack size in a life analysis, one can construct a life map that outlines regions of expected fatigue life in terms of stress and crack size. This format follows from the original work of Kitagawa and Takahashi [22]. These authors identified an apparent “safe region”, shown schematically in Fig. 11, that is bounded by the  $10^7$ -cycle fatigue limit,  $\Delta S_e$ , and the threshold stress intensity factor range,  $\Delta K_{th}$ . These two limiting lines intersect at the crack size  $a_0$ , and all combinations of stress range and crack size within the safe region are below both  $\Delta S_e$  and  $\Delta K_{th}$ . Another limiting region on the diagram is defined by the conditions whose exceedence would produce fracture in a single cycle: the ultimate tensile strength, UTS, and the effective fracture toughness,  $K_{Ic}$ . A third domain lies between the safe and fracture regions, defining the combinations of  $\Delta S$  and crack size that result in finite fatigue lifetimes.

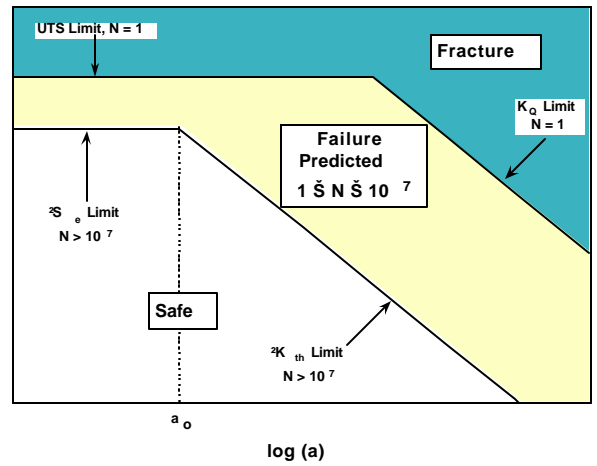


Figure 11: Schematic a life map showing regions of calculated resistance to cyclic loading in terms of stress range,  $\Delta S$ , versus crack size,  $a$ .

Figure 12 presents a life map for the duplex microstructure of alloy K5. The curves of constant life between the “safe” and “fracture” boundaries represent remaining crack propagation lifetimes calculated by numerical integration of Eq. 1 for an assumed semicircular surface crack. The crack growth calculations assume the large-crack data from Fig. 7 appropriately represent crack growth rates for small surface cracks; the implications of this assumption will be discussed later. The figure shows that the steep crack-growth-rate curve of this material translates into a relatively narrow region of crack growth between the limit lines for  $\Delta K_{th}$  and  $K_{Ic}$ . Assuming that large-crack behavior prevails, this figure indicates that once a crack exceeds  $\Delta K_{th}$  in this material, the crack length could increase only about a factor of three before fracture occurred. This situation presents a major obstacle to the effective application of a damage tolerant approach under low-cycle-fatigue conditions, since there would be relatively little opportunity for detection of a propagating crack and subsequent removal of the component from service.

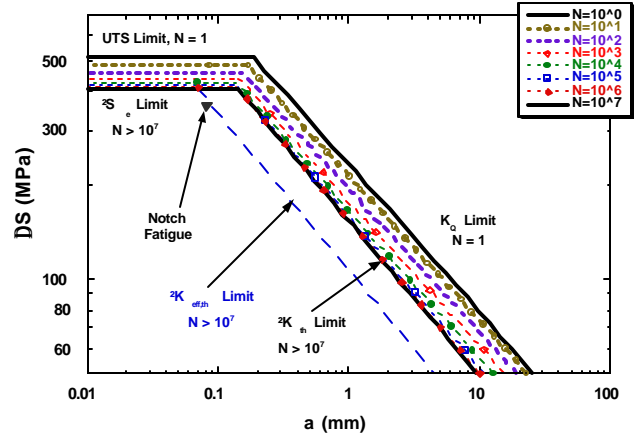


Figure 12: Fatigue life map for the duplex microstructure of alloy K5 under R=0.1 fatigue.

To assess the crack-size dependence of the life predictions depicted in Fig. 12, fatigue experiments were performed using smooth specimens containing multiple, semicircular surface notches of depth equal to 0.080 mm [16]. The resulting  $10^7$ -cycle fatigue limit for these notched specimens is also plotted as an individual data point on the figure. This result agrees well with the  $\Delta K_{eff,th}$  line, which represents the threshold-stress-intensity-factor range after correcting the data for crack closure. This good agreement might be expected,



since a given notch would be closure-free over its full initial length. The agreement also suggests that, for the duplex microstructure, the large-crack threshold may be applicable to cracks at least as small as 0.080 mm.

Similar multi-notch fatigue experiments were performed on the refined fully lamellar material of Fig. 1b, and as shown in Fig. 13, the agreement with the limit line corresponding to  $\mathbf{DK}_{eff,th}$  was again relatively good. In this case, experiments were performed using three distinct multi-notch depths: 0.080, 0.200, and 0.400 mm. The 0.080-mm notch data fell to the left of the  $\mathbf{DK}_{eff,th}$  prediction, which might be expected since the fatigue limit stress for these specimens approached  $\mathbf{D}_e$ . The figure also shows that the width of the region of crack propagation between the  $\mathbf{DK}_{th}$  and  $K_Q$  limit lines corresponds to an order-of-magnitude increase in crack size for this material.

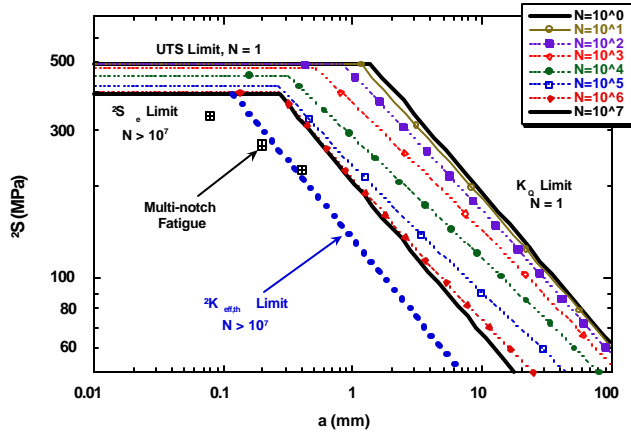


Figure 13: Fatigue life map for refined fully lamellar gamma alloy K5 with R=0.1.

Figure 14 presents a detailed life map for the coarse lamellar K5 alloy. This material also exhibited good crack growth resistance compared to the duplex material. As shown in the figure, however, fatigue tests of the K5-L specimens containing multiple, 0.080-mm-deep, semicircular surface notches produced an unusual result [23]. As shown by the open symbols, four of these specimens failed under loading conditions that were well below the predictions based on  $\mathbf{DK}_{eff,th}$ . A detailed examination of the fracture surfaces of these specimens indicated that the critical crack typically formed from a notch located in a lamellar colony such that the normal of the lamellar orientation was within  $\sim 20^\circ$  of the loading axis. Apparently this configuration led to nucleation of a crack in the weak lamellar colony orientation, and the crack grew quickly across the lamellar colony in the relatively low-toughness, interlamellar mode. At this point  $\mathbf{DK}$  of this ‘pop-in’ crack, conservatively calculated as a semicircular surface crack, was close to the bulk coarse lamellar threshold,  $\mathbf{DK}_{th} = 8.5 \text{ MPa}\sqrt{\text{m}}$ , and subsequent failure of the specimen occurred due to propagation from this flaw. The multi-notch specimen indicating the highest fatigue strength appeared to fail from the smallest ‘pop-in’ crack, which was also the most inclined to the loading axis – resulting in fatigue strength comparable to smooth specimens. The specimen with the poorest fatigue resistance failed in a lamellar colony with the hardest orientation, and had a neighboring colony with a sympathetic orientation within  $6^\circ$  of the original colony.

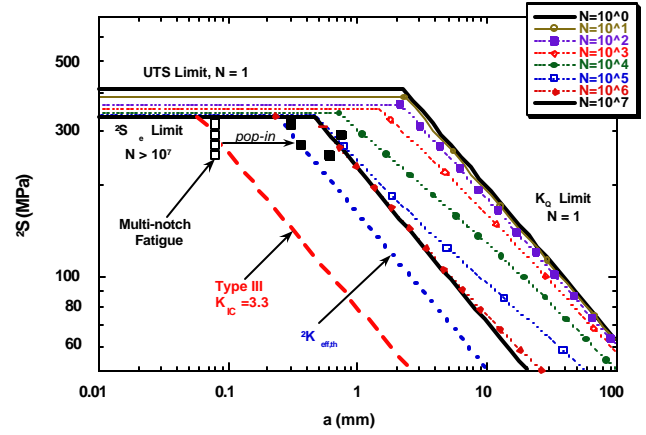


Figure 14: Fatigue life map for coarse lamellar gamma alloy K5 with R=0.1.

Some insight into these results may be gained by considering the findings of Yokoshima and Yamaguchi [24] on polysynthetically twinned (PST) crystals. These researchers determined fracture toughness as a function of crack plane for two typical gamma PST materials. They reported that a minimum in fracture toughness occurred when the axis of loading was normal to the lamellar planes, which they designated as Type III loading, noting that  $K_{IC(min-Type III)} = 3.3 \text{ MPa}\sqrt{\text{m}}$ . Using this approximate value, one may add the Type III limit line indicated in Fig. 14, and see that this trend agrees well with the multi-notch data assuming a 0.080-mm depth. The specimen that failed at the highest stress exhibited failure that was not strongly influenced by the notch. Hence, it fell close to the fatigue limit line. The other data fell below this line and close to the sloped line of the Type III  $K_{IC}$ . None of these specimens achieved  $10^7$  cycles without failure, which might be expected since it is likely that the threshold for fatigue crack propagation,  $K_{max,th}$ , is below  $K_{IC(min-Type III)}$ . This comparison of PST behavior with that from the random lamellar material indicates that fatigue initiation and early propagation are closely related to the behavior of a few, specifically orientated lamellar colonies, and that this effect should be designated as microstructurally-small-crack behavior.

## Discussion

As shown in Figs. 2 and 3, effects of alloy composition and microstructure can have a dramatic effect on the strength and fatigue performance of gamma titanium aluminide alloys. However, some of the alloys examined in this study exhibited a variety of processing defects that reduced this capability. Moreover, service-related damage, such as that produced by foreign object impact or by high-temperature oxidation, also affects the useful fatigue capability of these materials. Although continued improvements in processing practices will certainly reduce the occurrence of microstructural defects, it is highly unlikely that one can preclude the possibility of such defects, and service-related damage will be virtually impossible to eliminate. Therefore, one must accommodate the potential for intrinsic material defects and service damage.

As shown in Fig. 7 for the K5 alloy, effects of microstructure and temperature can have a dramatic effect on crack growth resistance, which leads to questions regarding life management criteria for components that require damage tolerance. Since turbine engine loading spectra may contain low- and high-cycle fatigue, a material's crack-growth-threshold and mid-range crack growth behaviors are both important. This complicates the material selection process since, as shown in the figure, the trend in crack-growth threshold may run counter to a material's mid-range crack growth resistance.

Although gamma alloys typically exhibit relatively steep crack growth rate curves, their comparatively high levels of  $\mathbf{DK}_{th}$  represent an extremely attractive feature.

For example, Fig. 10 shows that at the same stress level, the threshold crack size for the two K5 microstructures at all three temperatures is much greater than in the Ti-6246 at room temperature. The duplex condition of the gamma alloy, however, can only tolerate a very small crack extension prior to failure, which would make this material a poor choice for applications that are significantly influenced by low cycle fatigue. Alternatively, it was shown that the propagation condition for small fatigue cracks in lamellar microstructures, which is governed by interlamellar splitting of similarly-aligned, poorly-oriented colonies, falls well below the predictions based on large-crack fracture mechanics. Thus, this microstructure is poorly suited for applications requiring good threshold crack growth resistance for small flaws. It appears, however, that the worst-case crack propagation behavior associated with interlamellar cracking does not dictate fatigue capability and defect tolerance, if the colony size is sufficiently small. This suggests that a refined lamellar microstructure may be most attractive in many instances. Further insight into this materials design and selection problem could be gained through improved modeling and simulation capabilities.

Figure 15 provides some perspective on the significance of  $\mathbf{DK}_{th}$  and  $K_Q$  for component life management based on damage tolerance. The figure plots results for the duplex and lamellar K5 microstructures in comparison with the Ti-6246 material. The latter material provides an important scale of reference, as this high-strength material has been used in a variety of turbine engine components. Assuming a semicircular surface crack under fatigue at room temperature ( $R = 0.1$ ), the figure plots the relationships between crack depth and applied maximum stress corresponding to  $\mathbf{DK}_{th}$  and  $K_Q$ . The solid curves represent the combinations of crack depth and  $S_{max}$  that correspond to the fracture condition,  $K_Q$ . For each material, the region above the curve represents conditions that will produce fracture in a single cycle. In a similar manner, the dotted curves represent the crack-depth and  $S_{max}$  conditions corresponding to threshold crack growth,  $\mathbf{DK}_{th}$ . Crack growth should not occur in the regions below these curves, so long as large-crack data apply to the small cracks. As shown in the figure, the Ti-6246 represents the extremes in behavior. The advantage in  $\mathbf{DK}_{th}$  offered by the gamma alloys is evident, although the relatively small critical crack sizes required for fracture of duplex material is a key concern. The lamellar material looks more attractive in terms of both threshold crack growth and fracture resistance.

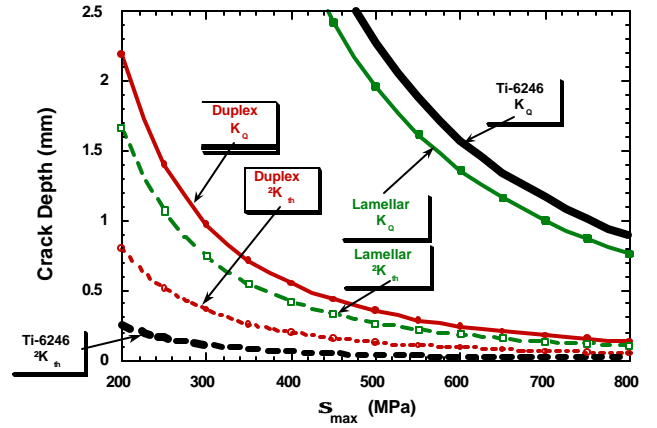


Figure 15: Critical crack sizes corresponding to threshold crack growth,  $\mathbf{DK}_{th}$ , and fracture,  $K_Q$ , plotted versus maximum stress for tests at room temperature.

The temperature dependence on fatigue crack growth rates, and the more severe debit in smooth-bar fatigue resistance after elevated temperature exposure, indicates that intermediate temperatures represent a worst case condition for gamma alloys. This effect should be a foremost consideration in design and use of these alloys. Moreover, if the increase in  $\mathbf{DK}_{th}$  at the highest temperatures is due to crack tip blunting, there could be an important crack-length/net-section-stress interaction that affects the small-crack behavior at the elevated temperatures. This effect could be beneficial, however, given that crack growth resistance tends to increase at temperatures above approximately 600°C. Ultimately, one should characterize the expected use-temperature spectra and assess the practical importance of the effects of intermediate temperature exposure for specific components.

The *small-crack-growth* implications of this work offer a different view of this problem than that presented by other researchers in the field [25-27]. These researchers have generated small-crack growth data using naturally initiated cracks in gamma alloys and have found “typical” small-crack behavior. That is, the small-crack growth rates are higher, and crack propagation thresholds are lower, than found for large cracks. These data, however, were generated at stresses above the endurance limit of the specific gamma alloys that were examined. This is clearly evident in the presentation of the data by Chan [27]. Since there are no plans to design turbine engine components in this high-stress regime [28], there are doubts as to the importance of these small-crack findings. The approach chosen for the current work was to consider the small-crack initiation and growth problem from the damage tolerant design point of view. Here, cracks were grown from EDM notches at stresses *below* the endurance limit of the materials. These data is more likely to represent the component stress conditions and more accurately assess the realistic response of the material. Based on the fracture toughness data of Yokoshima and Yamaguchi [24], it is apparent that all gamma components will develop cracks of the order of the lamellar colony size in colonies having a “hard” orientation (lamellae tending to be normal to the axis of loading). We believe that the critical event is the continued growth of these cracks, rather than their formation. The structural design, therefore, should *prevent the growth* of such cracks, and as such it must rely on a crack growth threshold.

In general, it appears that the development of improved damage-tolerant life-prediction methods is needed to utilize the full potential of gamma TiAl alloys as structural materials. The unique balance of properties offered by these alloys presents important opportunities for increased turbine engine performance, but the introduction of these materials into use for fracture-critical engine components must be accomplished without increasing the risk of failure. To *fully utilize* the inherent capability of gamma alloys will require an unprecedented level of accuracy in life prediction modeling for use in life management and in material and component design. Ideally, based on a detailed knowledge of component load and temperature spectra, one would want to simulate microstructural tailoring for specific components and then to predict long-term behavior and residual properties of the structure.

### Conclusions

- Gamma titanium aluminide alloys represent a major opportunity for significant weight savings in advanced gas turbine engines. However, before these materials can achieve confident, widespread service in engines, improvements are needed in the areas of in materials processing and life management. The exceptional smooth-bar fatigue resistance of gamma alloys (fatigue strengths =  $0.75 \cdot \text{UTS}$  or  $0.9 \cdot \sigma_y$ ) can be degraded by the presence of intrinsic material defects and service-induced damage. An important damage mode in this regard is elevated-temperature surface oxidation, which was shown to adversely affect post-exposure tensile and fatigue strength.
- Although improved processing practices can greatly reduce the occurrence of microstructural defects in the materials, service-induced damage cannot be precluded. Therefore, the U.S. Air force requires a damage tolerant approach for life management of fracture critical components in its engine. Gamma alloys appear to exhibit the fatigue crack growth characteristics needed to satisfy damage tolerance. However, improved analysis tools will be needed to apply damage tolerance to these materials with high confidence and reliability.
- Crack growth resistance in gamma alloys exhibits a minimum at intermediate temperatures centered about 600°C. In this temperature range, crack growth rates are highest, and values of  $DK_{th}$  are reduced, making intermediate temperatures a key area of consideration for damage tolerance life analyses. Based on detailed measurements of crack closure, and tests in ultra-high vacuum, it is concluded that the intermediate-temperature phenomenon occurs due to environmental embrittlement below the brittle-to-ductile transition temperature. Above this temperature, time-dependent deformation serves to blunt the crack tip, leading to a reduction in crack growth rate with further increases in temperature. Ultimately, however, the importance of the intermediate temperature behavior must be assessed in light of expected mission load and temperature spectra.
- For some engine components, gamma alloys must tolerate both low-cycle and high-cycle fatigue, which are dominated by crack growth resistance and  $DK_{th}$ , respectively. Under most circumstances, lifetimes of gamma alloys undergoing active crack propagation are limited to approximately  $10^5$  cycles, which greatly exceeds the nominal  $10^4$ -cycle low-cycle-fatigue life requirement for rotating engine components. For all practical purposes, fatigue lifetime requirements of approximately  $10^5$  cycles and greater can only be satisfied if crack-like damage does not exceed  $DK_{th}$ .
- When compared with a conventional high-strength titanium alloy, the gamma titanium aluminides exhibited exceptional levels of  $DK_{th}$ . The benefits of the high  $DK_{th}$  in the coarse lamellar K5 alloy was not retained in the presence of small defects, however, due to the rapid propagation of microstructurally small cracks. In this case, colony-size “pop-in” cracks formed along lamellar interfaces. The condition for formation of these “pop-in” cracks was in good agreement with predictions based on data from polysynthetically twinned material.
- For the gamma alloys examined here, the results suggest that a refined lamellar microstructure is preferable for most applications. The strength and fatigue-life behavior of this material can equal, or potentially exceed, that of the fine duplex material, and refinement of the lamellar colony size minimizes difficulties associated with microstructurally small cracks.

### Acknowledgments

This research was performed in the Air Force Research Laboratory, Materials and Manufacturing Directorate, Wright-Patterson Air Force Base, OH and was supported in part by the Air Force Office of Scientific Research under Task 2302BW1. The authors would like to acknowledge discussions with Y-W. Kim and D. M. Dimiduk and the technical assistance of Mr. Kevin Gross.

### References

1. U.S. Air Force, Engine Structural Integrity Program, (1984). Military Standard 1783, Aeronautical Systems Division, Wright-Patterson Air Force Base, OH.
2. P.L. Martin, D.A. Hardwick, D.R. Clemens, W.A. Konkel, and M.A. Stucke, “Scale-up of Ingot Metallurgy Wrought  $\gamma$ -TiAl,” Structural Intermetallics 1997, M. V. Nathal, et al., eds., (Warrendale, PA: The Minerals, Metals, & Materials Society, 1997), 387-404.
3. B. D. Worth, J. M. Larsen, and A. H. Rosenberger, “Threshold Crack Growth Behavior of the Gamma Titanium Aluminide Alloy Ti-46.5Al-3Nb-2Cr-0.2W Under High Cycle Fatigue Conditions,” Structural Intermetallics 1997, M. V. Nathal, et al., eds., (Warrendale, PA: The Minerals, Metals, & Materials Society, 1997), 563-569.
4. W.J. Porter, K. Li, and A.H. Rosenberger, “Processing Issues in Gamma Titanium Aluminides,” Gamma Titanium Aluminides 1999, Y-W. Kim, D. M. Dimiduk, M.H. Loretto, eds., (Warrendale, PA: The Minerals, Metals, & Materials Society, 1999), this volume.
5. Y-W. Kim, “Recent Advances in Gamma Titanium Aluminide Alloys,” High Temperature Ordered Intermetallic Alloys IV, J.O. Stiegler, L.A. Johnson, and D.P. Pope, eds., (Pittsburgh, PA: MRS, 1991), 777-794.
6. K. Li, W.J. Porter, A.H. Rosenberger, and J.M. Larsen, “Defects in Wrought Gamma Titanium Aluminides,” in press Proceedings of the Seventh International Fatigue Congress, Fatigue '99, Beijing, PRC, (1999).
7. T. S. Harding, J. W. Jones, P. S. Steif, and T. M. Pollock, “Room Temperature Fatigue Response of  $\gamma$ -TiAl to Impact Damage,” Scripta Materialia, 40/4 (1999), 445-449.
8. T. S. Harding, J. W. Jones, J.M. Larsen, and P. S. Steif, “Influence of Impact Damage on the Elevated Temperature Fatigue Behavior of Gamma Titanium Aluminide Alloys,” Gamma Titanium Aluminides 1999, Y-W. Kim, D. M. Dimiduk, M.H. Loretto, eds., (Warrendale, PA: The Minerals, Metals, & Materials Society, 1999), this volume.

9. W.E. Dowling and W.T. Donlon, "The Effect of Surface Film Formation from Thermal Exposure on the Ductility of Ti-48Al-1V-0.2C (at%)," Scripta Met., 27 (1992), 1663-1668.
10. T.J. Kelley, C.M. Austin, P.J. Fink, and J. Schaeffer, "Effect of Elevated Temperature Exposure on Cast Gamma Titanium Aluminide (Ti-48Al-2Cr-2Nb)," Scripta Met., 30 (9) (1994), 1105-1110.
11. D.S. Lee, M.A. Stucke, and D.M. Dimiduk, "Effects of Thermal Exposure on the Properties of Two  $\gamma$  Alloys," Mat Sci & Engrng, A192/193 (1995), 824-829.
12. S.K. Planck and A.H. Rosenberger, "The Effects of Prolonged High Temperature Air Exposure on the Monotonic and Cyclic Properties of a Gamma Titanium Aluminide Alloy," Gamma Titanium Aluminides 1999, Y-W. Kim, D.M. Dimiduk, M.H. Loretto, eds., (Warrendale, PA: The Minerals, Metals, & Materials Society, 1999), this volume.
13. D.C. Maxwell and T. Nicholas, "A Rapid Method for Generation of a Haigh Diagram for High Cycle Fatigue," Fatigue and Fracture Mechanics: 29th Volume, ASTM STP 1332, T.L. Panontin and S.D. Sheppaer, eds., (W. Cohnshohocken, PA: ASTM, in Press).
14. A.W. James, and P. Bowen, "Elevated Temperature Crack Growth Resistance of TiAl Under Monotonic and Cyclic Loading," Mat Sci & Engrng, A153 (1992), 486-492.
15. P. Bowen, R.A. Chave, and A.W. James, "Cyclic Crack Growth in Titanium Aluminides," Mat Sci & Engrng, A192/193 (1995), 443-456.
16. J.M. Larsen, B.D. Worth, S.J. Balsone, A.H. Rosenberger, and J.W. Jones, "Mechanisms and Mechanics of Fatigue Crack Initiation and Growth in TiAl Intermetallic Alloys," Fatigue '96, G. Lutjering and H. Nowack, eds. (Oxford, UK: Elsevier Science Ltd., 1996) 1719-1730.
17. J.P. Campbell, K.T. Venkateswara Rao, and R. O. Ritchie, "The Effect Microstructure on Fracture Toughness and Fatigue Crack Growth Behavior in  $\gamma$ -Titanium Aluminide Based Intermetallics," Met. and Mat Trans, 30A (1999), 563-577.
18. A.H. Rosenberger, B.D. Worth, and J.M. Larsen, "Effects of Microstructure, Temperature, and Environment on Fatigue Crack Growth in Ti-46.5Al-3Nb-2Cr-0.2W  $\gamma$  Titanium Aluminide," Structural Intermetallics 1997, M. V. Nathal, et al., eds., (Warrendale, PA: The Minerals, Metals, & Materials Society, 1997), 555-561.
19. K. T. Venkateswara Rao, Y-W. Kim and R. O. Ritchie, "High-Temperature Fatigue-Crack Growth Behavior in a Two-Phase (gamma + alpha-2) TiAl Intermetallic Alloy", Scripta Metallurgica et Materialia, 33 (1995), 459-465.
20. A. L. McKelvey, K. T. Venkateswara Rao, R. O. Ritchie, "On the Anomalous Temperature Dependence of Fatigue-Crack Growth in  $\gamma$ -based Titanium Aluminides"; Scripta Metallurgica et Materialia, 37 (11) (1997), 1797-1803.
21. J.C. Newman, Jr., "Crack-Opening Displacements in Center-Crack, Compact, and Crack-Line Wedge-Loaded Specimens," NASA TN-8268, NASA Langley Research Center, (1976).
22. H. Kitagawa and S. Takahashi, (1976). Proceedings of the Second International Conference on Mechanical Behavior of Materials, Boston, MA, pp. 627-631.
23. J. M. Larsen, A. H. Rosenberger, K. Li, W. J. Porter, and R. John, "Tailoring TiAl Intermetallic Alloys to Satisfy Damage Tolerance Requirements for High Performance Turbine Engines," in press, Proceedings of the Seventh International Fatigue Congress, Fatigue '99, Beijing, PRC, (1999).
24. S. Yokoshima and M. Yamaguchi, "Fracture Behavior and Toughness of PST Crystals of TiAl," Acta Mater., 44 (3) (1996), 873-883.
25. K. S. Chan and D.S. Shih, "Fundamental Aspects of Fatigue and Fracture in a TiAl Sheet," Met. and Mat Trans, 29A (1998) 73-87.
26. J.P. Campbell, J.J. Kruzic, S. Lillibridge, K.T. Venkateswara Rao, and R.O. Ritchie, "On the Growth of Small Fatigue Cracks in  $\gamma$ -based Aluminides," Scripta Mat., 37 (1997) 707-712.
27. K. S. Chan, "Fatigue Crack Growth Thresholds of TiAl Alloys," Gamma Titanium Aluminides 1999, Y-W. Kim, D. M. Dimiduk, M.H. Loretto, eds., (Warrendale, PA: The Minerals, Metals & Materials Society, 1999), this volume.
28. I.J. Perrin, "Design Approaches for Gamma-Titanium Aluminide Alloys," Advances in Turbine Materials, Design and Manufacturing: Proceedings of the Fourth International Charles Persons Turbine Conference, A. Strang, W.M. Banks, R.D. Conroy, and M.J. Goulette, eds., (London, UK: Institute of Materials 1997), 148-158.

# TAILORING TiAl INTERMETALLIC ALLOYS TO SATISFY DAMAGE TOLERANCE REQUIREMENTS FOR HIGH PERFORMANCE TURBINE ENGINES

J. M. Larsen\*, A. H. Rosenberger\*, K. Li<sup>†</sup>, W. J. Porter<sup>†</sup>, and R. John\*

\* Air Force Research Laboratory, Materials and Manufacturing Directorate, AFRL/MLLN, Wright-Patterson Air Force Base, Ohio, 45433, U.S.A.

<sup>†</sup> The University of Dayton Research Institute, Dayton, Ohio, 45469, U.S.A.

Gamma titanium aluminide intermetallic alloys offer major weight savings as replacement materials for the more conventional alloys used in today's advanced turbine engines. However, to fully utilize the potential of gamma alloys in fracture critical structural applications, an unprecedented capability for life prediction under demanding service conditions is required. Key issues in fatigue crack nucleation and growth are discussed, emphasizing the role of relevant microstructural features on crack-size effects in this class of alloys.

## INTRODUCTION

A variety of research programs are underway to develop improved high temperature structural alloys based on ordered crystal structures. The most mature of these intermetallic materials are gamma titanium aluminide alloys, which are nominally composed of two-phase mixtures of TiAl ( $\gamma$ -phase,  $L1_0$  structure) and  $Ti_3Al$  ( $\alpha_2$ -phase,  $DO_{19}$  structure). The newer gamma alloys are strong candidates for use as structural materials in high performance turbine engines as both static and rotating components. When considered on a density-corrected basis, gamma alloys have exceptional high-temperature specific stiffness, creep strength, and fatigue resistance (1,2), which give these alloys the potential to replace more dense titanium and nickel-base alloys in many applications. Compared with the more conventional materials, however, gamma alloys have relatively low tensile ductilities and fracture toughnesses, coupled with steep crack growth rate curves and relatively flat stress-life fatigue curves. To utilize the full potential of gamma alloys in the most demanding turbine engine applications will require special consideration of their unique balance of properties. Component design and life-management technologies must ensure that these materials can be used without increasing operational risks. In the end, for both the design and utilization of gamma alloys, a key goal is to achieve the maximum *useful* life of the material under actual usage conditions.

Since the fatigue limit of a typical gamma alloy tends to approach the material's yield strength, it may appear attractive to use a safe-life approach for life management, wherein allowable stresses are dictated by some lower bound of the fatigue limit. However, it is clear that the outstanding fatigue capability of these alloys in their pristine state overestimates the more realistic trend that would be found in service. For a large fleet of components, one must contend with a variety of potential defects and sources of material damage, which will reduce allowable stresses. The structural designer must specifically consider effects of intrinsic material defects (3), surface abrasion and impact damage, high-temperature oxidation (4), and loading spectra that may contain both low and high frequency fatigue. In addition, the U.S. Air Force requires that fracture critical components in its turbine engines be life-managed under a damage tolerance approach (5). This paper identifies some of the key factors that offer promise and present challenges in most effectively using gamma alloys in key structural applications.

## EXPERIMENTAL RESULTS AND DISCUSSION

Gamma titanium aluminide alloys may be processed and heat treated to produce dramatically different microstructures. Figures 1 and 2 illustrate two extremes in microstructural control that are available from an alloy developed by Kim (6), Ti-46.5Al-3Nb-2Cr-0.2W (at%), designated alloy K5. Figure 1 shows a fine duplex microstructure composed of a mixture of equiaxed gamma grains and fine colonies of lamellar  $\gamma$  plus  $\alpha_2$  phase. This forged material has comparatively good strength and moderate ductility but a relatively low fracture toughness (7). Figure 2 shows the same alloy after heat treatment to produce a microstructure of large colonies of fine lamellar  $\gamma$  plus  $\alpha_2$  laths. Compared to the duplex material, this microstructure is of lower strength and ductility but improved fracture toughness.

Figure 3 shows the fine-grained lamellar microstructure found in the K5-derivative alloy, KD-CBS (Ti-46Al-2Cr-2.7Nb-0.15Si-0.1B-0.2C, at%). This alloy exhibits a better balance of properties. As shown in Fig. 4, this alloy has excellent smooth-bar fatigue resistance. In order to utilize fully the fatigue capability of this material in fracture critical applications, consideration of damage tolerance and fatigue crack growth is required as a protection against the effects of defects and damage from other sources.

Figure 5 presents crack growth rate data as a function of temperature for the microstructures presented in Figs. 1 and 2. The crack growth behavior of the duplex material is clearly much faster than that of the lamellar condition, and the values of threshold stress intensity factor range,  $K_{th}$ , are much lower in the duplex material. A common feature of these alloys is that the worst-case crack growth condition occurs at intermediate temperatures. This fact is clearly illustrated by Fig. 6, which shows crack growth rate and  $K_{th}$  as a function of temperature for a refined lamellar K5 alloy, called K5-RFL, similar to that of Fig. 2. In Fig. 6 the growth rate data, which correspond to a constant value of  $K = 9 \text{ MPa} \sqrt{\text{m}}$ , reach a maxima at approximately  $600^\circ\text{C}$ , while  $K_{th}$  exhibits a minimum at approximately  $550^\circ\text{C}$ . As temperature is increased above approximately  $600^\circ\text{C}$ , the crack growth resistance increases substantially. This increase in crack growth resistance apparently results from the well-known brittle-to-ductile transition that occurs about  $700^\circ\text{C}$  for most gamma alloys. That is, as the temperature is increased significantly above the brittle-to-ductile transition temperature, it appears that crack tip deformation increases significantly due to extensive plasticity and creep, thereby reducing the effective  $K$  at the crack tip, which leads to decreased crack growth rates and higher values of  $K_{th}$ . Careful measurements of crack opening displacements by Rosenberger et al. (8) have shown only minor variations in the level of crack closure for a range of temperatures. As shown in Fig. 7, for the constant- $K_{max}$  results of Fig. 6, measurements of  $U = (P_{max} - P_{op}) / (P_{max} - P_{min}) = K_{eff} / K$  exhibited relatively little change from room temperature to  $800^\circ\text{C}$ . The maximum in  $U$  occurred at about  $700^\circ\text{C}$ , indicating that crack closure was a minimum at this temperature. As shown in the figure, the level of  $U$  dropped slightly as the temperature increased above  $700^\circ\text{C}$ , which corresponded to a small increase in the level of crack closure. This small change in closure cannot explain the dramatic decrease in crack growth rate observed as temperature approached  $800^\circ\text{C}$ .

In smooth-bar fatigue tests of typical gamma alloys, attempts to monitor the development of small fatigue cracks have been accomplished at stresses approaching the material's yield strength (e.g., 9,10). Under the more moderate stress levels typical of actual structural applications, detecting microcrack growth has been much more difficult. In an attempt to study the effects of surface defects under realistic operating stresses, Larsen et al. (7) and Worth et al. (11) performed a variety of studies using smooth fatigue specimens containing twelve, semicircular surface notches of depth equal to  $80 \mu\text{m}$ . These tests

were designed to establish a sufficient number of equivalent surface defects so as to make it highly likely that one or more of the defects would be located in a weakly oriented feature of the microstructure. In tests of the fine duplex microstructure of alloy K5 (Fig. 1), the effect of the small defects was to reduce the fatigue strength approximately 10 percent. The defect behavior agreed well with predictions using the closure corrected threshold stress intensity factor range,  $K_{eff,th}$ , for large cracks in this material (7). Similar tests of the coarse lamellar material shown in Fig. 2 were overestimated by the large-crack threshold behavior. A more detailed examination of the fracture surfaces of these specimens, Table 1, indicated that the critical crack formed from a notch located in a lamellar colony such that the normal of the lamellar orientation was within  $\sim 20^\circ$  of the loading axis. Apparently this configuration led to nucleation of a crack in the “hard” lamellar colony orientation, and the crack grew quickly across the lamellar colony in the relatively low-toughness interlamellar mode. At this point, the stress intensity factor range,  $\Delta K$ , of this ‘pop-in’ crack, conservatively calculated as a semicircular surface crack, was close to the bulk coarse lamellar threshold,  $K_{th} = 8.5 \text{ MPa}\sqrt{\text{m}}$ , and subsequent failure of the specimen occurred due to propagation from this initial flaw. Notice that the specimen indicating the highest fatigue strength, 350 MPa, appeared to fail from the smallest ‘pop-in’ crack, which was also the most inclined to the loading axis - resulting in fatigue strength identical to smooth specimens. The specimen with the poorest fatigue resistance failed in a lamellar colony with the hardest orientation,  $10.6^\circ$ , and had a neighboring colony with a sympathetic orientation within  $6^\circ$  of the original, Figure 8. In Table 1, the conservative ‘pop-in’ size probably significantly underestimates the true ‘pop-in’ crack size and  $\Delta K$ .

Table 1 Orientation of the failure site and nominal  $\Delta K$  in notched lamellar specimens.

Stress* (MPa)	Cycles to failure	Normal (deg)	~Pop-in size ( $\mu\text{m}$ )	$\sim \Delta K_{\text{Pop-in}}$ ( $\text{MPa}\sqrt{\text{m}}$ )	Comments
350	148626	$\sim 40$	300	6.9	
325	8808	13.1	750	10.1	
300	65915	21.0	360	6.5	
275	6068	10.6	600	7.7	2nd colony neighboring w/ $\sim 6.4^\circ$ difference in normal

\*R = 0.1,  $\nu = 20 \text{ Hz}$ , RT

Some insight into these results may be gained by considering the findings of Yokoshima and Yamaguchi (12) on polysynthetically twinned (PST) crystals. These researchers determined the fracture toughness as a function of crack plane for Ti-49.3Al and Ti-48.9Al-0.4Cr (at%) PST materials. They characterized the basic crack/microstructure orientations shown in Fig. 9. In these materials they reported approximate minimum fracture toughness values for the three basic configurations as:  $K_{IC(\text{min-Type I})} = 15.7 \text{ MPa}\sqrt{\text{m}}$ ,  $K_{IC(\text{min-Type II})} = 8.7 \text{ MPa}\sqrt{\text{m}}$ , and  $K_{IC(\text{min-Type III})} = 3.3 \text{ MPa}\sqrt{\text{m}}$ . Using these approximate values, one may construct a modified Kitagawa diagram corresponding to the different crack orientations as shown Fig. 10. This figure, which plots maximum stress versus crack depth (assumed semi-circular), shows horizontal lines as the limiting stress values corresponding to the smooth-bar fatigue limit,  $S_e$ , and the ultimate tensile strength, UTS. The diagonal lines represent the limiting fracture mechanics conditions corresponding to the three toughness values. The Type I toughness value was approximately equal to  $K_{IC}$  determined from the bulk coarse lamellar material shown in Fig. 2. Furthermore, the measured Type II toughness was approximately equal to the maximum K corresponding to  $K_{th}$  of the Fig. 2 material. Figure 10 also shows a line corresponding to the measured fracture toughness of the PST material in the Type III orientation. The notched K5-Lamellar data, Table 1, are plotted in Figure 10 as solid square symbols, for the  $80 \mu\text{m}$  notch depth. The specimen that failed at the highest stress exhibited failure that was not strongly influenced by the notch. Hence, it fell close to the endurance limit line (for  $10^7$  cycles).

The other data fall below this line and close to the sloped line of the Type III  $K_{IC}$ . None of these specimens achieved  $10^7$  cycles without failure, which might be expected since it is likely that the threshold for fatigue crack propagation  $K_{max,th}$  is below the fracture toughness (Type III  $K_{IC}$ ).

This comparison of PST behavior with that from the random lamellar material indicates that fatigue initiation and early propagation are closely related to the behavior of a few, specifically orientated lamellar colonies. A refinement in the colony size is a strong engineering means to minimize the deleterious effects of a few individual colonies, and some current efforts are aimed at determining the utility of this approach. Another ongoing effort is attempting to thoroughly understand the fatigue behavior within the colony and to link this behavior to an agglomeration of colonies. To accomplish this goal John et al. (13) have conducted fatigue crack growth tests on gamma alloy specimens that have been heat treated to produce very large colonies (approximately 5 mm in diameter). Using special mixed-mode crack growth specimens, it has been possible to obtain preliminary crack growth data suggesting that, for crack growth within a single colony, the value of  $K_{max}$  at threshold may be substantially lower than  $K_{IC(min-Type III)}$ , as may be expected.

### CONCLUDING REMARKS

Improved damage tolerance life prediction methods are needed to develop and utilize the full potential of gamma TiAl alloys as structural materials. The unique balance of properties offered by these alloys present important opportunities for improved turbine engine performance, but the introduction of these materials into fracture critical engine components must be accomplished without increasing the risk of failure. Key damage tolerance factors that must be addressed for gamma alloys include their unusual temperature dependence in crack growth, effects of defects and service-induced damage, and small-crack effects. It was shown that the propagation condition for small fatigue cracks in lamellar microstructures, which is governed by interlamellar splitting of similarly-aligned, poorly-oriented colonies, agrees well with predictions based on tests of single-colony and large-colony material. It appears, however, that the worst-case crack propagation behavior associated with interlamellar cracking does not govern fatigue capability and defect tolerance if the colony size is sufficiently small.

### ACKNOWLEDGEMENTS

This research was performed in the Air Force Research Laboratory, Materials and Manufacturing Directorate, Wright-Patterson Air Force Base, OH and was supported in part by the Air Force Office of Scientific Research under Task 2302BW1. The authors would like to thank Y.-W. Kim of Universal Energy Systems, Dayton, OH for his thoughtful discussions and for providing the K5 and KD-CBS alloys.

### REFERENCES

- (1) Kim, Y.-W., "Intermetallic Alloys Based on Gamma Titanium Aluminide," *JOM*, Vol. 41, No. 7, 1989, pp. 24-30.
- (2) Kim, Y.-W. and Dimiduk, D. M., "Progress in the Understanding of Gamma Titanium Aluminides," *JOM*, Vol. 43, No. 8, 1991, pp. 40-47.
- (3) Li, K. Porter, W.J., Rosenberger, A.H., and Larsen, J.M., "Defects in Wrought Gamma Titanium Aluminides," in *Fatigue '99*, this proceedings.



- 
- (4) Planck, S. K., "The Effect of Prolonged High Temperature Air Exposure on the Monotonic and Cyclic Properties of a Gamma Titanium Aluminide Alloy," M.S. Thesis, University of Dayton, Dayton, Ohio, 1998.
  - (5) U.S. Air Force, Engine Structural Integrity Program. *Military Standard 1783*, Aeronautical Systems Division, Wright-Patterson Air Force Base, OH, 1984.
  - (6) Kim, Y.-W., "Ordered Intermetallic Alloys, Part III: Gamma Titanium Aluminides," *JOM*, Vol. 46, No. 7, 1994, pp. 30-40.
  - (7) Larsen, J.M., Worth, B.D., Balsone, S.J., Rosenberger, A.H., and Jones, J.W., "Mechanisms and Mechanics of Fatigue Crack Initiation and Growth in TiAl Intermetallic Alloys," in *FATIGUE '96, Vol. III*, G. Lütjering and H. Nowack, Eds., Elsevier Science Ltd., Oxford, U.K., 1996, pp. 1719-1730.
  - (8) Rosenberger, A.H., Worth, B.D., and Larsen, J.M., "Effects of Microstructure, Temperature, and Environment on Fatigue Crack Growth in Ti-46.5Al-3Nb-2Cr-0.2W  $\gamma$  Titanium Aluminide," in *Structural Intermetallics 1997*, M. V. Nathal, et al., Eds., The Minerals, Metals, & Materials Society, Warrendale, PA, 1997, pp. 555-561.
  - (9) Campbell, J.P., Kruzic, J.J., Lillibridge, S., Venkateswara Rao, K.T., and Ritchie, R.O., "On the Growth of Small Fatigue Cracks in  $\gamma$ -Based Titanium Aluminides," *Scripta Materialia*, Vol. 37, 1997, pp. 707-712.
  - (10) Chan, K. S., and Shih, D.S., "Fundamental Aspects of Fatigue and Fracture in a TiAl Sheet Alloy," *Met. and Mater. Trans.*, Vol. 29A, 1989, pp. 73-87.
  - (11) Worth, B.D., Larsen, J.M., and Rosenberger, A.H., "Threshold Crack Growth Behavior of the Gamma Titanium Aluminide Alloy Ti-46.5Al-3Nb-2Cr-0.2W Under High Cycle Fatigue Conditions," in *Structural Intermetallics 1997*, M. V. Nathal, et al., Eds., The Minerals, Metals, & Materials Society, Warrendale, PA, 1997, pp. 563-569.
  - (12) Yokoshima, S. and Yamaguchi, M., "Fracture Behavior and Toughness of PST Crystals of TiAl," *Acta Mater.*, Vol. 44, No. 3, 1996, pp. 873-883.
  - (13) John, R., DeLuca, D., Porter, W.J., and Rosenberger, A.H., "Mixed Mode Crack Growth in a Gamma Titanium Aluminide," in *Fatigue '99*, this proceedings.

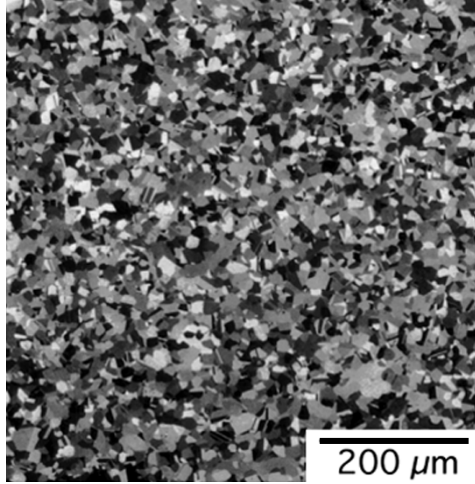


Figure 1 Duplex alloy K5

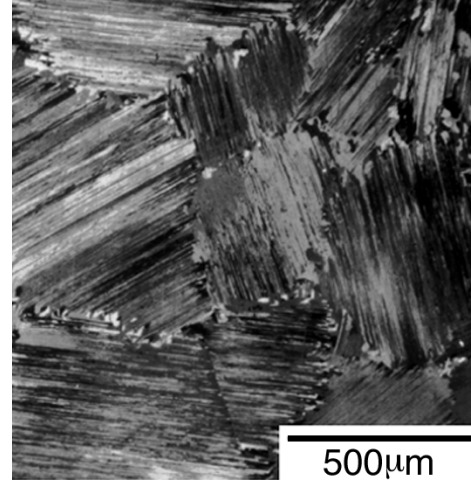


Figure 2 Coarse lamellar alloy K5

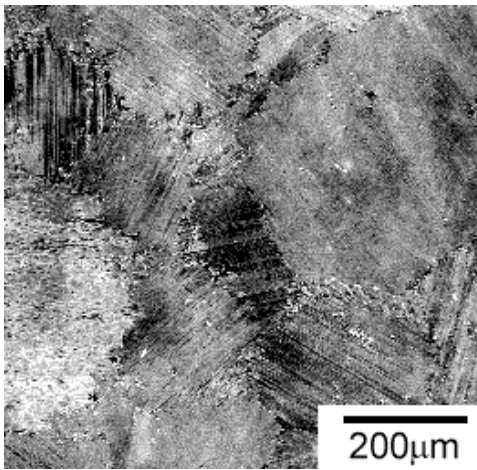


Figure 3 Refined lamellar alloy KD-CBS

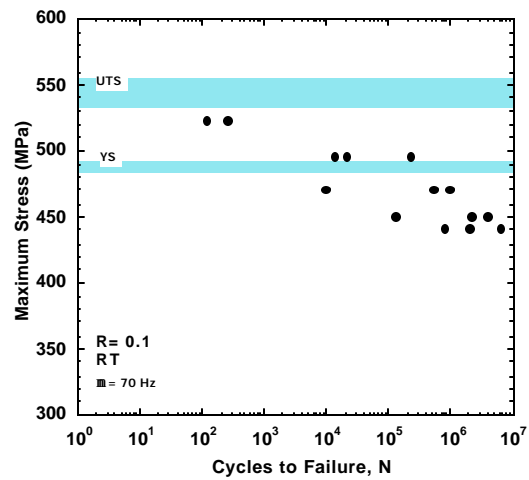


Figure 4 Fatigue of alloy KD-CBS

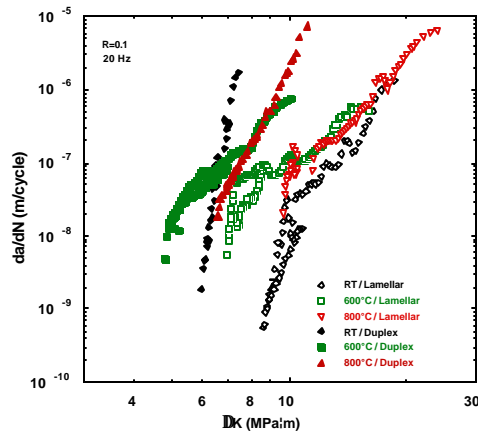


Figure 5 Effect of temperature on fatigue crack growth rate behavior in alloy K5 duplex and coarse lamellar microstructures.

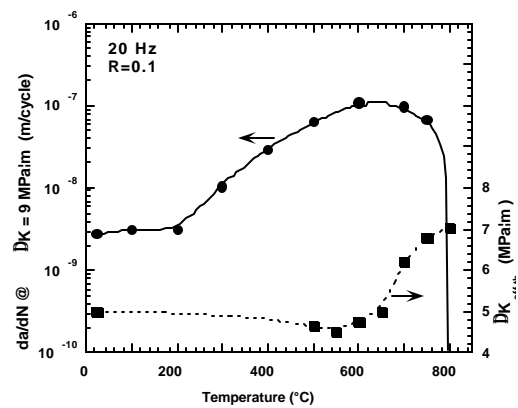


Figure 6 Effect of temperature on  $K_{th}$  and  $da/dN$  at  $K = 9 \text{ MPa}\sqrt{\text{m}}$ , showing worst-case behavior, in the K5-RFL alloy, at an intermediate temperature.

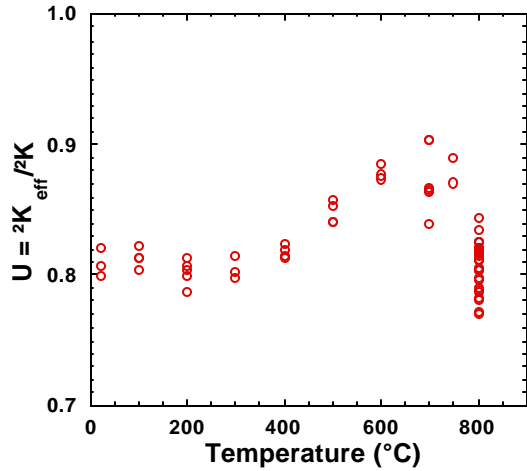


Figure 7 Measurements of  $U$  corresponding to the crack growth rate data of Fig. 6.

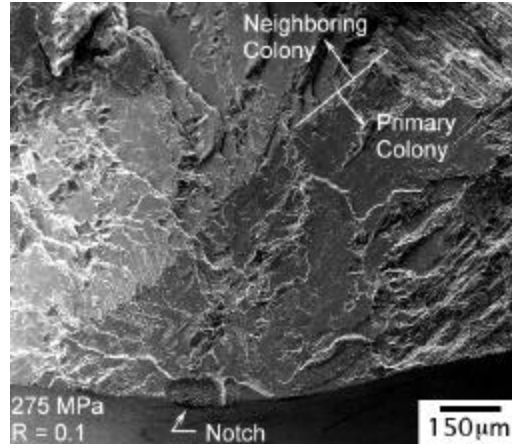


Figure 8 Failure origin of notched lamellar K5 specimen.

Figure 9 Crack/ microstructure definitions used by Yokoshima and Yamaguchi (12).

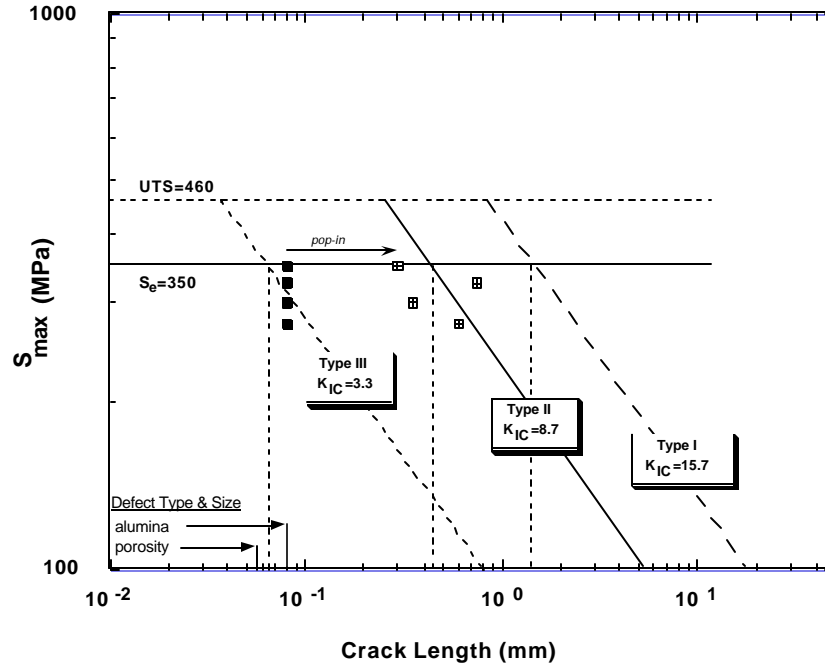


Figure 10 Plot of maximum stress versus crack length combining information from a variety of tests of defected and defect-free coarse lamellar gamma alloy K5.

This page intentionally left blank.

**THE ROLE OF NEAR-THRESHOLD SMALL-CRACK BEHAVIOR  
IN LIFE PREDICTION OF TITANIUM ALLOYS  
FOR USE IN ADVANCED TURBINE ENGINES**

J. M. LARSEN, R. JOHN, S. M. RUSS, D. C. MAXWELL\*,  
B. D. WORTH†, A. H. ROSENBERGER, K. LI\*, AND W. J. PORTER\*  
Air Force Research Laboratory  
Materials and Manufacturing Directorate (AFRL/MLLN)  
Wright-Patterson Air Force Base, OH 45433, U.S.A.

**ABSTRACT**

Increasingly accurate life prediction models are required to utilize safely the full capability of current and future structural materials in advanced gas turbine engines. As an aid to understanding the role of crack size and threshold crack growth in these life predictions, two classes of material are examined: a conventional high strength titanium alloy and a gamma TiAl intermetallic alloy. Residual life calculations and fatigue life maps are used to illustrate the significance of crack size under realistic loading. Using weight function analyses, it is shown that surface residual stresses can greatly increase the threshold crack size for propagation of surface cracks. In the conventional titanium alloy, large-crack fracture mechanics data appear to be applicable to small fatigue cracks of practical, or inspectable, sizes. In a coarse microstructure of the gamma alloy, however, the scale of small cracks and initial damage can be of the order of microstructural dimensions, leading to rapid crack propagation. Local anisotropy in this material is shown to explain this behavior, leading to guidance for optimizing microstructure to improve durability and useful lifetime under realistic loading conditions.

**KEYWORDS**

Microstructure, small crack, titanium alloy, gamma titanium aluminide, turbine engine

**INTRODUCTION**

Performance and life-cycle-cost goals for advanced gas turbine engines require accurate life prediction capabilities for materials subjected to extremely demanding operating conditions. During flight, rotating components in military engines are exposed to low frequency, low-cycle fatigue produced by variations in engine speed. Each flight involves one major fatigue cycle, produced by the ground-air-ground excursion, plus numerous additional low-frequency fatigue cycles of less severe amplitude. Components such as airfoils may also experience occasional transient intervals of high-cycle fatigue at frequencies up to several kilohertz.

To assure turbine engine reliability, since 1984 the Air Force has required that fracture critical components in its engines be designed and life-managed according to a damage tolerant approach specified by the Engine Structural Integrity Program (ENSIP) [1]. Under this specification a component must be capable of achieving its design lifetime in the presence of realistic, intrinsic material defects and service-induced damage. The damage tolerance requirement has been applied primarily to engine disks and spacers, while airfoils, which are normally not fracture critical, have typically been exempt. However, the high-cycle fatigue performance of turbine engine components has been the focus of recent attention [2-4], and efforts are underway to develop improved life-prediction methods to address this aspect of turbine engine fatigue.

Although life-management practices for today's engines have provided a high degree of safety, in many instances it appears that substantial gains in the *useful* life of major engine components can be achieved through improvements in life-prediction capabilities. Moreover, accurate life prediction is essential to facilitate the rapid introduction of new materials into widespread service. In some instances, uncertainties in the full-life capability of materials may limit the extent of their use in key structural applications. Under these circumstances, improvements in life-management practices can enable the insertion of these materials and help them to reach their full structural potential.

As one strives to extend the useful life of turbine engine materials and components, however, the behavior of small fatigue cracks becomes increasingly important for both component design and in-service reliability. Understanding the basic nature of the growth of small fatigue cracks is essential to the development of new, durable materials and

to the introduction of improved life-management practices. Key factors that must be addressed include material dependencies, effects of intrinsic material defects, service-induced damage, and usage conditions.

This paper examines the role of crack size in a damage-tolerance assessment, emphasizing threshold,  $DK_{th}$ , and near-threshold crack growth behavior under typical turbine engine loading conditions. Results are presented for a conventional high-strength titanium alloy and for three microstructures of a newer titanium intermetallic alloy, based on the TiAl gamma-titanium-aluminide phase. The conventional alloy is in widespread use in current engines for components that operate at low to moderate temperatures. The gamma-titanium-aluminide alloy is representative of materials being developed as candidates for replacement of more dense nickel-base alloys currently used in turbine engines at moderate to high temperatures.

## RESULTS AND DISCUSSION

### *Materials*

The conventional titanium alloy was Ti-6Al-2Sn-4Zr-6Mo (weight %) (Ti-6246), a high-strength material used in turbine engine airfoils and disks. This material was forged and heat treated to produce a fine duplex microstructure of equiaxed primary  $\alpha$  phase (hexagonal close packed) in a matrix of Widmanstätten  $\alpha + \beta$  (body-centered cubic) phase as shown in Fig. 1. The gamma titanium aluminide alloy, developed by Kim [5], was Ti-46.5Al-3Nb-2Cr-0.2W (atomic %), which has been designated as alloy K5. This material was forged and heat treated to produce three microstructures: duplex, refined fully lamellar (RFL), and coarse fully lamellar. Optical micrographs of the three microstructures are shown in Figs. 2-4. The duplex microstructure (K5-D) shown in Fig. 2 was composed of a mixture of equiaxed gamma grains ( $L1_0$  structure) and fine colonies of lamellar gamma plus alpha-2 phase ( $DO_{19}$  structure). The refined fully lamellar (Fig. 3, K5-RFL) and coarse lamellar (Fig. 4, K5-L) microstructures contain lamellar colonies of approximate diameter 280 and 700  $\mu\text{m}$ , respectively. The average lamellae thickness in the RFL microstructure was also less than that of the coarse lamellar material. The coarse lamellar microstructure had a lower strength than either the RFL or the duplex microstructure.

### *Fatigue Crack Propagation*

Fatigue crack growth experiments were performed using standard procedures [6] and compact type, C(T), specimens. The crack growth data were acquired under decreasing stress-intensity-factor-range,  $DK$ , fatigue followed by constant-load-amplitude fatigue. The resulting fatigue crack growth rate data from the four materials are shown in Fig. 5, along with lines representing a regression analysis performed using the equation

$$\log(da/dN) = C_1 \{ \text{arctanh}(C_2 [\log(DK) + C_3]) \} + C_4 \quad (1)$$

which provided a good representation of the growth rate behavior for these large cracks.

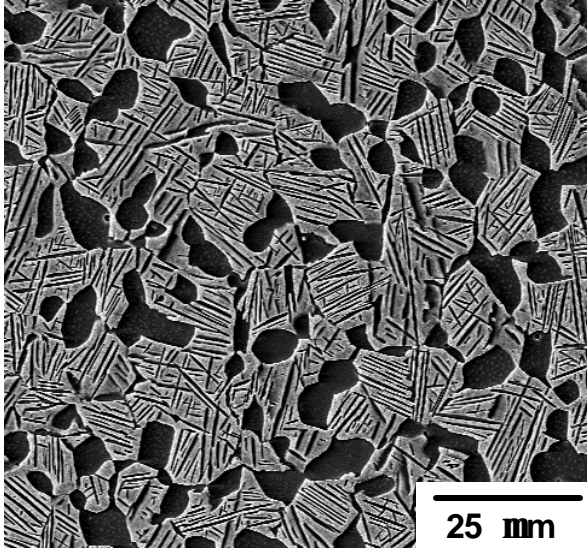


Fig. 1. Ti-6Al-2Sn-4Zr-6Mo.

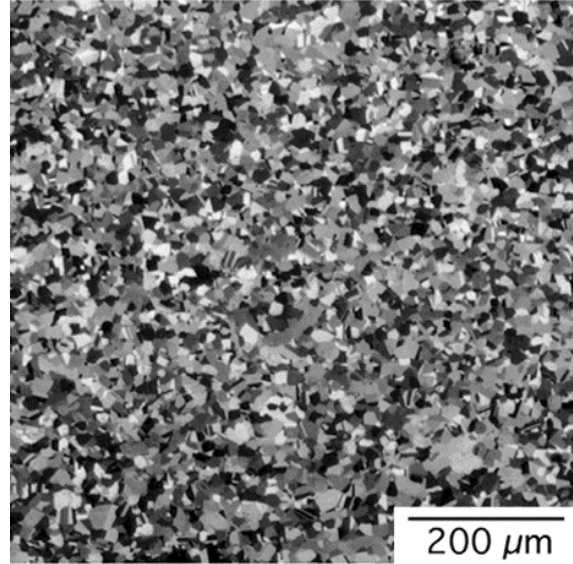


Fig. 2. Duplex TiAl alloy K5

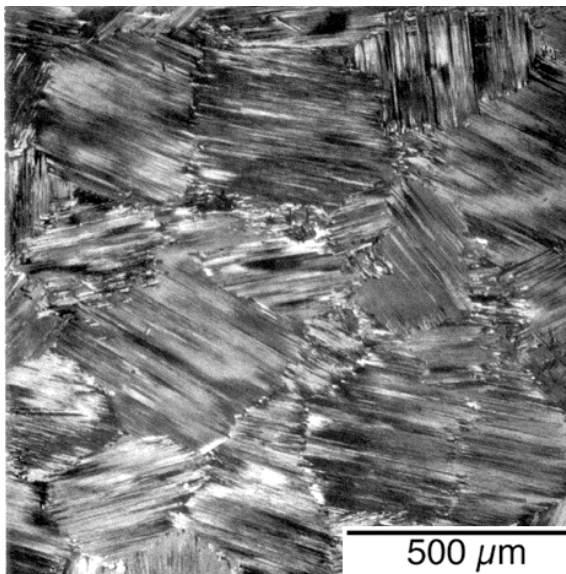


Fig. 3. Refined lamellar TiAl alloy K5

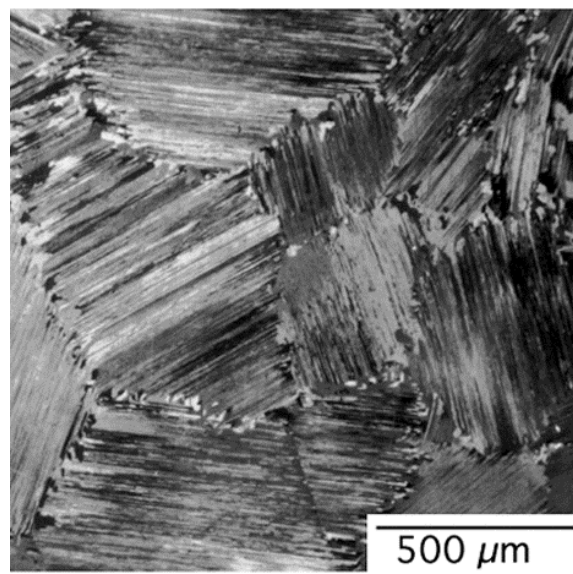


Fig. 4. Coarse lamellar TiAl alloy K5

#### *Residual Crack Propagation Lifetime*

As established by the Engine Structural Integrity Program [1], the damage tolerance approach to life management of military turbine engines requires the assumption that fracture critical components contain initial defects or damage. Generally, the scale of the assumed damage is defined by the detection limit of a chosen nondestructive inspection method. In this case the detection limit is the maximum crack size that can be missed by the inspection at a specified probability of detection level. The damage-tolerance life predictions are performed by calculating the number of cycles required to propagate a crack from an initial size,  $a_i$ , to failure. Assuming that large-crack behavior applies to the small cracks that grow in actual components, the crack propagation lifetime is given by

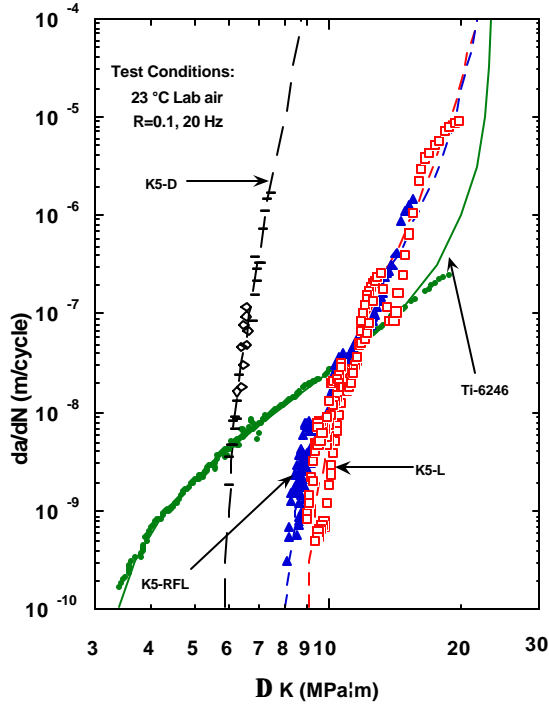


Fig. 5. Crack growth rate behavior for Ti-6246 and three alloy K5 microstructures

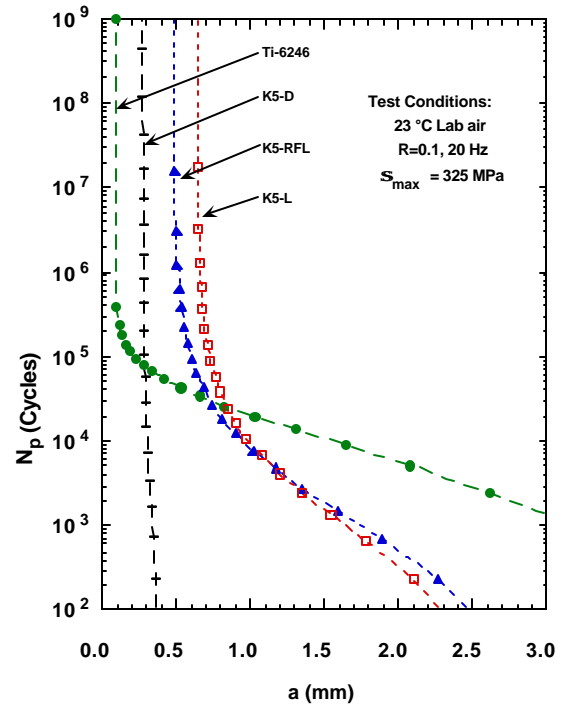


Fig. 6. Remaining crack propagation lifetime,  $N_p$ , plotted versus crack size,  $a$ .

$$N_p = \int_{a_i}^{a_c} \frac{da}{f(\Delta K)} \quad (2)$$

where  $a_c$  is the critical crack length corresponding to the material's effective fracture toughness in fatigue ( $K_Q$ ),  $f(\Delta K)$  is a crack-growth-rate function such as Eq. 1, and  $\Delta K$  is defined for a specific crack geometry and loading history. In the example calculations to follow, the crack was assumed to be a semicircular surface flaw of depth  $a$ , which is a typical crack geometry observed in actual components.

To examine the effect of the assumed initial crack size,  $a_i$ , on the calculated crack propagation lifetime,  $N_p$ , based on the large-crack data, Eq. 2 was solved numerically to construct the remaining-life plot shown in Fig. 6. For a given  $a_i$ , and a set of loading and temperature conditions,  $N_p$  is given by the ordinate on the plot. The four curves shown have features common to all life calculations performed using the crack growth data of Fig. 5. For combinations of  $a_i$  and loading conditions that result in  $\Delta K$  less than  $\Delta K_{th}$ ,  $N_p$  in Fig. 6 is infinite. When  $\Delta K_{th}$  is exceeded, however, there is a sharp transition from infinite predicted lifetime to finite lifetime. Based on the large-crack data, the threshold crack depths,  $a_{th}$ , corresponding to  $\Delta K_{th}$  are 0.07, 0.26, 0.48, and 0.64 mm for the Ti-6246, K5-D, K5-RFL, and K5-L materials, respectively, assuming  $S_{max} = 325$  MPa. As shown in the figure, for crack sizes exceeding these threshold values, the total remaining life in fatigue crack growth in each case was less than about  $10^6$  cycles. Thus, assuming that large-crack behavior applies to the physically small cracks of interest in engine components, for cyclic lives greater than about  $10^6$  cycles,  $\Delta K_{th}$  must not be exceeded if failure is to be avoided.



Since major rotating components in turbine engines are commonly life-limited by low-cycle fatigue, the overall crack-growth resistance is also of major importance. For example, turbine engine components in fighter aircraft are commonly designed for a full life of approximately 8,000 total accumulated cycles (TACs), and engine overhaul and inspection intervals are typically half the full life. This condition places great importance on overall crack growth resistance of a material, which, as shown in Fig. 6, can vary significantly for the various materials and microstructures.

#### Fatigue Life Maps

To help visualize the role of crack size in a life analysis, one can construct a life map that outlines regions of expected fatigue life in terms of stress and crack size. This format follows from the original work of Kitagawa and Takahashi [7]. These authors identified an apparent “safe region”, shown schematically in Fig. 7, that is bounded by the  $10^7$ -cycle fatigue limit,  $DS_e$ , and the threshold stress intensity factor range,  $DK_{th}$ . These two limiting lines intersect at the crack size  $a_0$ , and all combinations of stress range and crack size within the safe region are below both  $DS_e$  and  $DK_{th}$ . Another limiting region on the diagram is defined by the conditions whose exceedence would produce fracture in a single cycle: the ultimate tensile strength, UTS, and the effective fracture toughness,  $K_Q$ . A third domain lies between the safe and fracture regions, defining the combinations of  $DS$  and crack size that result in finite fatigue lifetimes.

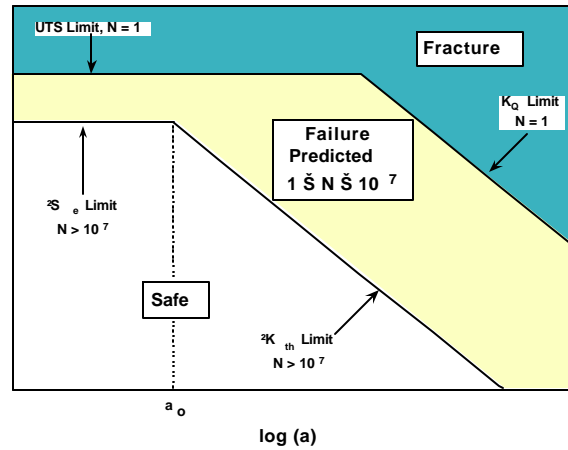


Fig. 7. Schematic of fatigue life map.

The practical implications of this type of plot are shown in Fig. 8 for the Ti-6246 alloy. The curves of constant life between the “safe” and “fracture” boundaries represent remaining crack propagation lives calculated by numerical integration of Eq. 2 using Eq. 1 to represent  $f(DK)$  for an assumed semicircular surface crack. Of course, these calculations assume the large-crack data from Fig. 3 appropriately represent crack growth rates for small surface cracks. For cracks of depth,  $a$ , greater than approximately 0.025 mm, this assumption was previously shown to be correct in experiments on naturally initiated small surface cracks in this alloy [8-11].

These fatigue maps represent a useful tool to visualize the conditions of stress level and flaw size under which a material can be used. The maps also highlight the utility of  $DK_{th}$  when designing for fatigue lives of  $10^7$  cycles or greater, especially if the assumed initial flaw depth exceeds approximately 0.025 mm. This flaw size range is of significance, since it is well below the typical depths of foreign object damage observed in service [12,4], which is shown on the figure as a probability density function. Also indicated on the figure is the approximate detection limit for focused, eddy-current inspection ( $\sim 0.125$  mm) currently used for some engine components. Based on these factors, it is clear that physically small fatigue cracks are of great practical interest for turbine engines components made of Ti-6246.

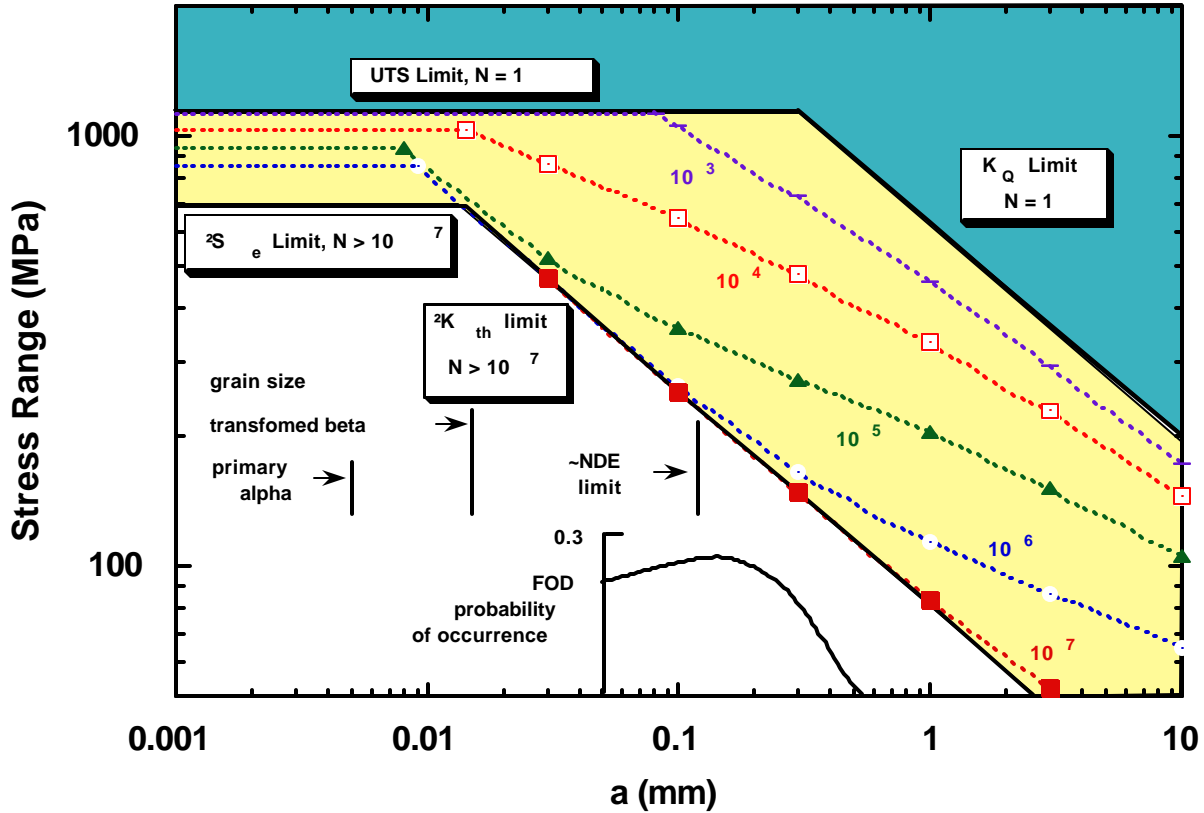


Fig. 8. Fatigue-life map for Ti-6246 plotted in terms of stress range and initial crack size for a surface flaw in an infinite solid under constant amplitude fatigue at room temperature and a stress ratio of  $R = 0.1$ .

#### Effects of Surface Residual Stress on Small-Crack Thresholds

The threshold-crack-growth resistance of small surface cracks can be influenced substantially by surface residual stresses. To assess the magnitude of this effect in the Ti-6246 alloy, the four surface residual stress profiles shown in Fig. 9 were chosen. These profiles represent a range of surface treatments that might be used for turbine engine components. The figure plots residual stress as a function of the distance,  $x$ , measured from the free surface. As shown in the figure, laser shock processing [13] can impart the deepest and most intense surface residual stress. A similar level of compressive surface residual stress can be developed by mechanical shot peening, although the depth penetration of this profile tends to be much shallower. Low stress grinding produces a very modest compressive residual stress, which quickly subsides as  $x$  increases. Also included in the figure is a residual stress profile produced by electro-discharge machining (EDM). This operation creates a tensile surface residual stress, which also subsides quickly.

The weight-function method was used to calculate effective residual-stress-intensity factors for part-through semicircular surface cracks subjected to each of the four residual stress profiles [14]. These results are shown in Fig. 10, which plots the calculated residual stress intensity factor at the crack depth,  $K_{a,r}$ , as a function of crack depth. As can be seen, both the shot peen and laser shock processing conditions have a major influence on the residual stress intensity factor, while a minimal effect is associated with the other two surface conditions.

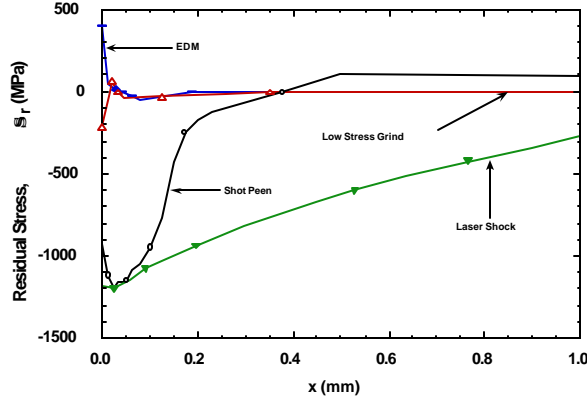


Fig. 9. Surface residual stress profiles for various types of surface finishing.

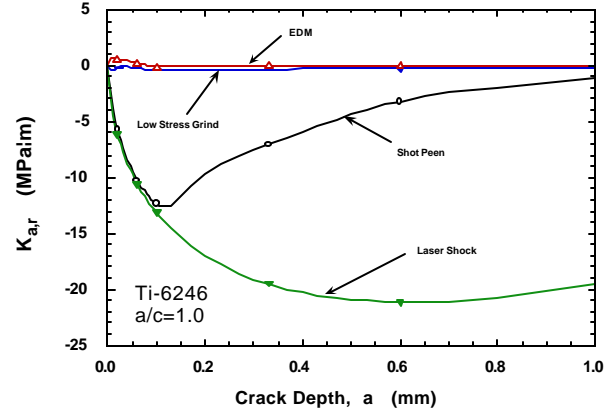


Fig. 10. Stress intensity factors produced by surface residual stress profiles shown in Fig. 8.

The influence of the residual stress on the threshold condition for propagation of a semicircular surface crack is illustrated in Fig. 11 for  $R = 0.1$  fatigue. This figure shows that both laser shock processing and shot peening dramatically increase the threshold crack size, particularly at the smaller crack sizes. At the maximum stresses shown, the crack size corresponding to threshold crack growth is increased by almost two orders of magnitude by the residual stress field produced by simulated laser shock processing, and shot peening increases this crack size by well over an order of magnitude. These benefits could be misleading, however, if subsurface cracks begin to initiate in preference to growth of surface cracks.

Figure 12 shows results for similar calculations for  $R = 0.8$  fatigue. In this instance, the benefits of both laser shock processing or shot peening are significant, but much less than for  $R = 0.1$  loading. This difference is produced by the effect of crack-wake contact under low-stress-ratio fatigue, which does not occur at  $R=0.8$ . At  $R=0.1$ , the residual stress tends to reduce the effective  $K_{max}$  at the crack tip, while the corresponding value of  $K_{min}$  can be reduced only to zero, due to contact of the crack faces. Thus, the effective  $DK$  may be greatly reduced, while changes in the effective stress ratio would be small. Under  $R = 0.8$  fatigue, however, the residual stress would reduce both  $K_{max}$  and  $K_{min}$  at the crack tip equally, until crack-wake contact occurred. Under this condition, the effective  $DK$  might undergo little change, while the effective  $R$  could be substantially reduced. The result of these combined effects is to diminish the beneficial nature of surface residual stresses on fatigue-crack-threshold behavior under high-stress-ratio fatigue. It should be noted, however, that the high stress ratio alone (smaller  $DK$  for a given  $s_{max}$ ) leads to a dramatic increase in threshold crack size as compared to the  $R = 0.1$  condition.

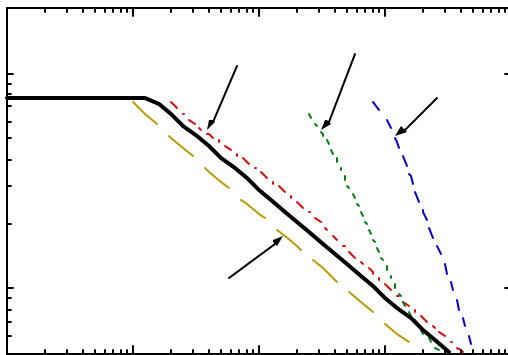


Fig. 11. Effects of surface residual stresses on crack growth threshold conditions under  $R = 0.1$  fatigue.

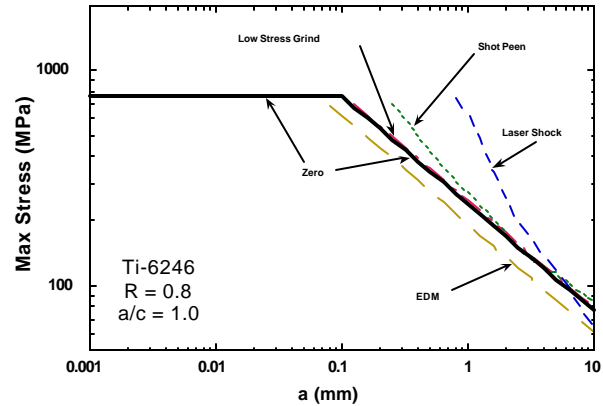


Fig. 12. Effects of surface residual stresses on crack growth threshold conditions under  $R = 0.8$  fatigue.

As shown in Fig. 5, the three microstructural conditions of the gamma TiAl alloy have substantially steeper crack-growth-rate curves than does the Ti-6246, but the gamma alloy microstructures also exhibit much higher values of  $DK_{th}$  than does the conventional titanium alloy. In addition, the gamma alloys typically show excellent resistance to fatigue crack initiation and have fatigue limits that are a large fraction of their tensile strength [15]. Thus, the gamma alloys appear to present both challenges and opportunities for use as structural materials in turbine engine components that require damage tolerance.

Figure 13 presents a life map for the duplex microstructure of the K5 gamma alloy, showing that the steep crack-growth-rate curve of this material translates into a relatively narrow region of crack growth between the limit lines for  $DK_{th}$  and  $K_Q$ . Assuming that large-crack behavior prevails, this figure indicates that once a crack exceeds  $DK_{th}$  in this material, the crack length could increase only about a factor of three before fracture occurred. This situation presents a major obstacle to the effective application of a damage tolerance approach under low cycle fatigue conditions, since there would be relatively little opportunity for detection of a propagating crack.

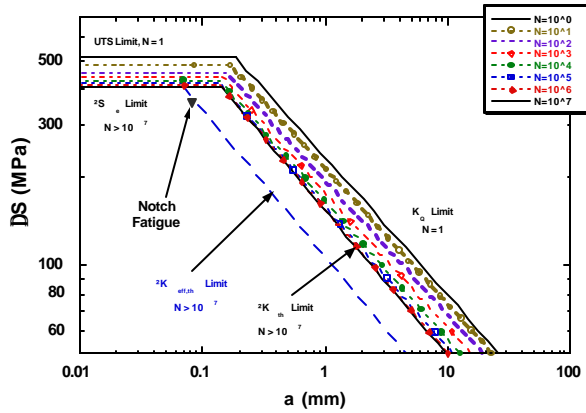


Fig. 13. Fatigue life map for duplex gamma alloy K5 with R=0.1.

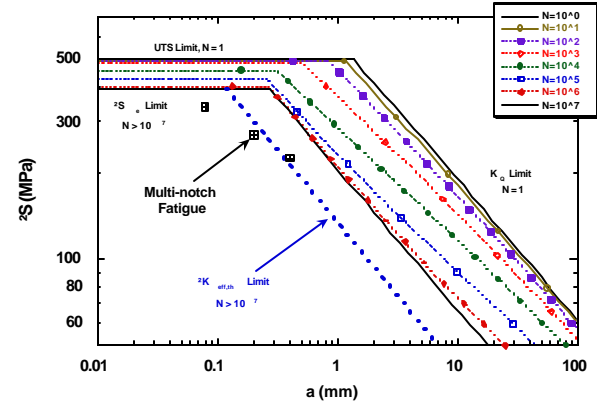


Fig. 14. Fatigue life map for refined fully lamellar gamma alloy K5 with R=0.1.

To assess the crack-size dependence of the life predictions depicted in Fig. 13, fatigue experiments were performed using smooth specimens containing multiple, semicircular surface notches of depth equal to 0.080 mm [7]. The resulting  $10^7$ -cycle fatigue limit for this notched specimen is also plotted as an individual data point in Fig. 13. This result agrees well with the  $DK_{eff,th}$  line, which represents the threshold-stress-intensity-factor range after correcting the data for crack closure. This agreement might be expected, since a given notch would be closure-free over its full initial length. The agreement also suggests that the large-crack threshold may be applicable to cracks at least as small as 0.080 mm.

Similar multi-notch fatigue experiments were performed on the refined fully lamellar material of Fig. 3, and as shown in Fig. 14, the agreement with the limit line corresponding to  $DK_{eff,th}$  was again relatively good. In this case, experiments were performed using three distinct multi-notch depths: 0.080, 0.200, and 0.400 mm. The 0.080 mm notch data fell to the left of the  $DK_{eff,th}$  prediction, which might be expected since the fatigue limit stress for these specimens approached  $DS_e$ . The figure also shows that the region of crack propagation between the  $DK_{th}$  and  $K_Q$  limit lines corresponds to an order-of-magnitude increase in crack size.

Figure 15 presents a detailed life map for the coarse lamellar K5 alloy. This material also exhibited good crack growth resistance compared to the duplex material. As shown in the figure, however, fatigue tests of the K5-L specimens containing multiple, 0.080-mm-deep, semicircular surface notches produced an unusual result [16]. As shown by the open symbols, four of these specimens failed under loading conditions that were well below the predictions based on  $DK_{eff,th}$ . A detailed examination of the fracture surfaces of these specimens indicated that the critical crack typically formed from a notch located in a lamellar colony such that the normal of the lamellar orientation was within  $\sim 20^\circ$  of the loading axis. Apparently this configuration led to nucleation of a crack in the weak lamellar colony orientation, and the crack grew quickly across the lamellar colony in the relatively low-toughness interlamellar mode. At this point, the stress intensity factor range,  $DK$ , of this 'pop-in' crack, conservatively calculated as a semicircular surface crack, was close to the bulk coarse lamellar threshold,  $DK_{th} = 8.5 \text{ MPa} \cdot \text{m}$ , and

subsequent failure of the specimen occurred due to propagation from this initial flaw. The multi-notch specimen indicating the highest fatigue strength appeared to fail from the smallest 'pop-in' crack, which was also the most inclined to the loading axis - resulting in fatigue strength comparable to smooth specimens. The specimen with the poorest fatigue resistance failed in a lamellar colony with the hardest orientation, and had a neighboring colony with a sympathetic orientation within  $6^\circ$  of the original colony.

Some insight into these results may be gained by considering the findings of Yokoshima and Yamaguchi [17] on polysynthetically twinned (PST) crystals. These researchers determined fracture toughness as a function of crack plane for two typical gamma PST materials. They reported that a minimum in fracture toughness occurred when the axis of loading was normal to the lamellar planes, which they designated as Type III loading, noting that  $K_{IC(min-Type III)} = 3.3 \text{ MPa} \cdot \text{m}$ . Using this approximate value, one may add the Type III limit line indicated in Fig. 15, and see that this trend agrees well with the multi-notch data assuming a 0.080 mm depth. The specimen that failed at the highest stress exhibited failure that was not strongly influenced by the notch. Hence, it fell close to the fatigue limit line. The other data fell below this line and close to the sloped line of the Type III  $K_{IC}$ . None of these specimens achieved  $10^7$  cycles without failure, which might be expected since it is likely that the threshold for fatigue crack propagation,  $K_{max,th}$ , is below  $K_{IC(min-Type III)}$ . This comparison of PST behavior with that from the random lamellar material indicates that fatigue initiation and early propagation are closely related to the behavior of a few, specifically orientated lamellar colonies, and that this effect should be designated as microstructurally-small-crack behavior.

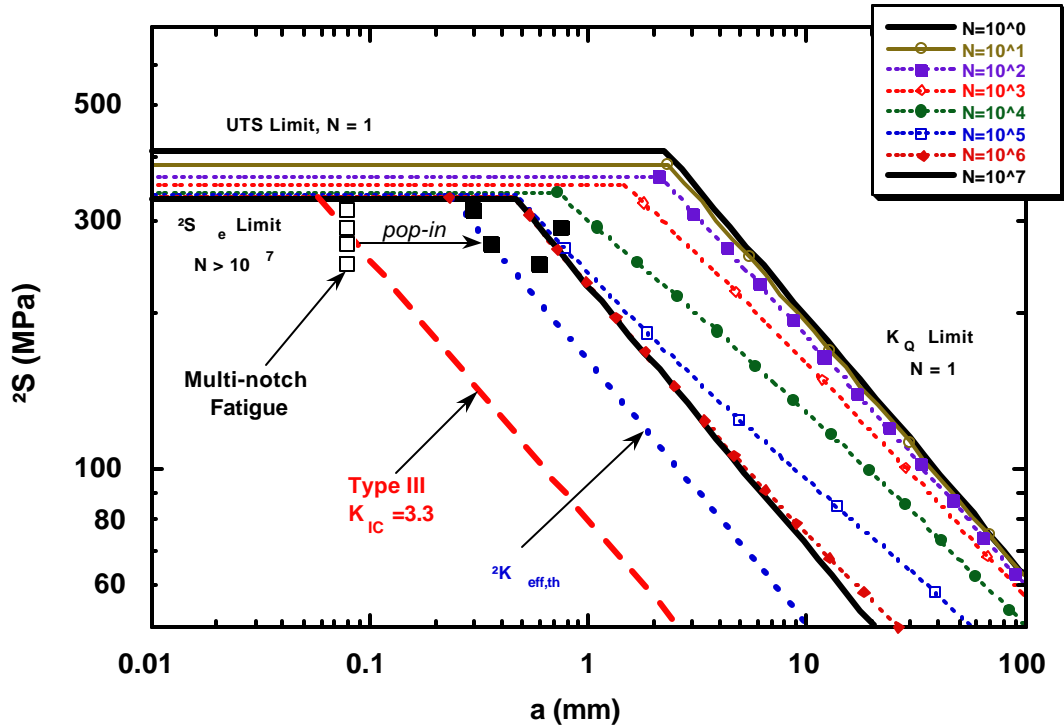


Fig. 15. Fatigue life map for coarse lamellar gamma alloy K5 with R=0.1.

## CONCLUDING REMARKS

As shown in Fig. 5, effects of alloy composition and microstructure can have a dramatic effect on crack growth resistance, which leads to questions regarding life management criteria for components that require damage tolerance. Since turbine engine loading spectra may contain low- and high-cycle fatigue, a material's crack-growth-threshold and mid-range crack growth behaviors are both important. This complicates the material selection process since, as shown in the figure, the trend in crack-growth threshold may run counter to a material's mid-range crack growth resistance. In both cases it is important to consider the effects of other sources of defects and service damage, including effects of intrinsic material defects, handling and foreign object damage, and initial manufacturing processes.

Given the current limits of nondestructive evaluation techniques, it appears that cracks of a detectable size in Ti-6246 can be predicted relatively well using large-crack fracture mechanics data. That is, small-crack effects in this material appear to occur at crack sizes that are well below the starting crack size that would be used in an inspection-based approach to life management. Moreover, the imposition of residual stresses on the surface of this material can dramatically increase the threshold crack size.

Although surface residual stresses should also promote resistance to initial crack growth in the gamma alloys, this class of materials presents special challenges. It appears that improved damage-tolerant life-prediction methods are needed to develop and utilize the full potential of gamma TiAl alloys as structural materials. The unique balance of properties offered by these alloys presents important opportunities for improved turbine engine performance, but the introduction of these materials into fracture-critical engine components must be accomplished without increasing the risk of failure. This will require an improved level of accuracy in life prediction modeling and the ability to simulate microstructural tailoring for specific application needs. For example, Fig. 6 shows that at the same stress level, the threshold crack size for all of the gamma microstructures is much greater than in the Ti-6246. The duplex condition of the gamma alloy, however, can only tolerate a very small crack extension prior to failure, which would make this material a poor choice for applications that contain significant contributions of low cycle fatigue. Alternatively, it was shown that the propagation condition for small fatigue cracks in lamellar microstructures, which is governed by interlamellar splitting of similarly-aligned, poorly-oriented colonies, falls well below the predictions based on large-crack fracture mechanics. Thus, this microstructure is poorly suited for applications requiring good threshold crack growth resistance for small flaws. It appears, however, that the worst-case crack propagation behavior associated with interlamellar cracking does not dictate fatigue capability and defect tolerance, if the colony size is sufficiently small.

## ACKNOWLEDGMENTS

This research was performed in the Air Force Research Laboratory, Materials and Manufacturing Directorate, Wright-Patterson Air Force Base, OH and was supported in part by the Air Force Office of Scientific Research under Task 2302BW1. The authors would like to acknowledge the thoughtful comments of Mr. Jay R. Jira and the technical assistance of Mr. Kevin Gross and Mr. Michael Shepherd.

1. U.S. Air Force, Engine Structural Integrity Program, (1984). *Military Standard 1783*, Aeronautical Systems Division, Wright-Patterson Air Force Base, OH.
2. Nicholas, T. and Zuiker, J. R. (1996). *Int. J. of Fracture*, Vol. 80, pp. 219-235.
3. Cowles, B. A., (1996). *Int. J. of Fracture*, Vol. 80, pp. 147-163.
4. Larsen, J. M., Worth, B. D., Annis, C. G., Jr., and Haake, F. K., (1996). *Int. J. of Fracture*, Vol. 80, pp. 237-255.
5. Y.-W. Kim, (1994). *JOM*, Vol. 46, No. 7, pp. 30-40.
6. ASTM E-647-95a, (1997). *1997 Annual Book of ASTM Standards*, Vol. 03.01, ASTM, Philadelphia, PA, pp. 557-593.

- 
7. Kitagawa, H. and Takahashi, S., (1976). *Proceedings of the Second International Conference on Mechanical Behavior of Materials*, Boston, MA, pp. 627-631.
  8. Larsen, J. M. and Jira, J. R., (1991). *Experimental Mechanics*, pp. 82-87.
  9. Larsen, J. M., Jira, J. R., and Weerasooriya, T., (1988). *Fracture Mechanics: Eighteenth Symposium, ASTM STP 945*, D. T. Read and R. P. Reed, ed., American Society for Testing and Materials, Philadelphia, PA, pp. 896-912.
  10. Jira, J. R., Weerasooriya, T., Nicholas, T., and Larsen, J. M., (1988). *Mechanics of Fatigue Crack Closure, ASTM STP 982*, J. C. Newman, Jr. and W. Elber, ed., American Society for Testing and Materials, Philadelphia, PA, pp. 617-635.
  11. Jira, J. R., Nicholas, T., and Larsen, J. M., (1987). *Fatigue 87*, Vol. IV, E. Starke and R. O. Ritchie, ed., Engineering Materials Advisory Services, Ltd., West Midlands, U. K., pp. 1851-1860.
  12. Haake, F. K. Salivar, G. C., Hindle, E. H., Fischer, J. W., and Annis, C. G., Jr., (1989). *U. S. Air Force Technical Report WRDC-TR-89-4085*. Wright-Patterson Air Force Base, OH.
  13. Mason, P. W., Lachtrupp, T. P., and Prevey, C. S., (1997). *Report # 674-6903*, Lambda Research, Inc., Cincinnati, OH.
  14. John, R. et al, "Effects of Residual Stress on the Threshold Fatigue Behavior of Small Surface Cracks in a Titanium Alloy," to be submitted for publication.
  15. Larsen, J.M., Worth, B.D., Balsone, S.J., Rosenberger, A.H., and Jones, J.W., (1996). In: *FATIGUE '96, Vol. III*, G. Lütjering and H. Nowack, Eds., Elsevier Science Ltd., Oxford, U.K., pp. 1719-1730.
  16. Larsen, J. M., Rosenberger, A. H., Li, K., Porter, W. J., and John, R., (1999). To be published in: *FATIGUE '99*.
  17. Yokoshima, S. and Yamaguchi, M., (1996). *Acta Mater.*, Vol. 44, No. 3, pp. 873-883.

This page intentionally left blank.



## MIXED MODE CRACK GROWTH IN A GAMMA TITANIUM ALUMINIDE

Reji John<sup>1</sup>, Dan DeLuca<sup>2</sup>, W. John Porter<sup>3</sup> and Andrew H. Rosenberger<sup>1</sup>

This paper describes the results of an investigation of mixed mode (mode I and mode II) loading on the crack growth behavior of a gamma titanium aluminide (TiAl) alloy. A centrally notched disk specimen was used, and the tests were conducted at room temperature. Mixed mode loading conditions were achieved by orienting the machined flaw at different angles to the loading axis. A specimen with large ( $\approx 5$  mm) grains was used to characterize the interlamellar growth under mixed mode loading conditions. Preliminary results indicate that the interlamellar mixed mode crack growth rate is  $\approx 10$ -100X faster than the transgranular mode I crack growth rate in a gamma TiAl and is also associated with a significantly lower  $\Delta K_{th}$ .

### INTRODUCTION

Gamma TiAl alloys are under consideration for use as structural materials in advanced aerospace engines (1). Although, the lamellar colonies are typically randomly oriented, closely aligned lamellar colonies could occur in a fully lamellar gamma TiAl component. Such closely aligned colonies are potential crack initiation sites, especially at locations experiencing mixed mode (tension + shear) loading. Larsen et al. (2) showed that, during tension-tension fatigue loading of specimens with a single, artificial semi-circular flaw, most of the gamma TiAl specimens did not fail at the location of the flaw. Damage initiation occurred at locations away from the machined notch, indicating that closely aligned and unfavorably oriented colonies could have created a crack initiation site. Hence, accurate prediction of the in-service life of gamma TiAl components will require a basic understanding of the influence of orientation on the crack growth behavior of a lamellar colony. This paper describes an investigation of the mixed mode interlamellar crack growth within a grain and transgranular crack growth in gamma TiAl alloys.

### EXPERIMENTAL PROCEDURE

The geometry adapted for testing under mixed mode loading was the “Brazilian” Disk with a Middle crack subjected to Compressive loading, DM(C), as shown in Fig. 1 (3). References for mode I stress intensity factor,  $K_I$ , and mode II stress intensity factor,  $K_{II}$ , solutions for this geometry can be found in Ref. (3). A wide range of the ratio  $K_{II}/K_I$  can be achieved at the crack tip by orienting the crack at different angles ( $\theta$ ) to the loading axis.

The baseline gamma TiAl alloy used during this study had the nominal composition Ti-47Al-2Cr-2Nb-1Mo-0.2B (at %) with an average lamellar grain size of  $\approx 100$   $\mu$ m. In this alloy, the boron is primarily used for grain refinement. A special heat treatment procedure was used on an identical material without boron, i.e. Ti-47Al-2Cr-2Nb-1Mo (at %), to obtain a large colony size,  $\approx 5$  mm, from which a DM(C) specimen was machined with a central large colony. The typical dimensions of the Ti-47Al-2Cr-2Nb-1Mo-0.2B specimens were: diameter,  $W \approx 26$  mm, thickness,  $B \approx 2$  mm, and initial crack length,  $2a_0 = 9.72$  mm, and those of Ti-47Al-2Cr-2Nb-1Mo with large grains were:  $W = 17.83$  mm,  $B = 1.86$  mm, and  $2a_0 = 0.8$  mm. The tests were conducted in laboratory air at a frequency of 10-20 Hz with a load ratio,  $R (=K_{min}/K_{max}$  at crack tip), of 0.1-0.3. The loading angles included  $\theta = 0, 16$  and  $26^\circ$ . Further details of testing can be found in Ref. (3). Using the measured crack length versus cycles response,  $K_I$ ,  $K_{II}$ , and the crack growth rate,  $da/dN$ , were calculated as a function of crack length. The  $K_I$  and  $K_{II}$  solutions were based on isotropic elasticity. During the initial tests, high stresses at the loading points resulted in significant deformation and/or failure at these locations. This problem was overcome by using aluminum or copper pads to distribute the contact load.

<sup>1</sup> Air Force Research Laboratory, Materials and Manufacturing Directorate, AFRL/MLLN, Wright-Patterson AFB, Ohio 45433, U.S.A.

<sup>2</sup> Pratt & Whitney, Mechanics of Materials, West Palm Beach, Florida 33410, U.S.A.

<sup>3</sup> University of Dayton Research Institute, Dayton, Ohio 45469, U.S.A.

## RESULTS AND DISCUSSION

### Crack Growth in Ti-47Al-2Cr-2Nb-1Mo-0.2B With Grain Size $\approx 100 \mu\text{m}$

Mode I tests ( $\theta = 0^\circ$ ) were conducted using DM(C) specimens of Ti-47Al-2Cr-2Nb-1Mo-0.2B. These data, as shown in Fig. 2, correlate well with the results obtained using compact tension, C(T) specimens (4). The apparent decrease in slope of the  $da/dN-\Delta K$  response of the DM(C) specimens at high  $\Delta K$  could be attributed to: (i) decrease in  $K$  for long cracks due to the assumption of point loads, while in practice the load was distributed at the loading points, and (ii) the large plastic zone formed around the loading points due to high stresses. The overall good correlation of the mode I data validates the use of the DM(C) geometry.

The crack path measured during the mixed mode test conducted with  $\theta=26^\circ$  is shown in Fig. 3. The mixed mode crack propagation path, predicted using the finite element code FRANC2D/L (5), correlates well with the measured path as shown in Fig. 3. From this finite element analysis, we obtained  $K_I$  and  $K_{II}$  along the curved crack propagation path as shown in Fig. 4. This test was started under pure mode II conditions with  $K_I = 0$  and  $K_{II} = 8 \text{ MPa}\sqrt{\text{m}}$ . Crack initiation occurred at an angle of  $\approx 70^\circ$  with respect to the starter flaw. As soon as the crack initiated,  $K_I$  increased to  $\approx 10 \text{ MPa}\sqrt{\text{m}}$  and  $K_{II}$  decreased to 0, consistent with the conventional mixed mode crack extension theories. The subsequent crack propagation occurred along a curved path (Fig. 3) towards the loading point associated with increasing  $K_I$  and  $K_{II}=0$  (Fig. 4). During mixed mode crack propagation, the equivalent stress intensity factor range at the crack tip,  $\Delta K_{eq}$ , can be obtained as  $\Delta K_{eq} = \sqrt{[\Delta K_I]^2 + [\Delta K_{II}]^2}$ . The transgranular mixed mode  $da/dN-\Delta K_{eq}$  behavior is also shown in Fig. 2. Since  $K_{II}$  was  $\approx 0.0$  during this test,  $\Delta K_{eq}$  was  $\approx \Delta K_I$  along the curved crack path. Hence, the mixed mode data correlated well with the mode I data. Similar mixed mode crack growth behavior was also seen in fine-grained Ti-6Al-4V and other materials (3).

### Crack Growth in Ti-47Al-2Cr-2Nb-1Mo With Grain Size $\approx 5 \text{ mm}$

Figure 5 shows the large, centrally located grain in the DM(C) specimen, which was used to study interlamellar mixed mode crack growth in Ti-47Al-2Cr-2Nb-1Mo. The initial flaw was located in the center of the large grain and oriented parallel to the lamellae. This specimen was tested with  $\theta=16^\circ$  and  $R=0.2$ . The test was started at low load levels, and the load was increased in steps until crack initiation was observed. After initiation, the crack propagated parallel to the initial flaw and the laths, in contrast to the curved path seen in Fig. 3. The corresponding loading history and the crack growth response are shown in Fig. 6. The crack growth was rapid soon after initiation and continued to increase even when the applied load was decreasing slightly. Figure 7 shows the variation of  $K_I$  and  $K_{II}$  during the interlamellar crack growth. The test was started with  $K_I$  and  $K_{II} \approx 1.8$  and  $2.8 \text{ MPa}\sqrt{\text{m}}$ , respectively. Subsequent interlamellar crack propagation was associated with  $K_{II}/K_I \approx 1.5 - 1.7$  and  $K_I > 0$ .

The interlamellar  $da/dN-\Delta K_{eq}$  behavior of Ti-47Al-2Cr-2Nb-1Mo is compared with the transgranular behavior of Ti-47Al-2Cr-2Nb-1Mo-0.2B in Fig. 8. In making this comparison, the boron found in the  $\approx 100 \mu\text{m}$  colony sized gamma TiAl is expected to have no effect other than to control the colony size, i.e., similarly processed Ti-47Al-2Cr-2Nb-1Mo is expected to have similar or lower crack growth rates compared to Ti-47Al-2Cr-2Nb-1Mo-0.2B. All the data shown in this figure were obtained using the DM(C) geometry. The interlamellar mixed mode crack growth rate at  $R=0.2$  is  $\approx 100X$  faster than the mode I  $da/dN$  at  $R=0.1$  and  $\approx 10X$  faster than the mode I  $da/dN$  at  $R=0.3$ . In addition, the trend in Fig. 8 appears to indicate that the threshold  $\Delta K$  ( $\Delta K_{th}$ ) for interlamellar mixed mode crack growth with  $K_I > 0$ , is significantly lower than that for mode I transgranular crack growth. Hence, the combination of low  $\Delta K_{th}$  and faster growth rates of unfavorably oriented grain(s) could result in premature failure during fatigue loading as discussed in Ref. (1). Additional tests and analysis are in progress to determine the differences between interlamellar and transgranular near-threshold crack growth behavior, and to assess the accuracy of using equations based on isotropic elasticity to calculate  $K_I$  and  $K_{II}$ .

## CONCLUSIONS

Mixed mode crack growth in the absence of significant friction between the crack surfaces in fine grained gamma TiAl is similar to that in isotropic materials. Preliminary results indicate that interlamellar mixed mode crack growth rate is  $\approx 10\text{-}100\text{X}$  faster than the transgranular mode I crack growth rate in a gamma TiAl and is also associated with significantly lower  $\Delta K_{th}$ .

## ACKNOWLEDGMENT

This research was conducted at the Air Force Research Laboratory, Materials and Manufacturing Directorate, Wright-Patterson Air Force Base, OH 45433-7817, USA, and was supported in part by the Air Force Office of Scientific Research under Task 2302BW1. Mr. John Porter was supported under on-site contract number F33615-98-C-5214.

## REFERENCES

- (1) Larsen, J. M., Rosenberger, A. H., Li, K., Porter, W.J., and John, R., Fatigue '99, Engineering Materials Advisory Services, Ltd., West Midlands, UK, (this publication), 1999.
- (2) Larsen, J.M., Worth, B.D., Air Force Research Laboratory, AFRL/MLLN, Wright-Patterson AFB, OH 45433, U.S.A., Unpublished results, 1997.
- (3) John, R., DeLuca, D., Nicholas, T., and Porter, W. J., in Mixed-Mode Crack Behavior, Editors. K. J. Miller and D. L. McDowell, ASTM STP 1359, American Society for Testing and Materials, West Conshohocken, PA, 1999.
- (4) A. H. Rosenberger, Air Force Research Laboratory, AFRL/MLLN, Wright-Patterson AFB, OH 45433, U.S.A., Unpublished results, 1998.
- (5) James, M. and Swenson, D., "FRANC2D/L: A Crack Propagation Simulator for Plane Layered Structures," Kansas State University, Manhattan, KS, U.S.A., Internet address: [www.mne.ksu.edu/~franc2d/](http://www.mne.ksu.edu/~franc2d/), 1997.

Figure 1 Schematic of a centrally notched disk subjected to compression.

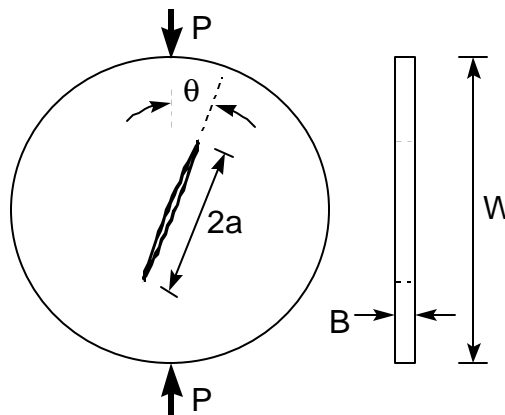


Figure 2 Transgranular mode I and mixed mode crack growth behavior of Ti-47Al-2Cr-2Nb-1Mo-0.2B.

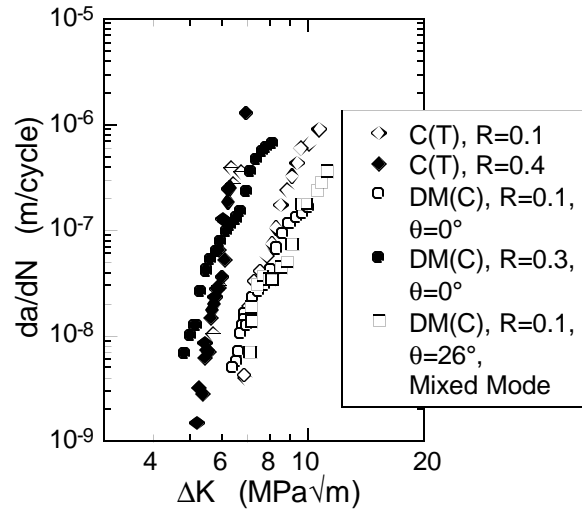


Figure 3 Mixed mode crack growth path in Ti-47Al-2Cr-2Nb-1Mo-0.2B. ( $\theta = 26^\circ$ , 1/4 section shown)

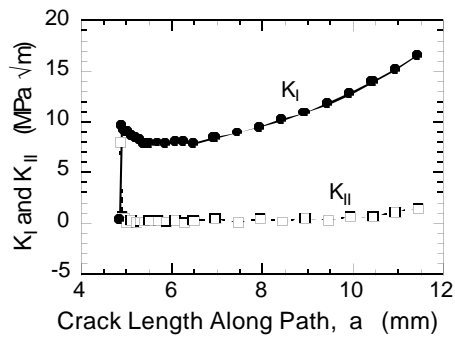
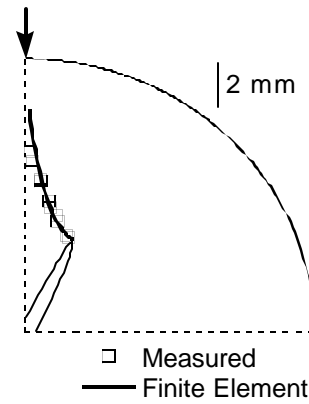


Figure 4 Variation of  $K_I$  and  $K_{II}$  during the crack growth shown in Figure 3.

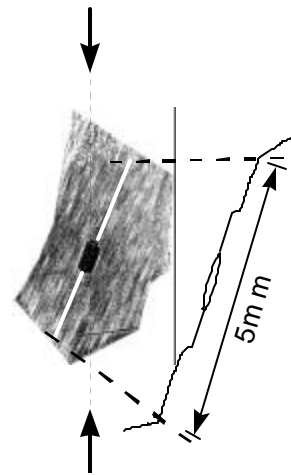


Figure 5 Interlamellar crack growth within a grain in Ti-47Al-2Cr-2Nb-1Mo. ( $\theta=16^\circ$ )

Figure 6 Loading history and crack growth within the grain in Ti-47Al-2Cr-2Nb-1Mo.

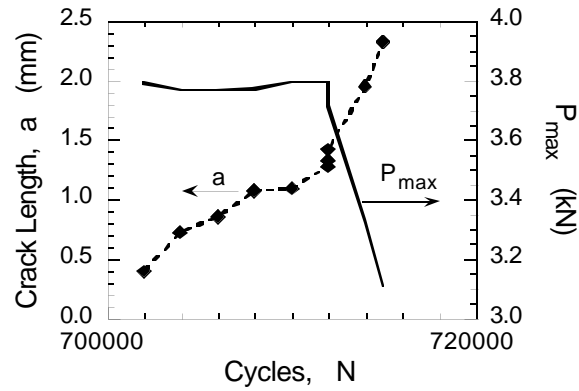


Figure 7  $K_I$  and  $K_{II}$  during crack growth within the grain in Ti-47Al-2Cr-2Nb-1Mo.

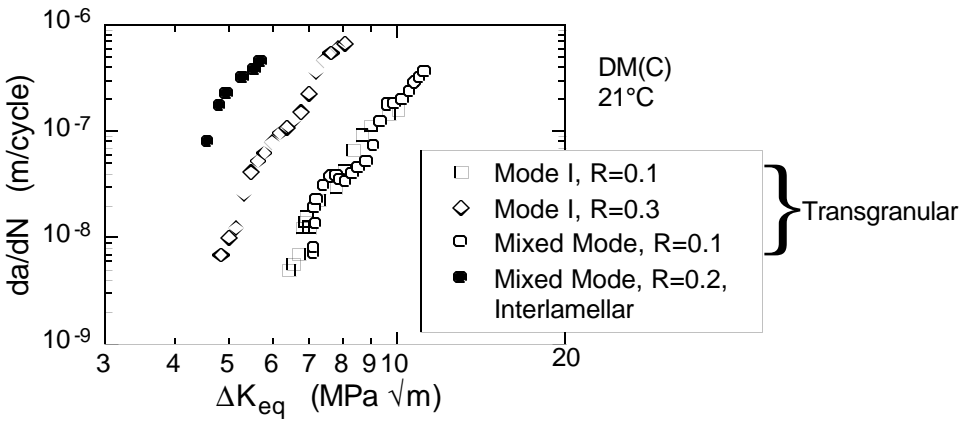
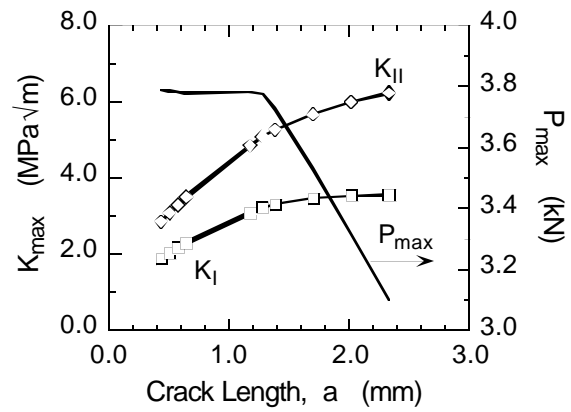


Figure 8 Comparison of transgranular & interlamellar crack growth behaviors.

This page intentionally left blank.

## MIXED MODE CRACK GROWTH IN A GAMMA TITANIUM ALUMINIDE ALLOY

Reji John, Andrew H. Rosenberger, Dan DeLuca<sup>1</sup>, W. John Porter<sup>2</sup>, and Kezhong Li<sup>2</sup>

Materials and Manufacturing Directorate (AFRL/MLLN),  
Air Force Research Laboratory, Wright-Patterson AFB, Ohio 45433, U.S.A.

<sup>1</sup> Pratt & Whitney, Mechanics of Materials, West Palm Beach, Florida 33410, U.S.A

<sup>2</sup> University of Dayton Research Institute, Dayton, Ohio 45469, U.S.A.

### Abstract

The results of an investigation of mixed mode (mode I and mode II) loading on the crack growth behavior of a gamma titanium aluminide (TiAl) alloy are discussed. A centrally notched disk specimen was used, and the tests were conducted at room temperature. Mixed mode loading conditions were achieved by orienting the machined flaw at different angles to the loading axis. A specimen with large ( $\approx 5$  mm) grains was used to characterize the interlamellar growth under mixed mode loading conditions. Preliminary results indicate that interlamellar mixed mode crack growth rate is  $\approx 10$ -100X faster than the transgranular mode I long crack growth rate and up to  $\approx 10$ X faster than small crack growth rate

### Introduction

Gamma TiAl alloys are under consideration for use as structural materials in advanced aerospace engines (1-3). These alloys may be processed and heat treated to produce different microstructures. One extreme is a fine *duplex* microstructure consisting of a mixture of equiaxed  $\gamma$  grains and fine colonies of lamellar  $\gamma$  plus  $\alpha_2$  phase. The average colony size of the duplex microstructure is  $\approx 20$ -40  $\mu\text{m}$ . This microstructure has comparatively good strength and moderate ductility but a relatively low fracture toughness (4). Using an appropriate heat treatment procedure, the duplex microstructure can be modified to a *lamellar* microstructure of large colonies of fine lamellar  $\gamma$  plus  $\alpha_2$  laths. The average colony size of the lamellar microstructure is  $\approx 300$ -500  $\mu\text{m}$ . Compared to the duplex material, this lamellar microstructure is of lower strength and ductility but improved fracture toughness (4). Alternate heat treatment procedures have also been developed to produce a fine-grained ( $\approx 100$ -200  $\mu\text{m}$ ) refined lamellar microstructure resulting in a better balance of properties (4,5).

In  $\gamma$  TiAl components with such lamellar microstructures, the colonies are typically randomly oriented. But, occasionally, closely aligned lamellar colonies could occur in these components. Such closely aligned colonies are potential crack initiation sites, especially at locations experiencing mixed mode (tension + shear) loading. Larsen and Worth (6) showed that, during tension-tension fatigue loading of specimens with a single, artificial semi-circular flaw, most of the gamma TiAl specimens did not fail at the location of the flaw. Damage initiation occurred at locations away from the machined notch, indicating that closely aligned and unfavorably oriented colonies could have created a crack initiation site. Hence, accurate prediction of the in-service life of gamma TiAl components will require a basic understanding of the influence of lamellar orientation on the cyclic crack growth within a colony. Although long (3,4,7-9) and small (8,9) cyclic crack growth data are available in the literature, very little understanding of the mixed mode crack growth within a lamellar colony (interlamellar crack growth) exists. This paper describes an investigation of the mixed mode interlamellar crack growth within a

grain and comparison with transgranular crack growth in gamma TiAl alloys.

### Experimental Procedure

The geometry adapted for testing under mixed mode loading was the “Brazilian” Disk with a Middle crack subjected to Compressive loading, DM(C), as shown in Fig. 1 (10,11).

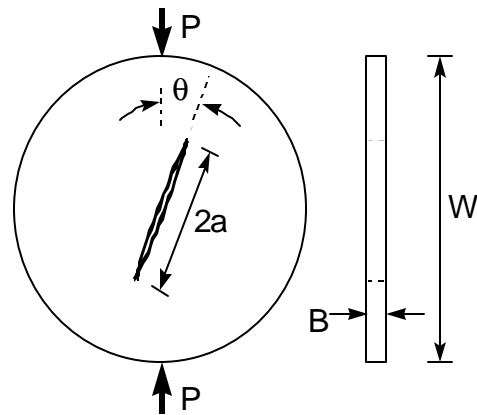


Figure 1: Schematic of a centrally notched disk subjected to compression.

References for mode I stress intensity factor,  $K_I$ , and mode II stress intensity factor,  $K_{II}$ , solutions for this geometry can be found in Ref. (10,11). A wide range of the ratio  $K_{II}/K_I$  can be achieved at the crack tip by orienting the crack at different angles ( $\theta$ ) to the loading axis.

The baseline gamma TiAl alloy used during this study had the nominal composition Ti-47Al-2Cr-2Nb-1Mo-0.2B (Alloy 3-95, at %) with an average lamellar grain size of  $\approx 100 \mu\text{m}$ . In this alloy, the boron is primarily used for grain refinement. Large (diameter  $\approx 70 \text{ mm}$ ) disks of TiAl alloys without boron, i.e. Ti-47Al-2Cr-2Nb-1Mo (at %) and Ti-46.5Al-3Nb-2Cr-0.2W (at %), were heat treated at  $1385^\circ\text{C}$  for 24 hours in high vacuum, to obtain a large colony size,  $\approx 5 \text{ mm}$ . These heat treated disks were machined to obtain mini-DM(C) specimens with a centrally located large through-thickness colony. The initial notches ( $=2a_0$ ) were created using electrical discharge machining (EDM). The typical dimensions of the Ti-47Al-2Cr-2Nb-1Mo-0.2B specimens were: diameter,  $W \approx 26 \text{ mm}$ , thickness,  $B \approx 2 \text{ mm}$ , and initial crack length,  $2a_0 = 9.72 \text{ mm}$ , and those of Ti-47Al-2Cr-2Nb-1Mo and Ti-46.5Al-3Nb-2Cr-0.2W with large grains were:  $W = 18 \text{ mm}$ ,  $B = 1.9 \text{ mm}$ , and  $2a_0 = 0.8 \text{ mm}$ . The tests were conducted in laboratory air at a frequency of 10-20 Hz with a load ratio,  $R (=K_{\min}/K_{\max}$  at crack tip), of 0.1-0.3. The loading angles included  $\theta = 0, 16$  and  $26^\circ$ . Crack length was monitored using the direct current electric potential (DCEP) technique and corrected using optical measurements. Further details of testing can be found in Ref. (10). Using the corrected crack length versus cycles response,  $K_I$ ,  $K_{II}$ , and the crack growth rate,  $da/dN$ , were calculated as a function of crack length. The  $K_I$  and  $K_{II}$  solutions were based on isotropic elasticity. During the initial tests, high stresses at the loading points resulted in significant deformation and/or failure at these locations. This problem was overcome by using aluminum or copper pads to distribute the contact load.

## Results and Discussion

### Transgranular Crack Growth in Ti-47Al-2Nb-2Cr-1Mo-0.2B With Colony Size $\approx 100 \mu\text{m}$

Mode I tests ( $\theta = 0^\circ$ ) were conducted using DM(C) specimens of Ti-47Al-2Cr-2Nb-1Mo-0.2B.

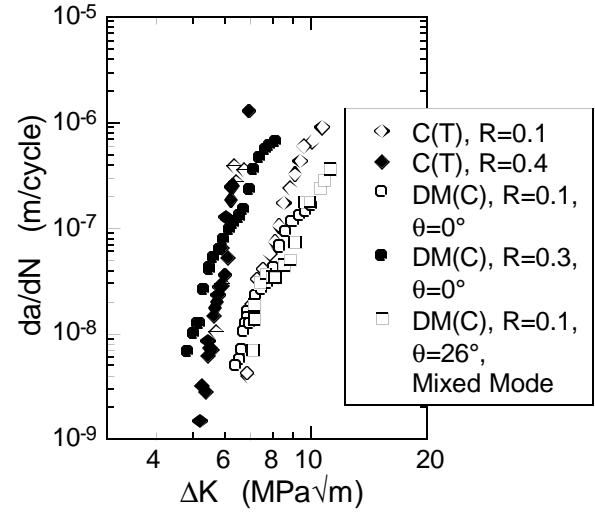


Figure 2: Transgranular mode I and mixed mode crack growth behavior of Ti-47Al-2Cr-2Nb-1Mo-0.2B.

These data, as shown in Fig. 2, correlate well with the results obtained using compact tension, C(T) specimens. The apparent decrease in slope of the  $da/dN$ - $\Delta K$  response of the DM(C) specimens at high  $\Delta K$  could be attributed to: (i) decrease in  $K$  for long cracks due to the assumption of point loads, while in practice the load was distributed at the loading points, and (ii) the large plastic zone formed around the loading points due to high stresses. The overall good correlation of the mode I data validates the use of the DM(C) geometry.

The crack path measured during the mixed mode test conducted with  $\theta = 26^\circ$  is shown in Fig. 3.

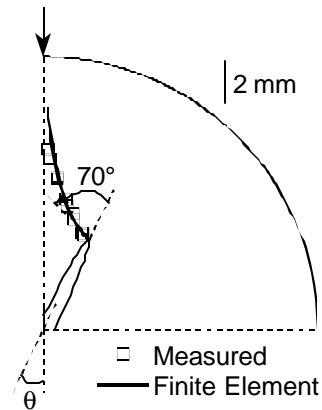


Figure 3: Mixed mode crack growth path in Ti-47Al-2Cr-2Nb-1Mo-0.2B. ( $\theta = 26^\circ$ , 1/4 section shown)

The mixed mode crack propagation path, predicted using the finite element code FRANC2D/L (12), correlates well with the measured path as shown in Fig. 3. From this finite element analysis, we obtained  $K_I$  and  $K_{II}$  along the curved crack propagation path as shown in Fig. 4.



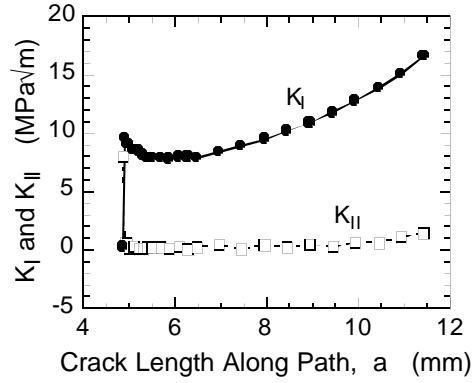


Figure 4: Variation of  $K_I$  and  $K_{II}$  during the crack growth shown in Figure 3.

This test was started under pure mode II conditions with  $K_I = 0$  and  $K_{II} = 8 \text{ MPa}\sqrt{\text{m}}$ . Crack initiation occurred at an angle of  $\approx 70^\circ$  with respect to the starter flaw. As soon as the crack initiated,  $K_I$  increased to  $\approx 10 \text{ MPa}\sqrt{\text{m}}$  and  $K_{II}$  decreased to 0, consistent with the conventional mixed mode crack extension theories. The subsequent crack propagation occurred along a curved path (Fig. 3) towards the loading point associated with increasing  $K_I$  and  $K_{II}=0$  (Fig. 4). During mixed mode crack propagation, the equivalent stress intensity factor range at the crack tip,  $\Delta K_{eq}$  can be obtained as  $\Delta K_{eq} = \sqrt{[\Delta K_I^2 + \Delta K_{II}^2]}$ . The transgranular mixed mode  $da/dN-\Delta K_{eq}$  behavior is also shown in Fig. 2. Since  $K_{II}$  was  $\approx 0.0$  during this test,  $\Delta K_{eq}$  was  $\approx \Delta K_I$  along the curved crack path. Hence, the mixed mode data correlated well with the mode I data. Similar mixed mode crack growth behavior was also seen in fine-grained Ti-6Al-4V and other materials (10).

#### Interlamellar Crack Growth in Ti-47Al-2Nb-2Cr-1Mo and Ti-46.5Al-3Nb-2Cr-0.2W With Grain Size $\approx 5 \text{ mm}$

Figure 5 shows the large, centrally located grain in the DM(C) specimen, which was used to study interlamellar mixed mode crack growth in Ti-47Al-2Cr-2Nb-1Mo.

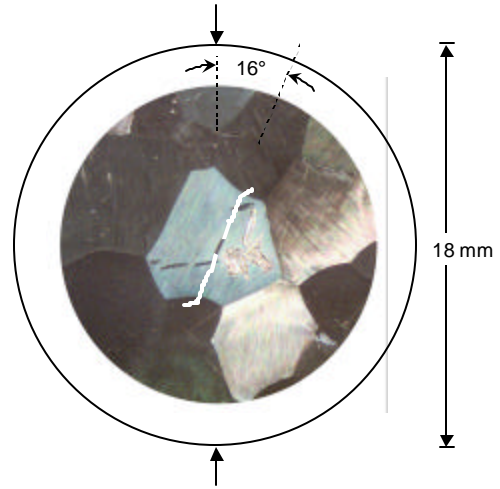


Figure 5: Interlamellar crack growth within a grain in Ti-47Al-2Cr-2Nb-1Mo. Crack path highlighted in white. ( $\theta=16^\circ$ )

The initial flaw was located in the center of the large grain and oriented parallel to the lamellae. This specimen was tested with  $\theta=16^\circ$  and  $R=0.2$ . The test was started at low load levels, and the load was increased in steps until crack initiation was observed. After initiation, the crack propagated parallel to the initial flaw and the laths, in contrast to the curved path seen in Fig. 3. The corresponding loading history and the crack growth response are shown in Fig. 6. The crack growth was rapid soon after initiation and continued to increase even when the applied load was decreasing slightly.

Figure 7 shows the variation of  $K_I$  and  $K_{II}$  during the interlamellar crack growth. The test was started with  $K_I$  and  $K_{II} \approx 1.8$  and  $2.8 \text{ MPa}\sqrt{\text{m}}$ , respectively. Subsequent interlamellar crack propagation was associated with  $K_{II}/K_I \approx 1.5 - 1.7$  and  $K_I > 0$ .

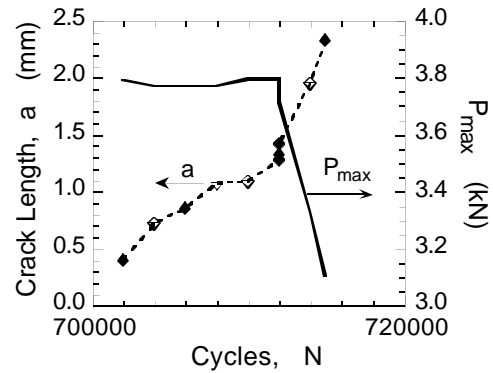


Figure 6: Loading history and mixed mode crack growth within the grain in Ti-47Al-2Cr-2Nb-1Mo.

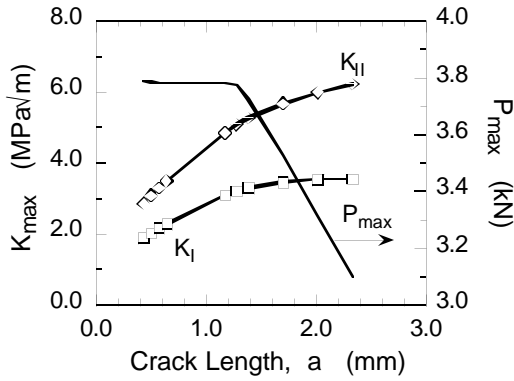


Figure 7:  $K_I$  and  $K_{II}$  during mixed mode crack growth within the grain in Ti-47Al-2Cr-2Nb-1Mo.

Figure 8 shows the loading history for mode I ( $\theta=0^\circ$ ) loading of a Ti-46.5Al-3Nb-2Cr-0.2W DM(C) specimen with a large colony size similar to that shown in Fig. 5. The initial flaw was located in the center of the large grain and oriented parallel to the lamellae. This specimen was tested with  $\theta=0^\circ$  and  $R=0.2$ . The test was started at low load levels, and the load was increased in steps until crack initiation was observed. The corresponding maximum stress intensity factor,  $K_{I,max}$  values are shown in Fig. 8. Crack extension as indicated by DCEP was not observed for  $K_{I,max} \leq 2.5$  MPa√m. When  $K_{I,max}$  was increased to 2.7 MPa√m, sudden crack extension was observed during the loading cycle. Note that the final crack length (center-to-tip) = 2.5 mm which corresponds to  $\approx$  half-colony size.

The sudden crack extension observed under mode I loading is consistent with the brittle fracture behavior observed during crack extension parallel to the lamellae in Polysynthetically Twinned (PST) crystals of TiAl (13,14).  $K_{I,max}$  obtained (= 2.7 MPa√m) at failure of a colony under mode I conditions is within the range of values reported for  $K_{I,max}$  for PST crystals (=2.7-4.3 MPa√m) of TiAl using compact tension (13) and three-point bending (14) specimens.

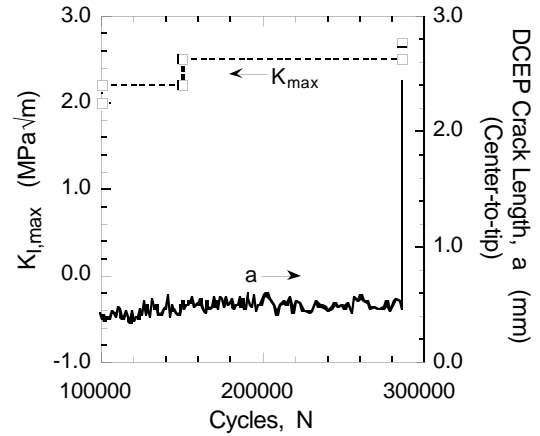


Figure 8: Loading history and mode I crack growth within the grain in Ti-46.5Al-3Nb-2Cr-0.2W. ( $\theta=0^\circ$ )

#### Discussion of Interlamellar and Transgranular Crack Growth Behaviors

The interlamellar  $da/dN-\Delta K_{eq}$  behavior of Ti-47Al-2Cr-2Nb-1Mo is compared with the transgranular behavior of Ti-47Al-2Cr-2Nb-1Mo-0.2B in Fig. 9. In making this comparison, the boron found in the  $\approx 100 \mu\text{m}$  colony sized gamma TiAl is expected to have no effect other than to control the colony size, i.e., similarly processed Ti-47Al-2Cr-2Nb-1Mo is expected to have similar or lower crack growth rates compared to Ti-47Al-2Cr-2Nb-1Mo-0.2B. All the data shown in this figure were obtained using the DM(C) geometry. The interlamellar mixed mode crack growth rate at  $R=0.2$  is  $\approx 100X$  faster than the mode I  $da/dN$  at  $R=0.1$  and  $\approx 10X$  faster than the mode I  $da/dN$  at  $R=0.3$ . In addition, the trend in Fig. 9 appears to indicate that the threshold  $\Delta K$  ( $\Delta K_{th}$ ) for interlamellar mixed mode crack growth with  $K_I > 0$ , could be lower than that for mode I long (transgranular) crack growth. Hence, the combination of low  $\Delta K_{th}$  and faster growth rates of unfavorably oriented grain(s) could result in premature failure during fatigue loading as discussed in Ref. (3).

The interlamellar crack growth behavior shown in Figs. 5 and 9 correspond to crack growth within a colony. Hence, the crack growth behavior obtained during this study was compared with the small crack data available from Chan and Shih (8) and Campbell, Kruzic, Lillibridge, Rao and Ritchie (9) as shown in Fig. 10. The small crack data shown in Fig. 10 correspond to the maximum growth rates as reported in Refs. (8) and (9). The data from a long crack growing in a TiAl with the duplex microstructure is also shown in Fig. 10. The small crack data were obtained from crack lengths of  $\approx 35$ -275  $\mu\text{m}$  in specimens with average colony size  $\approx 145$ -150  $\mu\text{m}$ . Mixed mode crack growth data obtained from this study and the lamellar small crack data from Refs. (8) and (9)

exhibit crack growth rates significantly faster than that for long cracks in a duplex TiAl. In addition, the interlamellar mixed mode crack growth rate could be up to 10X faster than the small crack growth behavior.

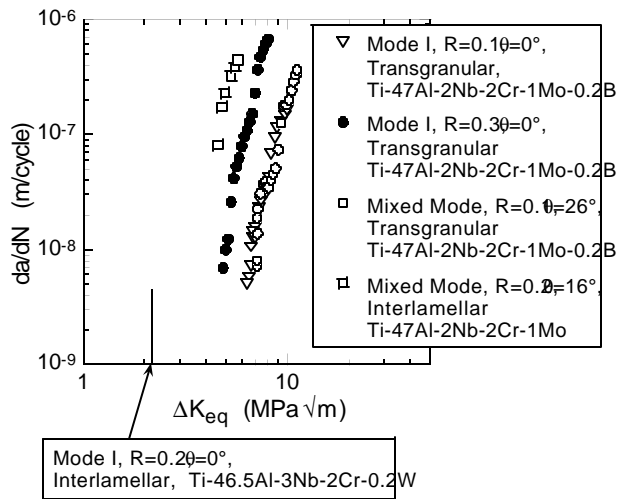


Figure 9: Comparison of transgranular and interlamellar crack growth behaviors. Geometry: DM(C).

Additional tests and analysis are in progress to determine the differences between interlamellar and transgranular near-threshold crack growth behavior, and to assess the accuracy of using equations based on isotropic elasticity to calculate  $K_I$  and  $K_{II}$ .

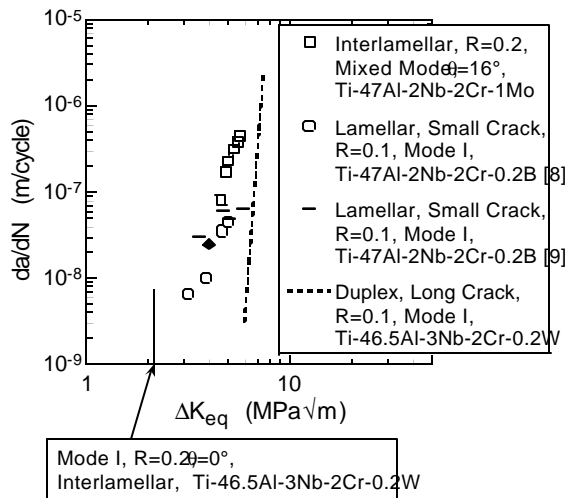


Figure 10: Comparison of interlamellar and small crack growth behaviors.

## Conclusions

Mixed mode crack growth in the absence of significant friction between the crack surfaces in fine grained gamma TiAl is similar to that in isotropic materials. Preliminary results indicate that interlamellar mixed mode crack growth rate is  $\approx 10$ -100X faster than the transgranular mode I long crack growth rate and up to  $\approx 10$ X faster than small crack growth rate.

## Acknowledgments

This research was conducted at the Air Force Research Laboratory, Materials and Manufacturing Directorate, Wright-Patterson Air Force Base, OH 45433-7817, USA, and was supported in part by the Air Force Office of Scientific Research under Task 2302BW1. Mr. John Porter and Dr. Kezhong Li were supported under on-site contract number F33615-98-C-5214.

## References

- (1) Y-W. Kim, "Intermetallic Alloys Based on Gamma Titanium Aluminide," *Journal of Metals*, Vol. 41, No. 7, pp. 24-29, July, 1989.
- (2) Y-W. Kim and D. M. Dimiduk, "Designing Gamma TiAl Alloys: Fundamentals, Strategy and Production," *Structural Intermetallics* 1997, Editors. M.V. Nathal, R. Darolia, et al., TMS, Warrendale, PA, pp.531-543, 1997.
- (3) J.M. Larsen, A.H. Rosenberger, K. Li, W.J. Porter, and R. John, "Tailoring TiAl Intermetallic Alloys To Satisfy Damage Tolerance Requirements For High Performance Turbine Engines," *Fatigue '99*, Engineering Materials Advisory Services, Ltd., West Midlands, UK, 1999.
- (4) J.M. Larsen, B.D. Worth, S.J. Balsone, A.H. Rosenberger, and J.W. Jones, "Mechanisms and Mechanics of Fatigue Crack Initiation and Growth in TiAl Intermetallic Alloys," *Fatigue '96*, Vol. III, G. Lütjering and H. Nowack, Eds., Elsevier Science Ltd., Oxford, U.K., pp. 1719-1730, 1996.
- (5) Y-W Kim, "Ordered Intermetallic Alloys, Part III: Gamma Titanium Aluminides," *Journal of Metals*, Vol. 46, No. 7, pp. 30-40, 1994.
- (6) J.M. Larsen, and B.D. Worth, Air Force Research Laboratory, AFRL/MLLN, Wright-Patterson AFB, OH 45433, U.S.A., Unpublished results, 1997.
- (7) P. Bowen, R.A. Chave, and A.W. James, "Cyclic Crack Growth in Titanium Aluminides," *Materials Science and Engineering*, Vol. 192/193A, pp. 443-456, 1995.
- (8) K.S. Chan and D.S. Shih, "Fatigue and Fracture Behavior of a Fine-Grained Lamellar TiAl Alloy," *Metallurgical and Materials Transactions*, Vol. 28A, No. 1, pp. 79-90, 1997.
- (9) J.P. Campbell, J.J. Kruzic, S. Lillibridge, K.T. Venkateswara Rao, and R.O. Ritchie, "On the Growth of Small Fatigue Cracks in  $\gamma$ -Based Titanium Aluminides," *Scripta Materialia*, Vol. 37, No. 5, pp. 707-712, 1997.

- (10) R. John, D. DeLuca, T. Nicholas, and W.J. Porter, "Near-Threshold Crack Growth Behavior of a Single Crystal Ni-Base Superalloy Subjected to Mixed Mode Loading," Mixed-Mode Crack Behavior, ASTM STP 1359, Editors. K. J. Miller and D. L. McDowell, American Society for Testing and Materials, West Conshohocken, PA, 1999.
- (11) R. John, D. DeLuca, W.J. Porter, and A.H. Rosenberger, "Mixed Mode Crack Growth in a Gamma Titanium Aluminide," Fatigue '99, Engineering Materials Advisory Services, Ltd., West Midlands, UK, 1999.
- (12) M. James and D. Swenson, "FRANC2D/L: A Crack Propagation Simulator for Plane Layered Structures," Kansas State University, Manhattan, KS, U.S.A., Available at Internet address: [www.mne.ksu.edu/~franc2d/](http://www.mne.ksu.edu/~franc2d/), 1997.
- (13) T. Nakano, T. Kawanaka, H.Y. Yasuda, and Y. Umakoshi, "Effect of Lamellar Structure on Fracture Behavior of TiAl Polysynthetically Twinned Crystals," *Materials Science and Engineering*, Vol. 194A, pp. 43-51, 1995.
- (14) S. Yokoshima and M. Yamaguchi, "Fracture Behavior and Toughness of PST Crystals of TiAl," *Acta Materialia*, Vol. 44, No. 3, pp. 873-883, 1996.

# PROCESSING ISSUES IN GAMMA TITANIUM ALUMINIDES

W. J. Porter<sup>1</sup>, K. Li<sup>1</sup>, and A. H. Rosenberger

Air Force Research Laboratory, Materials and Manufacturing Directorate, Metals, Ceramics & NDE Division  
(AFRL/MLLN), Wright-Patterson AFB, OH,

<sup>1</sup>University of Dayton Research Institute, Dayton, OH.

## Abstract

Processing issues regarding two wrought and one cast alloy based on TiAl are discussed. Various analytical techniques were used to investigate the microstructural anomalies. In the wrought alloys, chemical segregation issues were the primary finding. Significant variances in grain size and local inhomogeneities in the microstructures due to insufficient distribution of alloying elements are discussed. The primary issues for the cast material were the formation of a thick columnar microstructure at the investment mold/metal interface and the presence of a large inclusion which had been liberated from the investment shell. Suggestions are given for improving the processing methods.

## Introduction

Gamma titanium aluminides are being considered for utilization as rotating components in gas turbine engines. Their inherent light weight and good high temperature property retention qualifies them as candidates for replacing nickel-base superalloys in certain applications (1,2). Another advantage of this class of materials is that processing, either through wrought or cast approaches, can be accomplished using standard equipment and practices (3).

Significant effort has gone into attempts to eliminate the presence, or reduce the severity, of defects in conventional titanium alloys. Methods for improving alloy quality include triple vacuum arc remelting (VAR) or replacing a VAR step with an intermediate cold hearth melting step using electron beam or plasma arc sources (4,5). Triple melting provides ample opportunity for mixing of the alloying elements to minimize the chance of gross chemical segregation. Electron beam and plasma arc cold hearth melting enable the practical elimination of high density inclusions (HDI) such as broken carbide tool bits mixed in with lathe turnings or other revert material by allowing the HDI to sink to the bottom of the melt and out of the melt flow. The risk of low density inclusions (LDI) such as titanium nitride or alumina particles (in TiAl) surviving a cold hearth melting process is reduced by the increased residency time of the LDI in the molten metal. Simply put, the longer the nitride or alumina particle is suspended in the melt, the more likely it is to dissolve.

This paper will discuss a variety of processing-related issues encountered with three gamma titanium aluminide alloys. A variety of analytical techniques were used to characterize the microstructural abnormalities discovered. It should be noted that the materials used in this investigation were not processed to the extent that they would be if used in real-world application. The findings represented in this paper serve only to remind industry that when gamma titanium aluminide components become bill of material, processing procedures such as those used for conventional titanium alloy rotating components will be necessary.

## Experimental Procedure

### Material

The three alloys investigated in this study were Ti-46Al-2Cr-2.7Nb-0.2W-0.15Si-0.1B-0.2C, Ti-46Al-2Nb-2Cr-1Mo-0.2B, and Ti-47Al-2Mn-2Nb + 0.8 vol% TiB<sub>2</sub> (Table I). All compositions are in atomic percent unless otherwise noted. The alloys will be referred to as KD-CBS, 3-95, and 47XD™, respectively.

The KD-CBS was prepared by plasma arc melting (PAM) a 356 mm diameter ingot, extrusion to a diameter of 203 mm (5.6:1) and isothermally forging 203 mm billet sections at 1100°C to a 32 mm thickness. This material was then heat treated above the alpha transus temperature at 1380°C for 4 minutes (T<sub>α</sub>=1360°C) and subsequently stress-relieved at 900°C for 24 hours.

The 3-95 was also produced by plasma arc melting a 356 mm ingot, followed by 6 to 1 reduction via extrusion, and then isothermally forged. Heat treatment at 1370°C for 5 minutes was followed by air cooling to 900°C, and holding for 24 hours for stress relief.

The 47XD™ was induction skull melted into ingot form and subsequently vacuum arc remelted (VAR) and investment cast into 10x152.5x12.5mm plates using standard foundry practices. The material was then hot isostatically pressed (HIP) at 1185°C/175MPa for 4 hours.

The bulk chemistries for each alloy are shown in Table I. Room temperature tensile properties for the three alloys are shown in Table II.

### Analytical Tools

Various combinations of the following techniques were used in this investigation.

Microstructural characterization was done in a Leica 360 scanning electron microscope (SEM) using a backscattered electron detector (BSED). This technique provides chemical information using differences in 'Z' contrast, which are based on variations in the atomic number of an individual phase or region and morphological information due to electron channeling contrast.

Energy dispersive spectroscopy (EDS) was used to gain qualitative chemical information for specific grains or phases. Element distribution maps or dot maps, which combine SEM images with EDS information, were used to determine the presence (or absence) of specific elements in a specific field of view.

Microprobe analysis was used for quantitative phase chemistry determination where phase identification using SEM/EDS techniques were inconclusive.

Nondestructive evaluation (NDE) techniques, including ultrasonic immersion and x-ray inspection, allowed for determination of gross subsurface density differences due to porosity or chemical segregation.

Table II: Room Temperature Tensile Properties

Alloy	YS (MPa)	UTS (MPa)	El (%)	E (GPa)
KD-CBS	492	538	0.71	170
3-95	475	537	1.08	164
47XD™	358	447	1.44	171

### Results and Discussion

The microstructures for the three alloys are shown in Fig. 1. The KD-CBS is near-fully lamellar with intertwining lamellae at the grain boundaries. The 3-95 is nearly lamellar with some equiaxed gamma grains and B2 phase at the grain boundaries. The 47XD™ is approximately 85% lamellar with 15% gamma at the grain boundaries. The average grain sizes for the alloys are approximately 280, 100 and 150  $\mu\text{m}$ , respectively.

#### KD-CBS

Significant grain size differences and chemical segregation issues were observed in this alloy. Although an average grain size of 280  $\mu\text{m}$  was measured, average measurements from various

Table I: Alloy Compositions (at%)

Element	Al	Cr	Nb	W	Mo	Mn	Si	B	C	O	Ti
KD-CBS	47.1	2.1	3.0	0.3			0.2	0.1	0.23	0.10	46.9
3-95	46.5	2.1	2.0		1.1			0.2			48.1
47XD™	46.8		2.1			1.1	0.1	1.4	0.01	0.17	48.2

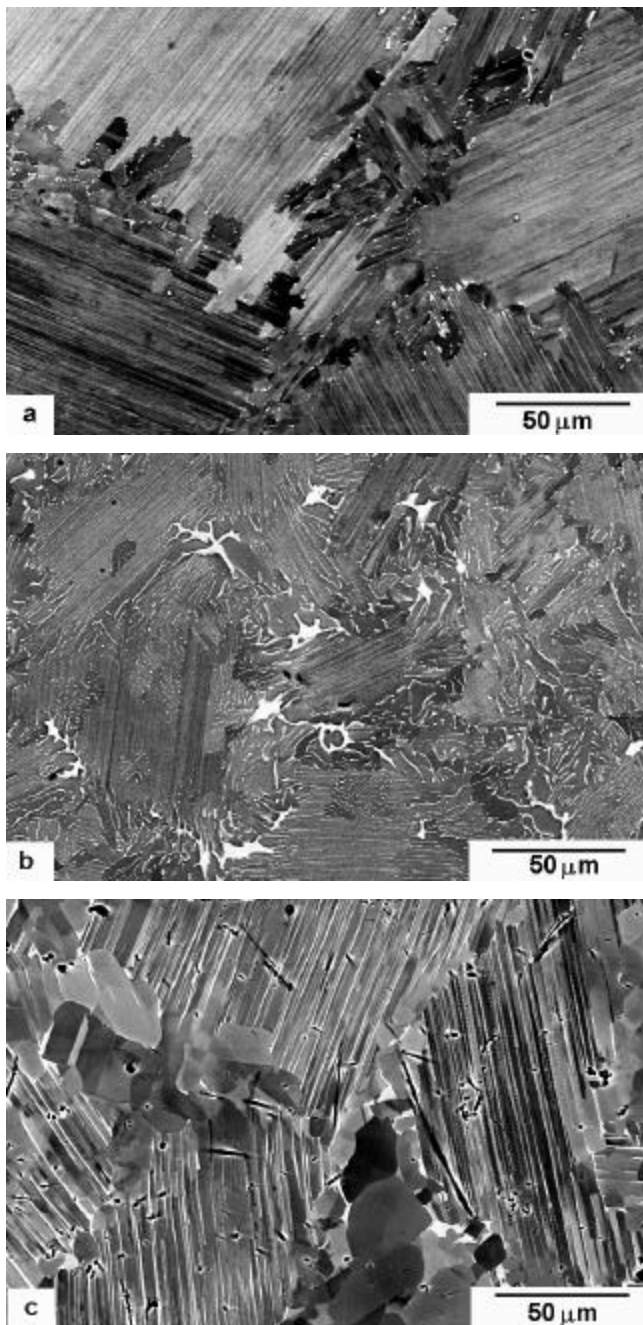


Figure 1: Microstructure of a) Ti-46Al-2Cr-2.7Nb-0.2W-0.15Si-0.1B-0.2C; KD-CBS, b) Ti-46Al-2Nb-2Cr-1Mo-0.2B; 3-95, c) Ti-47Al-2Mn-2Nb + 0.8 vol% TiB<sub>2</sub>; 47XD™.

locations (n=30) ranged from as high as 407  $\mu\text{m}$  to as low as 142  $\mu\text{m}$ . The largest individual grains were over 1 mm in diameter. Insufficient stirring or mixing of the molten metal to achieve widespread and uniform distribution of the alloying elements, in

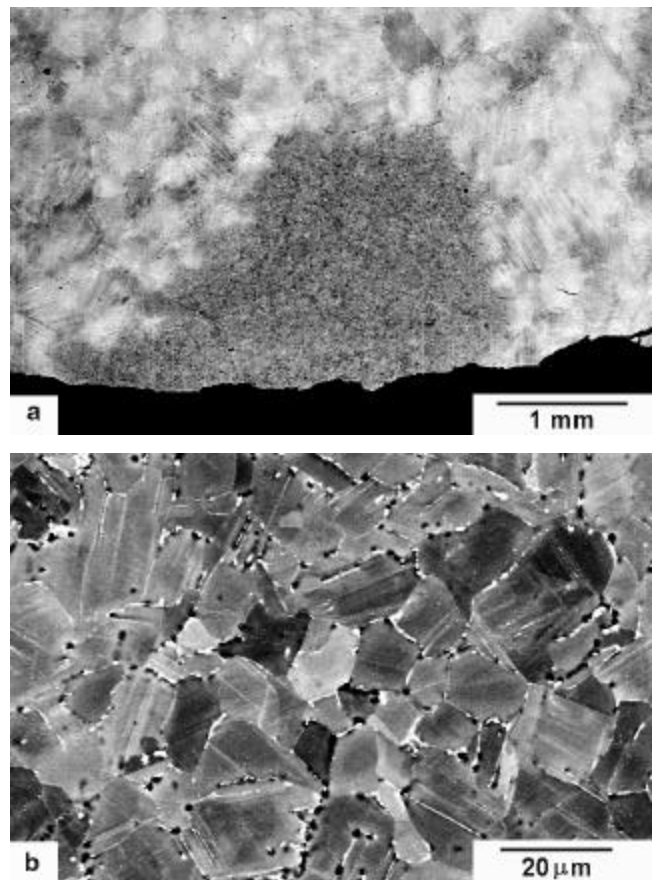


Figure 2: Boron-rich region (dark region) in forged + HT KD-CBS fatigue specimen, a) low magnification, and b) high magnification.

particular boron, probably contributed to the large difference in grain size.

This is especially important in fatigue where large, poorly-oriented grains could be ideal sites for crack initiation.

The microstructure of a fatigue sample taken immediately below the fracture surface, and a higher magnification micrograph from the same region, are shown in Fig. 2.

This region was at least 3 mm in diameter and was found to consist of small gamma grains (dark phase) with a (Si, Nb)-rich, Al-poor grain boundary phase (small bright phase) (Table III). As shown in Table III, the microprobe analysis did not account for all of the elements present in the grain boundary phase. The missing element is probably a light element, in this case boron, whose atomic weight is below the limit of the detector used in this study. A localized, elevated boron content is consistent with the fine grain size of the adjacent gamma-phase grains. Such microstructural anomalies could lead to areas of strain incompatibility where fatigue crack initiation would be more likely to occur.

Figure 3 is a BSED image of a segregated area in the as-forged condition. The bands in this area were up to 15 mm long. The dark lines consist of small

Table III: KD-CBS Microprobe Results of Forged + Heat Treated Material (wt%)

Element	Al	Cr	Nb	W	Si	Ti	Total (%)
duplex/ near- $\gamma$	35.3	2.0	5.7	0.6	0.1	56.4	100.1
gb phase within defect	9.5	2.9	8.1	1.3	13.0	61.2	96.0
lamellar	32.2	2.6	6.8	1.1	0.1	58.0	100.8

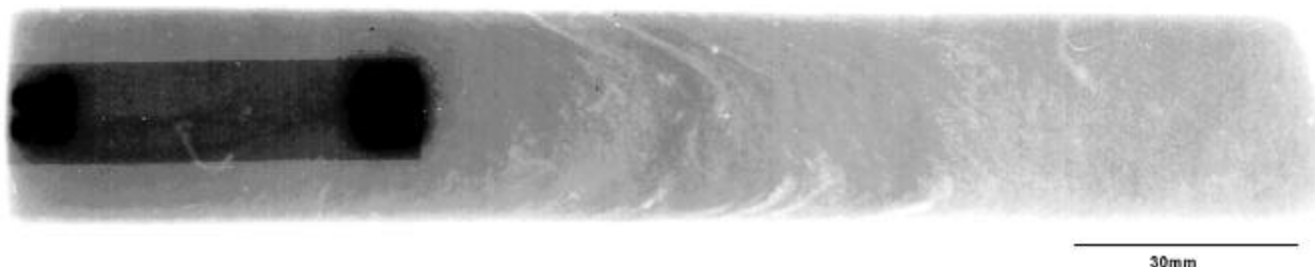


Figure 4: X-ray image highlighting elemental segregation and associated banding in as-forged alloy 3-95. Note: the dark rectangular object on the left side of the x-ray is a lead marker used for determining differences in density.

gamma grains associated with elevated amounts of boron, which were confirmed through auger electron mapping and microprobe analysis (6). Elemental distribution maps also indicated high levels of boron and low levels of aluminum in the dark bands of Fig. 3.

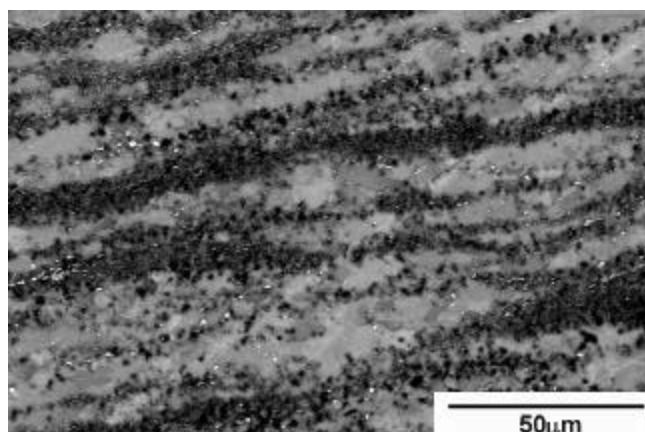


Figure 3: Banding of boron-rich zones (dark bands) in as-forged KD-CBS.

### 3-95

An x-ray image of a through-thickness cross section of a 3-95 forging prior to heat treatment is shown in Fig. 4. The straight edge (left side) represents the center of the forging.

The sample was approximately 6 mm in thickness. As seen in the radiograph, comma-shaped, brighter-contrast flow lines are visible in the middle third of the forging. The segregation represented by the flow lines is likely a remnant of the structure in the original ingot and may have remained through the extrusion and primary forging process. This is similar to the segregation seen in the KD-CBS alloy.

In addition to the difficulties associated with segregation, the 3-95 alloy also contained stringers of alumina particles and sporadic porosity, as shown in Figure 5a and b, respectively. The alumina particles (Fig. 5a) were exposed by electropolishing.

The porosity shown in Figure 5b was the initiation failure site of a fatigue test run at 540°C. That the pore did not heal or close during the forming steps is symptomatic of either unacceptably large porosity during ingot casting or insufficient work introduced during forming.

### 47XD™

Being the only cast material in this study, the issues with this alloy are different in nature from those of the wrought alloys. Figure 6a shows a cross-section from a typical 47XD™ casting. From the investment mold/metal interface to approximately 2 mm into the casting, columns of nearly-lamellar, similarly-oriented grains dominate the microstructure. This region transitions into the microstructure seen in Fig. 1c. Figure 6b displays a higher magnification view of the columnar region. Significantly different behavior can be expected for the columnar region versus the 85% lamellar, 15% equiaxed gamma duplex structure seen in the casting interior (7). The columnar microstructure is likely due to the slow cooling rate of the 150x100x12mm slab castings. Castings with thinner wall thicknesses have not shown this extent of columnar microstructure formation (8). Removal of the surface columnar material would require significant machining and associated expense.



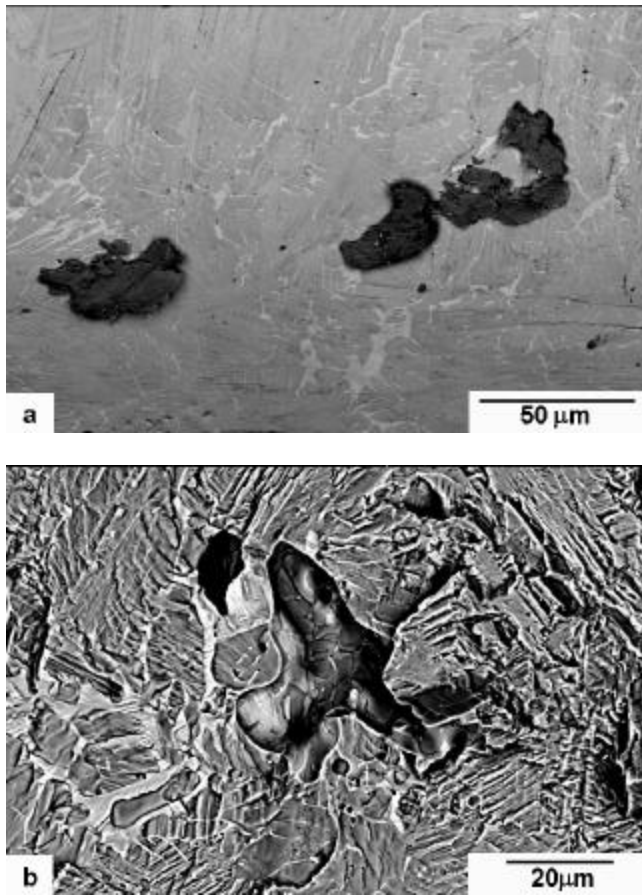


Figure 5: Photomicrographs of a) alumina particles in forged + HT 3-95 and b) residual casting porosity on fracture surface of 3-95 fatigue specimen.

A large (approximately 600 μm in diameter) inclusion was found on the fracture surface of a 540°C tensile specimen. Table IV presents a comparison of 540°C tensile results between the sample with the inclusion and two 'clean' samples. A significant drop in strength and ductility was observed in the sample with the defect. The inclusion was large enough to be seen in radiographs taken of the sample before testing.

Elemental distribution, or dot maps, and a secondary electron image of the inclusion are shown in Fig. 7. As mentioned, dot maps combine SEM images with EDS information and are used to determine the presence (or absence) of specific elements in a particular field of view. Three distinct regions appear on these maps: the bulk metal surrounding the inclusion, the inclusion, and the lower edge (in the photo) of the inclusion. The bulk metal is shown to contain the expected elements of Ti, Al, and Nb; the inclusion is shown to include Al and O; the lower

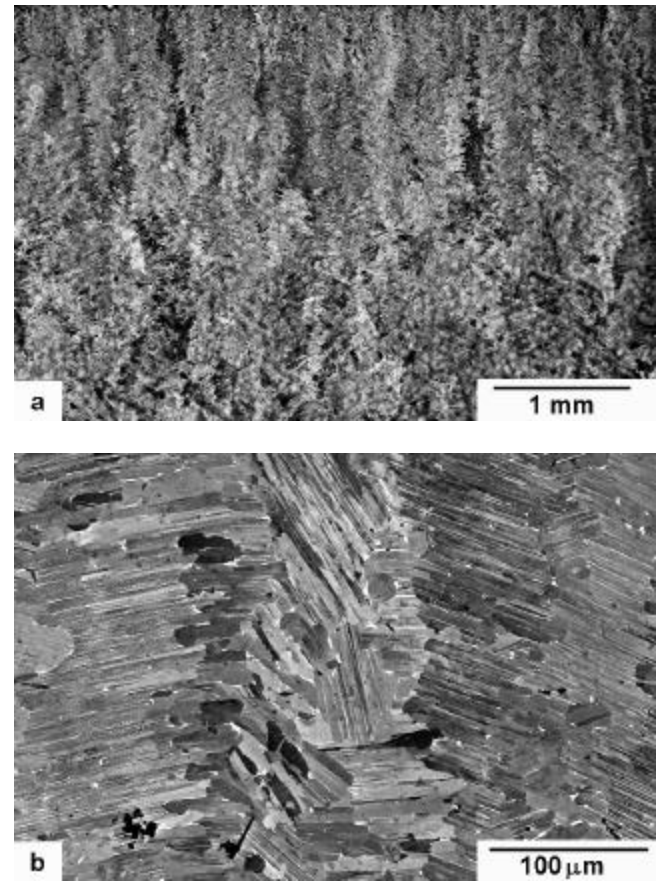


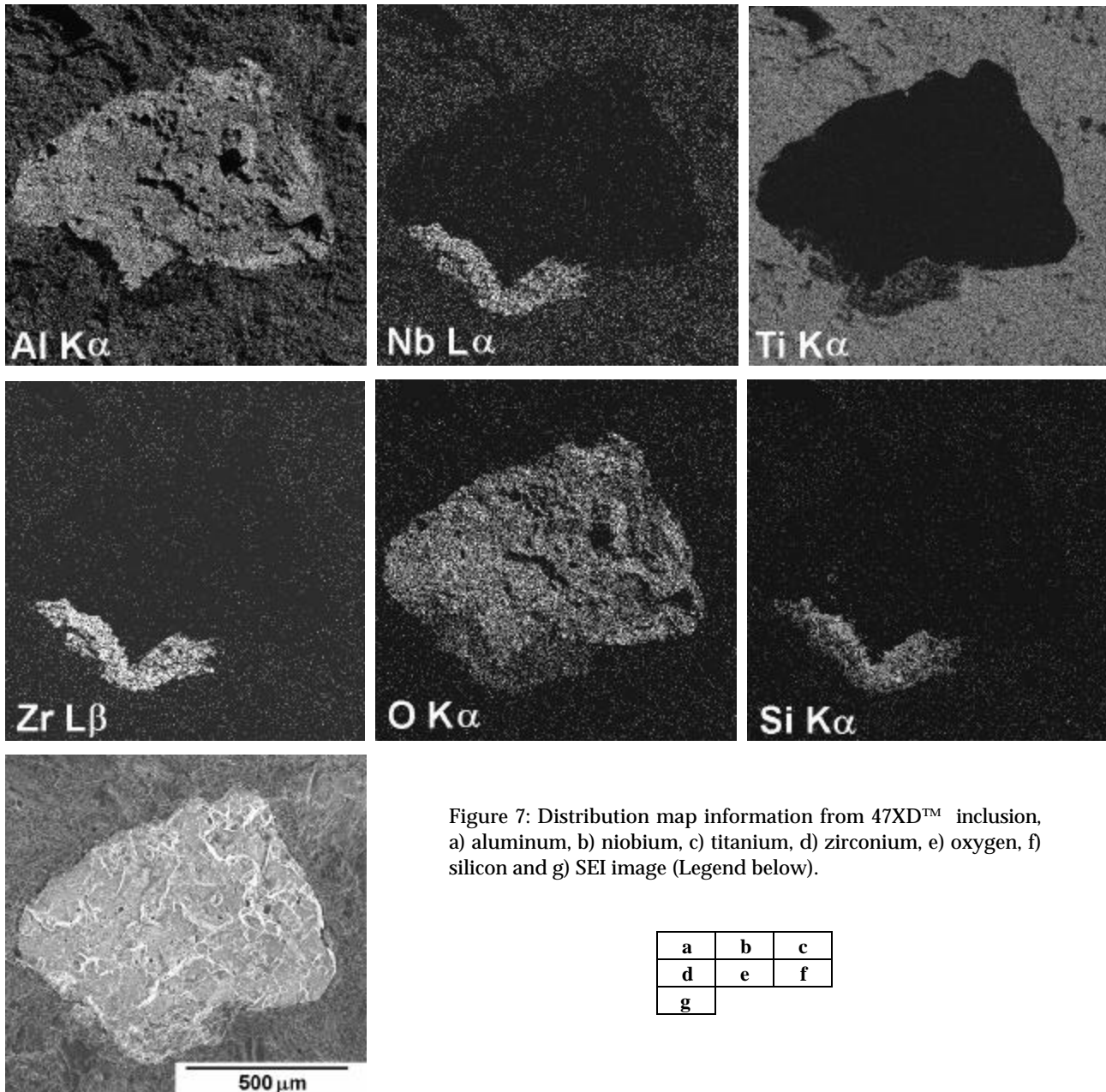
Figure 6: Columnar microstructure of 47XD™, a) low magnification, b) high magnification.

Table IV: Comparison of 47XD™ 540°C Tensile Results

Sample	YS (MPa)	UTS (MPa)	El (%)
99-016*	315	347	0.56
99-008	341	530	3.40
99-010	334	534	3.63

\*Sample with large inclusion

edge of the inclusion consists of Zr, Si, O, and Nb. The inclusion appears to be a piece of the investment shell that broke loose during introduction of the molten metal into the mold. The (Zr, Nb, Si)-rich portion is most likely from the non-reactive facecoat of the mold that comes into direct contact with the molten metal, while the (Al, O)-rich portion is from the material giving structural integrity to the mold.



### Conclusions

1. A variety of melt-related defects were identified in wrought and cast materials.
2. The primary concerns with the wrought alloys were related to elemental segregation and subsequent inhomogeneous microstructures. Issues related to the presence of alumina particles and porosity were also observed in these materials.
3. The cast material revealed a columnar microstructure emanating from the mold/metal interface. The columnar structure transitioned into a duplex microstructure approximately 2 mm into the sample. A large inclusion, most likely a liberated piece of the investment shell, was also discovered.
4. As in conventional titanium alloys, triple melting practices would significantly improve elemental distribution and decrease the occurrence of macrosegregation and impurity contents seen in the wrought alloys. Improved microstructural homogeneity and mechanical behavior should result. The cast material might be improved by increasing the cooling rate of thick-section castings to retard formation of the columnar microstructure. Inclusion-related issues can be addressed through improved shell manufacturing and NDE techniques.

### Acknowledgments

This work was performed at the Air Force Research Laboratory, Materials and Manufacturing Directorate, Wright-Patterson Air Force Base, OH. The UDRI effort was funded under Air Force Contract F33615-98-C-5214. We would like to acknowledge Luann Piazza (UES) for her assistance with the elemental distribution maps. Joe Henry (UES) and Ed Porter (UTC) are acknowledged for their help with the microprobe analysis and x-ray work, respectively.

### References

1. Y-W. Kim, "Intermetallic Alloys Based on Gamma Titanium Aluminide," JOM, 41 (7) (1989), 24-30.
2. Y-W. Kim and D.M. Dimiduk, "Progress in the Understanding of Intermetallic Gamma Titanium Aluminides," JOM, 43 (8) (1991), 40-47.
3. P.L. Martin and C.G Rhodes, "Microstructure and Properties of Refractory Metal Modified Ti-48at%Al-2at%Nb-2at%Cr", in Titanium '92, F.H. Froes and I.L. Caplan, eds., ( Warrendale, PA, TMS, 1993) , 399-406.
4. J.L. Henry, S.D. Hill, W.E. Anable and J.L. Schaller, "Source and Control of Nitride Inclusions in Titanium," Report of Investigations 7933, U.S. Bureau of Mines, (Washington, D.C., 1974).
5. A. Mitchell, "Melting, Casting, and Forging Problems in Titanium Alloys," JOM, 49 (6) (1997), 40-42.
6. K. Li, W.J. Porter, A.H. Rosenberger, and J.M. Larsen, "Defects in Wrought Gamma Titanium Aluminides," to be published in Fatigue '99 (Oxford, U.K., Elsevier Science Ltd., 1999).
7. J.M. Larsen, B.D. Worth, S.J. Balsone, A.H. Rosenberger and J.W. Jones, "Mechanisms and Mechanics of Fatigue Crack Initiation and Growth in TiAl Intermetallic Alloys," Fatigue '96, Vol. III, G. Lütjering and H. Nowack, eds., (Oxford, U.K., Elsevier Science Ltd., 1996), 1719-1730.
8. Chris M. Jensen, private communication, 18 March 1999.

This page intentionally left blank.

## **Defects in Wrought Gamma Titanium Aluminides**

K. Li\*, W. J. Porter<sup>†</sup>, A. H. Rosenberger<sup>†</sup> and J. M. Larsen<sup>†</sup>

Various defects were observed in several wrought gamma titanium aluminide alloys. Most of the defects are believed to originate from melting and casting processes and have survived through the subsequent forging and homogenizing heat treatment processes. The defects in these materials include serious compositional segregation, porosity and oxides. While the presence of defects is an obvious concern, fatigue initiation is not always associated with defects of this type and primarily occurs in colonies with lamellae oriented normal to the loading direction. The nature of the defects observed, their effects on fatigue, and the relationship between the anisotropic behavior of the lamellar microstructure and fatigue initiation are discussed.

### **INTRODUCTION**

Gamma titanium aluminides (TiAl) are the most promising intermetallic alloys for potential application in aircraft gas turbine engines. However, their relatively poor low-temperature ductility, fracture toughness, and impact resistance have been areas of significant concern (1). Considering the need to ensure reliability in service and to satisfy specific structural requirements, the damage tolerance of gamma TiAl must be demonstrated with respect to intrinsic or service-generated defects, as well as their inherent microstructure. The overall objectives of the present research were to: 1) detect and determine the nature of intrinsic defects in wrought gamma TiAl and 2) develop an understanding of the effects of defects and lamellar microstructure on fatigue initiation behavior. The defects referred to in this study vary from compositional segregation to porosity and the presence of oxide inclusions.

### **EXPERIMENTAL PROCEDURE AND RESULTS**

Two wrought gamma TiAl alloys were employed in the present study (compositions in at.%): Ti-46Al-2Nb-2Cr-1Mo-0.2B (3-95), and Ti-46Al-2Cr-2.7Nb-0.1B-0.2W-0.15Si-0.2C (KD-CBS). Both were plasma arc melted, extruded, hot isostatically pressed and isothermally forged to pancakes. The pancakes were then heat treated to obtain nearly-fully lamellar microstructures. All fatigue testing was done using smooth bar samples at 21°C and a stress ratio, R, of 0.1 at a frequency of 50Hz.

#### **Elemental Segregation**

Most as-forged gamma TiAl alloys exhibit banded microstructures (2). Attempts at eliminating this segregation due to interdendritic gamma have proven difficult, even when aging at temperatures above the alpha transus ( $T_\alpha$ ), which can result in severe grain growth - even for short time excursions. To detect the presence of segregation-related defects, x-ray techniques were used to inspect 6mm thick cross sections taken from each forging (perpendicular to the forging direction). X-rays revealed the presence of flow lines due to segregation, which appear as alternating light and dark bands. The low contrast flow lines correspond to cast interdendritic regions, and the arching of the bands is indicative of the plastic deformation resulting during the forging process. Noticeable macrosegregation was detected by x-ray radiography in KD-CBS and 3-95. Figure 1 is an x-ray taken of 3-95 clearly showing flow lines related to the macrosegregation. X-rays revealed significant banding, indicating segregation, close to the mid-thickness running parallel to the forging surfaces. Ultrasonic C-scans of the same material were consistent with the x-ray information.

Similar defects, seen in the KD-CBS material, were approximately 15 mm long and 0.5 mm wide. Backscattered scanning electron (BSE) microscopy under low magnification revealed a low "Z" contrast, confirming the x-ray radiography observation. However, at relatively high magnification, a BSE image revealed a banded microstructure with profound bright and dark contrast, Fig. 2a,b. Energy dispersive x-ray spectrum (EDS) analysis of the dark bands showed these regions to be rich in boron. This conclusion was further confirmed by boron mapping using an auger electron microscope.

---

\* University of Dayton Research Institute, 300 College Park, Dayton, OH, 45469, U.S.A.

† Air Force Research Laboratory, Materials and Manufacturing Directorate, AFRL/MLLN, Wright-Patterson Air Force Base, OH, 45433, U.S.A.

To further verify the identification of different particles, a microprobe (wavelength dispersive x-ray spectroscopy) was utilized. The results in Table 1 are averages of at least three particles of each phase or contrast. The total weight percent of particles in the dark bands of the segregation region are significantly less than 100%, indicating some light element (in this case boron) was not measured. It is apparent that boride particles are aluminum lean compared to  $\alpha_2$  and  $\gamma$ . Cr and W partition into the  $\alpha_2$  phase rather than  $\gamma$  phase, while Nb seems to be equally partitioned to each phase.

TABLE 1 - Microprobe results of segregation region of KD-CBS (wt. %)

Phase ID	Al	Si	Ti	Cr	Nb	W	Total (%)
$\gamma$	32.6	0.0	58.0	2.3	6.4	0.9	100.2
$\alpha_2$	21.5	0.2	58.9	8.3	6.3	4.6	99.8
B-rich region (dark band)	10.1	0.1	60	1.6	5.8	0.9	78.5

### Porosity

Porosity was occasionally observed on fracture surfaces of fatigued 3-95 specimens. The initiation site of a fatigued specimen subjected to thermal exposure at 760°C for 500 hrs in air and tested at 540°C was identified using stereo-optical microscopy. The initiation region was found to be subsurface and had a circular shape, which was bright gray in color when viewed optically. Clearly, a crack initiated and grew slowly for a certain number of cycles prior to final fast fracture. As a result, the initiated crack surface was subjected to prolonged oxidation at 540°C. A relatively high magnification BSE image revealed porosity, which served as a fatigue initiation site, Fig. 3. The pore is approximately 60  $\mu\text{m}$  in diameter and is surrounded by a few small satellite pores. It is interesting to note that the porosity is actually located in a 'hard mode'-oriented lamellar colony. Pores about 20  $\mu\text{m}$  in diameter were also observed on the fracture surface of room temperature fatigued specimens. Even though ingots are routinely hot isostatically pressed (HIP'ed) to heal any porosity associated with the casting process, porosity has still been reported in cast  $\gamma\text{TiAl}$  (3).

### Alumina

Irregularly shaped particles were frequently observed on the polished specimens of the 3-95 material. The individual particles ranged in size from 20 to 30  $\mu\text{m}$ . However, particles distributed in chains were also occasionally observed, Fig. 4. EDS results confirmed that the particles are alumina, which apparently originated from the melting process. For conventional titanium alloys, a major quality concern for rotating components in aircraft engines is melt-related defects. These include hard  $\alpha$  and high-density inclusions (HDI). Hard  $\alpha$  inclusions are interstitially stabilized, while HDI are refractory-metal (such as Mo, Ta or W), beta-stabilized inclusions having higher densities and melting points than titanium alloys. Hard  $\alpha$  inclusions have proven to be a more significant production problem to eliminate than HDI (4).

### Fatigue Behavior

A comparison of the fatigue performance is shown in Figure 5 for the 3-95, and KD-CBS alloys from the current study and results (5) for the K5 alloy, (Ti-46.5Al-2Cr-3Nb-0.2W at %) having two different lamellar microstructures. The 3-95, KD-CBS, and K5-RFL (Refined Fully Lamellar) had average colony sizes of 100, 280, and 300 $\mu\text{m}$ , respectively, while the K5-FL (Fully Lamellar) had a colony size of 700 $\mu\text{m}$ . As seen in Figure 5, the finer-grained materials performed in a similar fashion in fatigue, while the coarse-grained K5-FL exhibited much poorer fatigue performance. These results are not surprising in that the fatigue limits of gamma alloys trend towards the yield strength, and the finer grained materials had substantially higher yield strengths than the K5-FL (3-95: 442MPa, K5-RFL: 479MPa, and KD-CBS: 480MPa vs K5-FL: 375MPa). The failures of all these specimens were not associated with defects, except for two of the KD-CBS samples tested at the 440 MPa stress level (near run-out). These two KD-CBS samples initiated at areas with very large (1-2mm) microstructural inhomogeneities associated with insufficient boron distribution during ingot production, similar to the defect in Fig. 2. The remaining initiation sites, including the 3-95 specimen that failed in 23 cycles at a maximum stress of 440 MPa, were associated with 'hard' orientation grains (6) having normals within approximately 20° to the loading direction. The short-lived 3-95 specimen had a near surface cluster of 4 colonies having similar hard orientations –

leading to the remarkably low life. Overall, these results highlight the very anisotropic nature of the lamellar grains (6). Even though most, if not all, of these fatigue samples had defects similar to those reported in this paper, it was the unfavorable orientation of the lamellar colonies that was the overriding 'weak-link' leading to fatigue initiation. The interesting point is that the relatively high degree of scatter, up to two orders of magnitude in fatigue life, observed in the 3-95 and KD-CBS alloys cannot be attributed to material defects, but is a consequence of the intrinsic fatigue behavior of lamellar gamma alloys.

The approximate variation in lamellar colony size is shown, Figure 6, on a modified Kitagawa-Takahashi diagram (7) constructed for the two materials (having similar endurance limits). More details of this diagram can be found in Ref. (8). Overall, the 3-95 material has tighter microstructural control than the KD-CBS alloy, which exhibits colony sizes occasionally as large as 1 mm. It would be expected, based on this diagram, that the KD-CBS alloy would be substantially poorer in fatigue resistance than the 3-95 alloy. The distribution of colony sizes is wider and clearly extends into the crack propagation region - even with the higher crack growth threshold. Also, the large regions of microstructural segregation were found in this alloy which could clearly impact the fatigue resistance. The two specimens that failed at this type of inhomogeneity, however, failed within one order of magnitude of a specimen that initiated a crack in the "normal" lamellar microstructure. Other KD-CBS specimens that failed from a hard oriented lamellar colony had regions of macrosegregation - indicating that this defect is not *always* critical.

The greater fatigue scatter in the 3-95 alloy, Fig. 5, can be partially explained by considering the behavior of groups of hard oriented colonies. Figure 6 shows the minimum fracture toughness,  $K_{IC}$ , for hard-mode polysynthetically twinned (PST) material from Ref. (6). A 40  $\mu\text{m}$  flaw, or possibly smaller, could lead to failure of the entire colony - especially when considering the *fatigue* threshold for hard-orientation colonies. It is possible, for both materials, that this pop-in crack could be above the crack growth threshold and lead to rapid failure under the steep crack growth rate curve typical of these gamma alloys. In the very short-life 3-95 specimen, the pop-in size was several times the average colony size and was additionally located in the near surface region, which has been found to be a very damaging location in nodular cast iron (9). It appears, however, that scatter in 3-95 is not solely attributable to this type of pop-in event and indicates that there are intrinsic differences in the two materials.

## SUMMARY AND CONCLUSIONS

The defects in this study are believed to have originated from the melting and casting process and survived through subsequent forging or homogenizing heat treatments. Extensive SEM fractographic examinations were conducted on fatigued specimens tested under a variety of conditions. Fatigue initiation sites were observed to be associated with porosity and severe elemental segregation regions. However, in most instances, the defects observed did not lead to initiation; rather fatigue failure originated from "hard" mode-oriented lamellar colonies. Thus, the fatigue behavior will be significantly affected by lamellar colony size, orientation and lamellar spacing, defect nature, size, shape and distribution.

## ACKNOWLEDGEMENTS

This work was performed at the Air Force Research Laboratory, Materials and Manufacturing Directorate. The UDRI effort was funded under Air Force Contract F33615-94-C-5200. We acknowledge the assistance of Ed Porter (UTC) for the x-ray radiograph work and Dave Stubbs (UDRI) on ultrasonic inspection of the materials. The help of Jim Solomon (UDRI) and Joe Henry (UES) with the auger and microprobe, respectively, is also acknowledged.

## REFERENCES

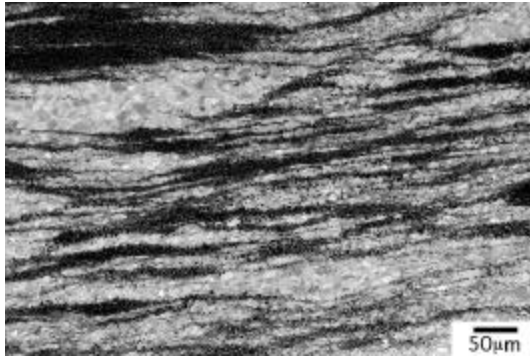
- (1) Kim, Y.W. and Dimiduk, D.M., JOM, Vol. 43, 1991, pp. 40-47.
- (2) Martin, P.L., Rhodes, C.G. and McQuay, P.A., in *Structural Intermetallics*, Darolia et al., Eds., TMS, Warrendale, PA, 1993, pp. 177-186.
- (3) Larsen, D.E. and Govern, C., in *Gamma Titanium Aluminides*, Y.-W. Kim, et al., Eds., TMS, Warrendale, PA, 1995, pp. 405-414.
- (4) Buttrill, W.H., Shamblen, C.E., and Hunter, G.B., in *Proceedings of the Third Japan International SAMPE Symposium*, Kishi, et al., Eds., SAMPE, Japan, 1993.
- (5) Worth, B.D., Larsen, J.M., and Rosenberger, A.H., in *Structural Intermetallics 1997*, M.V. Nathal, et al., Eds., TMS, Warrendale, PA, 1997, pp. 563-569.
- (6) Yokoshima, S. and Yamaguchi, M., *Acta Metall. Mater.*, Vol. 44, No. 3, 1996, pp. 873-883.
- (7) Kitagawa, H., and Takahashi, S., in *Proceedings of the Second International Conference on Mechanical Behavior of Materials*, Boston, MA 1976, pp. 627-631.

- (8) Larsen, J.M., Worth, B.D., Balsone, S.J., Rosenberger, A.H. and Jones, J.W., in *Fatigue '96*, Vol. III, G. Lütjering and H. Nowack, Eds., Elsevier Science Ltd., Oxford, U.K., 1996, pp. 1719-1730.
- (9) Clement, P., Angeli, J.P., and Pineau, A., *Fat. Engng. Mater. Struct.* Vol. 7, No.4., 1984, pp. 251-265.

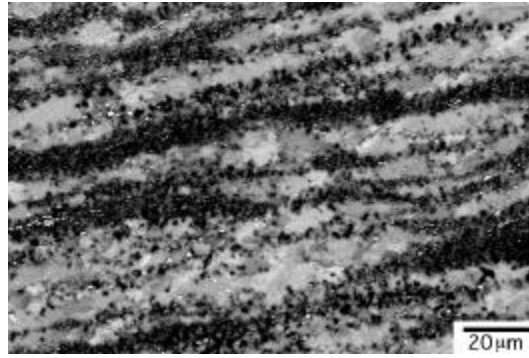




Figure 1- X-ray radiograph of a cross-section of forged 3-95 showing macrosegregation-related banding (dark rectangular area is used to characterize X-ray sensitivity).



(a)



(b)

Figure 2 SEM backscattered image of KD-CBS, (a) at low magnification, and (b) a banding microstructure with small precipitates.

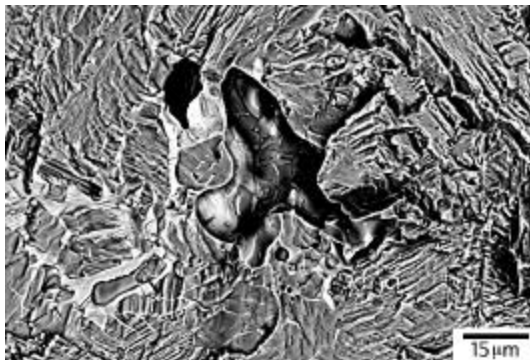


Figure 3 Porosity-related fatigue initiation site in 3-95 of a test run at 540°C.



Figure 4 BSE image of typical alumina particles.

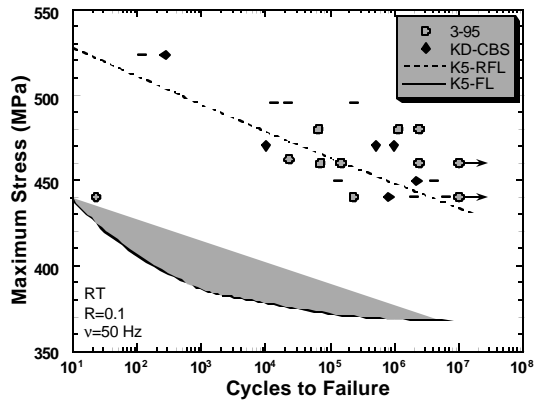


Figure 5 S-N comparison of various the gamma alloys.

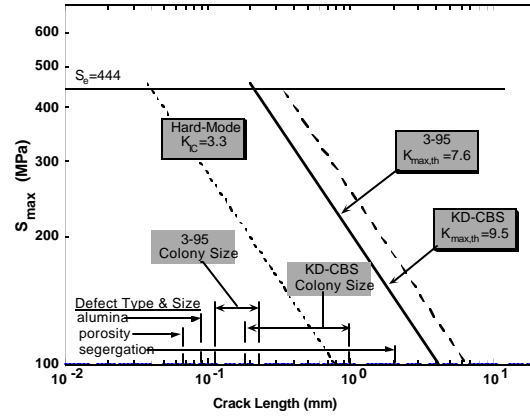


Figure 7 Kitagawa diagram showing the relationship of defect size and microstructural scale to the fatigue and crack growth resistance.

# HIGH-CYCLE-FATIGUE BEHAVIOR AND LIFE ESTIMATES OF A GAMMA TITANIUM ALUMINIDE

E. J. Dolley, jr.<sup>1</sup>, N. E. Ashbaugh<sup>2</sup>, and B. D. Worth<sup>2</sup>

Materials and Manufacturing Directorate, Air Force Research Laboratory (AFRL/MLLN)  
Wright-Patterson AFB, OH 45433-7817

## *Abstract*

The isothermal high-cycle fatigue behavior of the Ti-46.5Al-3Nb-2Cr-0.2W (at%) gamma titanium aluminide alloy is strongly influenced by temperature and microstructure. The high-cycle fatigue behavior beyond  $10^8$  cycles is characterized by performing high-frequency, high-cycle-fatigue testing at 23, 600, and 800°C on nearly-lamellar and duplex microstructures at a test frequency of 350 Hz and a stress ratio of 0.1.

The duplex microstructure when compared to the nearly-lamellar microstructure has slightly better fatigue strength at 23°C and considerable higher fatigue strength at 600°C for lives up to  $10^8$  cycles. The fatigue strengths of the duplex and nearly-lamellar microstructures are about the same at 800°C for lives up to  $10^8$ .

Crack initiation sites are identified at 23, 600, and 800°C along with the damage mechanisms associated with these initiation sites for the duplex and nearly-lamellar microstructures. Initial and final crack sizes are determined and used to estimate fatigue crack growth life. Defects, such as porosity that were found in this forged alloy, shorten the fatigue life of the duplex microstructure considerably.

A comparison of the predicted fatigue crack growth life to the experimental fatigue life suggests that the majority of nearly-lamellar fatigue life at 600 and 800°C consists of crack propagation at high stresses and crack initiation at low stresses. The majority of duplex fatigue life at 800°C consists of crack propagation at high and low stresses.

**Keywords:** Gamma titanium aluminide; Duplex and nearly-lamellar microstructures; High cycle fatigue; Fatigue life.

## *1. Introduction*

Gamma titanium aluminides [1-6] have been considered for gas turbine engine and automotive applications due to their oxidation resistance and attractive density corrected properties. Since these materials may be used in fracture critical components, a need to obtain a basic understanding of their high-cycle-fatigue behavior exists. One alloy that has shown promising properties is Ti-47Al-3Nb-2Cr-0.2W (at%) gamma titanium aluminide [1]. Fatigue crack growth rates for this alloy were very rapid at 23, 600, and 800°C for the fully-lamellar and duplex microstructures [7]. Since the fatigue crack growth rates were rapid, the amount of time needed to propagate to a critical crack size may be a short part of the material's fatigue life. A fatigue limit methodology should be used in conjunction with a damage tolerance methodology to predict fatigue lives at a given temperature and stress level. Complete characterization of the initiation site is essential since the majority of the life of a component is spent in crack initiation. Potential component applications for TiAl base alloys require that a complete understanding of the high frequency high-cycle fatigue behavior be gained to assist in the design process.

Previous high-cycle fatigue data for this alloy at  $10^7$  cycles were obtained at low frequencies of 25 Hz and 40 Hz and with a stress ratio ( $R=\sigma_{\min}/\sigma_{\max}$ ) of 0.1. One study was conducted at 23°C and a test frequency of 40 Hz for fully-lamellar and duplex microstructures [6]. Another study was conducted at 600 and 800°C and a test frequency of 25 Hz for refined-fully-lamellar and duplex microstructures [8]. Fatigue strength at  $10^7$  cycles was not less than 75 % of the ultimate tensile

strength at the test temperature. Other gamma titanium aluminide alloys [4,9,10] have shown similar fatigue strength results at  $10^7$  cycles.

The objective of this study was to develop a basic understanding of the effects of temperature and microstructure on the isothermal high-cycle-fatigue behavior of the Ti-47Al-3Nb-2Cr-0.2W (at%) gamma titanium aluminide alloy. Fatigue lives up to  $10^9$  cycles were characterized at 23, 600, and 800°C and at 350 Hz for the nearly-lamellar and duplex microstructures. Damage mechanisms at crack initiation sites were investigated and evaluated with the use of optical and scanning electron microscopy, for each microstructure and temperature. Initial and final flaw sizes were determined to evaluate stress intensity factors at initiation and fracture and to investigate the relationship of crack propagation life to the overall fatigue life.

## *2. Experimental Considerations*

### Material Processing and Characterization

Test specimens were obtained from two forgings, identified as forgings 1 and 2, of material with a nominal composition of Ti-46.5Al-3Nb-2Cr-0.2W (at%). A skull melting/casting technique was used to produce the initial ingots of material. The ingots were then hot isostatic pressed (HIP'ed) and isothermally forged in two steps with an intermediate annealing process between the two forging steps. The ingots were subjected to a 91% height reduction to produce forged pancakes of approximately 24 cm diameter and 1.22 cm. thick.

Typical nearly-lamellar and duplex microstructures are shown in Fig. 1. As a result of a 0.4 at% difference in aluminum composition between the two forgings [11], a different heat treatment for each forging was required to produce similar microstructures. The nearly-lamellar microstructure had a lamellar colony size of approximately 120  $\mu\text{m}$  with equiaxed gamma grains of approximately 15  $\mu\text{m}$ . The duplex microstructure had an equiaxed gamma grain size of approximately 20  $\mu\text{m}$ . Approximately 10% of the duplex microstructure consisted of equiaxed  $\alpha_2$  and lamellar grains. Grain size calculations were determined using ASTM Standard 112-88.

Local regions of inhomogeneity that were shaped like platelets were observed in the duplex microstructure material. The platelets were approximately 100  $\mu\text{m}$  thick with a range of diameters from 500  $\mu\text{m}$  to 600  $\mu\text{m}$ . The thickness direction of the platelets was parallel to the forging direction of the pancake. An outline of an approximate quarter-section of a platelet with thickness exposed between the specimen surface and the fracture surface is shown in Fig. 2a. These platelets were composed of approximately 50  $\mu\text{m}$  equiaxed gamma grains that formed during material processing. Energy dispersive spectroscopy (EDS) was used to determine the composition of the platelets and the base microstructure. The EDS results showed that the platelets were rich in aluminum. Due to the increased aluminum content in the platelets, the alpha phase was not present during the solution treatment to inhibit the growth of the gamma grains. Unfortunately, these gamma platelets existed in all of the duplex specimens.

Porosity was also discovered in the duplex microstructure test specimens. Since the porosity was elongated normal to the forging direction, it was most likely present prior to the forging process. The porosity may be a result of an insufficient HIP cycle that was performed after the ingot was cast. No relative change in the alloy composition was noted from the pores to the baseline microstructure using EDS.

### Test Specimen Preparation and Experimental Setup

The test specimen geometry was a flat dogbone with a uniform gage length of 20Lx6.0Wx1.8T mm. The test specimens were machined by electric discharge machining (EDM), followed by low stress grinding, from the forged pancake with the width (W) direction parallel to the forging direction. The test specimen gage section was then electropolished to remove 100  $\mu\text{m}$  of material to eliminate compressive residual stress on the surface of the test specimen. Residual surface stress measurements on a Ti-6Al-2Sn-4Zr-6Mo (at%) specimen [12] showed that the residual surface

stresses were negligible when 25  $\mu\text{m}$  of material was removed by electropolishing after EDM and mechanical polish.

The high-frequency, high-cycle-fatigue tests were performed on a fully automated test system [13]. An axial cyclic load was applied to the specimen using an electromagnetic shaker having an operational range from 100 Hz to 1000 Hz. The mean load on the specimen was generated pneumatically. From the results of modal analysis and frequency response of the specimen mounted in the test system, a frequency of 350 Hz was selected. At this frequency, specimen bending was less than 1% and no unwanted mode shapes were present. The signals from strain gages on opposite sides of the specimen were in phase, and differences in magnitude of these signals were less than a 0.8%.

The elevated specimen temperatures were generated using a three-zone quartz lamp configuration with a feedback control. Thermocouples were attached to the test specimen using a wire wrap technique [11].

### **3. Results and Discussion**

Fatigue lives as a function of microstructure at 23, 600, and 800°C are shown in Figs. 3, 4, and 5, respectfully. The ultimate strengths of these materials are plotted at 0.5 cycle fatigue life in Fig. 3-5. The duplex microstructure exhibited superior fatigue lives at 23 and 600°C compared to the lives for the nearly-lamellar microstructure. At 800°C, the duplex and nearly-lamellar microstructures exhibited similar fatigue lives. The characterization of fatigue lives beyond  $10^7$  cycles indicated that an endurance limit for these microstructures was not present. The fact that an endurance limit does not exist up to  $10^9$  cycles shows that caution must be used when an attempt is made to extrapolate data beyond a known fatigue strength at a certain life.

Damage mechanisms at initiation sites have been determined for the nearly-lamellar and duplex microstructures at 600 and 800°C. The crack initiation sites for the elevated temperature tests were identified by heat tinting that occurred on the fracture surface during a test and by the identification of transgranular failure in the surrounding gamma grains. Gamma grains fail in a transgranular mode in the low to medium  $\Delta K$  ranges at elevated temperatures [14]. In the high  $\Delta K$  and overload regions, the gamma grains fail in an intergranular mode.

For the nearly-lamellar microstructure, interlamellar and translamellar damage mechanisms were observed at crack initiation sites on the fracture surfaces for the elevated temperature tests. Interlamellar fracture was observed at every crack initiation site that led to the dominant crack. In the case of the translamellar initiation sites, the crack did not propagate beyond the grain in which the crack had initiated. The translamellar initiation sites occurred in specimens that also had an interlamellar initiation site. All of the initiation sites in the nearly-lamellar microstructure were located at the surface of the test specimen. For the room temperature tests, the initiation sites in the nearly-lamellar microstructure could not be identified.

For the duplex microstructure, the critical flaws initiated either at porosity or at a large gamma grain in a gamma platelet. The presence of porosity in a specimen generally preempted the failure associated with large gamma grains in platelets. Porosity lowered the fatigue lives by as much as 6 orders of magnitude compared to lives of specimens that did not contain porosity [11]. For a large gamma grain, the fracture initiation was transgranular failure and then transitioned to intergranular failure as the crack advanced. The failure lives shown in Fig. 3-5 for the duplex microstructure are associated with initiation at large gamma grains in a platelet.

Fatigue life was predicted using initial and final flaw sizes,  $a_i$  and  $a_f$ , that were determined using scanning electron microscopy. The predicted lives were then compared to the experimental lives. Initial and final crack sizes were determined for the duplex microstructure at 800°C and for the nearly-lamellar microstructure at 600 and 800°C. The flaw was assumed to be semicircular at initiation and throughout crack propagation. A power law relationship was assumed for the crack growth rates as

$$\frac{da}{dn} = C(\Delta K)^n, \quad (1)$$

where C was the power law constant and n was the power law exponent. The expression for  $\Delta K$  was expressed as

$$\Delta K = \beta \Delta \sigma \sqrt{pa}, \quad (2)$$

where  $\beta$  was the crack geometry factor,  $\Delta \sigma$  was the stress range, and a was the crack length. Since the surface flaw was assumed to be semicircular throughout crack propagation and small relative to the specimen thickness,  $\beta$  is a constant equal to  $2.2/\pi$  [15].

The substitution of equation (2) into equation (1) and integration yielded

$$N_{pred} = \frac{1}{C \Delta \sigma^n b^n p^{\frac{n}{2}} \left( \frac{n}{2} - 1 \right)} \left[ a_i^{\left( 1 - \frac{n}{2} \right)} - a_f^{\left( 1 - \frac{n}{2} \right)} \right]. \quad (3)$$

The power law constants and exponents for the crack growth data [14] are shown in Table 1. The relationships of the predicted crack growth lives to the experimental lives are shown in Figs. 6-8. The

Table 1. Power law constants and exponents at R = 0.1 for Ti-47Al-3Nb-2Cr-0.2W (at%).

	600°C		800°C	
	C	n	C	n
Nearly-Lamellar Microstructure	$2.8 \times 10^{-12}$	4.2	$1.7 \times 10^{-13}$	5.5
Duplex Microstructure	$6.6 \times 10^{-12}$	5.4	$8.9 \times 10^{-17}$	10.3

fatigue lives for the nearly-lamellar microstructure were comprised entirely of crack growth at high stress levels. Fatigue lives were dominated by initiation at low stress levels as much as three orders of magnitude in fatigue life for the nearly-lamellar microstructure.

The predicted fatigue lives for the duplex microstructure at 800°C showed more scatter than the nearly-lamellar predicted fatigue lives. The scatter may be relative to the severity of the inhomogeneities in the test specimen. The data suggest that crack propagation is a large portion of the fatigue life for the 800°C duplex microstructure.

#### 4. Conclusion

The isothermal high-cycle-fatigue behavior of the Ti-47Al-3Nb-2Cr-0.2W (at%) gamma titanium aluminide is strongly influenced by temperature and alloy microstructure. The Ti-47Al-3Nb-2Cr-0.2W (at%) gamma titanium aluminide alloy does not exhibit an endurance limit under high-cycle fatigue beyond  $10^7$  cycles for the nearly-lamellar and duplex microstructures. Fatigue lives well beyond  $10^7$  cycles were conveniently obtained at 350 Hz.

An increase of temperature reduced the fatigue strength of the nearly-lamellar microstructure. The fatigue strengths at lower lives of the duplex microstructure were slightly higher at 600°C than at room temperature. The duplex microstructure showed superior fatigue strength compared to the nearly-lamellar microstructure at 23 and 600°C. The nearly-lamellar and duplex microstructures produced similar fatigue strengths at 800°C even though it was when compared to the two lower temperatures.

For the nearly-lamellar microstructure at 600 and 800°C, initiation sites occurred at the surface of each test specimen. Every critical crack initiated by interlamellar fracture of a lamellar colony that intersected the free surface of the test specimen. Transgranular initiation sites were observed at the specimen surface but the crack did not propagate beyond the lamellar colony in which it initiated.

For the duplex microstructure at 600 and 800°C, initiation sites occurred at the interior of the test specimen. The critical crack initiated at either a gamma disk or porosity in every duplex test specimen. Transgranular fracture of a single gamma grain was observed at the initiation sites. The crack initiated at the large gamma grain in a transgranular mode and then propagated into the surrounding region.

Porosity, with a size approximately the same as the microstructure grain size (10µm), had a detrimental effect on the duplex microstructure fatigue life. The porosity acted as a pre-existing flaw that eliminated the crack initiation portion of the fatigue life, which appears to be a major part of the fatigue life for this material in the high cycle regime at 23 and 600°C. Thus, the fatigue life will be reduced drastically possibly causing catastrophic failure if non-destructive evaluation techniques cannot identify this type of flaw.

A comparison of the predicted fatigue life to the experimental fatigue life suggested that the majority of nearly-lamellar fatigue life at 600 and 800°C consisted of crack propagation at high stresses and crack initiation at low stresses. The majority of the duplex fatigue life at 800°C consisted of crack propagation at high and low stresses.

## Acknowledgements

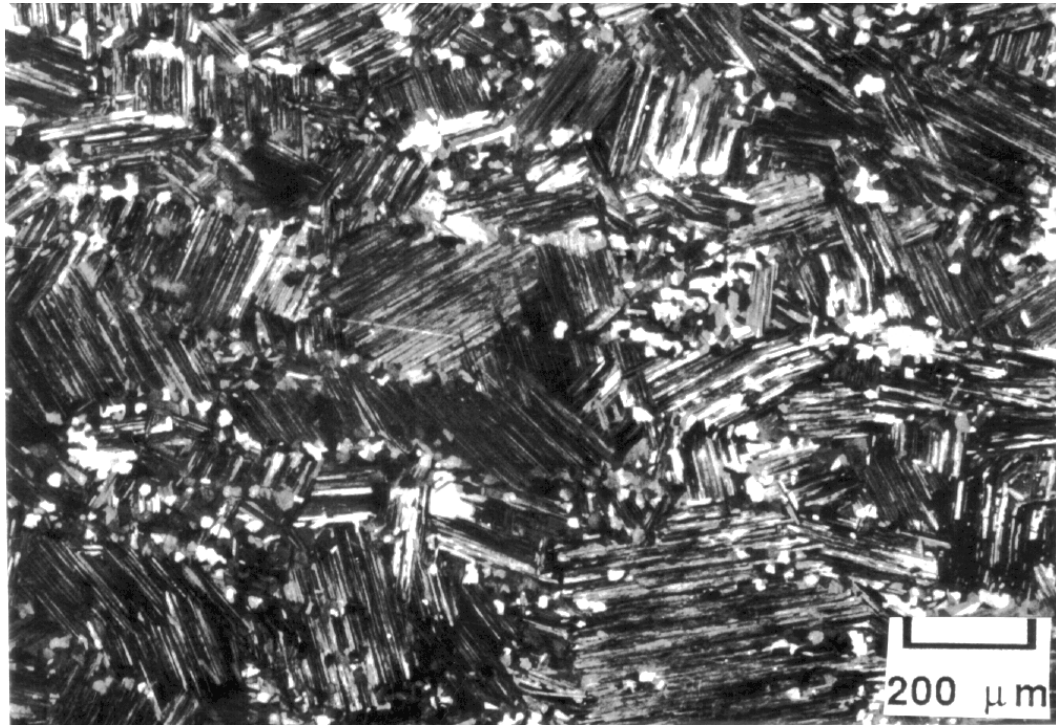
Research performed at AFRL/MLLN with support from AF Contract Nos. F33615-94-C-5200 and F33615-98-C-5214.

## References

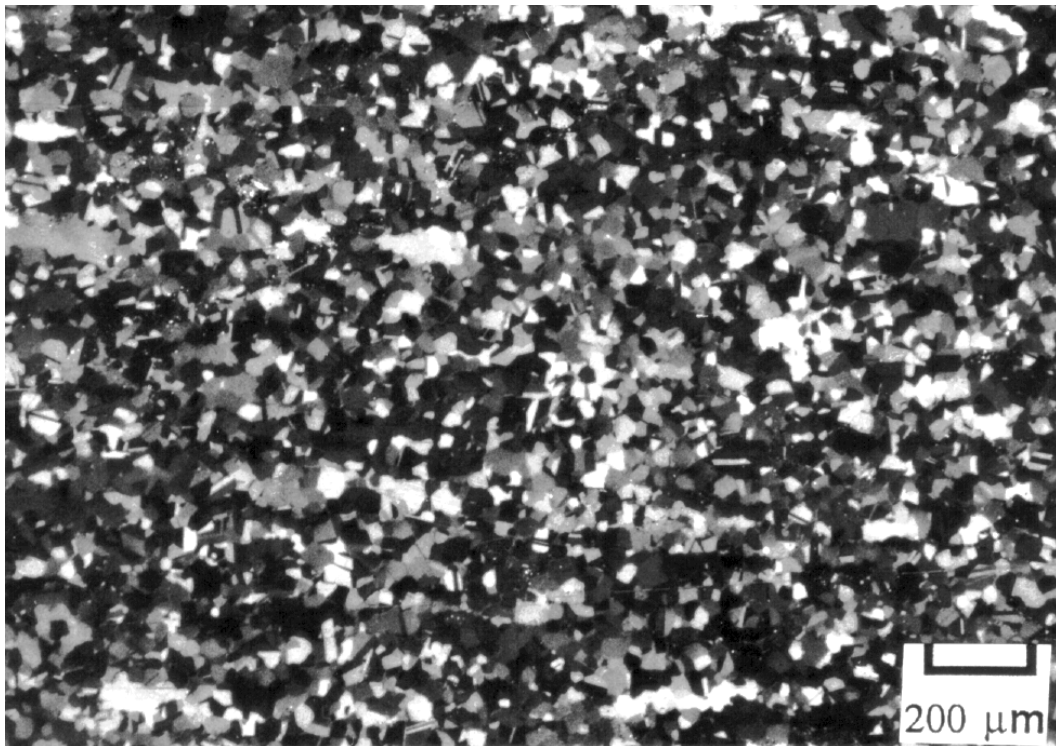
1. Y-W. Kim, Journal of Materials 46, 39 (1994).
2. Y-W. Kim, Intermetallic Compounds (3rd Japan Inter. SAMPE Symp.), M. Yamaguchi and H. Fukutomi, Eds., p. 1310, Japan Charter of SAMPE Tokyo Japan (1993).
3. W. E. Dowling, J. E. Allison, L. R. Swank, and A. M. Sherman, New Engine Design and Engine Component Technology (SAE SP-972), p.31, Society of Automotive Engineers, Warrendale, PA, USA. (1993).
4. W. V. Vaidya, K.-H. Schwalbe, and R. Wagner, Gamma Titanium Aluminides, Y-W. Kim, R. Wagner, and M. Yamaguchi, Eds., p. 867, The Minerals, Metals, & Materials Society, Warrendale, PA USA (1995).
5. S. J. Trail and P. Bowen, Gamma Titanium Aluminides, Y-W. Kim, R. Wagner, and M. Yamaguchi, Eds., p. 883, The Minerals, Metals, & Materials Society, Warrendale, PA USA (1995).
6. J. M. Larsen, B. D. Worth, S. J. Balsone, and J. W. Jones, Gamma Titanium Aluminides, Y-W. Kim, R. Wagner, and M. Yamaguchi, Eds., p. 821, The Minerals, Metals, & Materials Society, Warrendale, PA USA (1995).
7. S. J. Balsone, J. M. Larsen, D. C. Maxwell, and J. W. Jones, Material Science and Engineering 192/193, 457 (1994).
8. J. Kumpfert, Y-W. Kim, and D. M. Dimiduk, Material Science and Engineering 192/193, 465 (1994).
9. W. E. Dowling, Jr., W. T. Donlon, and J. E. Allison, Mat. Res. Soc. Symp. Proc. 213, p. 561, Material Research Society, Warrendale, PA USA (1991).
10. K. S. Chan and D. L. Davidson, Structural Intermetallics, R. Darolia, J. J. Lewandowski, C. T. Liu, P. L. Martin, D. B. Miracle and M. V. Nathal, Eds., p. 223, The Minerals, Metals, & Materials Society, Warrendale, PA USA (1993).
11. E. J. Dolley, University of Dayton Master Thesis, University of Dayton, Dayton, OH (1995).

12. J. M. Larsen, J. R. Jira, and K. S. Ravichandran, Small-Crack Test Methods ASTM STP 1149, J. M. Larsen and J. E. Allison, Eds., p. 57, American Society for Testing and Materials, Philadelphia, PA USA (1992).
13. N. D. Schehl, University of Dayton Research Institute Report UDR-TR-94-139, University of Dayton, Dayton, OH (1994).
14. B. D. Worth, J. M. Larsen, S. J. Balsone, , and J. W. Jones, Titanium '95 Science and Technology, P. A. Blenkinsop, W. J. Evans, and H. M. Flower, Eds., p. 286, The Institute of Materials, The University Press, Cambridge UK (1995).
15. N. E. Dowling, Mechanical Behavior of Materials, p. 297, Prentice-Hall Publishing, Englewood Cliffs, NJ USA, (1993).



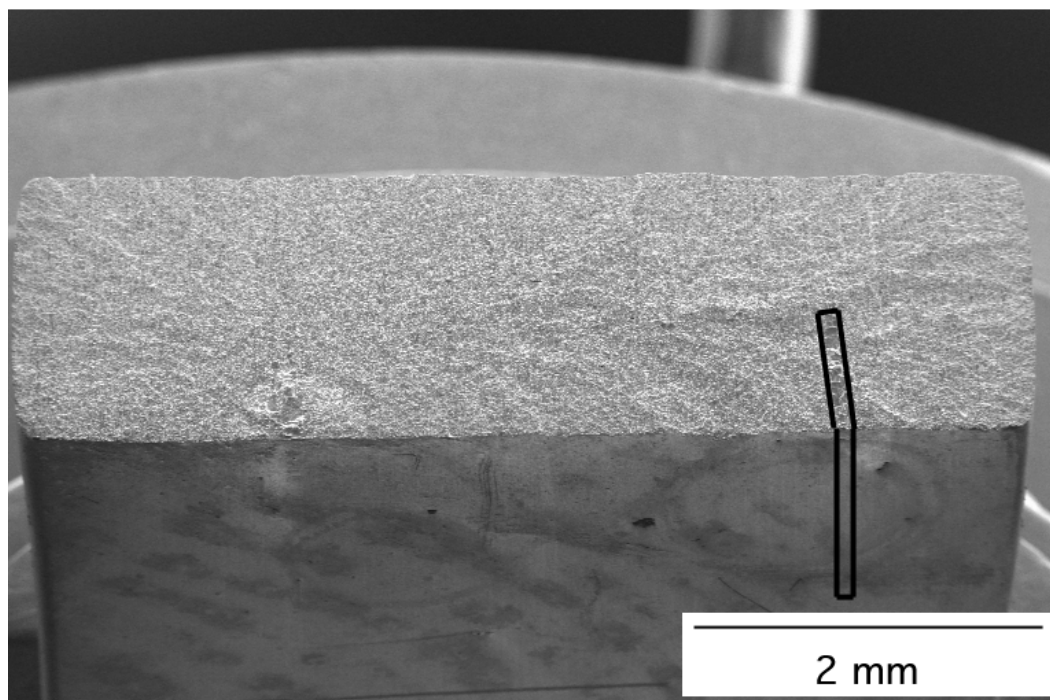


(a)

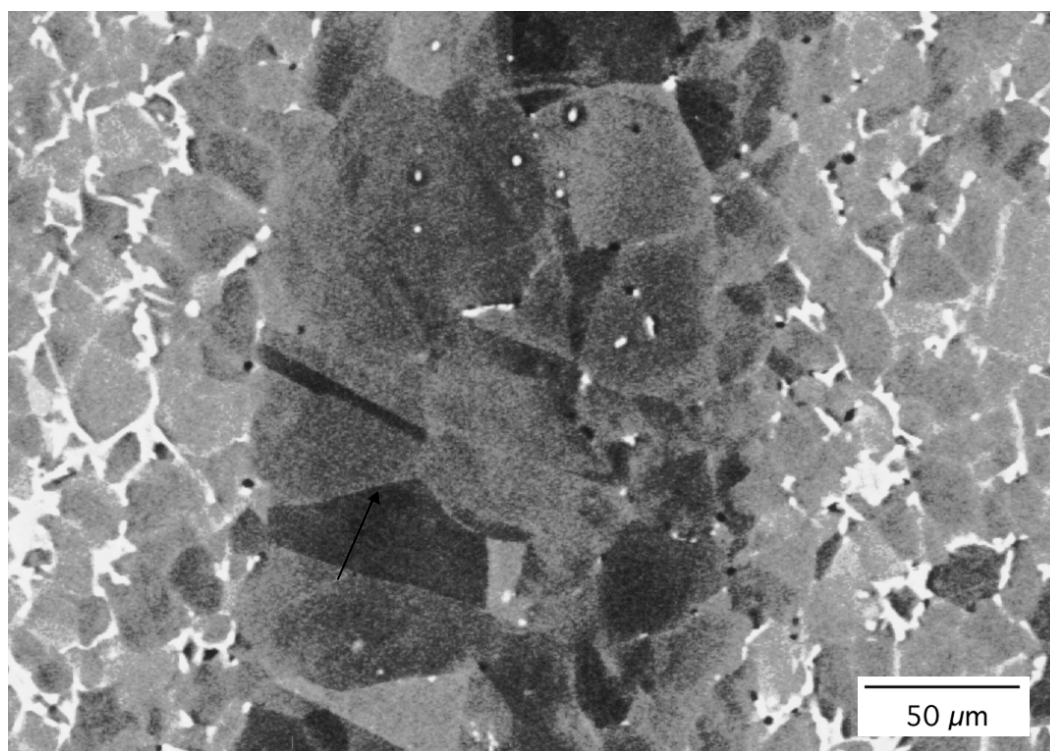


(b)

Figure 1. Typical nearly-lamellar (a) and duplex (b) microstructures of forgings 1 and 2.



(a)



(b)

Figure 2. Typical gamma platelet in the duplex microstructure showing the orientation relative to the specimen fracture surface (a) and the platelet microstructure (b).

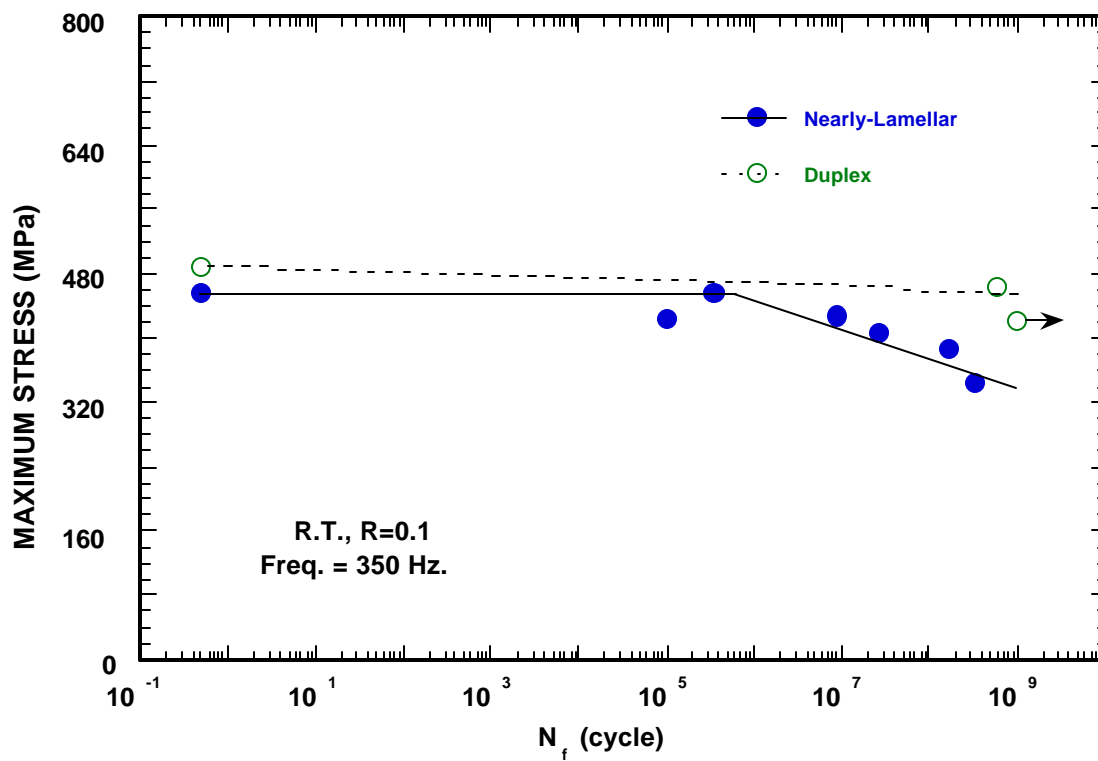


Figure 3. Effects of stress and microstructure on fatigue life,  $N_f$ , at room temperature.

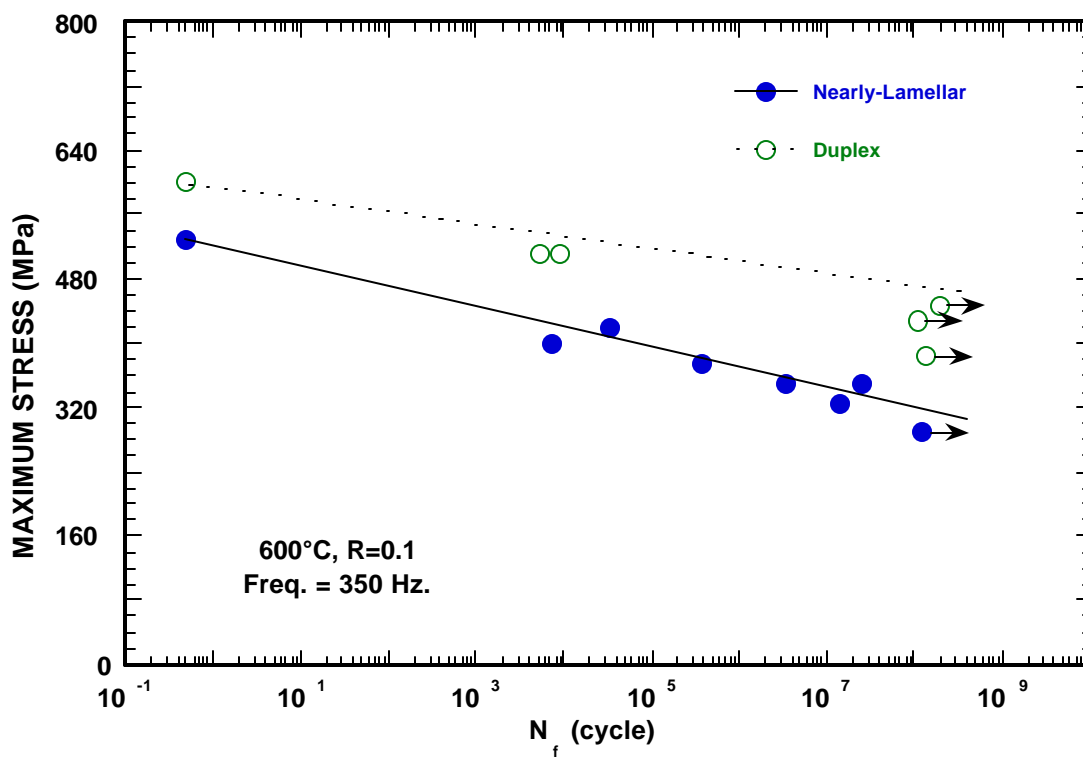


Figure 4. Effects of stress and microstructure on fatigue life,  $N_f$ , at 600°C.

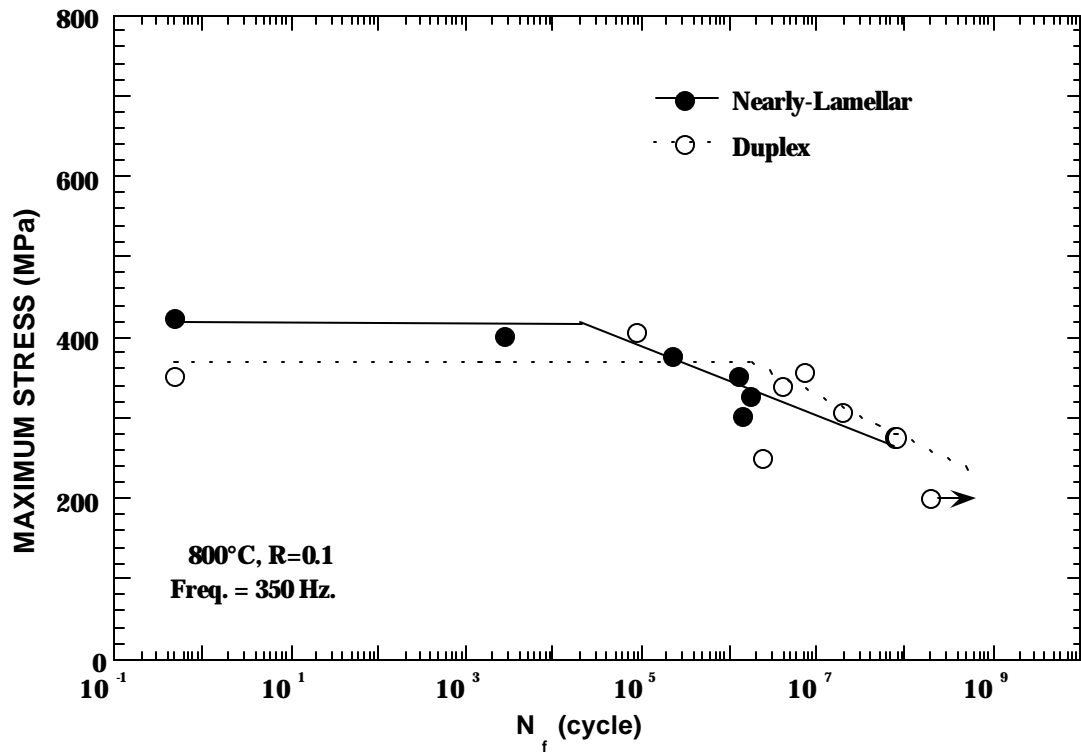


Figure 5. Effects of stress and microstructure on fatigue life,  $N_f$ , at 800°C.

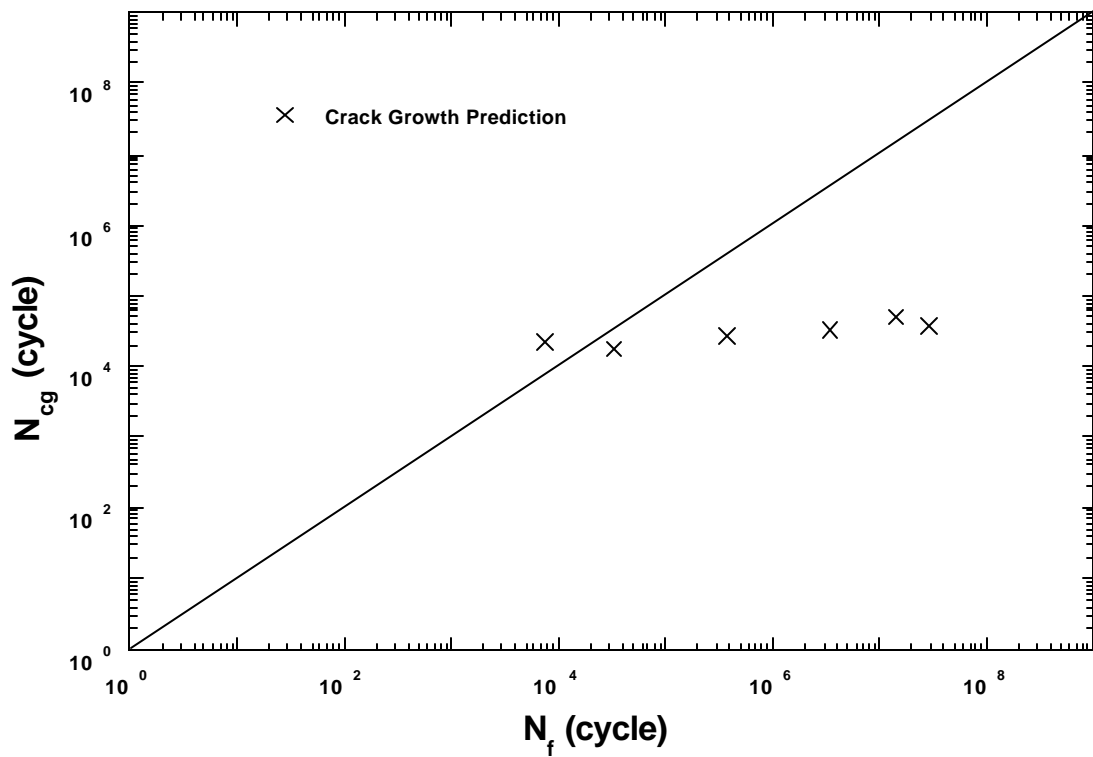


Figure 6. Predicted crack growth life,  $N_{cg}$ , compared to fatigue life,  $N_f$ , of the nearly-lamellar microstructure at 600°C.

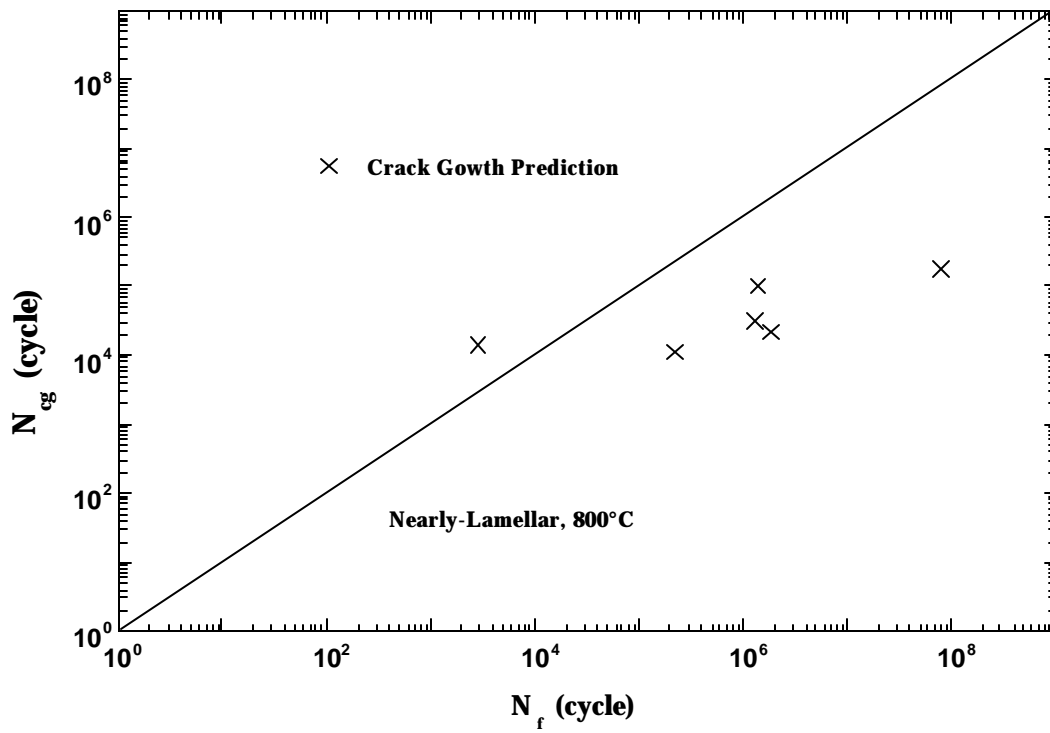


Figure 7. Predicted crack growth life,  $N_{cg}$ , compared to fatigue life,  $N_f$ , of the nearly-lamellar microstructure at 800°C.

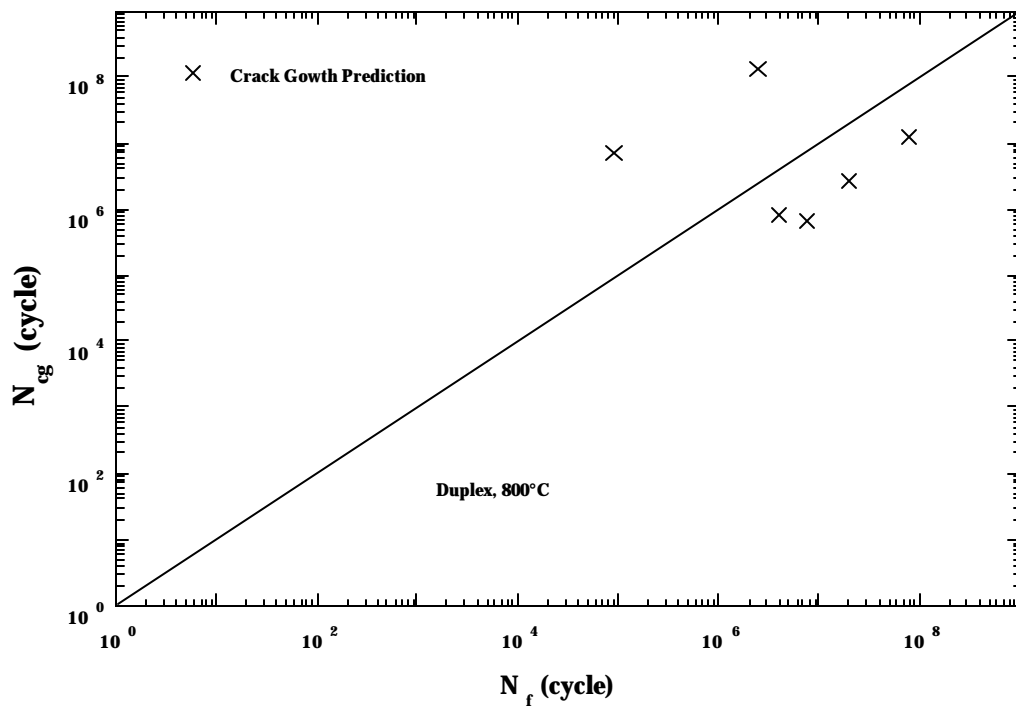


Figure 8. Predicted crack growth life,  $N_{cg}$ , compared to fatigue life,  $N_f$ , of the duplex microstructure at 800°C.

This page intentionally left blank.

# **Bridging Stress Distributions During Fatigue Crack Growth in Continuously Reinforced [0] Metal Matrix Composites**

**Reji John and Dennis J. Buchanan\***

Materials and Manufacturing Directorate,  
Air Force Research Laboratory (AFRL/MLLN),  
Wright-Patterson AFB, OH 45433-7817, U.S.A.

\* University of Dayton Research Institute, Dayton, OH 45469-0128, U.S.A.

## **ABSTRACT**

An optimization procedure was developed to deduce the fiber bridging stresses from crack opening displacements measured *in situ* during crack growth. This procedure was used to determine the bridging stress distribution during fatigue crack growth in a unidirectionally reinforced metal matrix composite (SCS-6/TIMETAL®21S). The bridging stress is non-zero at the crack tip contrary to predictions from conventionally used shear lag models. The bridging stress at the crack tip is proportional to the applied farfield stress. The deduced bridging law is similar to the new shear lag models with non-zero bridging stresses at the crack tip. Any bridging model can be used to predict the crack growth behavior by choosing appropriate values of the frictional shear stress ( $\tau$ ). Consequently, the magnitude of the stresses in the fibers bridging the crack will depend on the fiber bridging model. Hence, the fiber tensile strength required to predict the onset of fiber failure will also depend on the fiber bridging model.

**Keywords:** bridging stress, bridging stress intensity factor, crack growth, fatigue, fiber bridging, metal matrix composite, shear lag, titanium matrix composite

## INTRODUCTION

A variety of models have been developed to describe bridging in concrete, ceramics, ceramic matrix composites (CMC) and metal matrix composites (MMC) during crack growth under monotonic and cyclic loading [1-30]. In monolithic and short fiber reinforced concrete, and ceramics [27-30], increasing crack opening displacement (COD) results in an initial increase, followed by a decrease of the bridging stress. In contrast, continuously reinforced CMC and MMC [1-26] exhibit continuously increasing bridging stress with increasing COD in the bridged region. In CMC and MMC systems, the bridging mechanisms were modeled as a distributed closing pressure exerted on the crack surface with the applied load in the direction of the fibers (Figure 1). The models used to describe crack growth in continuously reinforced CMC and MMC include shear lag [1-16,19-26], constant bridging stress distributions [11,17,18] and fiber pressure models [17]. These fiber bridging models for continuously reinforced CMC and MMC predict a wide range of bridging stress distributions. The shear lag models developed by Marshall et al. [1] and McCartney [2] enforce zero bridging stress at the crack tip. In contrast, shear lag models proposed by Majumdar et al. [5], Danchaivijit and Shetty [6], Chiang et al. [7], and Meda and Steif [8] predict non-zero bridging stress at the crack tip. All these shear lag models show a similar trend of an increase in bridging stress with an increase in distance away from the crack tip. Similar to the latter shear lag models, the fiber pressure [17] and constant bridging stress [11,17,18] models predict non-zero bridging stress at the crack tip. The differences in these fiber bridging models result in prediction of significantly different magnitudes of stresses in the fibers bridging a crack subjected to the same loading conditions [11,13]. Consequently, the prediction of onset of fiber breakage and eventual failure of the composite would require values of fiber strength which depend on the fiber bridging model.

An independent verification of the fiber bridging stress distribution can be achieved by direct comparison of the predicted COD profile with the measured COD data [10-21,26-30]. Recently, many investigators [12,13,15,20,21,26-30] have used the measured COD profile to deduce the bridging stress range,  $\Delta\sigma_b$  as a function of COD and location along the crack in various materials. Hutson, John and Jira [15] measured the COD profile *in situ* and deduced  $\tau$  as a function of temperature in SCS-6/TIMETAL®21S. Connell and Zok [21] prepared specimens with edge-to-edge through cracks from center-cracked specimens which were tested under fatigue. The load versus crack opening displacement response of these specimens was used to deduce  $\tau$  as a function of temperature in Sigma/Ti-6Al-4V. Hutson, John and Jira [15] and Connell and Zok [21] used cyclic bridging laws, in which the bridging stress range,  $\Delta\sigma_b$  is proportional to the square root of the half-COD range,  $\Delta v$ , i.e.

$$\Delta\sigma_b = \beta \sqrt{\Delta v} \quad (1)$$

where  $\beta$  = bridging stiffness parameter. Note that Eqn. (1) implies that  $\Delta\sigma_b = 0$  at the crack tip. In contrast, John et al. [12], Buchanan et al. [13], and Zheng and Ghonem [20], used COD data to deduce the fiber bridging stress distribution without assuming a specific relationship between  $\Delta\sigma_b$  and  $\Delta v$ . The results from SCS-6/TIMETAL®21S [12,13] and SM1240/TIMETAL®21S [20] showed that fiber bridging stress distribution is linear or near-constant along the crack with non-zero values at the crack tip.

The above studies [12,13,15,20,21,26-30] were based on COD measured at discrete locations along the crack. The number of locations of measurement depends on the crack length and the technique used to measure the COD. The use of scanning electron microscope (SEM) [17] and Moiré interferometry [29] yield numerous COD data along the crack. During crack growth in MMC, the load versus COD response at various locations along the crack enables the deduction of the effect of cyclic loading on the bridging mechanism. The laser interferometric displacement gage (IDG)



system [31,32], which enables such measurements, was used by John et al. [12,14], Buchanan et al. [13], and Zheng and Ghonem [20] to obtain the COD data during crack growth in MMC systems. The laser IDG method typically results in 3 to 6 locations of COD measurements along the crack. Using extensive finite element analysis, Buchanan et al. [13] showed that the entire bridging stress distribution along the crack can be deduced reliably using the COD data at a few locations. This paper describes additional results obtained using the method proposed in Ref. [13] for multiple maximum stress levels and a wide range of crack lengths. The results are also compared with some available fiber bridging models.

## **EXPERIMENTAL PROCEDURE AND RESULTS**

The MMC tested was TIMETAL®21S™ matrix reinforced with silicon carbide (SCS-6™) fibers in a  $[0]_4$  layup. The radius ( $R_f$ ) and modulus ( $E_f$ ) of the SCS-6 fiber is 71  $\mu\text{m}$  and 393 GPa, respectively. The modulus of the matrix ( $E_m$ ) is equal to 114 GPa. In each ply of the MMC, the average center-to-center fiber spacing was 0.197 mm (i.e. 129 fibers per 25.4 mm). Some relevant properties of the MMC are reported in Table I. Additional details of the composite and the constituents can be found in Ref. [16]. The middle tension M(T) geometry, shown in Figure 1, was used in this study. The dimensions and properties of the two specimens tested during this study are reported in Table I. The initial flaws were produced by electrical discharge machining (EDM). These specimens were fatigue loaded at various maximum stress levels ( $\sigma_{a,\text{max}}$ ) with the applied stress ratio,  $R (= \sigma_{a,\text{min}} / \sigma_{a,\text{max}}) = 0.1$  and frequency of loading = 1 Hz. All the tests were conducted at room temperature in laboratory air.

Crack extension from the initial flaw was monitored using a direct current electric potential (DCEP) technique. The DCEP crack lengths were corrected using optical measurements, which were obtained periodically during the tests. The optical measurements were made on the front and back sides using a 20X traveling microscope. The measured average crack length as a function of the number of applied cycles and the corresponding  $\sigma_{a,\text{max}}$  is shown in Figures 2(a) and 2(b) for the specimens 93411 and 93413, respectively. The crack length versus cycle count response is typical of fully bridged crack growth exhibiting decreasing crack growth rate ( $da/dN$ ) with increasing crack length [9,10,11,14,16-18,20-26]. The specimen 93411 was stopped at  $\approx 7.87 \times 10^6$  cycles, COD profiles measured, and the matrix removed using an etchant. There were no broken fibers confirming fully bridged crack growth during this test [12].

During the crack growth tests, the COD profile was measured at different crack lengths using a laser IDG system [31,32]. This technique has been successfully used to measure COD during crack growth in SCS-6/Ti-24Al-11Nb [10,11] and SCS-6/TIMETAL®21S [12,13,15,16], SCS-6/Ti-6Al-4V [14] and SM1240/TIMETAL®21S [20] at room and elevated temperatures. The crack lengths at which the COD profiles were measured are identified as hollow circles in Figures 2(a) and 2(b). Figure 3 shows a schematic highlighting the location of the COD measurements along the crack. The indents, which were  $\approx 25 \times 25 \mu\text{m}$ , were placed  $\approx 50 \mu\text{m}$  above and below the crack surface such that the spacing between the indents at a given location is  $\approx 100 \mu\text{m}$ . The indent pairs were typically located 0.8 mm apart along the crack with the last set of indents usually  $\approx 0.075$  mm behind the crack tip. Since the indents are located  $\approx 50 \mu\text{m}$  away from the crack surface, the displacements measured between the indents could be different from that of the true COD at that location. This difference was estimated to be  $\approx 1.5\%$ , based on linear elastic fracture mechanics expressions for displacements near a crack tip in an unbridged isotropic material. Hence, during this study, the COD at a given location was assumed equal to the displacements measured between the indents. Additional details of the measurement technique can be found in Ref. [13,31,32].

The measured COD profiles for specimens 93411 and 93413 are shown in Figures 4 and 5, respectively. The half-COD range ( $\Delta v$ ) is typically  $\leq 1 \mu\text{m}$  along most of the crack and  $\approx 2\text{-}4 \mu\text{m}$  only close to the machined notch tip. The steep increase in  $\Delta v$  near the machined notch tip can be attributed to lack of bridging fibers between those locations and the center of the machined notch. The magnitude of  $\Delta v$  shown in Figures 4 and 5 are consistent with those reported by Ghosn et al. [17] and Zheng and Ghonem [20].

### ANALYTICAL PROCEDURE

This section briefly describes the optimization procedure to deduce the bridging stress distribution from measured COD profiles. Further details can be found in Ref. [13]. The weight function method as given by Equation (2) was used to calculate the half-COD range due to an arbitrary stress distribution on the crack surface.

$$\Delta v(x) = \frac{1}{E_o} \int_x^a \left[ \int_0^{\bar{a}} h(\bar{x}, \bar{a}) \Delta \sigma_s d\bar{x} \right] h(x, \bar{a}) d\bar{a} \quad (2)$$

where

$\Delta v(x)$  = half crack opening displacement range, (see Figure 1),  
 $E_o$  = orthotropic modulus [16,19],  
 $h(x,a)$  = weight function [13], and  
 $\Delta \sigma_s$  = surface stress range.

In general,  $\Delta \sigma_s$  can be calculated as

$$\Delta \sigma_s = \Delta \sigma_a - \Delta \sigma_b \quad (3)$$

where

$\Delta \sigma_a$  = applied stress range, and

$\Delta \sigma_b$  = bridging stress range.

The applied stress range was,  $\Delta \sigma_a = \sigma_{a,\text{max}} - \sigma_{a,\text{min}}$  where  $\sigma_{a,\text{max}}$  = maximum applied stress and  $\sigma_{a,\text{min}}$  = minimum applied stress. Note that  $\Delta \sigma_a$  was constant along the surface in the crack plane. The bridging stress range,  $\Delta \sigma_b$  is the closing stress on the crack due to the interfacial sliding between the fiber and the matrix and is active only in the range  $a_o \leq x \leq a$ .  $h(x,a)$  is the weight function for a central crack in a plate with finite width. Details of the weight function used during this study can be found in Ref. [13].

The bridging stress range was chosen to be a function of three undetermined coefficients ( $A_0$ ,  $A_1$ ,  $A_2$ ) and the normalized crack length,  $\rho$ , as given by Equation (4), where  $x$ ,  $a$ ,  $a_o$  in Equation (4) are defined in Figure 1. John et al. [12] and Fett et al. [28] used a similar form (up to 10 constants) to deduce the bridging stress distribution in a MMC and CMC, respectively.

$$\Delta \sigma_b = A_0 + A_1 \sqrt{\rho} + A_2 \rho \quad (4)$$

where

$$\rho = \frac{a - x}{a - a_0} . \quad (5)$$

Note that the crack tip corresponds to  $\rho = 0$  and the initial machined notch tip to  $\rho = 1$ . Equation (4) can accommodate increasing or decreasing  $\Delta\sigma_b$  with increasing distance away from the crack tip depending on the magnitude and sign of the constants  $A_i$ . In addition, non-zero or zero  $\Delta\sigma_b$  at the crack tip can be accommodated.

The coefficients ( $A_0, A_1, A_2$ ) are not known *a priori* and must be determined such that the square of the normalized difference between the measured and the calculated half-COD is minimized as given by Equation (6). An IMSL [33] optimization routine was employed to determine the values of  $A_i$  that minimize the sum in Equation (6).

$$\sum_{i=1}^n \left[ \frac{\Delta\bar{v}(x)_i^{\text{measured}} - \Delta\bar{v}(x)_i^{\text{calculated}}}{\Delta\bar{v}(x)_i^{\text{measured}}} \right]^2 = \text{minimum} , \quad (6)$$

where  $n$  = number of locations of COD measurements along the crack. During this study,  $n$  typically ranged from 3 to 6 depending on the crack length. For each crack length, the optimization of the constants,  $A_i$ , was terminated when the normalized sum of squares reached a specified tolerance of  $1 \times 10^{-6}$ .

Knowing  $\Delta\sigma_b$ , the fiber stress range,  $\Delta\sigma_f$  can be calculated as

$$\Delta\sigma_f = \frac{\Delta\sigma_b}{V_f} , \quad (7)$$

where  $V_f$  = volume fraction of fibers in the composite. Knowing  $\Delta\sigma_b$ , the corresponding bridging stress intensity factor range,  $\Delta K_b$  was calculated using the weight function method as

$$\Delta K_b = \int_{a_0}^a \Delta\sigma_b(x) h(x, a) dx . \quad (8)$$

The above analytical procedure to determine  $\Delta\sigma_b$  from  $\Delta v$  was verified using extensive finite element analysis [13]. Using finite element analysis, Buchanan et al. [13] studied the sensitivity of the deduced bridging stress to location of near-tip COD data. The results showed that the error in deduced  $\Delta\sigma_b$  was within  $\pm 1.1\%$  for near-tip data located within 0.05 to 0.18 mm from the crack tip [13]. As discussed earlier, the available COD data near the crack tip was typically measured at  $\approx 0.075$  mm from the crack tip. Hence, the near-tip stress distribution deduced from the COD data should be sufficiently accurate.

## RESULTS AND DISCUSSION

### Bridging Stress Distribution

Figure 6 compares the measured COD with the optimized fit using the procedure described earlier. The optimized fit correlates well with the data except close to the machined notch tip, i.e. at  $x = 2.2\text{-}2.4$  mm. The coefficients  $A_0$ ,  $A_1$  and  $A_2$  of the optimized fit for the two specimens are reported in Table II. The resulting bridging stress range,  $\Delta\sigma_b$  as a function of normalized location along the crack length ( $\rho$ ) is shown in Figure 7 for 6 crack lengths analyzed in this study. Note that at  $\rho=0$  (crack tip),  $\Delta\sigma_b = A_0$ , and at  $\rho=1$  (machined notch tip),  $\Delta\sigma_b = A_0 + A_1 + A_2$ .

Figure 7 clearly shows that  $\Delta\sigma_b$  is non-zero at the crack tip ( $\rho=0$ ) and increases gradually with increasing distance from the crack tip. The increase in  $\Delta\sigma_b$  is almost linear for  $\rho \geq 0.1$ . This distance corresponds to  $\approx 0.2\text{-}0.5$  mm from the crack tip depending on the crack length. Hence, the bridging stress distribution range is near-linear after  $\approx 1\text{-}3$  times the center-to-center fiber spacing behind the crack tip. The maximum fiber stress range  $\approx 1250$  MPa, which is less than the reported [16,18,20,23,25] failure strength of the virgin SCS-6 fibers ( $\approx 3750$  MPa). Numerous investigators [10-12,14,16,20,21,23,25] have suggested that the *in situ* failure strength of the SiC fibers is significantly lower than the virgin strength. The lower *in situ* failure strength can be attributed to the surface/coating damage induced during the fatigue loading [34]. Using shear lag models, John et al. [14] and Connell and Zok [21] have shown that the *in situ* failure strength of the SiC fibers is close to the bundle strength. The reported bundle strength of the SCS-6 fiber is  $\approx 2600\text{-}3200$  based on numerous tension tests on fibers extracted from untested and tested specimens [35]. The maximum fiber stress shown in Figure 7 is significantly lower than the reported bundle strength. The low magnitude of the deduced fiber stresses as shown in Figure 7 is also consistent with the fully bridged crack growth behavior shown in Figure 2. Figure 7 shows that  $\Delta\sigma_b$  increased with increase in  $\sigma_{a,\max}$  (or  $\Delta\sigma_a$ ).  $\Delta\sigma_b$  increased by  $\approx 20$  and  $80\%$  at the crack tip and the machined notch tip, respectively, corresponding to  $\approx 54\%$  increase in  $\Delta\sigma_a$ . Interestingly, the specimen tested at  $\sigma_{a,\max} = 270$  MPa shows that  $\Delta\sigma_b$  versus  $\rho$  is almost independent of crack length for  $3.6 \leq a \leq 6.9$  mm.

Figure 8 shows  $\Delta\sigma_b$  at the crack tip,  $\Delta\sigma_{b,\text{tip}}$  as a function of the applied net-section stress range,  $\Delta\sigma_{a,\text{net}} (= \Delta\sigma_a / [1 - 2a_0/W])$ . The deduced values of  $\Delta\sigma_{b,\text{tip}}$  increase with increase in  $\Delta\sigma_{a,\text{net}}$ . In an uncracked structure, the stress range in the fiber,  $\Delta\sigma_f$  at a location can be calculated as  $\Delta\sigma_{a,\text{net}} * E_f/E_c$  using strain compatibility. When the crack tip arrives at that location,  $\Delta\sigma_{b,\text{tip}}$  can be determined as  $V_f * \Delta\sigma_f$ . Thus,  $\Delta\sigma_{b,\text{tip}}$  can be related to  $\Delta\sigma_{a,\text{net}}$  using the following equation.

$$\Delta\sigma_{b,\text{tip}} = \Delta\sigma_{a,\text{net}} \frac{V_f E_f}{E_c} \quad (9)$$

As shown in Figure 8, the prediction obtained using Equation (9) is close to that deduced from the measured COD.  $\Delta\sigma_{b,\text{tip}}$  is generally within 25% of Equation (9) although most of the values are slightly lower than the predicted trend.

### Bridging Law and Comparison With Fiber Bridging Models

Knowing  $\Delta\sigma_b$  versus  $\rho$  from the optimization procedure (Fig. 7), the relationship between  $\Delta\sigma_b$  and  $\Delta v$ , i.e. the bridging law can be determined. Figure 9 shows the deduced bridging law for the

various stress levels and crack lengths. As discussed earlier,  $\Delta\sigma_b$  is non-zero when  $\Delta v=0$ , i.e. at the crack tip.  $\Delta\sigma_b$  increases  $\approx 100\%$  when  $\Delta v$  increases from 0.0 to 1  $\mu\text{m}$ . When  $\Delta v$  increases from 1 to 4  $\mu\text{m}$ ,  $\Delta\sigma_b$  increases gradually by  $\approx 33\%$ . For large  $\Delta v$  ( $\Delta v \geq 2.5 \mu\text{m}$ ),  $\Delta\sigma_b \approx 390\text{-}400 \text{ MPa}$ , independent of crack length and applied stress level. This near-constant bridging stress range for large  $\Delta v$  is higher than that predicted based on the net-section stress, as discussed later. The bridging law shown in Fig. 9 is compared with available fiber bridging models next.

The fiber bridging models commonly used to describe crack growth perpendicular to fibers in MMC are either shear lag models [9,10-12,14-26] or constant bridging stress models [11,17,18]. These shear lag models assume that the fiber/matrix interface has negligible debonding energy, initial stresses are zero and the sliding stress,  $\tau$  is constant. Since the initial stresses are zero, the bridging stresses predicted by these shear lag models are zero at the crack tip. Recently, new shear lag models [5-8] with non-zero bridging stress at the crack tip have been developed. These new shear lag models [5-8] predict bridging stress distributions similar to that observed during this study (Figs. 7-9). Hence, the results from this study (Fig. 9) provide an opportunity to evaluate the predictive capability of the conventionally used and new fiber bridging models.

Representative shear lag models with zero crack-tip-bridging stress, constant bridging stress models, and shear lag models with non-zero crack-tip-bridging stress, will be briefly discussed next, prior to comparison with our results. McCartney (McC) [2] derived Equation (10) to describe the fiber bridging behavior in CMC systems.

$$\sigma_b(x) = \beta \sqrt{v(x)} \quad \text{where} \quad \beta = \sqrt{\frac{4V_f^2 E_c^2 E_f \tau}{(1 - V_f)^2 E_m^2 R_f}}, \quad (10)$$

and  $\tau$  = fiber/matrix interfacial shear stress. Equation (10) is similar to Equation (1) and predicts zero fiber bridging stresses at the crack tip because  $\Delta v = 0$  at the crack tip. The bridging laws derived by Marshall, Cox and Evans (MCE) [1] and Hutchinson and Jensen (HJ) [3] are similar (in form) to Equation (10). These models, derived in Refs. [1] – [3], will predict similar bridging law corresponding to different values of  $\tau$ .

In contrast to the above models, Majumdar et al. [5], Danchaivijit and Shetty [6], Chiang et al. [7], and Meda and Steif [8] derived shear lag models with non-zero bridging stresses at the crack tip. Assuming that the stresses in the fiber and the matrix at the end of the slip zone are the same as the far-field stresses, Danchaivijit and Shetty (DS) [6] derived Equation (11).

$$\sigma_b(x) = \frac{\sigma_{a,net} V_f E_f}{2 E_c} \left\{ 1 + \sqrt{1 + \frac{16 E_c^2 \tau}{\sigma_{a,net}^2 E_f R_f}} \sqrt{v(x)} \right\} \quad (11)$$

Assuming that the pull-out displacement is more directly related to the load transfer from the fiber to the matrix rather than to the fiber force at the matrix-crack plane, Meda and Steif [8] derived Equation (12).

$$\sigma_b(x) = \frac{\sigma_{a,net} V_f E_f}{E_c} + \left( 1 - V_f \frac{E_f}{E_c} \right) \beta \sqrt{v(x)}, \quad (12)$$

where  $\beta$  = bridging stiffness parameter as defined in models such as those by Marshall, Cox and Evans [1], McCartney [2], and Hutchinson and Jensen [3]. During this study,  $\beta$  in Equation (12) was assumed equal to  $\beta$  defined in Equation (10). Note that Equations (11) and (12) reduce to Equation (9) at the crack tip, i.e. when  $v(x)=0$ . The use of Equations (10)-(12) generally involves an iterative procedure to predict the crack growth behavior in a composite. To overcome this problem, Ghosn et al. [17] proposed Equation (13) for a center-crack type geometry.

$$\sigma_b(x) = \sigma_{a,net} = \frac{\sigma_{a,max}}{1 - \frac{2a_0}{W}} \quad (13)$$

Equation (13) was not based on bridging mechanisms but was successfully used to predict bridged crack growth in a MMC. John et al. [10,11] evaluated the applicability of Equation (13) to predict the crack growth from holes in SCS-6/Ti-24Al-11Nb plates with finite width.

Equations (10)-(13) correspond to monotonic loading. Cyclic bridging laws are available [9,17] for Equations (10) and (13) but unavailable for Equations (11) and (12). Hence, the monotonic forms shown above were used for all the models evaluated during this study to enable direct comparison of the trends and the value of  $\tau$ . In Equations (10)-(12), all the parameters are known except for the fiber/matrix interfacial shear stress,  $\tau$ . In this study,  $\tau$  was determined such that the resulting bridging law was reasonably close to the deduced bridging law shown in Figure 9. The corresponding bridging laws predicted using Equations (10)-(13) are compared with bridging law from this study in Figures 10-13. The corresponding values of  $\tau$ , if applicable, are also shown in the figures.

Figure 10 shows that the models similar to Equation (10) [1-3] predict zero  $\Delta\sigma_b$  at the crack tip contrary to the results from this study. Since these models are similar, only the McCartney (McC) model is discussed here.  $\Delta\sigma_b$  predicted by the shear lag models is close to our results in the range  $0 < \Delta v \leq 2 \mu\text{m}$ , which corresponds to most of the crack length as shown in Figures 4 and 5. The predicted  $\Delta\sigma_b$  starts at zero and increases rapidly within  $\Delta v < 0.2 \mu\text{m}$ , i.e. within a fiber spacing behind the crack tip, and subsequently is close to our results. For large  $\Delta v$ , i.e.  $\Delta v \geq 2.5 \mu\text{m}$ , the McC model predicts steady increase in  $\Delta\sigma_b$  with increasing  $\Delta v$  contrary to near-plateau behavior of the deduced bridging stress distribution. The overprediction by Equations (10) could be as high as 45%. As shown in Figure 10,  $\tau \approx 4.7 \text{ MPa}$  for the McCartney model is consistent with results presented by Larsen et al. [16] for SCS-6/TIMETAL®21S (after accounting for the use of cyclic bridging law in Ref. [16]). Note that in Ref. [16], the estimated value of  $\tau$  was based on correlation with crack growth behavior and not COD range.

Figures 11 and 12 compare the results from this study with that obtained using the bridging laws proposed by Danchaivijit and Shetty (DS) [6] and Meda and Steif (MS) [8], respectively. The corresponding values of  $\tau$  are also shown in the figures. These models predict non-zero bridging stresses at the crack tip consistent with the results from this study. Figures 11 and 12 show the model predictions for two values of  $\tau$ . Comparison of the predictions for  $\sigma_{a,max} = 175$  and  $270 \text{ MPa}$  with the same value of  $\tau$  shows that bridging relationship depends on the applied stress range and is always offset by an amount equal to that at  $\Delta v=0$ , i.e. at the crack tip. As discussed earlier (Figure 9), the deduced  $\Delta\sigma_b$  appears to be independent of the applied stress for  $\Delta v \geq 2.5 \mu\text{m}$ . To simulate this trend, we predicted the  $\Delta\sigma_b$ - $\Delta v$  relationship for  $\sigma_{a,max} = 175 \text{ MPa}$  for the DS and MS models using higher values of  $\tau$ . These predictions, which are shown as dashed lines in Figure 11 and 12, correlate better with the data for  $\Delta v \geq 2.5 \mu\text{m}$ . This correlation implies that  $\tau$  could be decreasing with the increase in

$\sigma_{a,max} \tau$  decreases by about 23% and 41% for the DS and MS models, respectively, corresponding to an increase of 54% increase in  $\sigma_{a,max}$ . Extensive analysis conducted by John et al. [14], Larsen et al. [16], Bakuckas and Johnson [23], and Connell and Zok [21], using shear lag models similar to Equation (10) show that a single value of  $\tau$  can be used to predict the crack growth behavior over a wide range of stress levels. In contrast, the results in Figures 11 and 12 show that if we use models similar to Equations (11) and (12),  $\tau$  required to predict the crack growth behavior should be decreased with increase in applied stress.

In metal matrix composites reinforced with fibers containing carbon coatings,  $\tau$  occurs primarily due to the residual compressive radial stresses exerted on the fiber by the matrix. These residual stresses are generated during the fabrication process due to mismatch between the coefficient of thermal expansion of the fiber and the matrix. During bridged crack growth, the load is transferred from the matrix to the fiber through the slip zone. The slip zone begins at the crack surface and extends along the fiber. When the farfield applied stress is absent, the residual radial stresses (compressive) will ensure a reasonably good contact between the fiber and the matrix along the length of the slip length. When a farfield tensile stress is applied on the composite, the matrix near the crack surface can be expected to pull away from the fiber. Note that at this location, the fiber stresses are also high, which results in reduction in size of the fiber. Hence, the presence of the applied longitudinal tensile stresses will tend to reduce the magnitude of the effective radial stresses at the fiber/matrix interface. This decrease in the radial stresses due to the increase in applied stress could result in the decrease of  $\tau$  acting along the slip length. Hence,  $\tau$  could decrease with increase in applied stress.

Figure 13 compares the net-section based fiber pressure model proposed by Ghosn et al. [17] with the results from this study. The net-section model predicts bridging stresses which are proportional to the applied stress and independent of  $\Delta v$ . As shown in Fig. 13, the bridging stresses predicted by the fiber pressure models could be significantly different ( $\approx \pm 50\%$ ) from that required to predict the crack opening displacement over a wide range of  $\Delta v$ .

### Bridging Stress Intensity Factor

The results shown in Figures 10-13 highlight the wide range of bridging stresses (magnitude and distribution) predicted by the various fiber bridging models. However, as discussed earlier, most of these models were successfully used by many investigators to predict crack growth versus cycles response in various MMC systems subjected to fatigue loading. One of the important parameters required to predict the fatigue crack growth response is the bridging stress intensity factor range,  $\Delta K_b$ . Using Equations (10)-(13) in conjunction with Equations (2), (3) and (8), the normalized  $\Delta K_b$  ( $=\Delta K_b/\Delta K_a$ ) predicted by the various bridging models was determined and plotted in Figure 14. The results in Figure 14 corresponds to  $\sigma_{a,max}=270$  MPa,  $R=0.1$ ,  $W=19$  mm and  $2a_0/W=0.2$ . The applied stress intensity factor range,  $\Delta K_a$  was calculated using the expressions available [36] in the literature. The values of  $\tau$  used for the shear lag models correspond to those shown in Figures 10-12. We assumed that the bridging stress range distribution is independent of crack length (see Fig. 7 for  $\sigma_{a,max}=270$  MPa) to predict  $\Delta K_b/\Delta K_a$  corresponding to our results. Figure 14 clearly shows that  $\Delta K_b/\Delta K_a$  predicted by the various distinctly different bridging models is almost identical over a wide range of crack lengths. This similarity in the predicted  $\Delta K_b$  confirms the ability of these models to predict the fatigue crack response with similar accuracy.

The important differences in the bridging models are in the assumed values of  $\tau$  (Figs. 10-12) and the predicted fiber bridging stress distribution along the crack. The differences in the predicted  $\Delta \sigma_b$  are highlighted in Figure 15 for the parameters shown in Figure 14 at  $a/a_0 = 2.0$ , i.e.  $2a/W=0.40$ .

This crack length corresponds to  $\Delta K_b/\Delta K_a = 0.75-0.80$  as shown in Figure 14. Two main differences between the model predictions can be seen in Figure 15: (1)  $\Delta\sigma_b$  at the crack tip ranges from 0.0 - 300 MPa, and (2)  $\Delta\sigma_b$  at the machined (EDM) notch tip ranges from 300-550 MPa. Close to the crack tip,  $\Delta\sigma_b$  predicted using the McC model increases rapidly from 0.0 consistent with the results shown in Figure 10. The DS and MS model's prediction is close to that obtained from this study. As expected, the Ghosn et al. model predicts constant  $\Delta\sigma_b$ . The differences in the predicted  $\Delta\sigma_b$  at the machined (EDM) notch tip imply that the magnitude of the fiber stress required to predict the onset of fiber failure will depend on the bridging model. Prediction of the onset of fiber failure is based on comparison of the fiber stresses at the machined notch tip with measured fiber strength. Hence, based on comparison of the stresses at the machined notch tip in Fig. 15, we can conclude that the McC [2] model predicts  $\approx 38\%$  higher fiber stress and Ghosn et al.'s [7] model predicts  $\approx 25\%$  lower fiber stress at the onset of fiber failure.

### Discussion on Deduced $\tau$

The value of  $\tau$  deduced (4.7-20 MPa) in this study compares well with that reported in the literature [9-11,14-18,20-23,25,26], but it is lower than the results generally reported from push-out tests [16-18,20,23]. The effect of fatigue loading has been suggested as a possible reason for the low value of  $\tau$  [14,34]. An important point to be noted is that all models and experiments indicate that the slip length  $\approx 1-2$  mm at room temperature. This implies that the correct value of  $\tau$  can be deduced only if a pull-out type test is conducted on specimens in which the fatigued slip zone is interrogated. In general, such specimens (from within 1-2 mm from the crack surface) are nearly impossible to obtain. Most of the reported data are based on push-out tests using specimen sections that were located at distances  $> 2-5$  mm from the crack surfaces. Hence, the push-out results tend to yield higher values of  $\tau$ . An independent verification of the deduced value of  $\tau$  is possible if the predicted slip length can be compared with slip length measurements. Although, slip length measurements have been reported in the literature [14,18,23], exact measurements are not always possible. Some idea of the slip length could be deduced based on the damage to the fiber coating and/or the reaction products between the fiber and the matrix. The reliability of such measurements has not yet been established.

### Discussion on Deduced Fiber Stresses

During this study, the bridging forces were assumed to act on the crack surface. This assumption could become invalid if large scale sliding occurs between the fiber and the matrix. In this case, as shown by Xia et al. [4], the stress in the fiber located at the end of the unbridged notch could be significantly lower than that predicted assuming small slip lengths. Hence, the actual bridging stresses in the fibers could be lower than that obtained during this study (Figs. 7 and 9). The results shown in Figs. 7 and 9 coupled with Xia et al.'s [4] conclusions imply that the predicted fiber stress at the onset of failure is significantly lower than the values used or deduced in previous investigations, as discussed earlier.

Using shear lag models with zero crack-tip-bridging stress, John et al. [14], and Connell and Zok [21] concluded that the *in situ* fiber strength required to predict the onset of failure is close to the bundle strength instead of the virgin mean strength. The results from this study show that if shear lag models with non-zero crack-tip-bridging stress are used, the fiber strength required to predict the onset of failure will be lower ( $\approx 38\%$  lower) than the bundle strength. The lower *in situ* fiber strength could be attributed to the damage to the fiber/matrix interface during the fatigue loading [34].



## SUMMARY

An optimization routine using the weight function method was used to deduce the fiber bridging stress distribution from the measured crack opening displacement profiles. This procedure was used to determine the bridging stress distribution during fatigue crack growth in a unidirectionally reinforced metal matrix composite (SCS-6/TIMETAL®21S). The bridging stress is non-zero at the crack tip contrary to predictions from conventionally used shear lag models. The bridging stress at the crack tip is proportional to the applied farfield stress. The deduced bridging law is similar to the new shear lag models with non-zero bridging stresses at the crack tip. Any bridging model can be used to predict the crack growth behavior by choosing appropriate values of the frictional shear stress ( $\tau$ ). Consequently, the magnitude of the stresses in the fibers bridging the crack will depend on the fiber bridging model. Hence, the fiber tensile strength required to predict the onset of fiber failure will also depend on the fiber bridging model.

## ACKNOWLEDGMENTS

The research was conducted at the Materials and Manufacturing Directorate, Air Force Research Laboratory (AFRL/MLLN), Wright-Patterson Air Force Base, OH 45433-7817, USA. Dennis Buchanan was supported under an onsite contract number F33615-98-C-5214. The authors gratefully acknowledge the assistance of Mr. A. F. Lackey in conducting the detailed experiments and related technical discussions with Dr. Noel E. Ashbaugh.

## REFERENCES

1. Marshall, D.B., Cox, B.N. and Evans, A.G., "The Mechanics of Matrix Cracking in Brittle-Matrix Fiber Composites," *Acta Materialia*, Vol. 33, No. 11, 1985, pp. 2013-2021.
2. McCartney, L.N., "Mechanics of Matrix Cracking in Brittle-Matrix Fiber-Reinforced Composites," *Proceedings of Royal Society of London*, Vol. A409, 1987, pp. 329-350.
3. Hutchinson, J.W. and Jensen, H.M., "Models of Fiber Debonding and Pullout in Brittle Composites with Friction," *Mechanics of Materials*, Vol. 9, 1990, pp. 139-163.
4. Xia, Z.C., Hutchinson, J.W., Evans, A.G., and Budiansky, B., "On Large Scale Sliding in Fiber-Reinforced Composites," *Journal of the Mechanics and Physics of Solids*, Vol. 42, No. 7, 1994, pp. 1139-1158.
5. Majumdar, B.S., Newaz, G.M. and Rosenfield, A.R., "Yielding Behavior of Ceramic Matrix Composites," *Advances in Fracture Research, Proceedings of the 7th International Conference on Fracture*, Houston, Texas, Vol. 4, 1989, pp. 2805-2814.
6. Danchaivijit, S. and Shetty, D.K., "Matrix Cracking in Ceramic-Matrix Composites," *Journal of the American Ceramic Society*, Vol. 76, No. 10, 1993, pp. 2497-2504.
7. Chiang, Y.-C., Wang, A.S.D., and Chou, T.-W., "On Matrix Cracking in Fiber Reinforced Ceramics," *Journal of the Mechanics and Physics of Solids*, Vol. 41, No. 7, 1993, pp. 1137-1154.
8. Meda, G. and Steif, P.S., "A Detailed Analysis of Cracks Bridged by Fibers – II. Cracks of Intermediate Size," *Journal of the Mechanics and Physics of Solids*, Vol. 42, No. 8, 1994, pp. 1323-1341.
9. McMeeking, R.M. and Evans, A.G., "Matrix Fatigue Cracking in Fiber Composites," *Mechanics of Materials*, Vol. 9, No. 3, 1990, pp. 217-227.
10. John, R., Jira, J.R., Larsen, J.M. and Ashbaugh, N.E., "Analysis of Bridged Fatigue Cracks in Unidirectional SCS-6/Ti-24Al-11Nb Composites," *Fatigue 93*, Engineering Materials Advisory Services Ltd., West Midlands, U. K., Vol. II, 1993, pp. 1091-1096.

11. John, R., Kaldon, S.G. and Ashbaugh, N.E., "Application of Fiber Bridging Models to Describe Fatigue Crack Growth in Unidirectional Titanium Matrix Composites," *Titanium Metal Matrix Composites II*, WL-TR-93-4105, Air Force Research Laboratory, Wright-Patterson AFB, OH 45433, 1993, pp. 270-290.
12. John, R., Stibich, P.R., Johnson, D.A., and Ashbaugh, N.E., "Bridging Fiber Stress Distribution During Fatigue Crack Growth in [0]<sub>4</sub> SCS-6/TIMETAL®21S," *Scripta Materialia*, Vol. 33, 1995, pp. 75-80.
13. Buchanan, D.J., John, R., and Johnson, D.A., "Determination of Crack Bridging Stresses From Crack Opening Displacement Profiles," *International Journal of Fracture*, Vol. 87, No. 2, 1997, pp. 101-117.
14. John, R., Jira, J.R., and Larsen, J.M., "Effect of Stress and Geometry on Fatigue Crack Growth Perpendicular to Fibers in Ti-6Al-4V Reinforced With SiC Fibers," *Composite Materials: Fatigue and Fracture, Seventh Volume, ASTM STP 1330*, R. B. Bucinell, Ed., American Society for Testing and Materials, West Conshohocken, PA, pp. 122-144, 1998.
15. Hutson, A., John, R., and Jira, J.R., "The Effect of Temperature on Fiber/Matrix Interface Sliding in SCS-6/TIMETAL®21S," *Scripta Materialia*, Vol. 40, No. 5, pp. 529-535, 1999.
16. Larsen, J.M., Jira, J.R., John, R., and Ashbaugh, N.E., "Crack-Bridging Effects in Notch Fatigue of SCS-6/TIMETAL®21S Composites Laminates," *Life Prediction Methodology of Titanium Matrix Composites, ASTM STP 1253*, W.S. Johnson, J.M. Larsen and B.N. Cox, Eds., American Society for Testing and Materials, Philadelphia, PA, 1996, pp. 114-136.
17. Ghosn, L.J., Telesman, J., Kantzos, P., "Specimen Geometry Effects on Fiber Bridging in Composites," *Fatigue 93*, Engineering Materials Advisory Services Ltd., West Midlands, U. K., Vol. II, 1993, pp. 1231-1238.
18. Davidson, D.L., "The Micromechanics of Fatigue Crack Growth at 25°C in Ti-6Al-4V Reinforced with SCS-6 Fibers," *Metallurgical Transactions*, Vol. 23A, 1992, pp. 865-879.
19. Cox, B.N. and Marshall, D.B., "The Determination of Crack Bridging Forces," *International Journal of Fracture*, Vol. 49, 1991, pp. 159-176.
20. Zheng, D. and Ghonem, H., "High Temperature/High Frequency Fatigue Crack Growth in Titanium Metal Matrix Composites," *Life Prediction Methodology of Titanium Matrix Composites, ASTM STP 1253*, W.S. Johnson, J.M. Larsen and B.N. Cox, Eds., American Society for Testing and Materials, Philadelphia, PA, 1996, pp. 137-163.
21. Connell, S.J. and Zok, F.W., "Measurement of the Cyclic Bridging Law in a Titanium Matrix Composite and It's Application to Simulating Crack Growth," *Acta Materialia*, Vol. 45, 1997, pp. 5203-5211.
22. Cardona, D.C., Barney, C., and Bowen, P., "Micromodelling of Effective Stress Intensities For Bridged Cracks in Fibre Reinforced Titanium Metal Matrix Composites," *Composites*, Vol. 24, 1993, pp. 122-128.
23. Bakuckas, J.G. and Johnson, W.S., "A Methodology to Predict Damage Initiation, Damage Growth, and Residual Strength in Titanium Matrix Composites," *Life Prediction Methodology of Titanium Matrix Composites, ASTM STP 1253*, W.S. Johnson, J.M. Larsen and B.N. Cox, Eds., American Society for Testing and Materials, Philadelphia, PA, 1996, pp. 497-519.
24. Cox, B.N., "Life Prediction for Bridged Fatigue Cracks," *Life Prediction Methodology of Titanium Matrix Composites, ASTM STP 1253*, W.S. Johnson, J.M. Larsen and B.N. Cox, Eds., American Society for Testing and Materials, Philadelphia, PA, 1996, pp. 552-572.
25. Warriar, S.G., and Majumdar, B.S., "Effects of Interface on the Fatigue Crack Growth Response of Titanium Matrix Composites: Modeling and Impact on Interface Design," *Materials Science & Engineering A*, Vol. 237, 1997, pp. 256-267.

26. Hermann, D.J. and Hillberry B.M., "A New Approach to the Analysis of Unidirectional Titanium Matrix Composites With Bridged and Unbridged Cracks," *Engineering Fracture Mechanics*, Vol. 56, No. 5, 1997, pp. 711-726.
27. Rödel, J., Kelly, J.F. and Lawn, B.R., "In Situ Measurements of Bridged Crack Interfaces in the Scanning Electron Microscope," *Journal of the American Ceramic Society*, Vol. 73, 1990, pp. 3313-3318.
28. Fett, T., Munz, D., Seidel, J., Stech, M., and Rödel, J., "Correlation between Long and Short Crack R-Curves in Alumina Using the Crack Opening Displacement and Fracture Mechanical Weight Function Approach," *Journal of the American Ceramic Society*, Vol. 79, 1996, pp. 1189-1196.
29. Guo, Z.K., Kobayashi, A.S. and Hawkins, N.M., "Further Studies on Fracture Process Zone for Mode I Concrete Fracture," *Engineering Fracture Mechanics*, Vol. 46, 1993, pp. 1041-1049.
30. Hay, J.C. and White, K.W., "Grain Boundary Phases and Wake Zone Characterization in Monolithic Alumina," *Journal of the American Ceramic Society*, Vol. 78, 1995, pp. 1849-1854.
31. Hartman, G.A. and Nicholas, T., "An Enhanced Laser Interferometer for Precise Displacement Measurements," *Experimental Techniques*, Vol. 2, No. 2, 1987, 24-26.
32. Sharpe, W.N., Jira, J.R., and Larsen, J.M., "Real-Time Measurements of Small-Crack Opening Behavior Using an Interferometric Strain/Displacement Gage," *Small-Crack Test Methods, ASTM STP 1149*, J. Larsen and J. Allison, Eds., American Society for Testing and Materials, West Conshohocken, Philadelphia, PA, 1992, pp. 92-115.
33. IMSL, Problem-Solving Software Systems, User's Manual, Math/Library Version 2.0, Houston, TX, USA, 1996.
34. Kantzos, P., Eldridge, J., Koss, D.A., and Ghosn, L.J., "The Effect of Fatigue Loading on the Interfacial Shear Properties of SCS-6/Ti-Based MMCs," *Intermetallic Composites II*, D.B. Miracle, D.L. Anton, and J.A. Graves, Eds., MRS Proceedings, Pittsburgh, PA, Vol. 273, 1992, pp. 135-142.
35. Buchanan, D.J., Ashbaugh, N.E., Rosenberger, A.H., "Damage and Deformation Prediction of [0] Titanium Matrix Composites Under Fatigue-Dwell Loading," To be submitted for publication, 1999.
36. Tada, H., Paris, P.C., and Irwin, G.R., The Stress Analysis of Cracks Handbook, Paris Productions Inc., St. Louis, MO, 1985.

**Table I. Specimen Dimensions and Material Properties.**

Specimen ID	Width, W (mm)	Thickness, B (mm)	Initial Crack Length, $a_0$ (mm)	$V_f$ *	Composite Modulus, $E_c$ ** (GPa)	Orthotropic Modulus, $E_o$ (GPa)
93411	18.96	0.95	1.90	0.339	209	179
93413	18.90	0.97	2.08	0.332	207	178

Note \* Calculated based on specimen thickness, fiber spacing and fiber diameter.

\*\* Calculated using rule of mixtures,  $E_c = E_f V_f + E_m (1 - V_f)$

**Table II. Coefficients  $A_0$ ,  $A_1$ , and  $A_2$  for Bridging Stress Distributions Deduced from COD Measured During Crack Growth.**

Specimen ID	Maximum Stress, $\sigma_{a,max}$ (MPa)	Stress Ratio, R	Crack Length to Width Ratio, $2a/W$	$A_0$ (MPa)	$A_1$ (MPa)	$A_2$ (MPa)
93411	270	0.1	0.38	188.8	128.4	93.7
		0.1	0.62	171.8	208.1	14.4
		0.1	0.73	170.8	138.7	92.7
93413	175	0.1	0.42	131.0	15.5	201.4
	190	0.1	0.46	100.7	52.1	234.7
	218	0.1	0.58	133.0	40.9	222.5

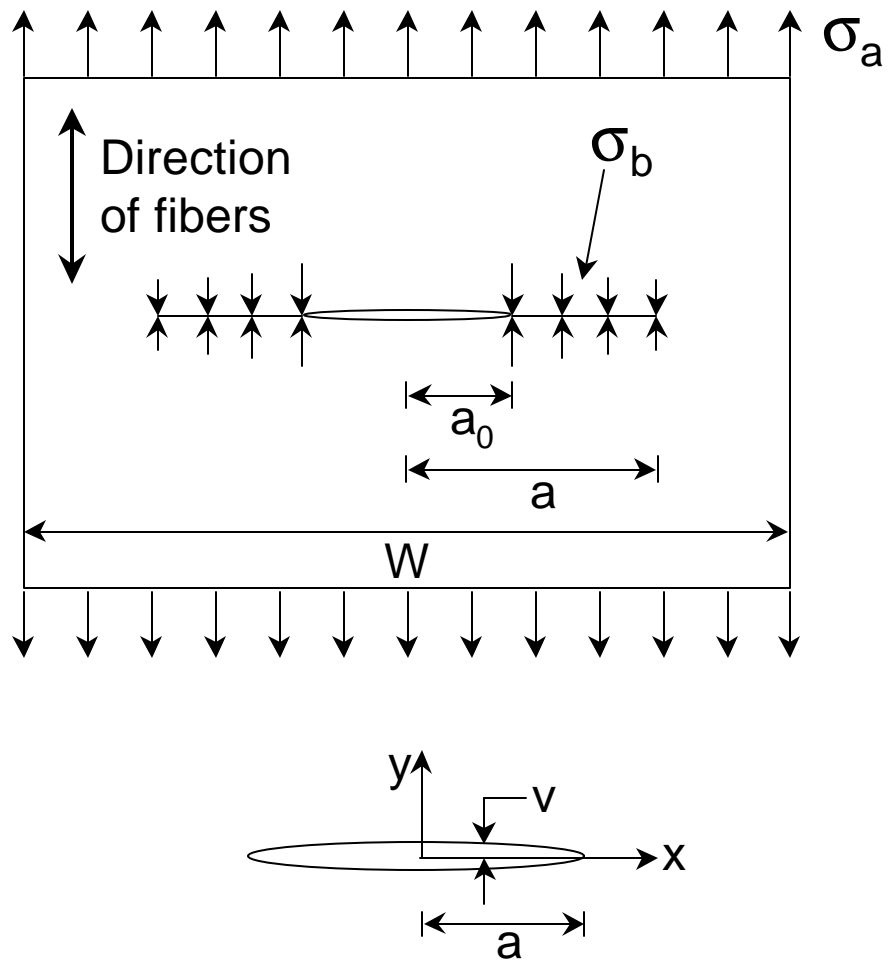


Figure 1. Schematic of fiber bridged crack growth in a unidirectional reinforced composite.

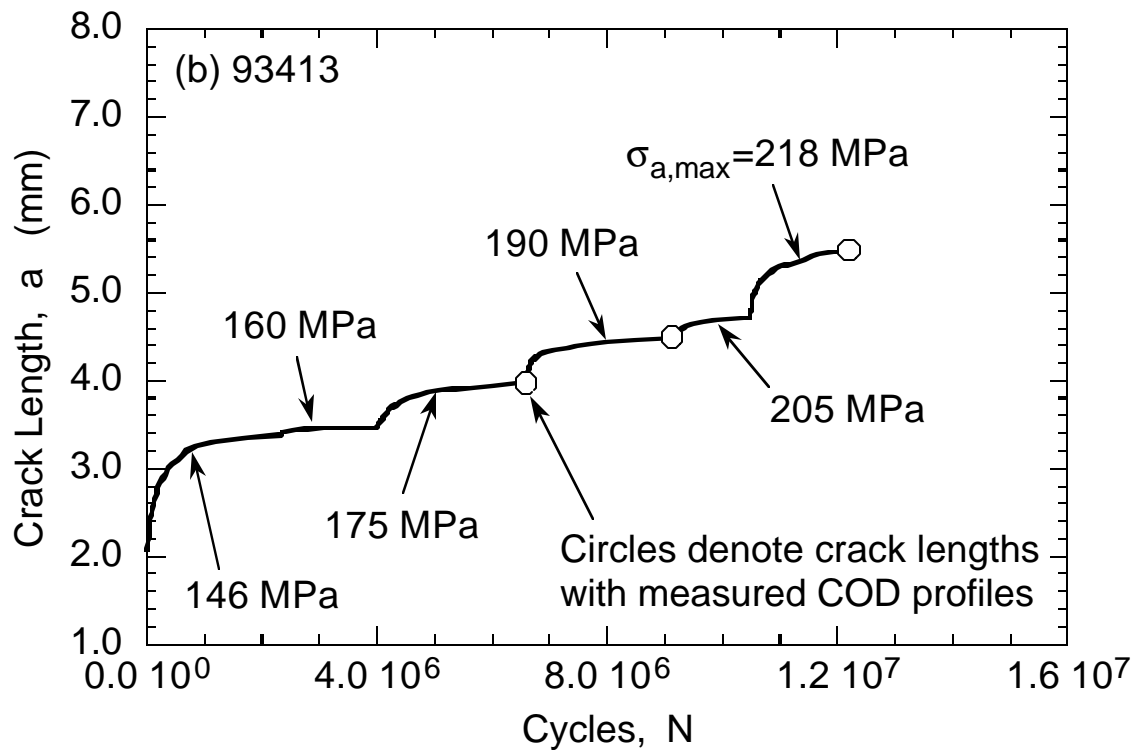
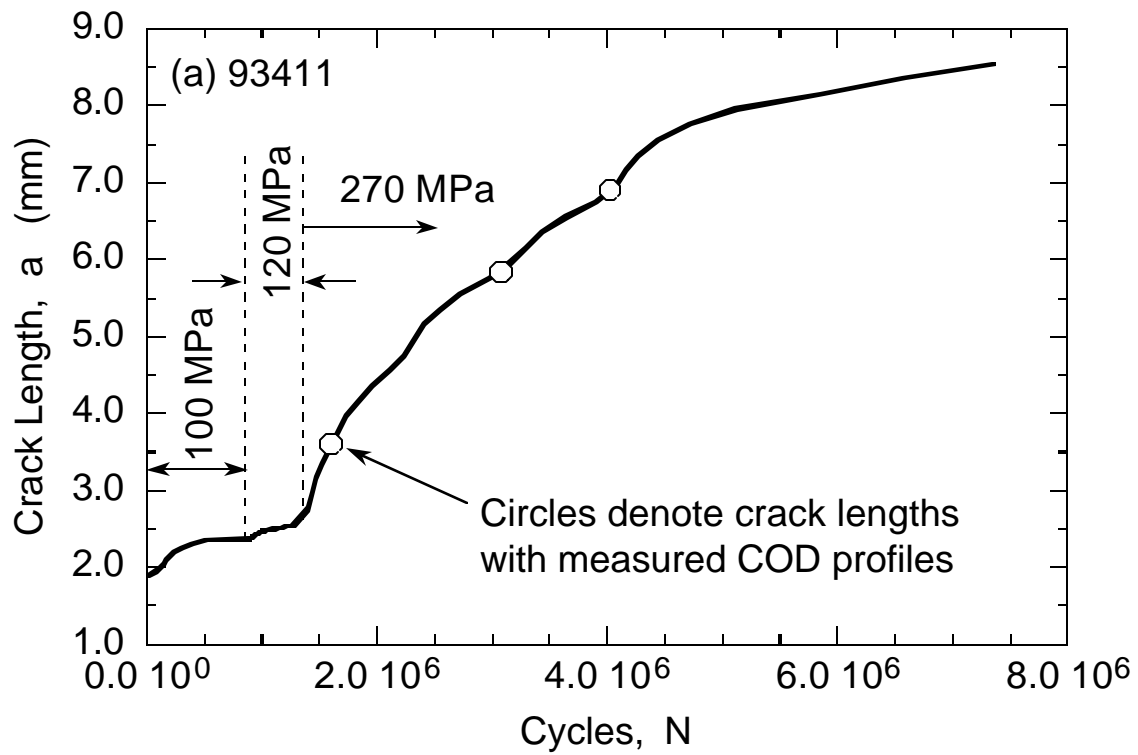


Figure 2. Crack length versus cycles response for [0]<sub>4</sub> SCS-6/TIMETAL®21S tested at room temperature. (a) Specimen: 93411 & (b) Specimen: 93413.

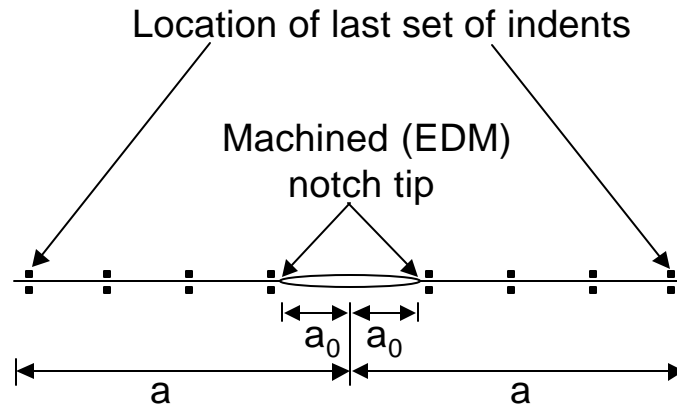


Figure 3. Schematic of COD locations during crack growth in SCS-6/TIMETAL®21S.

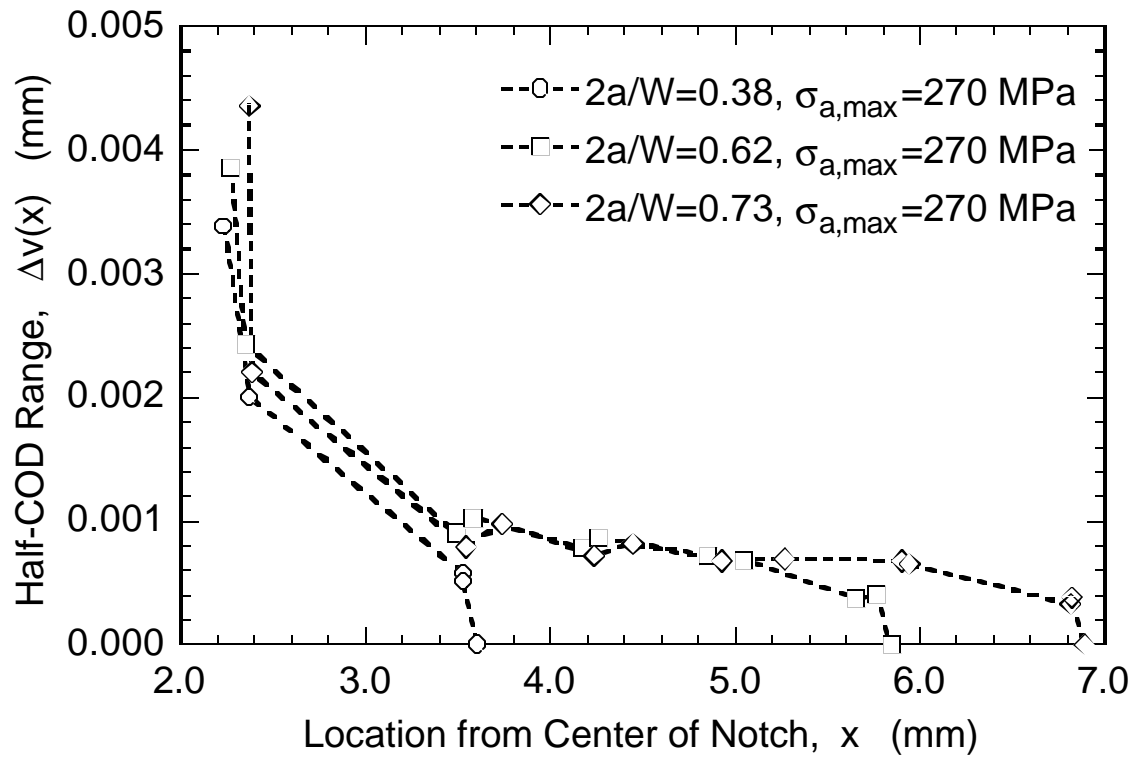


Figure 4. Half-COD range as a function of location for 3 crack lengths for the specimen tested at  $\sigma_{a,max}=270$  MPa with  $R=0.1$ . Specimen ID: 93411.

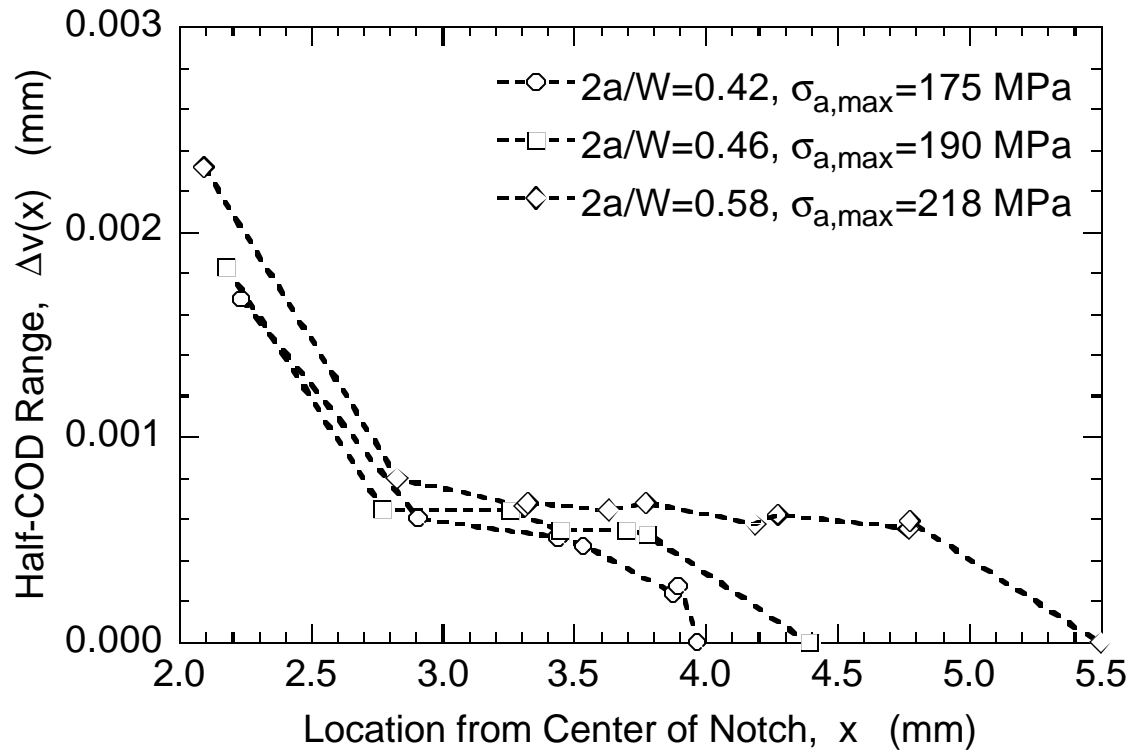


Figure 5. Half-COD range as a function of location for 3 crack lengths for the specimen tested at  $\sigma_{a,max}=175, 190$  &  $218 \text{ MPa}$  with  $R=0.1$ . Specimen ID: 93413.



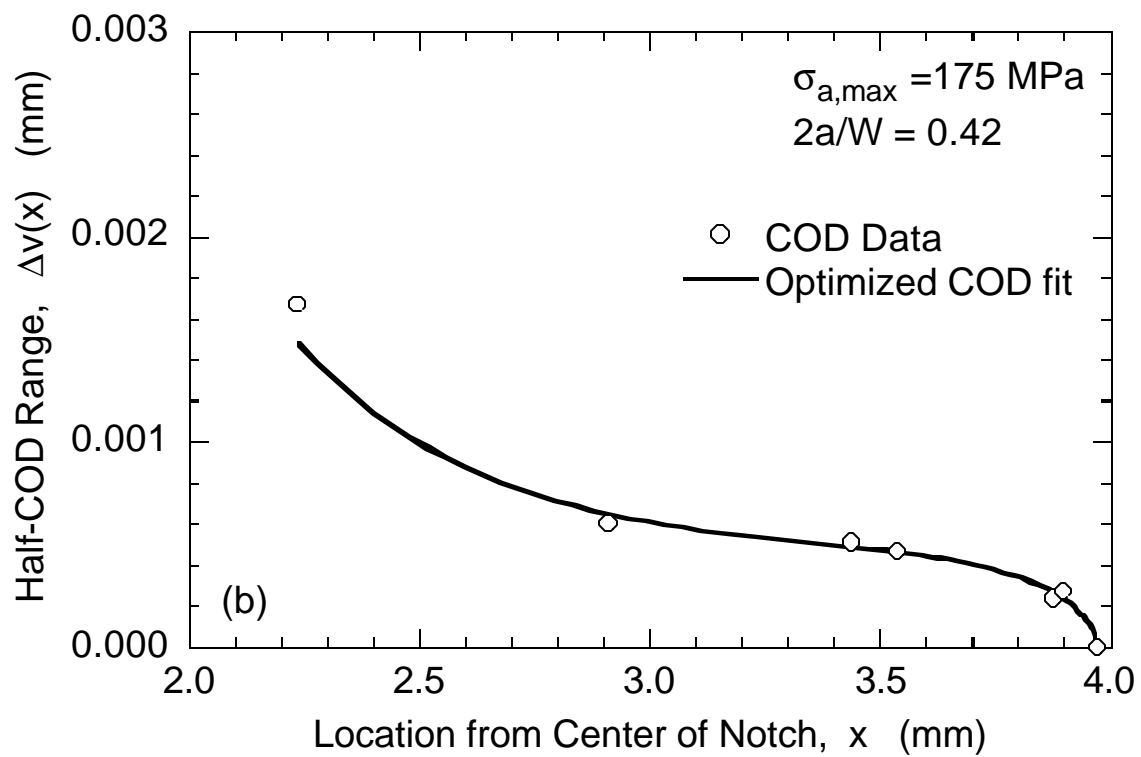
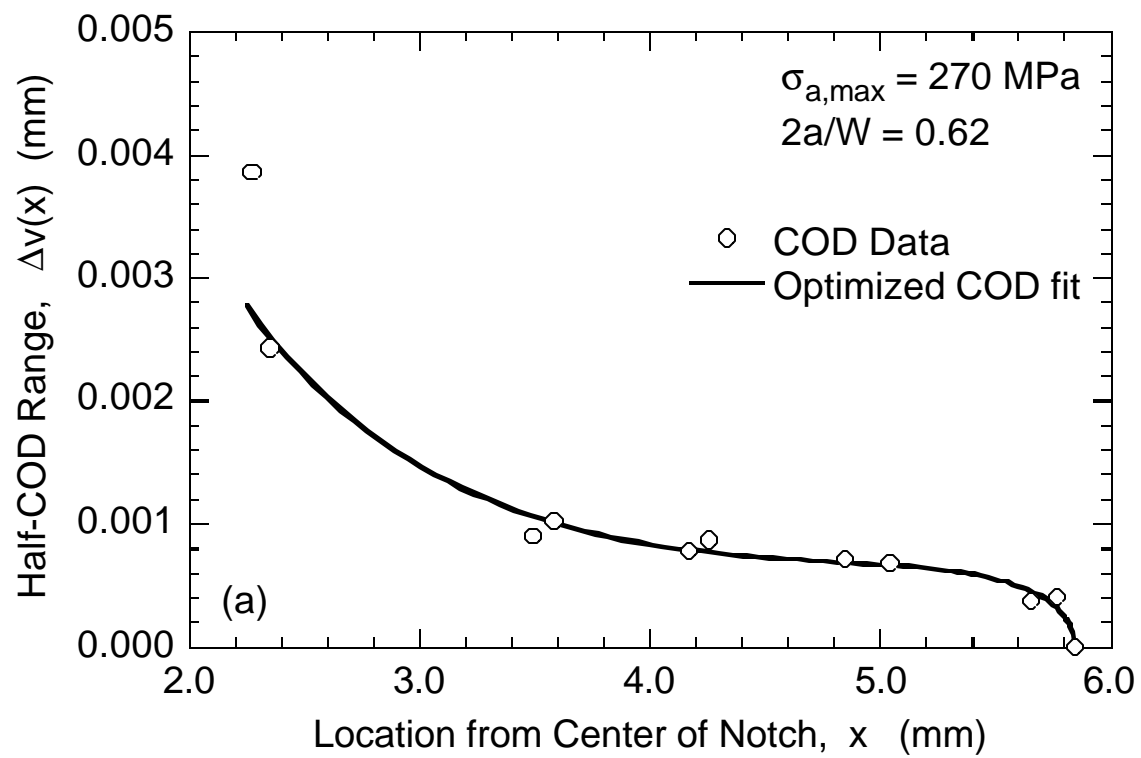


Figure 6. Comparison of optimized half-COD profile and measured half-COD Data. (a) Specimen 93411 (b) Specimen 93413.

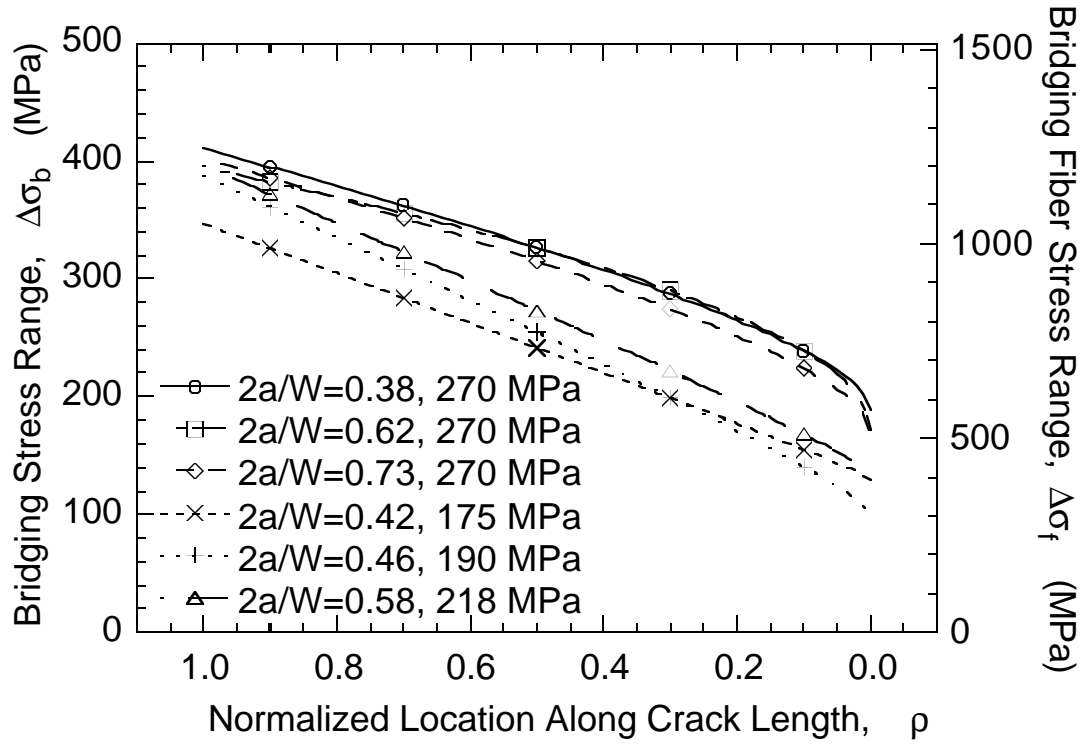


Figure 7. Deduced bridging stress distribution in  $[0]_8$  SCS-6/TIMETAL®21S plotted as function of normalized location along crack length. Note that  $\rho = 0$  corresponds to the crack tip and  $\rho = 1$  to the initial machined notch tip.

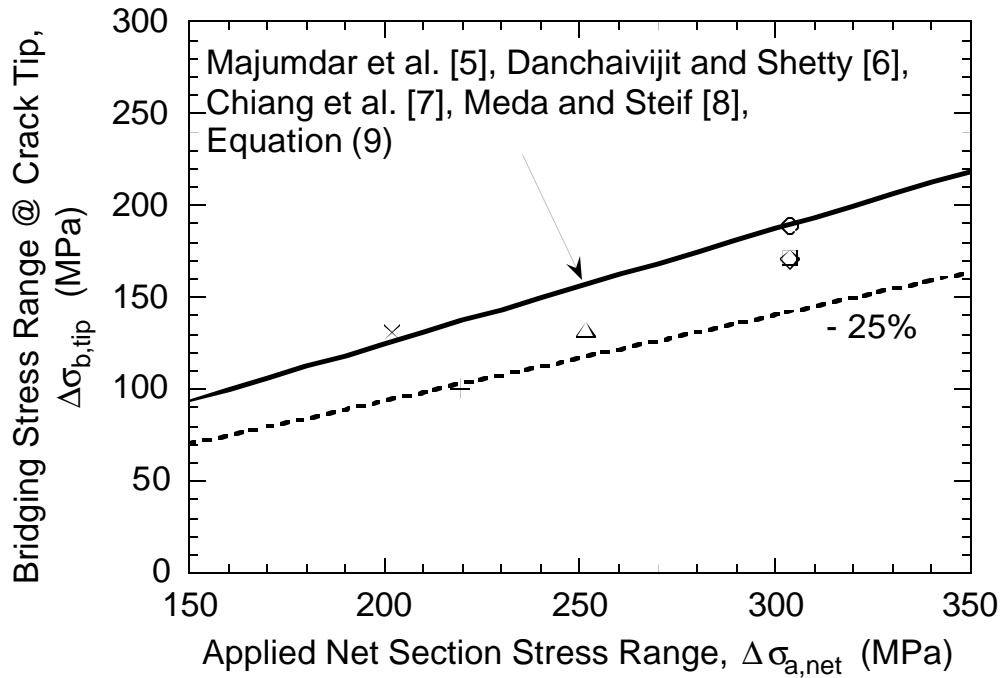


Figure 8. Bridging stress range at the crack tip as a function of the applied stress. Symbols correspond to the data shown in Figure 7.

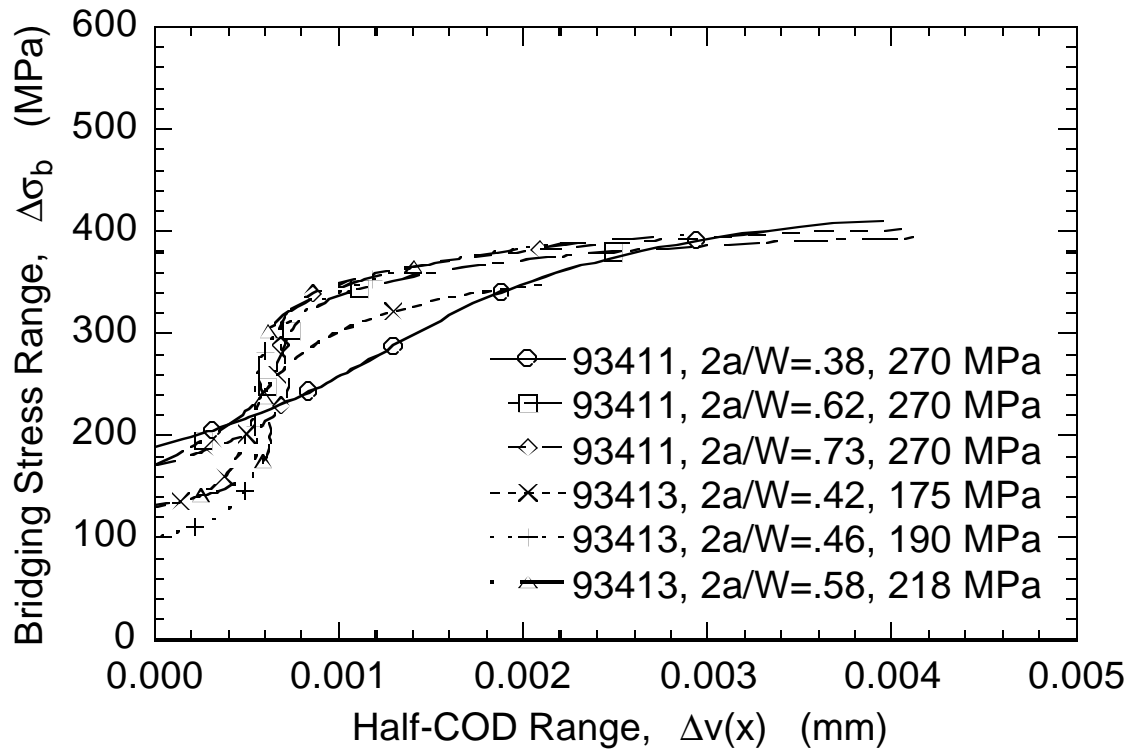


Figure 9. Deduced relationship between bridging stress range,  $\Delta\sigma_b$  and half-crack opening displacement range,  $\Delta v$ .

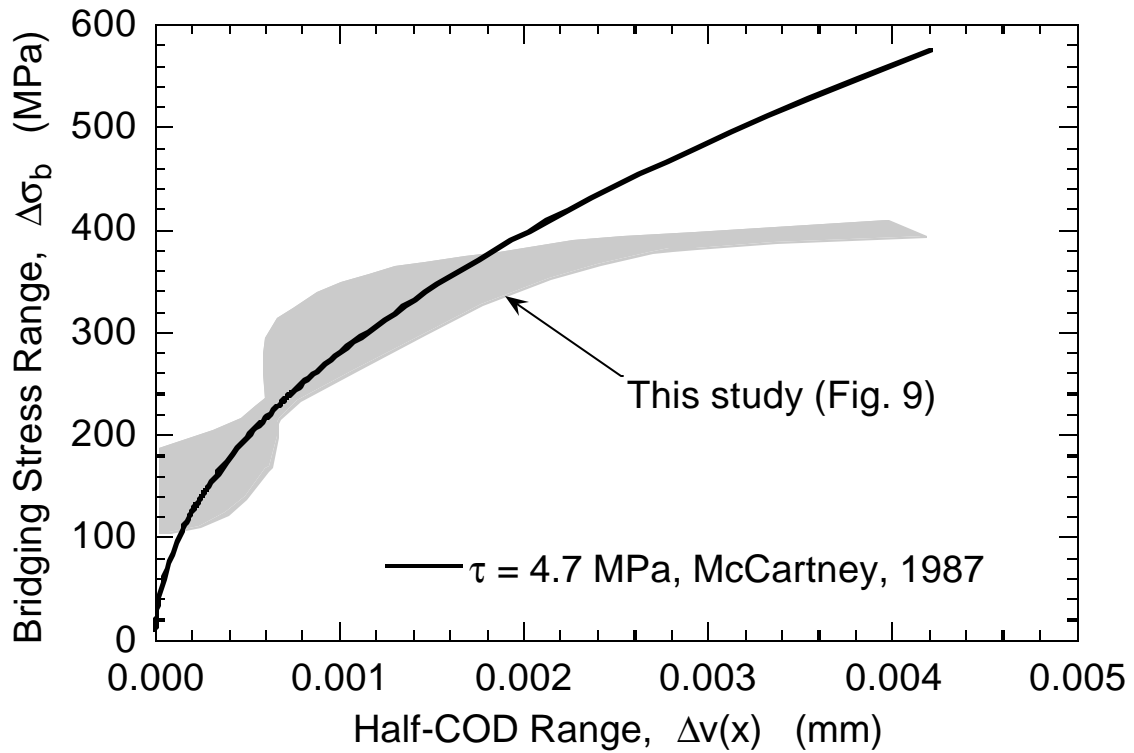


Figure 10. Comparison of deduced bridging law with the shear lag model by McCartney (1987).

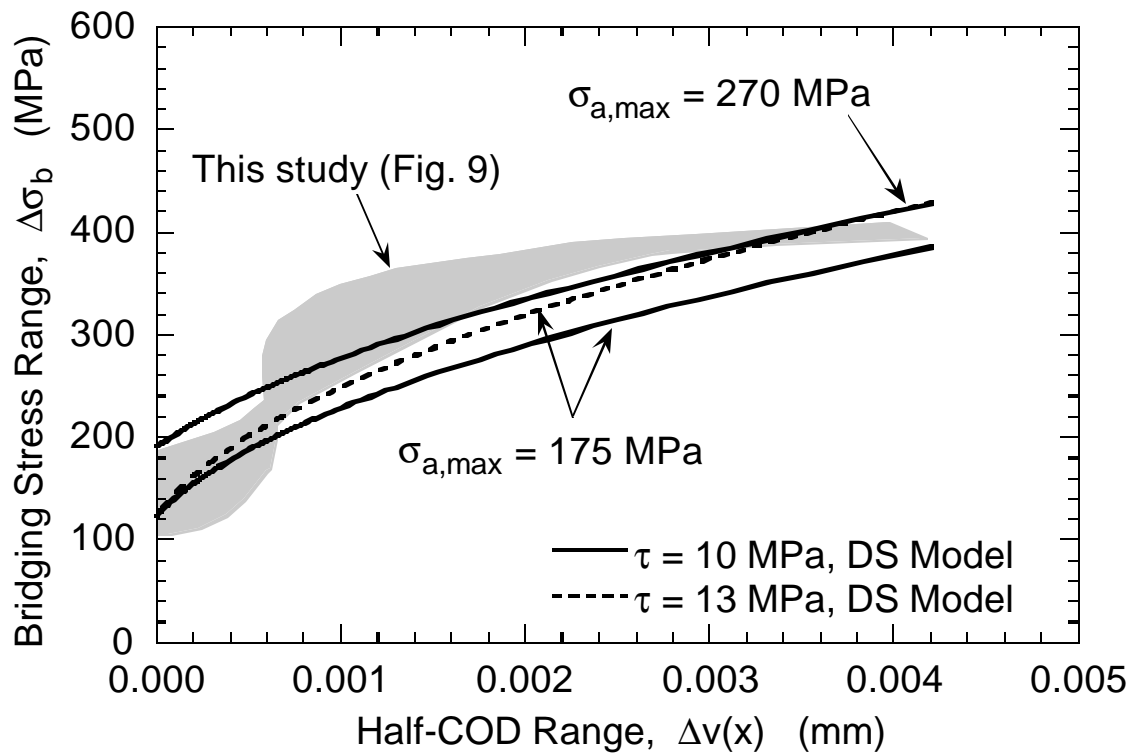


Figure 11. Comparison of deduced bridging stress distribution with the shear lag model by Danchaivijit and Shetty (1993).

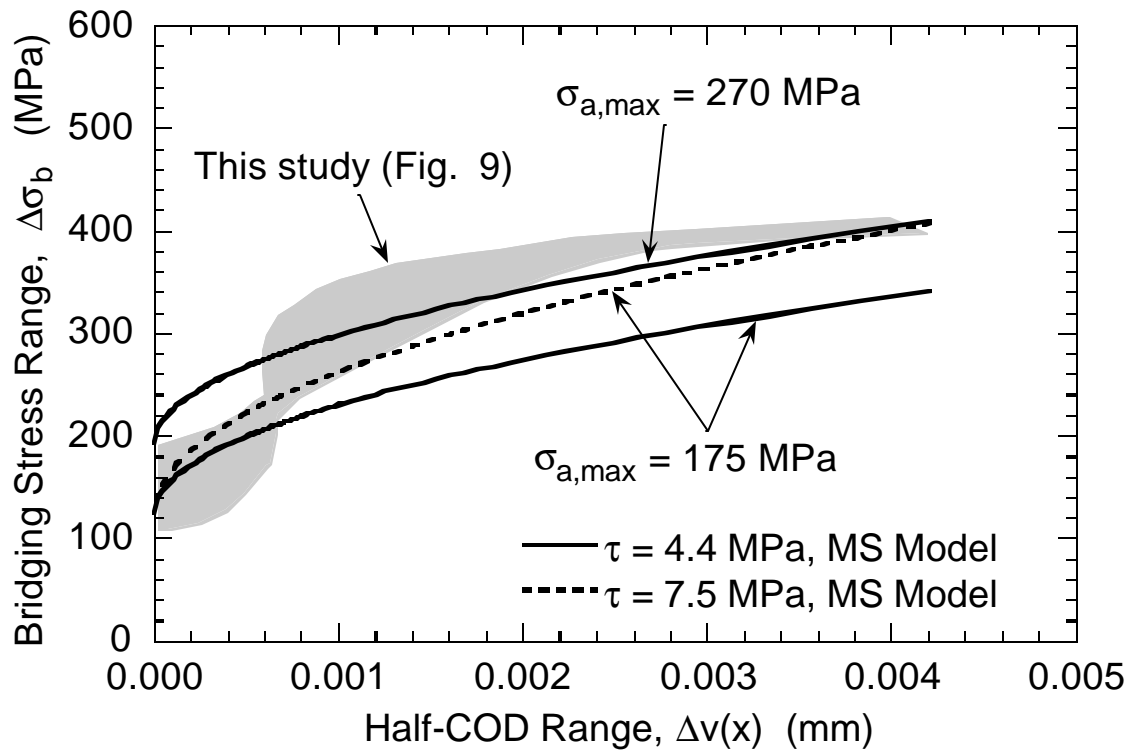


Figure 12. Comparison of deduced bridging stress distribution with the shear lag model by Meda and Steif (1994).

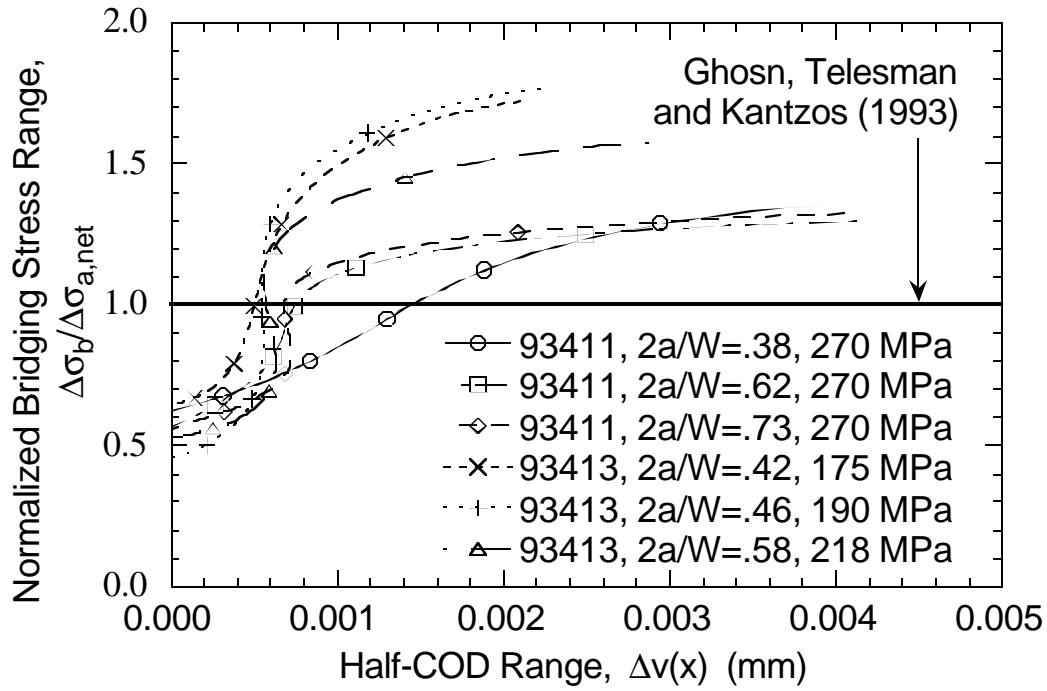


Figure 13. Comparison of deduced bridging stress distribution with the net-section (fiber pressure) model by Ghosn, Telesman and Kantzos (1993).

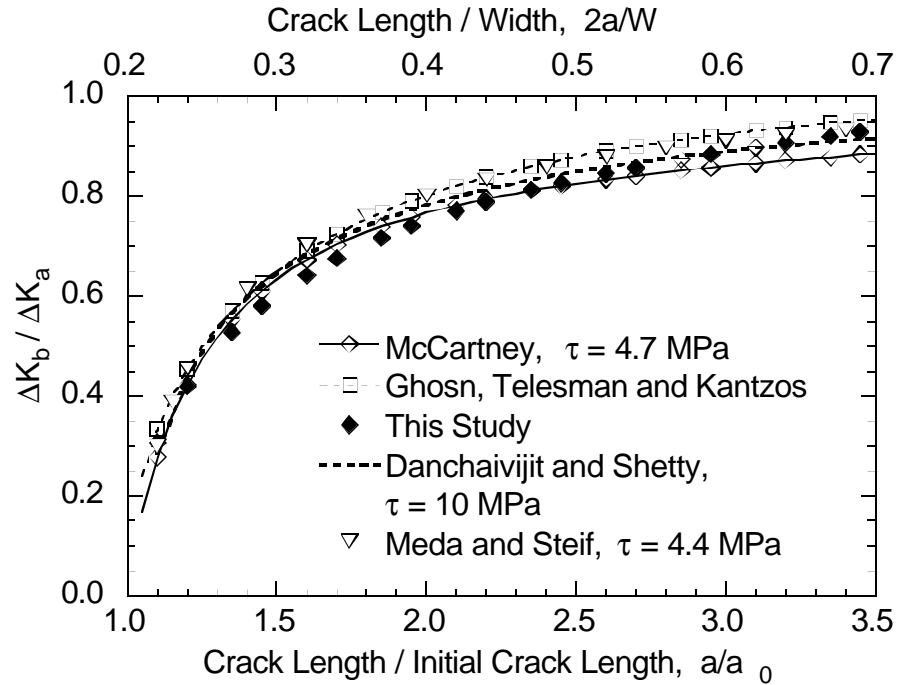


Figure 14. Predicted normalized bridging stress intensity factor range ( $\Delta K_b/\Delta K_a$ ) as a function crack growth from an unbridged flaw. ( $\sigma_a=270$  MPa,  $R=0.1$ ,  $2a_0/W=0.2$  and  $W=19.0$  mm)

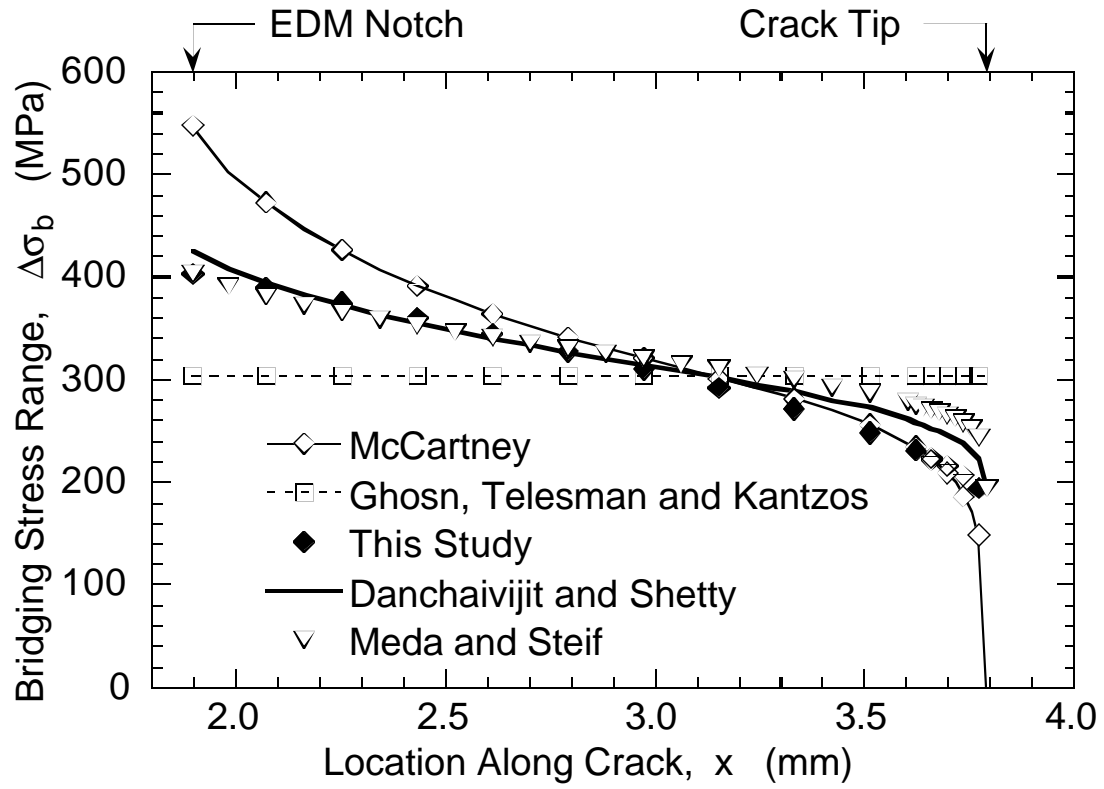


Figure 15. Comparison of predicted bridging stress distribution along the crack for the specimen tested at  $\sigma_{a,max}=270$  MPa corresponding to  $2a/W=0.40$ , i.e.  $a/a_0=2$  and  $\Delta K_b/\Delta K_a = 0.75-0.80$ .

# **Effect of Flat-on-Flat Contact Fretting Fatigue on the Fatigue Life of Ti-6Al-4V**

Mrs. Alisha Hutson\*

Advanced Materials Characterization Group, Structural Integrity Division  
University of Dayton Research Institute, Dayton, OH 45469-0128, USA.

Dr. Ted Nicholas

Air Force Research Laboratory (AFRL/MLLN), Materials & Manufacturing Directorate; Wright-Patterson Air Force Base, OH 45433-7817, USA.

## **Introduction**

Fretting fatigue damage is caused by localized recurring relative motion in the contact region between two components under load, and can result in premature crack initiation and failure. Such damage has been indicated as the cause of many premature disk and blade failures in turbine engines and, as a result, has been the focus of numerous studies over the years [1-9]. The applicability of the results of many of these studies is questionable because the geometries studied are not always directly comparable to the actual hardware. Turbine engine blade roots, and the companion component region on the disks, experience fretting in a flat-on-flat contact with rather large radii at the edges of contact. Most research, on the other hand, has been conducted on cylinder-on-flat, punch-on-flat, or Hertzian (ball-on-flat) geometries because of the availability of closed form analytical solutions for the resulting stress distributions. While analytical solutions allow the researcher to correlate test results and ultimately predict laboratory behavior, only limited progress has been made in the development of accurate life prediction models for complex components based on the results of these efforts [10]. The experimental observations and modeling of a more representative geometry are required to develop a life prediction model that bridges the gap between laboratory and service conditions.

The following summarizes work to date on two separate studies: an evaluation of fretting fatigue damage on fatigue life, and the investigation of the effect of Cu-Ni coating on fretting fatigue behavior. Both studies are designed to answer questions specific to the dovetail blade attachment geometry found in gas turbine engines. In addition to acquiring data on fatigue life and fatigue limits, SEM inspection of fretted and fracture surfaces was used to qualitatively analyze fretting damage and to evaluate failure mechanisms.

## **Testing Apparatus**

The fretting experiment used in both studies was designed to closely simulate the primary loading conditions under which fretting fatigue damage occurs in turbine engine blade attachment areas. The geometry in the test apparatus employed flat fretting pads, with a radius at the edge of contact, against a flat specimen under axial fatigue, as in Figure 1. The test system used to conduct fretting fatigue tests imposed a static normal load via instrumented bolts, whose internal strain gages allowed for quantification of the normal load. Axial loads were applied via an electromagnetic shaker system. Removable fretting pads facilitated control of the surface conditions. The test configuration, which employs identical gripping at both ends of the specimen, produced two nominally identical fretting fatigue tests per specimen. Fretting damage occurred at both ends of the specimen at the edges of contact, shown in the magnified view in Figure 1. Additional details on the test apparatus can be found in [11].

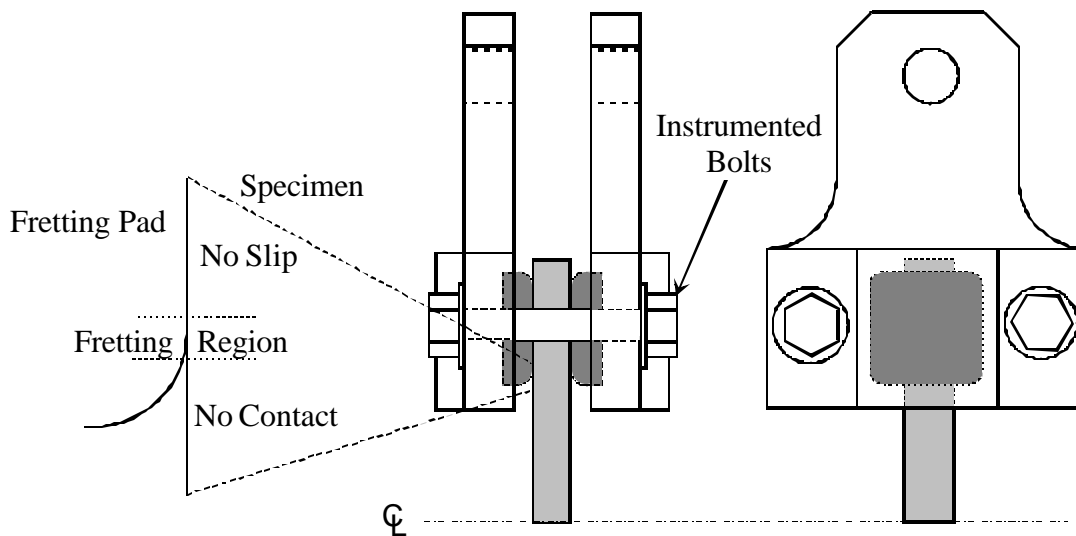


Figure 1. Schematic of the fretting fatigue gripping system and location of fretting damage.

All tests were conducted at constant frequency of either 300 or 400 Hz in lab air at room temperature. Two Ti-6Al-4V microstructures have been tested to date. Bar stock, which refers to a vacuum annealed and stress relieved microstructure, and plate stock, which refers to the forged AMS4928 microstructure with TE01 heat treatment that has been used for the bulk of the High Cycle Fatigue Program testing. The usage for each material is summarized in Table 1. All specimens and fretting pads were low stress ground to an # 8 surface finish.

	Axial specimens ( 1 per test)	Fretting Pads (4 per test)
<b>Baseline [11]</b>	bar stock	bar stock
<b>Cu-Ni coating study</b>	plate stock	plate stock
<b>Fretting Fatigue Damage Effects study</b>	bar stock	plate stock

Table 1. Material allocation summary.

### Effect of Fretting Fatigue Damage on Fatigue Life

The purposes of this study were to evaluate the effect of prior fretting fatigue damage on fatigue strength, to analyze fretting fatigue damage using optical and SEM techniques, and to identify fretting fatigue failure mechanisms. Baseline data [11] are presented here to assist the reader in understanding the basis for selection of the current test conditions.

In the baseline study of fretting fatigue parameters, a range of shear forces (proportional to the axial stress in the specimen), and the resultant shear stress distribution was achieved by varying contact length and contact radius using a range of pad geometries, and by varying the normal contact load. Baseline data for two stress ratios are presented in Figure 2 for eight test conditions produced through selection of two each of the aforementioned parameters. Nominal contact lengths were 25.4 mm and 12.7 mm; static normal loads were 35 kN and 21 kN; and contact radii were 3.2 mm and 0.4 mm. All baseline tests were conducted using the step loading approach developed by Maxwell & Nicholas [12]. The results, summarized in Figure 2, show that for a given condition of contact radius and applied stress ratio, the axial stress in the specimen corresponding to fatigue life of  $10^7$  cycles is relatively independent of normal stress. Therefore, for the current study, two normal stresses, 140 MPa and 420 MPa, were selected assuming that changes in normal stress would not produce changes



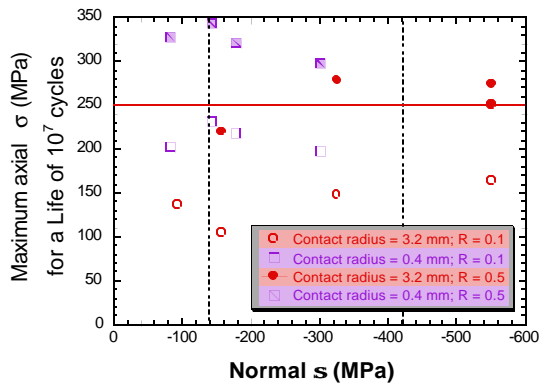


Figure 2. Summary of baseline test results [11] and test conditions for fretting fatigue damage effect study.

$10^5$ , and  $10^6$  cycles, which correspond to 0.1, 1.0, and 10 percent of the  $10^7$  cycle life, respectively. Three samples were tested for each normal stress and damage level, resulting in a total of eighteen samples tested, as summarized in Table 2. After applying the desired amount of fretting fatigue damage, each sample was removed from the test machine and inspected. Following the inspection, one end was cut off to yield one 100mm and one 50 mm piece per sample. The long end was sent to have a reduced section machined for subsequent fatigue testing [Figure 3]. The short end was retained for characterization of fretting damage via SEM and metallographic techniques. Inspection of the fretted surfaces from all of the tests indicated very low levels of damage. Even with 1 million cycles applied, corresponding to 10 percent of the estimated life, and a high value of normal stress of 420 MPa, the fretting damage on the surface was nearly indistinguishable from the machined surface [Figure 4a]. A similar observation can be made for the sample with the lower normal stress of 140 MPa [Figure 4b].

in the resulting maximum stress for a life of  $10^7$  cycles. These stresses represent values which are typical of the upper and lower limit of normal stresses observed in some fan blade dovetail attachments, and are shown in Figure 2 by dashed vertical lines. The two contact lengths from the baseline study and a single normal load of 26 kN were used to obtain the normal stresses desired. A contact radius of 3.2 mm, and a stress ratio of 0.5 were chosen because of the similarity to dovetail geometry and loading conditions, respectively. The average of the baseline maximum stress results at this condition was 250 MPa, shown by the solid horizontal line in Figure 2. Three levels of damage were investigated:  $10^4$ ,

Cycles of Fretting	140 MPa Normal stress	420 MPa Normal stress
10,000	3 test @ $R=0.5$	3 test @ $R=0.5$
100,000	3 test @ $R=0.5$	3 test @ $R=0.5$
1,000,000	3 test @ $R=0.5$	3 test @ $R=0.5$
total	9 tests	9 tests

Table 2. Test matrix for fretting fatigue damage effect study.

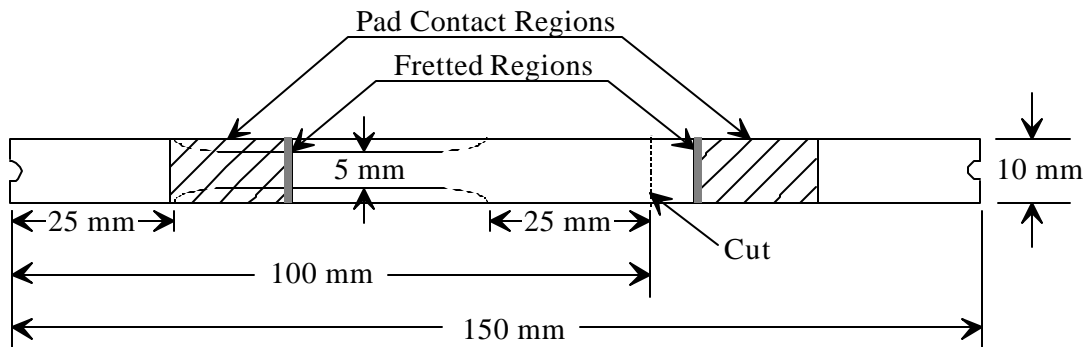


Figure 3. Machining schematic for samples subjected to prior fretting fatigue damage.

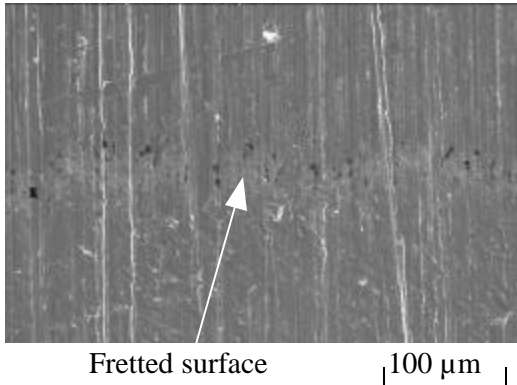


Figure 4a. Horizontal fretting scar at 10% damage level for 420 MPa normal stress. Fatigue loading axis is vertical.

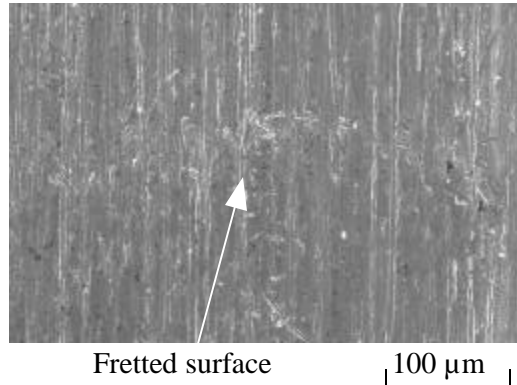


Figure 4b. Horizontal fretting scar at 10% damage level for 140 MPa normal stress. Fatigue loading axis is vertical.

The apparently benign nature of the fretting fatigue damage prompted the decision to reduce the gage section of specimens before subjecting them to residual uniaxial fatigue strength testing. Specimens at the 10% damage level were tested first, because if there were no reduction in life observed at the higher levels of damage, one could assume no reduction in life at lower levels of damage. The three samples for which results are reported were subjected to 140 MPa normal stress, indicated by gray shading in Table 2. The first sample was block loaded at a stress ratio of 0.5. The initial stress was selected assuming little or no damage to the specimen due to fretting, based on observations of the fretted surface. The resulting Haigh stress is shown in Figure 5 compared with baseline data from Maxwell and Nicholas [12]. While failure did occur at the line of fretting damage, there is no apparent reduction in fatigue properties of the fretted material.

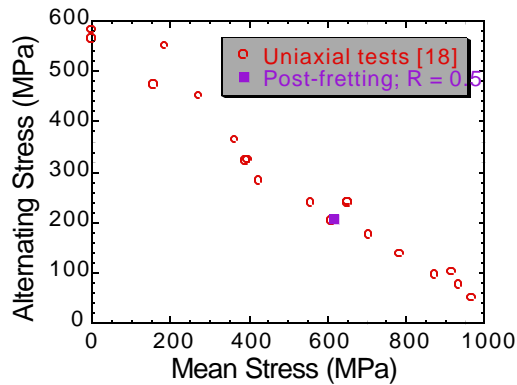


Figure 5. Residual fatigue strength under step loading for 10% damage level at 140 MPa normal stress.

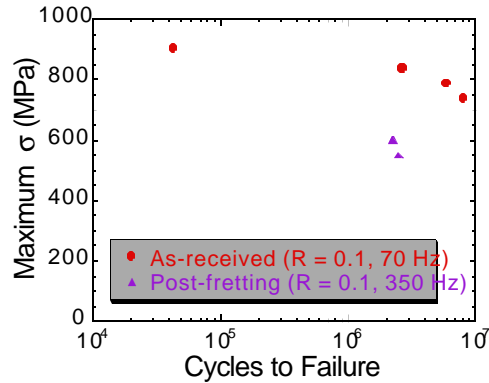


Figure 6. Residual fatigue strength under constant stress for 10% damage level at 140 MPa normal stress.

The next two samples were fatigue tested under uniaxial conditions at  $R = 0.1$ . Both samples suffered a reduction in fatigue stress of approximately twenty percent; however, they failed five to ten millimeters away from the pad contact area. The resulting S-N data are presented in Figure 6. The data to which the results are compared was collected at 70 Hz, but little difference has been observed in tests under identical conditions @ 70 Hz & 350 Hz [12]. SEM characterization of the fracture surfaces indicated anomalies in the material at the crack nucleation site that seem to be the source of the premature failures. Both of the photos in Figure 7 came from a single specimen, but similar features were observed on the fracture surfaces from both of the prematurely failed specimens. While fractography cannot identify the source of this feature with certainty, it's

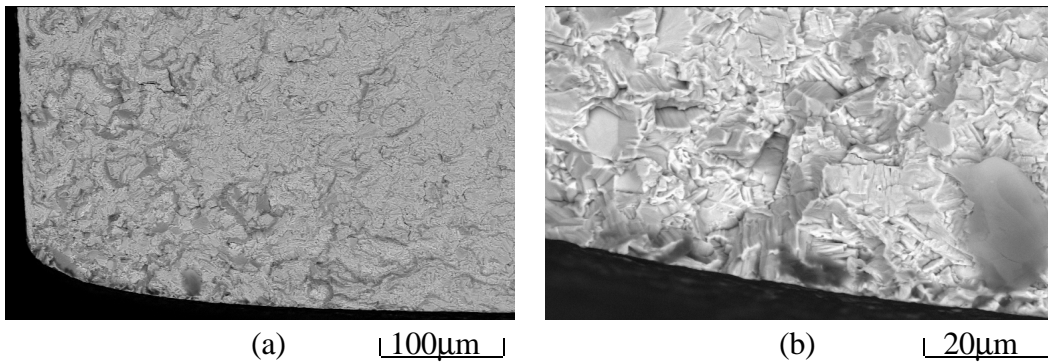


Figure 7. Fractographs of material inhomogeneity located at crack nucleation sit of a specimen showing a reduction in fatigue strength unrelated to fretting damage.

appearance indicates an inhomogeneity consisting of linked pathways of primary alpha phase. This hypothesis will be confirmed by sectioning one of these specimens near the anomaly to characterize the grain structure.

The results to date for this study are largely inconclusive; however, residual fatigue strength test results indicate no measurable reduction in axial fatigue strength due to fretting fatigue under a static normal stress of 140 MPa. Further testing is required to verify this conclusion, since a single valid datum is statistically meaningless. In any case, the levels of damage observed optically were very clear: fretting damage accumulated to 10 percent of fretting fatigue life was nearly indistinguishable from the machined surface.

#### Effect of Cu-Ni Coating on Fretting Fatigue Life

The purpose of this investigation was to determine the effect of contact material on fretting fatigue strength, the effect of accumulated cycles on coating integrity, and the effect of surface roughness on fretting fatigue strength. The first set of tests allowed comparison of resultant fretting fatigue strengths for specimens tested against uncoated Ti-6Al-4V pads and Cu-Ni plasma spray coated Ti-6Al-4V pads. The second set of tests was designed to provide information on the integrity of the Cu-Ni coating when used for several tests. To achieve this goal, five different specimens were tested in succession against a single set of Cu-Ni coated pads. A similar was run with uncoated pads to provide a comparison of later tests in the series. Finally, it was observed that the surface of the coated pads was rougher than the uncoated pads. Thus a few tests were conducted using rougher uncoated fretting pads, to determine the effect of surface roughness on the fretting fatigue strength. The rougher pads were grit-blasted and stress relieved to approximate the roughness achieved with the plasma spray coating technique.

<u>Pad Type</u>				
		<b>As-received</b> (#8 finish)	<b>Cu-Ni coated</b> (~#64 finish)	<b>Roughened</b> (~#64 finish)
<u>Test Type</u>	<b>Baseline (step loaded)</b>	2 (1 complete)	1 (complete)	_____
	<b>"Series of 5" (S-N)</b>	2 (1 complete)	1 (complete)	1 (in progress)
	<b>S-N</b>	6 (1 complete)	1	1

Table 3. Test matrix for the Cu-Ni coating study.

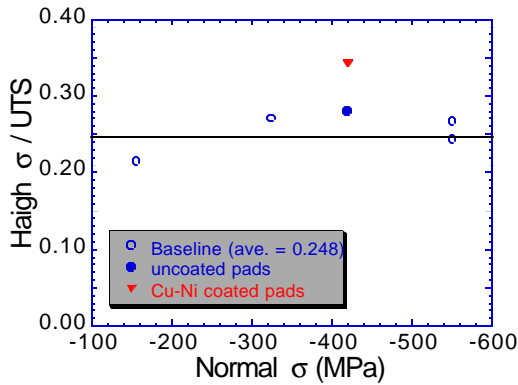


Figure 8. Comparison of normalized Haigh stresses from specimens tested against as-received uncoated and Cu-Ni coated pads.

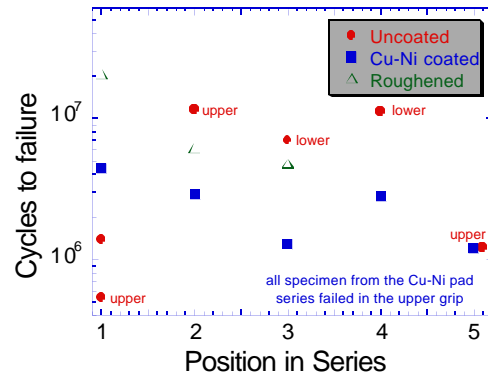


Figure 9. Comparison of fatigue lives from “series of 5” tests against Cu-Ni coated, as-received uncoated, and roughened uncoated pads.

The tests listed in Table 3 were proposed to investigate the aforementioned parameters. All of the tests were run at 400 Hz with a static normal stress of 420 MPa and an axial stress ratio of 0.5 using as-received specimens. For these tests, fatigue life was the experimentally observed quantity. To achieve this, S-N tests were run with an axial fatigue stress of 300 MPa, which was chosen based on results obtained using the step loading technique. For the first step loading test, one specimen was run against uncoated pads. Then a nominally identical test was run against Cu-Ni coated pads. The results for both tests are shown in Figure 8, which presents the data in the form of Haigh stress normalized with the Ultimate Tensile Strength (UTS). Normalized data are shown to allow comparison of the baseline data indicated by the hollow symbols, which were conducted on bar stock, to the current tests conducted on plate stock. Once normalized, the results for the uncoated pads showed no deviation from the baseline data. The results from Cu-Ni coated pads indicated a marked improvement on the resulting Haigh stress; however, the stress was stepped up eight times to obtain the result. To verify the datum, another test was conducted against coated pads with an initial starting stress of 300 MPa. The test finished in 4.5 million cycles.

Because of the time and expense involved in coating additional pads, fatigue lives were determined for the remaining tests, allowing the “early” failure of the last test to be the first in the “series of 5” tests with coated pads. The “series of 5” tests involved testing a specimen until failure, retaining the pads, and testing another specimen with the used pads. This was done for a total of five tests for each set of pads. Once this “series of 5” was completed with coated pads, two more series

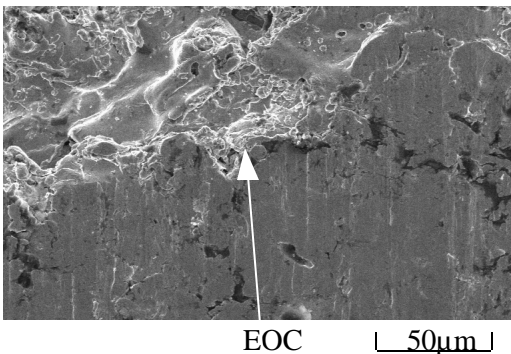


Figure 10a. Edge of contact for Cu-Ni coated pad. Flattened region in lower 1/2 of uncoated #8 finish pad. Upper 3/4 of photo was subjected to fretting.

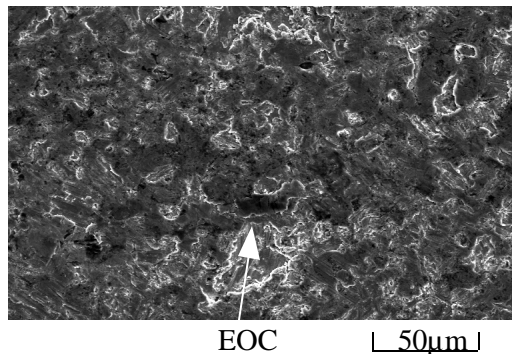


Figure 10b. Edge of contact for an uncoated pad. Upper 3/4 of photo was subjected to fretting.

were run, one with as-received uncoated pads and one with roughened uncoated pads. Results are presented in Figure 9, which shows the cycles to failure for each test as a function of the test position in the series.

For the first test in the series, the performance for Cu-Ni coated pads was better than the as-received uncoated pads. However, the second test in the series sees the reverse effect: the life of the specimen against the as-received uncoated pad is improved compared to Cu-Ni coated pads. This trend is maintained until test 5 for which no difference is observed between coated and as-received uncoated pads. Also, the lives of specimens tested against Cu-Ni coated pads have decreased somewhat compared to the first test in the series, although the behavior for the subsequent tests is fairly constant after the initial “seating in”. The conclusion from this is that the coating remains intact and provides improved fretting fatigue performance compared to the initial test against uncoated pads. This slight improvement may be attributed to surface roughness, and not the presence of the coating. Specimens tested against uncoated Ti-6Al-4V pads of comparable roughness to the coated pads showed improved performance over specimens tested against both Cu-Ni coated and as-received uncoated pads. As with the Cu-Ni coated and the as-received uncoated series, the first test served as a “seating in”, and subsequent tests completed to date fall between the other data, for each position in the series.

It is interesting to note that while all of the specimens tested against the rougher (Cu-Ni coated and roughened uncoated pads) failed in the upper grip, the failure locations in the specimens tested against as-received uncoated pads was less consistent [Figure 9]. The region of the coated pads where failures occurred were inspected, but nothing obvious was noted that might cause preferential crack nucleation. In fact, fretting damage of pads was minimal, in general [Figures 10a & 10b]. It should be noted here that the trends described above are based on one of each of the pad types. It is possible that the trends are nothing more than specimen to specimen variability which is quite large, in general, under fretting conditions.

### Fractographic Results

Inspection of the baseline specimen fracture surfaces in the SEM revealed four major regions: debris populated crack nucleation zones, debris-free crack nucleation zones, a crack propagation zone, and a fast fracture zone. It is suspected that the crack nucleation zones with the greatest amount of debris present, as in Figures 11a and 11b, are the earliest crack nucleation sites. Their position along the line of fretting is relatively consistent from test to test, and the multiaxial stress state imposed at the beginning of the test may be the source of mixed mode crack opening during the crack initiation phase. Such a crack opening would produce relative motion between the two crack faces, resulting in debris formation from the crack faces rubbing against each other, not

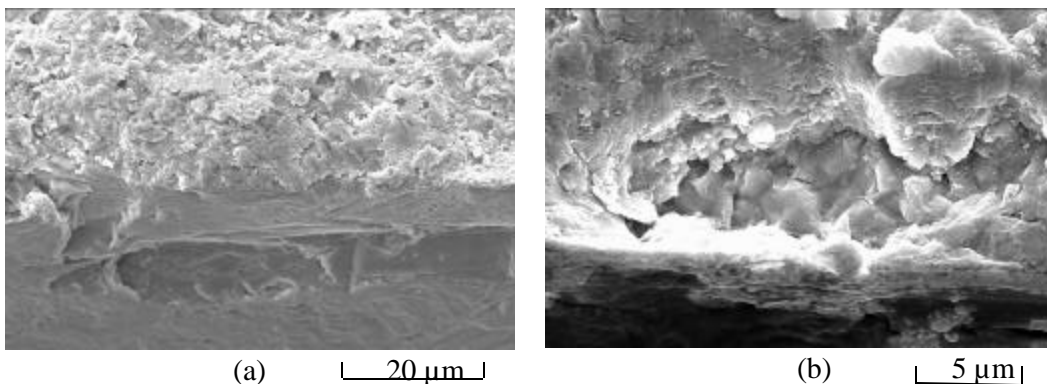


*Figure 11. Oblique views ~1.2 mm apart of debris populated crack nucleation sites. The fracture surface is shown on the upper half of each photo; the fretting contact region is shown in the lower half.*

from fretting between specimen and pad. Examples of crack nucleation sites without debris are shown in Figure 12, which is montage taken along one fretting region. The right side of the upper photo overlaps the left side of the bottom photo.

The overall crack front appears to be moving from the lower right corner to the upper left in addition to the local crack fronts whose nucleation sites are indicated by arrows. Features such as this occur near the middle of the specimen where, although a Mode 1 dominated crack is propagating, the local stress state at the edge of contact is sufficient to nucleate cracks ahead of the dominant crack tip.

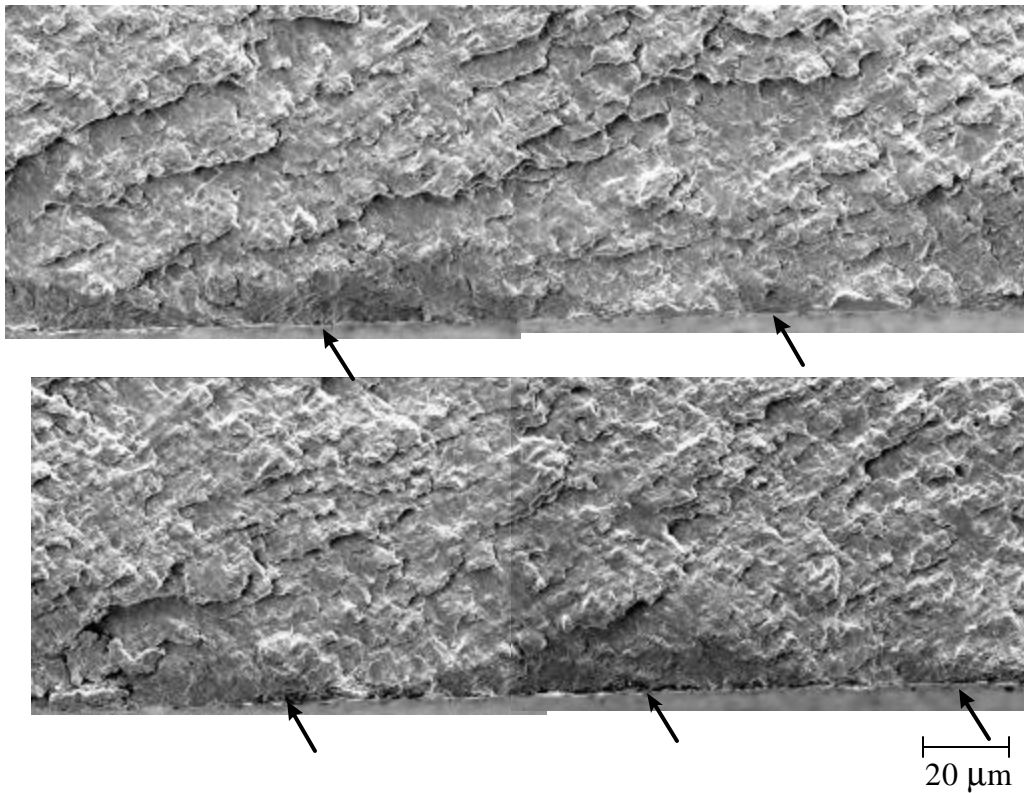
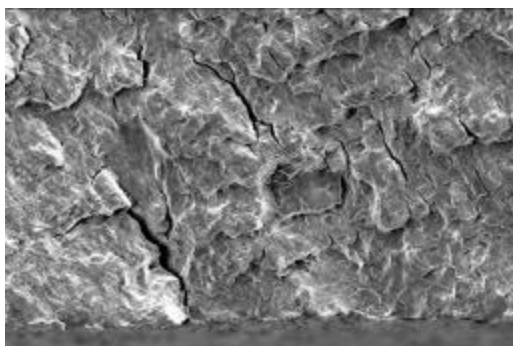


*Figure 12. Secondary crack nucleation sites without debris.*

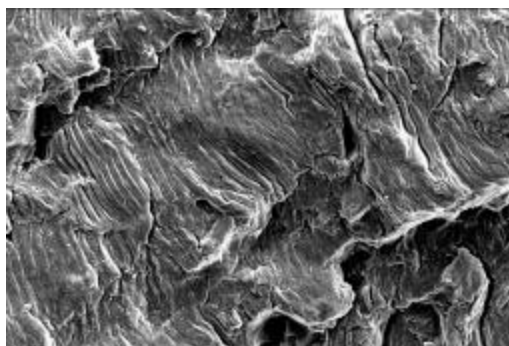
Representative photos of the crack propagation zone are shown in Figures 13 and 14. Here the crack is fully Mode 1 dominated; however, the complex stress state is sufficient to produce microcracking perpendicular to the loading axis [Figure 13]. This phenomenon has the added benefit of enhancing fatigue striations, which otherwise might not be visible on the fracture surface [Figure 14].





30 μm

Figure 13. Representative photo of secondary cracking in the crack propagation region of the fracture surface.



5 μm

Figure 14. Fretting Fatigue fracture surface showing fatigue striations enhanced by secondary cracking in crack propagation zone.

### Acknowledgments

This research was conducted at the Materials Directorate, Air Force Research Laboratory (AFRL/MLLN), Wright-Patterson Air Force Base, OH, USA. A. Hutson was supported under on-site contract number F33615-98-C-5214. Special thanks is extended to Dr. Mitsuo Niinomi from Toyohashi University of Technology, supported under Systran contract # F33615-94-C-5804, for his expertise on fretting fatigue behavior of coated Ti-6Al-4V. The authors would also like to acknowledge Dr. D. Eylon from the University of Dayton Research Institute (contract # F33615-98-C-5214) and Mr. Eric Shell from the University of Dayton Center for Materials Diagnostics (DARPA/MURI contract # F49620-96-1-0442) for their assistance in characterizing tested samples.

### References

1. Ruiz, C., Boddington, P. H. B., and Chen, K. C., "An Investigation of Fatigue and Fretting in a Dovetail Joint," *Experimental Mechanics*, vol. 24, 1984, pp. 208-217.
2. Bryggman, U. and Söderberg, S., "Contact Conditions and Surface Degradation Mechanisms in Low Amplitude Fretting," *Wear*, vol. 125, 1988, pp. 39-52.
3. Del Puglia, A., Pratesi, F., and Zonfrillo, G., "Experimental Procedure and Parameters Involved in Fretting Fatigue Tests," *Fretting Fatigue, ESIS 18*, R.B. Waterhouse and T.C. Lindley, Eds., Mechanical Engineering Publications, London, 1994, pp. 219-238.
4. Fellows, L. J., Nowell, D., and Hills, D. A., "On the Initiation of Fretting Fatigue Cracks," *Wear*, vol. 205, 1996, pp. 120-129.
5. Fouvry, S., Kapsa, P., and Vincent, L., "Quantification of Fretting Damage," *Wear*, vol. 200, 1996, pp. 186-205.
6. Vingsbo, O. and Schon, J., "Gross Slip Criteria in Fretting," *Wear*, vol. 162-164, 1993, pp. 347-356.
7. Zhou, Z. R. and Vincent, L., "Mixed Fretting Regime," *Wear*, vol. 181-183, 1995, pp. 551-536.
8. Adibnazari, S. and Hoepfner, D.W., "The Role of Normal Pressure in Modeling Fretting Fatigue," *Fretting Fatigue, ESIS 18*, R.B. Waterhouse and T.C. Lindley, Eds., Mechanical Engineering Publications, London, 1994, pp. 125-133.
9. Waterhouse, R.B., "Effect of Material and Surface Conditions on Fretting Fatigue," *Fretting Fatigue, ESIS 18*, R.B. Waterhouse and T.C. Lindley, Eds., Mechanical Engineering Publications, London, 1994, pp. 339-349.
10. Szolwinski, M.P., Harish, G., McVeigh, P.A., and Farris, T.N., "Experimental Study of Fretting Crack Nucleation in Aerospace Alloys with Emphasis on Life Prediction," *Fretting Fatigue: Current Technologies and Practices, ASTM STP 1367*, D.W. Hoepfner, V. Chandrasekaran, and C.B. Elliot, Eds., American Society for Testing and Materials, West Conshohocken, PA, 1999.

11. Hutson, A. and Nicholas, T., "Fretting Fatigue of Ti-6Al-4V Under Flat-on-Flat Contact", submitted to International Journal of Fatigue, June 1998.
12. Maxwell, D.C. and Nicholas, T., "A Rapid Method for Generation of a Haigh Diagram for High Cycle Fatigue," Fatigue and Fracture Mechanics: 29th Volume, ASTM STP 1321, T.L. Panontin and S.D. Sheppard, Eds., American Society for Testing and Materials, 1998, submitted for publication.



## **Fretting Fatigue Behavior of Ti-6Al-4V against Ti-6Al-4V under Flat-on-Flat Contact with Blending Radii**

---

**Reference:** Hutson, A. and Nicholas, T., “Fretting Fatigue Behavior of Ti-6Al-4V against Ti-6Al-4V under Flat-on-Flat Contact with Blending Radii,” *Fretting Fatigue: Current Technology and Practices*, ASTM STP 1367, D. W. Hoepfner, V. Chandrasekaran and C. B. Elliot, Eds., American Society for Testing and Materials, West Conshohocken, PA, 1999.

**Abstract:** A study was conducted to evaluate fretting fatigue damage of Ti-6Al-4V under flat-on-flat contact at room temperature. Results were obtained to establish the fatigue limit of the material. Axial stresses necessary to fail specimens at  $10^7$  cycles for different contact radii, applied normal stresses, and stress ratios were evaluated to determine the baseline fretting fatigue behavior. Then, the effect of fretting fatigue on specimen life was quantified by conducting interrupted fretting tests for various load ratios and normal stresses followed by residual strength uniaxial fatigue tests. Fractography was used to characterize the nature of fretting damage. Results indicate that no degradation in fatigue limit is observed when the material is subjected to up to 10 percent of fretting fatigue life.

**Keywords:** fretting fatigue, high cycle fatigue, Ti-6Al-4V, flat-on-flat contact, fatigue damage

### **Introduction**

Fretting fatigue is the damage caused by localized relative motion between contact surfaces on adjacent components, of which at least one component is under vibratory load, and may produce premature crack initiation and failure. Many studies [1-12] and literature surveys [13-16] of this phenomenon have focussed on fretting fatigue damage nucleation and crack propagation, in efforts to eliminate unanticipated failures of turbine engine disks and blades subjected to fretting fatigue in the dovetail attachment region. The manner in which the results of these studies may be applied to the understanding of the dovetail fretting problem is a subject for debate because the geometries and stresses in laboratory specimens are not usually directly comparable to those in actual components. Turbine engine blade roots experience fretting in a flat-on-flat contact region with rather large radii at the edges of contact. Some limited work has been performed to evaluate the dovetail geometry [1], but specimens are expensive, the stress distribution is unknown, and the results are difficult to model. Conversely, most research has been conducted on punch-on-flat [2-8], or Hertzian [9-12], contact geometries because of the availability of closed form analytical solutions for the resulting stress distributions. In these cases, a fretting pad is usually used to apply normal and shear loads against a thin test specimen, which most often is under axial fatigue loading. While analytical solutions applied to ideal geometries like a half space allow the researcher to correlate test results and ultimately predict laboratory behavior, only limited progress has been made in the development of accurate life prediction models for complex components as a result of these efforts. Development of an accurate life prediction model that bridges the gap between laboratory and service conditions requires experimentation and modeling of a more representative geometry.

---

<sup>1</sup>Assistant Research Engineer, Structural Integrity Division, University of Dayton Research Institute, 300 College Park, Dayton, OH 45469-0128.

<sup>2</sup>Senior Scientist, Metals, Ceramics & NDE Division, Materials and Manufacturing Directorate, Air Force Research Laboratory (AFRL/MLLN), Wright-Patterson AFB, OH 45433-7817.

The focus of this study was twofold: to evaluate the effect of prior fretting damage on fatigue strength using a test apparatus with a contact geometry similar to the dovetail, and to analyze fretting damage failure mechanisms using optical and scanning electron microscopy (SEM) techniques.

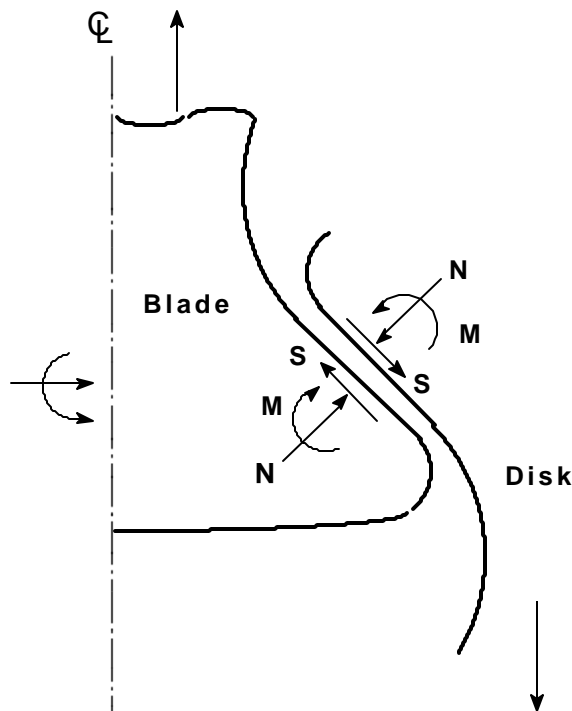


Figure 1a - Representation of blade root loading condition.

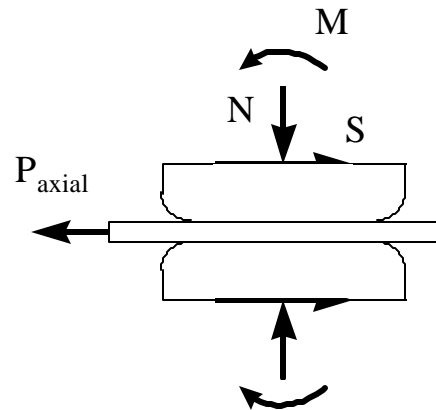


Figure 1b - Representation of test configuration designed to simulate blade root loading condition.

### Experimental Approach

The ideal test system for a study such as this would exactly duplicate the dovetail blade root loading condition in Figure 1a. However, the results would be difficult to analyze and machine tooling costs would be exorbitant. The problem was simplified by assuming that the bending moment found in the dovetail geometry was not a significant contributor, and did not affect the magnitude of the relative motion responsible for fretting fatigue damage. This assumption resulted in the elimination of the complex dovetail geometry, thus simplifying test hardware and specimen fabrication. The test apparatus for this study, however, simulated the essential features of the blade root geometry by employing flat fretting pads, with a radius at the edge of contact, against a flat specimen. Imposed normal and shear loads on the contact surfaces were reproduced in the test geometry, as shown in Figure 1b. The bending moment present in the test geometry did not represent the moment imposed in the dovetail geometry and, in fact, has not yet been calculated. This test geometry differed from the conventional fatigue test with a fretting pad in that the stress in the specimen was zero on one end of the pad. Thus, the shear force into the pad was known by measuring only the applied stress in the specimen. As in a conventional test, only the axial and shear stresses were oscillatory: the clamping stress was static, which would not be true in a blade. Symmetry in the apparatus (see Figure 2) provided a specimen which failed on one end, leaving the other end with a fretting scar and damage obtained under nominally identical conditions corresponding to 100 percent of full life of that particular specimen.

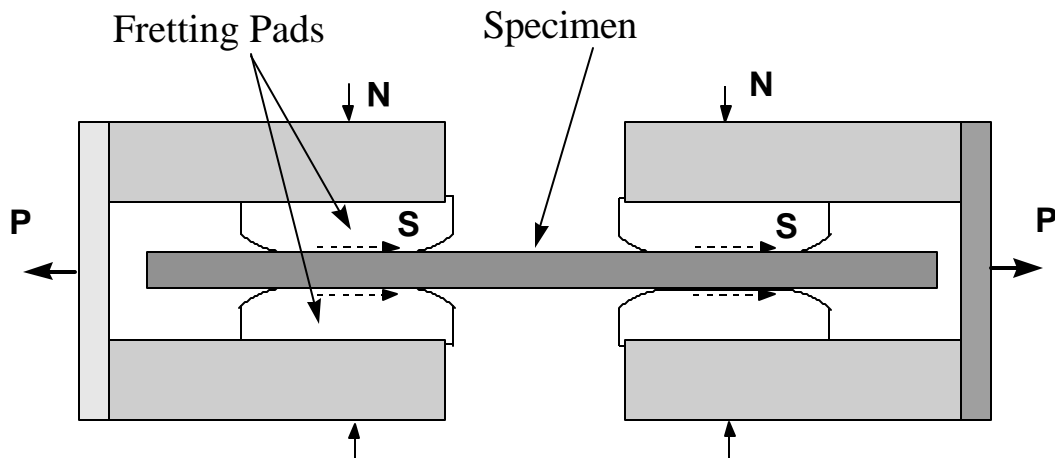


Figure 2 - Test load train schematic. The apparatus produces two nominally identical regions of fretting for each test specimen.

The test system used for this study was modified from a uniaxial high cycle fatigue system, which experienced a number of fretting fatigue induced failures in the specimens within the grip region. The new system was an electro-dynamic shaker system that could test at frequencies up to 500 Hz, and had a mean load capacity of 20 kN and a dynamic load capacity of 12 kN peak-to-peak at frequencies up to 300 Hz. Mean and dynamic loads were applied independently via a pneumatic cylinder and the electro-dynamic shaker, respectively, to maximize dynamic capability. System modifications were limited to the test gripping apparatus. Each grip was fitted with removable fretting pads, as shown in Figure 3, to facilitate control of surface conditions. Standard bolts, used to apply the clamping force were replaced by bolts instrumented with strain gages in the shank to allow accurate measurement of static clamping, or normal loads. Symmetric clamping of the specimen was achieved through the use of a specific torque pattern. Fretting damage occurred at the edge of contact, shown schematically in the magnified view in Figure 3.

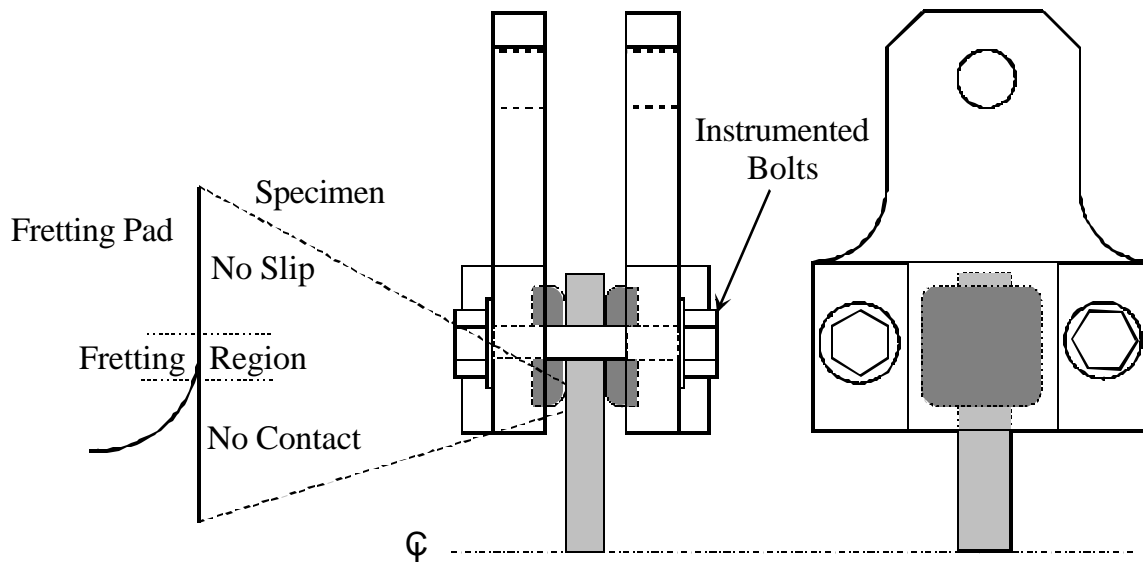


Figure 3 - Fretting fatigue gripping system and stress state induced in contact region.

All axial (fretting fatigue) specimens and a portion of the fretting pads were machined from vacuum annealed and hot rolled Ti-6Al-4V bar stock. The material was vacuum treated at 705°C for two hours, static argon cooled to below 149°C, vacuum annealed at 549°C for two hours, and static argon cooled to less than 149°C. This treatment produced a microstructure of 90% wide, plate-like  $\alpha$  with 10% intergranular  $\beta$  that is approximately equiaxed in the transverse section, with a slight elongation in the longitudinal section along the longitudinal axis of the bar. The balance of the fretting pads were machined from forged AMS4928 Ti-6Al-4V with TE01 heat treatment. All specimens and fretting pads were low stress ground to an RMS 8 surface finish.

A preliminary study of fretting fatigue parameters was conducted earlier using this apparatus [17]. An overview of the test method and results from that investigation are summarized here to provide the baseline conditions for the present investigation. A range of shear stress levels and distributions were investigated by varying contact length, contact radius, and normal contact load. The actual stress distributions have not yet been evaluated, but the contact radius is expected to have an effect on the distribution of both shear stress and normal stress. Only two values of each parameter were selected for the preliminary experiments to determine if changing the parameters would produce trends in the test results. Nominal pad lengths were 25.4 mm and 12.7 mm; contact radii were 3.2 mm and 0.4 mm; and static normal loads were 35 kN and 21 kN. Each of the resulting eight test conditions was conducted at two load ratios,  $R = 0.1$  and  $R = 0.5$ , as shown in Table 1. The “initial axial stresses” in parentheses refer to arbitrarily selected values of axial stresses, which were used during the first block of a step loading procedure described below. Average specimen thickness was 2 mm; average width was 10 mm. Two specimen lengths were used: the bulk of the data was obtained using specimens with an average length of 100 mm; a few tests were conducted using 150 mm specimens to validate the tests described below. All tests were conducted in lab air at room temperature. Two different frequencies were required for each of the two specimen lengths to avoid harmonic resonance and bending modes in the specimen. The 100 mm long specimens were tested at 300 Hz while the 150 mm long specimens were tested at 400 Hz. No difference in test results was detectable between data for the two test frequencies. The contact areas listed in Table 1 are the nominal contact areas after allowing for the nominal contact radii and nominal specimen width of 10 mm. The results of the preliminary investigation are presented in Figure 4, which show that the maximum stress increases with increasing stress ratio or decreasing contact radius, but does not change appreciably with normal stress. The maximum axial stress is also referred to as “Goodman” stress, which is defined as the maximum (interpolated) stress corresponding to a fatigue limit of  $10^7$  cycles as determined from the step loading procedure. The  $10^7$  cycle fatigue limit was selected as a value commonly used in design, and as a reasonable number of cycles to obtain in laboratory tests.

All tests that were intended to run to failure were conducted using the step loading approach developed by Maxwell and Nicholas [18]. This technique employed constant amplitude loading blocks (see Figure 5) where the initial axial stress was set below the anticipated stress for a given fatigue limit (defined here as  $10^7$  cycles). Each loading block was applied for the selected number of cycles ( $10^7$  cycles in this case), or until the specimen failed. If the specimen did not fail in the first load block, the axial stress was raised by a percentage of the initial axial stress, and run for another  $10^7$  cycles. This process was repeated for each subsequent block until the specimen failed. The fatigue limit stress, or Goodman stress was interpolated from the failure stress, the number of cycles at the failure stress, and the stress level of the previous step. The technique was validated in three separate studies where data from step loading tests were shown to coincide with those obtained using extrapolation and interpolation of conventional stress-life tests to the fatigue limit of the step tests [18-20].

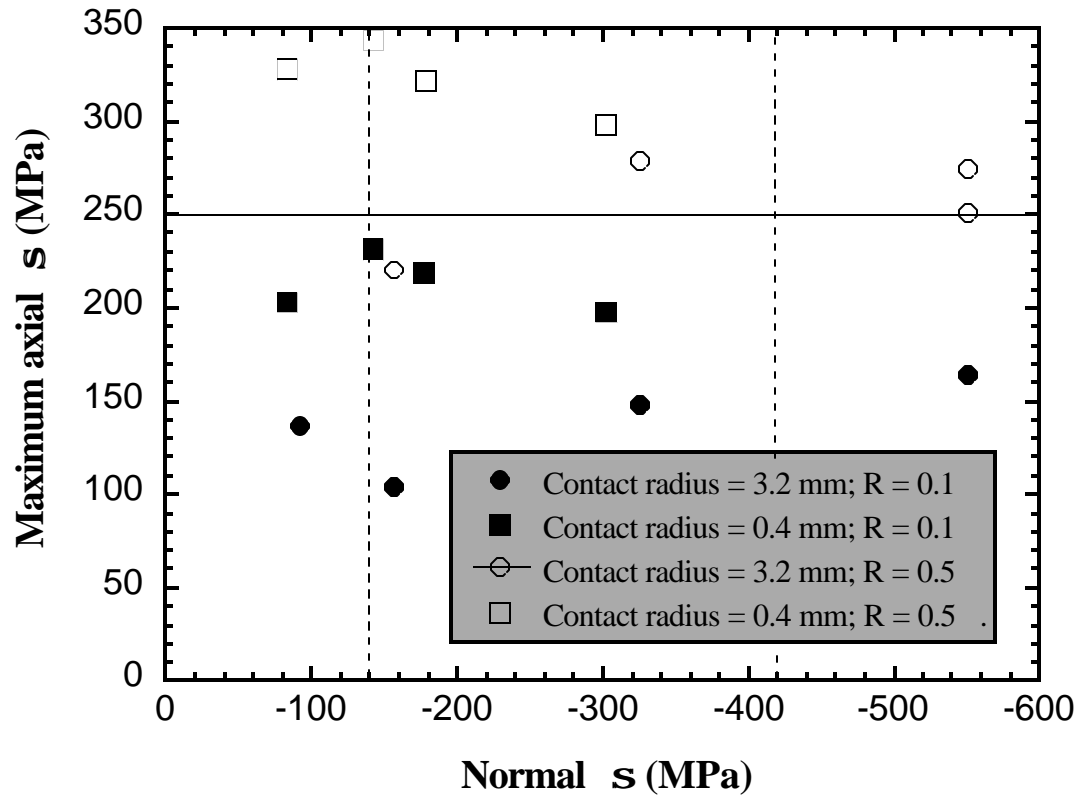


Figure 4 – Fretting fatigue test results for a life of  $10^7$  cycles.

Table 1 - Test matrix indicating normal loads, calculated contact areas, and load ratios. Arbitrarily selected initial axial stresses are shown in parentheses [17].

Normal Load	Contact Area			
	65 mm <sup>2</sup>	120 mm <sup>2</sup>	190 mm <sup>2</sup>	245 mm <sup>2</sup>
35 kN	( $\sigma_{\text{axial}} = 150$ MPa) R = 0.1	( $\sigma_{\text{axial}} = 150$ MPa) R = 0.1	( $\sigma_{\text{axial}} = 150$ MPa) R = 0.1	( $\sigma_{\text{axial}} = 150$ MPa) R = 0.1
	( $\sigma_{\text{axial}} = 270$ MPa) R = 0.5	( $\sigma_{\text{axial}} = 220$ MPa) R = 0.5	( $\sigma_{\text{axial}} = 220$ MPa) R = 0.5	( $\sigma_{\text{axial}} = 220$ MPa) R = 0.5
21 kN	( $\sigma_{\text{axial}} = 135$ MPa) R = 0.1	( $\sigma_{\text{axial}} = 100$ MPa) R = 0.1	( $\sigma_{\text{axial}} = 80$ MPa) R = 0.1	( $\sigma_{\text{axial}} = 170$ MPa) R = 0.1
	( $\sigma_{\text{axial}} = 220$ MPa) R = 0.5	( $\sigma_{\text{axial}} = 220$ MPa) R = 0.5	( $\sigma_{\text{axial}} = 220$ MPa) R = 0.5	( $\sigma_{\text{axial}} = 220$ MPa) R = 0.5

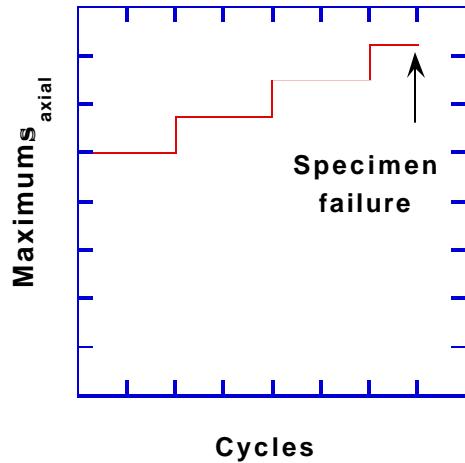


Figure 5 - Step loading pattern used for Goodman stress determination.

results of the preliminary work (Figure 4), given the contact radius and desired stress ratio of  $R = 0.5$ . Since no trend was observed in the preliminary Goodman stresses as a function of normal stress, the same axial stress was used for both values of normal stress, shown by the solid line in Figure 4. After the sub-critical fretting fatigue damage was applied, one end of the specimen was removed, and the fretted region was machined into a dogbone sample, as shown in Figure 6, where the fretted region was now within the test section of the dogbone geometry. The dogbone samples were tested in uniaxial fatigue at stress ratios of  $R = 0.1$  and  $R = 0.5$  using the step loading technique previously described. Because of the apparently low level of fretting damage, as observed visually, initial stresses were selected assuming no appreciable damage was present.

Table 2 - Phase 2 test matrix indicating normal stresses, load ratio, and the number of cycles of fretting.

Cycles of Fretting	140 MPa Normal stress	420 MPa Normal stress
10,000	3 test @ $R=0.5$	3 test @ $R=0.5$
100,000	3 test @ $R=0.5$	3 test @ $R=0.5$
1,000,000	3 test @ $R=0.5$	3 test @ $R=0.5$
total	9 tests	9 tests

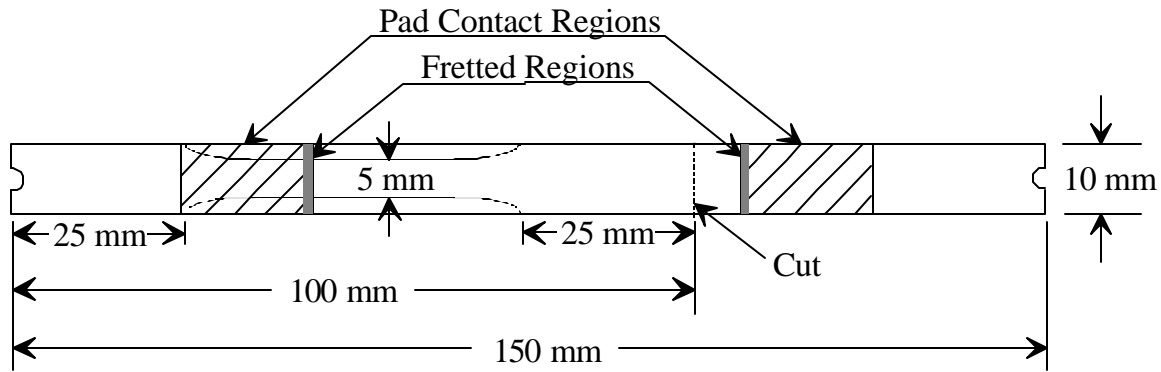


Figure 6 - Schematic of post-fretting machining for 150 mm fretting specimen.

## Results / Discussion

The results from a limited number of tests on specimens tested to 10 percent of the total fretting life appear to preclude the necessity of testing specimens with lower levels of damage. All eighteen specimens, which covered life ranges from 0.1 to 10 percent, were fretted and the scars were inspected optically. Representative fretting scars are shown in Figure 7 for both 140 MPa (Figure 7a) and 420 MPa (Figure 7b) normal stresses. The fretting scars, indicated by the white arrows, appear approximately horizontal in the photos, and the loading axis is vertical. Three specimens subjected to one million fretting fatigue cycles (10% of life) at 140 MPa normal stress were tested to failure. The specimen tested at  $R = 0.5$  failed at the fretting scar, but with no debit in fatigue strength compared to the baseline fatigue limit. Figure 8a shows this datum compared with data on unfretted specimens [18], as presented on a constant life plot of mean stress vs. alternating stress. The datum falls within the scatter band of the baseline. The two remaining specimens at this damage level were tested at  $R = 0.1$ . Both specimens failed at lower stresses than the baseline (Figure 8b), but damage nucleated well away from the fretted region.

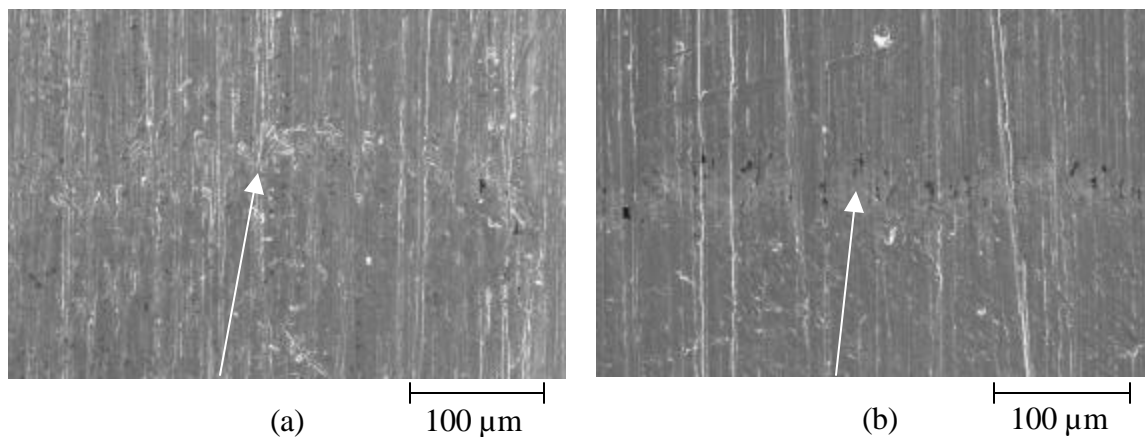


Figure 7 – Representative fretting scars from interrupted fretting tests: (a) tested for  $10^6$  cycles at a 140 MPa normal stress, (b) tested for  $10^6$  cycles at 420 MPa normal stress

SEM inspection of the fracture surfaces from these two specimens revealed crack nucleation from embrittled features not found in the bulk of the material (Figure 9). Machining anomalies were determined to be the source of these regions. From these limited results, the authors find it reasonable to conclude that fretting damage at or below 10% of total life was not detrimental to the fatigue strength of the material. In support of this, Adibnazari and Hoepfner did not report a decrease in fatigue resistance until 20-40% of life for Ti-6Al-4V under an average normal stress of 750 MPa [9]. In spite of these

results, which imply no detrimental damage, fretting scars at the edge of contact have been clearly identified.

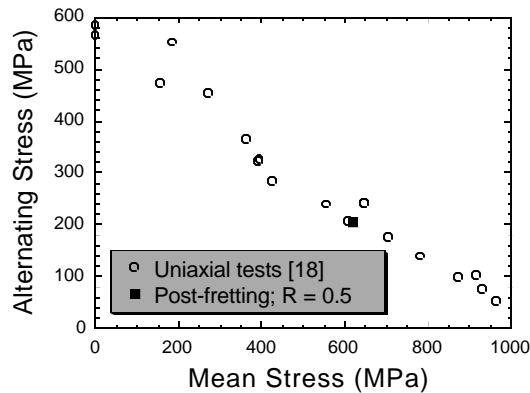


Figure 8a - Comparison of post-fretting fatigue results indicating no change for fretting damage accumulated to ten percent of fretting life.

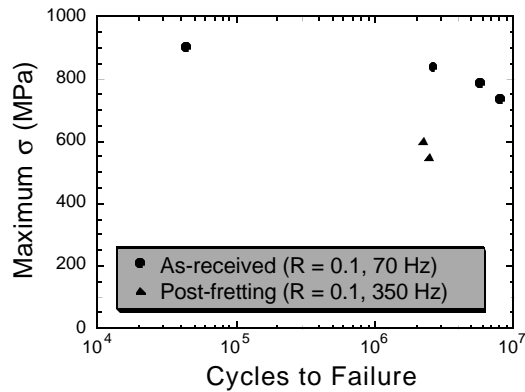


Figure 8b - S-N curve presenting post-fretting specimens that failed prematurely compared to baseline data.

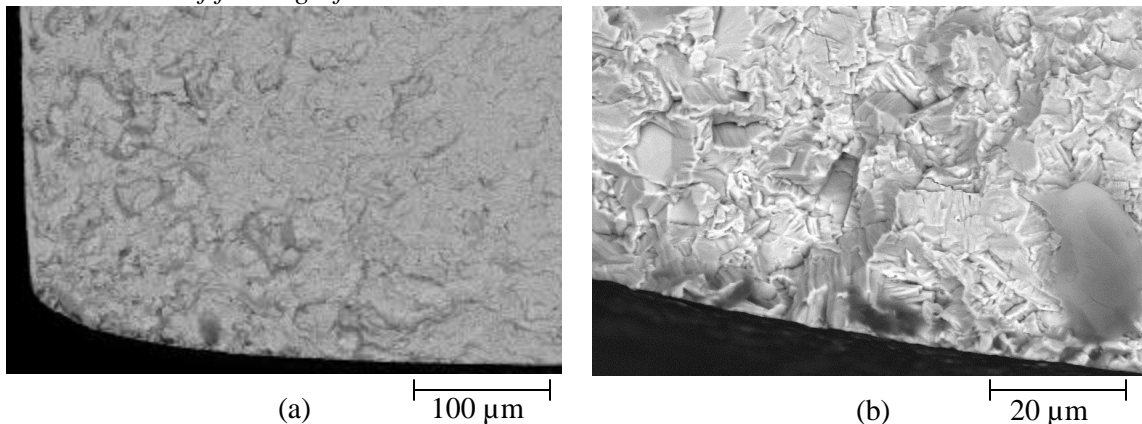


Figure 9 - Crack nucleation site for a post-fretting fatigue test, which failed away from the fretted region: (a) region at 300X showing typical material structure in the upper right-hand corner, and the damaged region in the lower left-hand corner, (b) crack nucleation feature at 1500X.

For all the fretting fatigue tests in the preliminary study [18] failures occurred consistently at the edge of contact. In that study, the unfailed ends of the specimens, corresponding to 100 percent of life, exhibited fretting scars with varying levels of damage from specimen to specimen under both optical and SEM inspection. Figure 10 shows two representative micrographs of fretting damage observed on the unfailed ends of a typical test specimen. Fretted regions appear to the left of the dashed lines; machined surfaces are to the right. The diagonal texture throughout Figures 10 and 11 was a product of the low stress grind process, and was presumed to be non-detrimental since it was not perpendicular to the loading axis (approximately horizontal in Figure 10). Although no cracks were apparent in Figure 10, some specimens did show evidence of cracking on the unfailed end of the specimen (Figure 11). Regardless of whether or not cracking was present, fretting damage ranged from nearly invisible deformation of the machined surface near the center of the specimen (Figure 10b), to small pits produced by local adhesion and delamination near the edge of the specimen (Figure 10a). The range of damage shown in Figure 10 occurred on the same fretting scar, implying a change in stress state from the center to the edge of the



specimen. This stress gradient may prove problematic if additional testing and characterization indicate primary crack nucleation at or near the edge of contact.

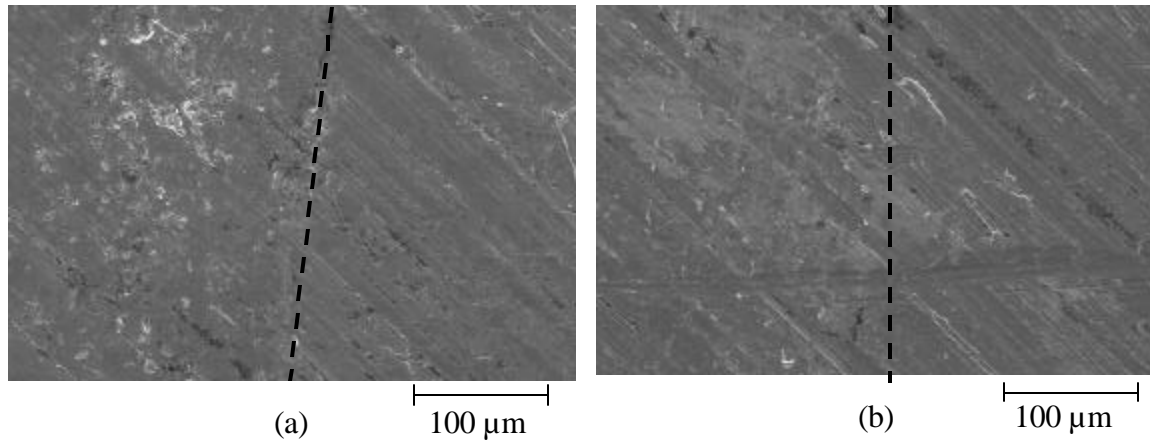


Figure 10 - Two regions of a representative fretting scar from the unfailed end of a typical test specimen. a) Damage near the edge of the specimen. b) Damage near the center of the specimen. The loading axis is approximately horizontal.

The crack shown in Figure 11 continued to the edge of the specimen, but did not appear to nucleate there. Rather, nucleation sites appear to have occurred 150 - 300  $\mu\text{m}$  from the specimen edge. Attempts have been made to quantify the states of stress along the fretting zone using finite element analysis (FEA) to better understand this crack nucleation phenomenon, but the program selected did not have the appropriate elements for the solution of the contact problem.

SEM characterization of the fracture surfaces from the preliminary testing also revealed several unique features. Overall, a representative fracture surface was divided into four sections: oxide populated crack nucleation sites, oxide-free crack nucleation sites, a crack propagation region, and a tensile fracture region. The photos in Figure 12 exhibited debris populated crack nucleation sites (see arrow in Figure 12a). These oblique views of two different specimens displayed fretting scars on the bottom halves of the photos, and the fracture surfaces on the top halves. Spectral analysis of the white particles on the fracture surface indicated a relatively large amount of oxygen indicative of wear debris observed in many of

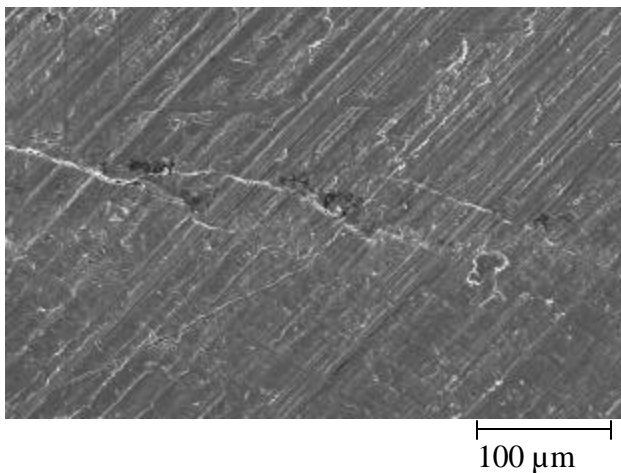


Figure 11 - Fretting scar with crack from the unfailed end of a failed specimen.

fretting. Whether the oxide particles developed during crack nucleation or crack propagation was unclear; however, crack nucleation sites showing no debris (Figure 13) were also present. The nucleation sites with the debris were presumed to have nucleated earlier than those without debris, since those with debris tended to have material smeared across them (Figure 12b), indicating a localized influence of Mode 2 as well as Mode 1 crack growth. The influence of Mode 2 crack growth will tend to diminish as the crack propagates, so cracks nucleating later will have less smeared material.

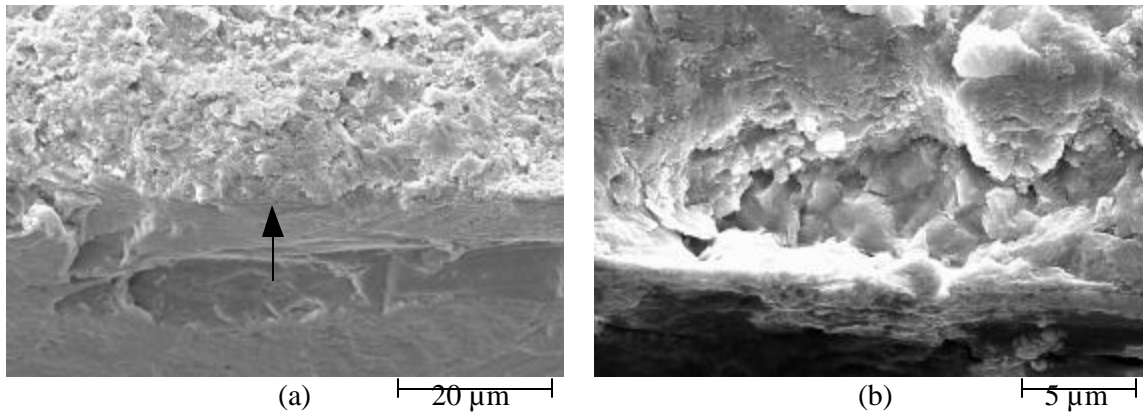


Figure 12 - Fracture surface photos showing presence of (a) fretting debris particles and (b) material smearing.

Figure 13 shows a series of four fractographs, which overlap to form a montage that illustrates the presence of five crack nucleation sites without debris (indicated by arrows) within less than 500  $\mu\text{m}$ . Multiple nucleation sites were features found in low cycle fatigue (LCF) failures, but the limited results from tests reported here seemed to refute the idea that these are LCF failures. Crack nucleation under LCF is usually evident within the first ten percent of life. The fretting fatigue specimens tested here show no evidence of crack nucleation up to ten percent of life. Multiple crack nucleations might occur after some period of growth for a single, primary crack. The combination of a reduced net section and imposed bi-axial stresses may produce small secondary cracks later in life. All four photos in Figure 13 were taken near the center of the specimen. The overall crack front appeared to be propagating to the left, further evidence that these cracks were not the first to nucleate. The lack of debris on these sites indicated that the major crack driving force is coming from the Mode I component.

The crack propagation region of the fracture surface was generally free of debris, which left two additional features unobscured. Secondary cracking perpendicular to the dominant crack plane was evident to varying degrees throughout the crack propagation zone, as in Figure 14, where the specimen edge is shown in the lower part of the photo.

These cracks provided evidence of a multi-axial stress state through the thickness of the specimen. Fatigue striations with spacing on the order of  $10^{-7}$  m/cycle were also visible, partially due to enhancement by secondary cracking. An example is shown in Figure 15, which was taken  $\sim 1.2$  mm away from the region shown in Figure 14, where the specimen edge would appear  $\sim 20$   $\mu\text{m}$  below the photo as shown. Although the overall crack front was not clear, correlation of growth rates derived from these striations with uniaxial crack growth data might provide information on crack front locations and crack propagation rates under complex loading.

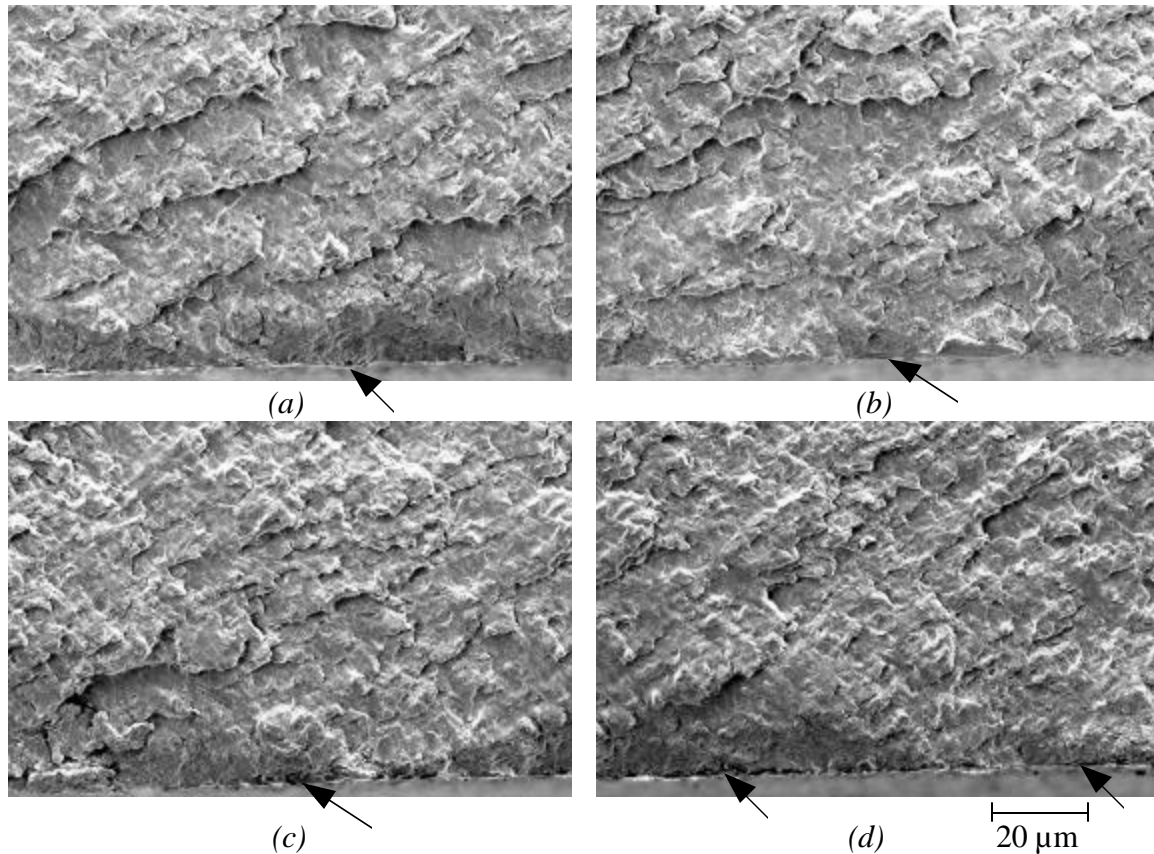


Figure 13 - A series of fracture surface photos illustrating several crack nucleation sites.

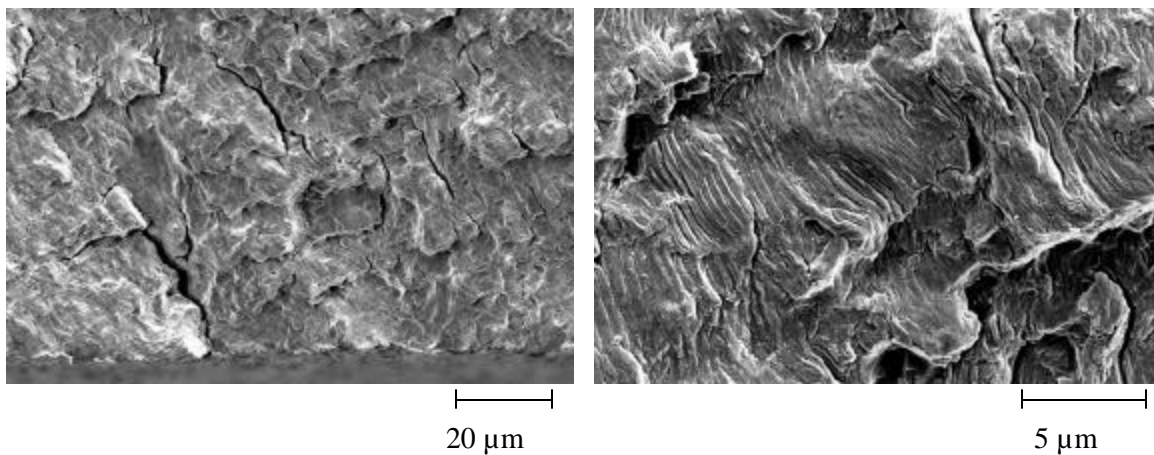


Figure 14 - Fracture surface showing secondary cracking perpendicular to the crack plane as evidence of multi-axial stresses.

Figure 15 - Fracture surface showing prominent fatigue striations.

## Conclusions

Limited tests results indicated that no measurable reduction in axial fatigue strength occurred if fretting fatigue conditions were removed at 10 percent of fretting fatigue life under a normal stress of 140 MPa. Further testing is required to statistically verify this conclusion.

Levels of fretting damage for interrupted fretting fatigue tests at life fractions below 10 percent were nearly indistinguishable from the machined surface.

Inspection of fracture surfaces revealed multiple crack nucleation sites, some fretting debris, prominent fatigue striations, and evidence of a tri-axial stress state in the form of secondary cracking.

#### *Acknowledgments*

This research was conducted at the Materials & Manufacturing Directorate, Air Force Research Laboratory (AFRL/MLLN), Wright-Patterson Air Force Base, OH, USA. A. Hutson was supported under on-site contract numbers F33615-94-C-5200 and F33615-98-C-5214. The authors gratefully acknowledge many helpful discussions with Dr. D. Eylon and Dr. N. Ashbaugh, at the University of Dayton, and Mr. Rick Goodman for his assistance in the experimental portion of the program.

#### **References**

1. Ruiz, C., Boddington, P. H. B., and Chen, K. C., "An Investigation of Fatigue and Fretting in a Dovetail Joint," *Experimental Mechanics*, Vol. 24, 1984, pp. 208-217.
2. Bryggman, U. and Soderberg, S., "Contact Conditions and Surface Degradation Mechanisms in Low Amplitude Fretting", *Wear*, Vol. 125, 1988, pp. 39-52.
3. Del Puglia, A., Pratesi, F., and Zonfrillo, G., "Experimental Procedure and Parameters Involved in Fretting Fatigue Tests," *Fretting Fatigue, ESIS 18*, R.B. Waterhouse and T.C. Lindley, Eds., Mechanical Engineering Publications, London, 1994, pp. 219-238.
4. Elkholy, A. H., "Fretting Fatigue in Elastic Contacts Due to Tangential Micro-motion," *Tribology International*, Vol. 29, No. 4, 1996, pp. 265-275.
5. Fellows, L. J., Nowell, D., and Hills, D. A., "On the Initiation of Fretting Fatigue Cracks," *Wear*, Vol. 205, 1996, pp. 120-129
6. Fouvry, S., Kapsa, P., and Vincent, L., "Quantification of Fretting Damage," *Wear*, Vol. 200, 1996, pp. 186-205.
7. Vingsbo, O. and Schon, J., "Gross Slip Criteria in Fretting," *Wear*, Vol. 162-164, 1993, pp. 347-356.
8. Zhou, Z. R. and Vincent, L., "Mixed Fretting Regime," *Wear*, Vol. 181-183, 1995, pp. 551-536.
9. Adibnazari, S. and Hoeppe, D.W., "The Role of Normal Pressure in Modeling Fretting Fatigue," *Fretting Fatigue, ESIS 18*, R.B. Waterhouse and T.C. Lindley, Eds., Mechanical Engineering Publications, London, 1994, pp. 125-133.
10. Dobromirski, J. and Smith, I. O., "Metallographic Aspects of Surface Damage, Surface Temperature and Crack Initiation in Fretting Fatigue," *Wear*, Vol. 117, 1987, pp. 347-357.
11. Fayeulle, S., Blanchard, P., and Vincent, L., "Fretting Behavior in Titanium Alloys," *Tribology Transactions*, Vol. 36, No. 2, pp. 267-275, 1993.

12. Lindley, T. C. and Nix, K. J., "Fretting Fatigue in the Power Generation Industry: Experiments, Analysis, and Integrity Assessment," *Standardization of Fretting Fatigue Test Methods and Equipment, ASTM STP 1159*, M. Helmi Attia, and R. B. Waterhouse, Eds., American Society for Testing and Materials, Philadelphia, 1992, pp. 153-169.
13. Waterhouse, R.B., "Effect of Material and Surface Conditions on Fretting Fatigue," *Fretting Fatigue, ESIS 18*, R.B. Waterhouse and T.C. Lindley, Eds., Mechanical Engineering Publications, London, 1994, pp. 339-349.
14. Dobromirski, J.M., "Variables of Fretting Processes: Are There 50 of Them?," *Fretting Fatigue, ESIS 18*, R.B. Waterhouse and T.C. Lindley, Eds., Mechanical Engineering Publications, London, 1994, pp. 60-66, 1994.
15. Attia, M. H., "Fretting Fatigue Testing: Current Practices and Future Prospects for Standardization," *Standardization of Fretting Fatigue Test Methods and Equipment, ASTM STP 1159*, M. Helmi Attia and R. B. Waterhouse, Eds., American Society for Testing and Materials, Philadelphia, 1992, pp. 263-275.
16. Hoepfner, D.W., "Mechanisms of Fretting Fatigue," *Fretting Fatigue, ESIS 18*, R.B. Waterhouse and T.C. Lindley, Eds., Mechanical Engineering Publications, London, 1994, pp. 3-19.
17. Hutson, A. and Nicholas, T., "Fretting Fatigue of Ti-6Al-4V Under Flat-on-Flat Contact", *International Journal of Fatigue*, Special Issue on High Cycle Fatigue, 1999 (in press).
18. Maxwell, D.C. and Nicholas, T., "A Rapid Method for Generation of a Haigh Diagram for High Cycle Fatigue," *Fatigue and Fracture Mechanics: 29th Volume, ASTM STP 1321*, T.L. Panontin and S.D. Sheppard, Eds., American Society for Testing and Materials, 1999, pp. 626-641.
19. Bellows, R. S., Muju, S. and Nicholas, T., "Validation of the Step Test Method for Generating Goodman for Ti-6Al-4V," *International Journal of Fatigue*, Special Issue on High Cycle Fatigue, 1999 (in press).
20. Lanning, D., Haritos, G.K. and Nicholas, T., "Notch Size Effects in HCF Behavior of Ti-6Al-4V," *International Journal of Fatigue*, Special Issue on High Cycle Fatigue, 1999 (in press).
21. Van Stone, R., "Fretting and High Cycle Fatigue in Titanium," presented at the 3<sup>rd</sup> National Turbine Engine High Cycle Fatigue Conference, San Antonio, TX, 1998.

This page intentionally left blank.

# Evolution and Effects of Damage in Ti-6Al-4V under High Cycle Fatigue

Ted Nicholas  
U.S. Air Force Research Laboratory  
Wright-Patterson AFB, OH, USA

David C. Maxwell  
University of Dayton Research Institute  
Dayton, OH, USA

## **Introduction**

High cycle fatigue (HCF) failures in materials used in rotating components of gas turbine engines have often been found to be attributable to fatigue loading on materials which have sustained damage from other sources. Damage can be present from initial material or manufacturing defects, or can develop during service operation. In-service damage, while not catastrophic by itself, can degrade the HCF resistance of the material so that the fatigue limit, plotted on a constant life Haigh (or Goodman) diagram, for example, is reduced. Three major sources of in-service damage which can alter the HCF resistance individually or in conjunction with one another are low cycle fatigue (LCF), foreign object damage (FOD), and fretting. In each case, the resultant high cycle fatigue properties, specifically the fatigue limit, is reduced.

The determination of a fatigue limit can be time consuming if the limit corresponds to a large number of cycles such as  $10^7$  or greater. Recently, an accelerated test procedure has been adopted to try to reduce testing time while accurately determining the same fatigue limit as one would obtain using conventional S-N testing, curve fitting, and extrapolating to the desired number of cycles [1]. The test procedure has been validated by others on both smooth and notched samples [2], but its validity to damaged samples in FOD and fretting experiments is still in doubt, particularly since an occasional test requiring a large number of steps produces very high fatigue limit stresses, a possible indication of a coaxing effect. Thus, the use of an accelerated test procedure and high frequency machines can overcome this difficulty. The validity of the method, particularly for damaged materials, is yet to be established. The purpose of this paper is to explore the accumulation of damage in a material

subjected to HCF with particular emphasis on the coaxing effect.

## **Coaxing Effect and Accelerated Tests**

By early in this century, numerous accelerated tests for endurance limit had been proposed and rejected because they did not prove to be reliable. Among these early accelerated tests was that of Moore and Wishart [3] who developed an "overnight" test based on application of a fixed number of HCF cycles followed by determination of tensile strength. The basis of this test was that fatigue testing below the endurance limit increases the tensile strength and endurance limit, while above the endurance limit, cracks form and ultimately degrade the tensile strength. Commenting on this paper, Gough stated that "I have arrived definitely at the conclusion that no reliable form of short-time test known has yet been devised." and he saw "no fundamental reason why any short-time test can be *expected* to prove reliable."

Later, Prot [4] developed a rapid test for determining the fatigue limit without using constant stress tests. His technique involved starting at a stress below the estimated fatigue limit and increasing the stress at a constant rate until failure occurs. In his approach, one test specimen is required for each rate of increase in stress. Still, it was claimed that this method reduces testing time by nine-tenths.

The concern with an increasing load method of determining a fatigue limit is the effect that understressing might have in increasing the true fatigue limit. The increase in the fatigue limit, due to extensive prior cycling below the fatigue limit, is referred to as coaxing. Nonetheless, the Prot method was validated by Ward, et al. [5] on welded SAE 4340 steel and found to be applicable

to ferrous metals with a well-defined endurance limit [6]. However, Corten et al. [6] noted that for ferrous metals that are susceptible to coxing, the Prot procedure appreciably raises the endurance limit compared to that obtained by conventional methods. In a discussion of their paper, they pointed out the following: "Only if coxing is absent and the number of cycles in each step is sufficiently large (possibly  $10^7$  cycles), does it appear reasonable to expect that the fracture stress data obtained from the step-up method will agree with the endurance limit obtained from conventional tests." Other work by Dolan et al. [7] showed that improvement in the fatigue life by understressing depended a great deal on the relative difference between the understress level and the endurance limit. Retesting with a small increase in stress level resulted in abnormally long life, but retesting with a large difference in stress level showed no apparent coxing effect. The existence of a coxing effect, while important in establishing the validity of an accelerated test procedure of the type due to Prot, does not appear to have an established scientific basis.

Another possible explanation of the coxing effect is one which is purely statistical in nature. Epremian and Mehl [8] point out that elimination of the weaker specimens during fatigue testing below the fatigue limit biases the population of specimens tested at higher stress levels. Because of the statistical selectivity, specimens subsequently tested above the fatigue limit tend to show longer lives. For either of the proposed explanations, it is not felt that coxing is a real phenomenon in titanium alloys and, therefore, the step loading test procedure introduced here is valid for determination of the fatigue limit. The Prot approach has been found to be reasonably reliable for a titanium alloy [9].

## **Experiments**

Test specimens were machined from two product forms of Ti-6Al-4V. The "bar" material was in the form of 45 mm diam. stock which was heat treated as follows: vacuum treat at 705°C for two hours, static argon cool to below 149°C, anneal in a vacuum at 549°C for two hours, and static argon

cool to less than 149°C. This produced a microstructure of wide, plate-like  $\alpha$  with intergranular  $\beta$  containing approximately 90%  $\alpha$ -phase, 10%  $\beta$ -phase. The material properties in the longitudinal direction were as follows:  $\sigma_y = 980$  MPa,  $\sigma_{UTS} = 1030$  MPa. The "plate" material was forged from a parent bar produced in accordance with AMS 4928. After forging, the plate was preheated at 938 °C for 30 minutes, solution heat treated at 932 °C for 75 minutes, and fan air cooled. The plate was then mill annealed in vacuum at 704 °C for two hours, and fan cooled in argon. This produced an alpha-beta microstructure having acicular (plate-like) Widmanstätten structures of approximately 60% primary alpha with the remainder transformed beta. The mechanical properties of the plate were as follows:  $\sigma_y = 930$  MPa,  $\sigma_{UTS} = 978$  MPa.

Tests conducted as part of this investigation used uniform gage length cylindrical specimens loaded axially in either a servo-controlled test frame or in a specialized high cycle fatigue test machine capable of a frequency of 1800 Hz using a magnetostrictive actuator. Some tests were conducted under constant load until failure or a predetermined runout number of cycles was reached. Other tests were conducted using the step loading technique described in Ref. [1].

## **Analysis**

To examine the expected outcome using the step loading technique, consider the schematic of Fig. 1. One can define a fatigue limit on an S-N curve arbitrarily as  $N_f$ , even though there is no assurance that this is a true endurance limit corresponding to "infinite" life. At  $N_f$  there will exist a unknown cumulative distribution function (CDF) which will define the failure function at that number of cycles over some range of stresses. The stress corresponding to CDF=0 defines the stress level below which there are no failures within  $N_f$  cycles. When CDF=1, the corresponding stress defines the condition under which all specimens fail at or below  $N_f$  cycles. If there is a large amount of scatter as in curve "A", which may occur if the S-N curve is very flat, then a larger number of steps



in the step-loading technique will be required to cover all of the possible values of stress corresponding to  $N_f$ . If, however, there is less scatter, or the S-N curve is steeper which will essentially cut off the higher values of stress which cause failure at lower numbers of cycles, then the number of steps is fewer. In either case, the

larger the number of steps in a test, the higher is the expected stress. Thus, what appears to be a "coaxing" effect is no more than the statistics of the distribution of material fatigue strength. The actual number of steps in a step loading experiment depends on the starting

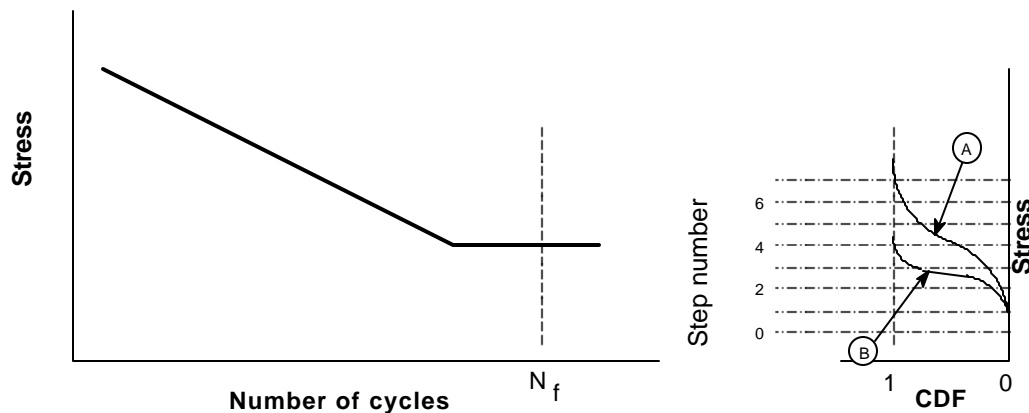


Fig. 1 Schematic of S-N curve and CDF for two different degrees of scatter.

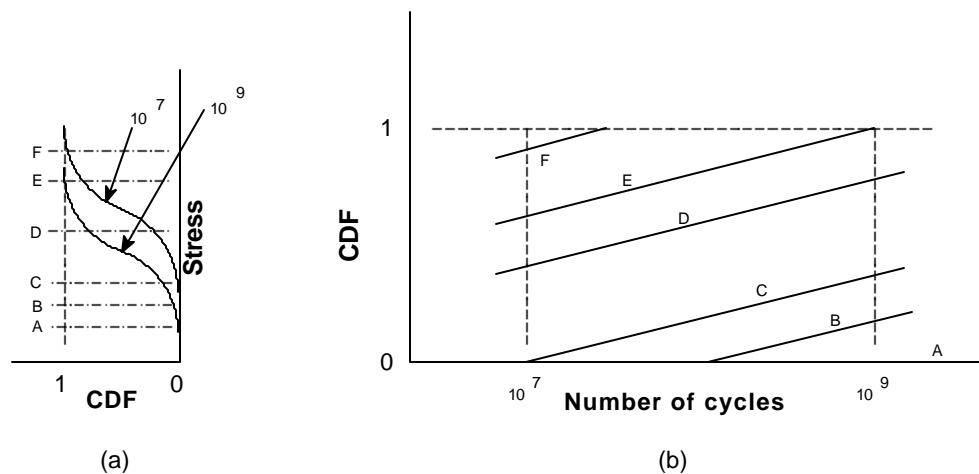


Fig. 2 Schematic of CDF (a) for two different values of  $N_f$ , (b) as a function of  $N$ .

stress, the distribution function or range in stress levels, and the size of the step.

An alternate approach for determining the fatigue limit is to conduct tests at various values of stress up to the number of cycles corresponding to the fatigue limit. Two types of data are obtained. First, some specimens will fail before  $N_f$  is reached, and these will provide data for a S-N curve which can be fit and extrapolated to  $N_f$ . The second

type of data will be stress levels for which no failure was obtained within  $N_f$  cycles. These stress levels will be denoted as runouts or lower bounds on the fatigue limit. In conducting tests under constant stress, consider the case where the S-N curve is relatively flat such as when the number of cycles,  $N_f$ , is very large. As a hypothetical example, consider the fatigue behavior in the region between  $10^7$  and  $10^9$  cycles where it has been shown that the S-N curve still has a slightly negative slope [10]. For

illustrative purposes, the CDF for failure within a given number of cycles is shown schematically in Fig. 2 (a) for either  $10^7$  or  $10^9$  cycles. At  $10^7$  cycles, there is no failure for stresses below level "C" and all samples will fail at or above "F". Similarly, at  $10^9$  cycles, no failure occurs below "A" and all samples will fail at "E" or above. Clearly, "A" corresponds to the fatigue limit at  $10^9$  cycles. Consider, however, what happens in a typical experimental investigation. The CDF is shown as a function of number of cycles in Fig. 2 (b) for several stress levels depicted in Fig 2 (a). As shown, there are no failures at "A" while at "F" most samples will have failed below  $10^7$  and none will reach  $10^9$ . At "E" there is a higher probability of survival beyond  $10^7$  but all fail by  $10^9$ . At some intermediate level "D", some will fail by  $10^7$  and most will have failed by  $10^9$ , but as the stress level decreases to "C" or "B", the likelihood of failure before  $10^9$  decreases. Considering the time and cost of conducting such long life tests, the likelihood of determining the probability density functions for a number of stress levels and, it turn, defining the fatigue limit, is poor. In this situation, the step loading procedure may provide an equally good answer with fewer tests.

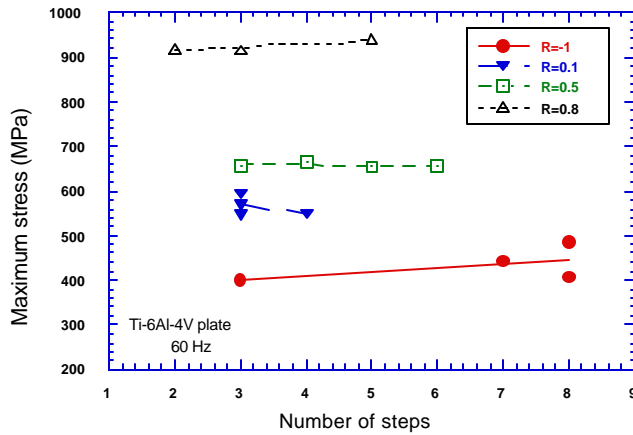


Fig. 3 Fatigue limit stress vs. number of steps.

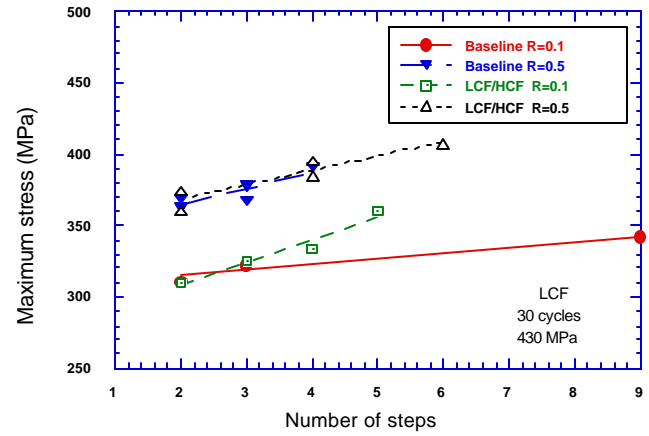


Fig. 4 Fatigue limit stress vs. number of steps.

## Results and Discussion

Experimental data using the plate material and employing the step loading procedure [2] are shown in Fig. 3. In that investigation, the values of the fatigue limit for four different values of  $R$  were not known a priori. Thus, the initial stress value in the step loading procedure was highly variable. The results, plotted against the number of steps, shows no indication of a systematic increase with number of steps and, therefore, no evidence of coaxing. On the other hand, experimental results which show an increase in stress with number of steps is shown in Fig. 4 where the starting stress for any of the four conditions was either the same or very similar. The tests are on a notched sample with  $K_t=2.2$  with one batch untested and the other subjected to LCF cycling as indicated on the plot [11]. The plots of stress versus number of steps shows a linear increase. Since the starting stresses are the same for each condition, the slope is related to the size of the step. Thus, this increase with number of steps is not necessarily coaxing, it is probably no more than the scatter in material behavior as described above.

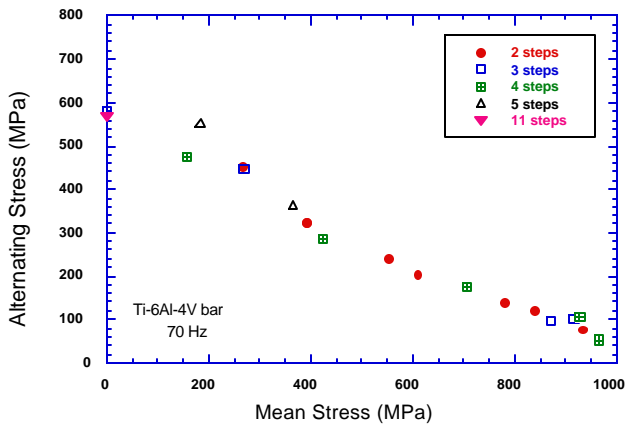


Fig. 5 Haigh diagram for bar material.

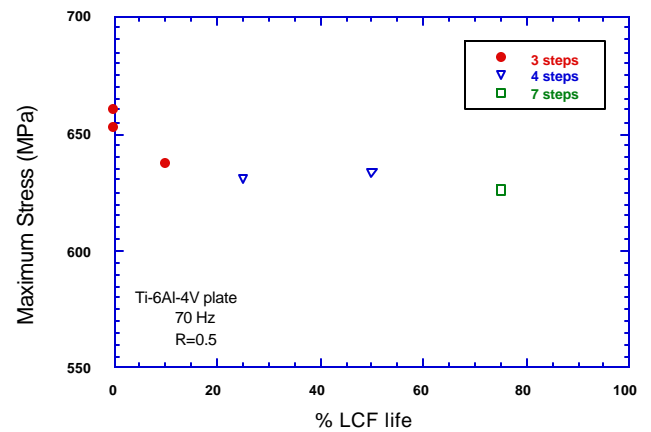


Fig. 7 Fatigue limit against % LCF life.

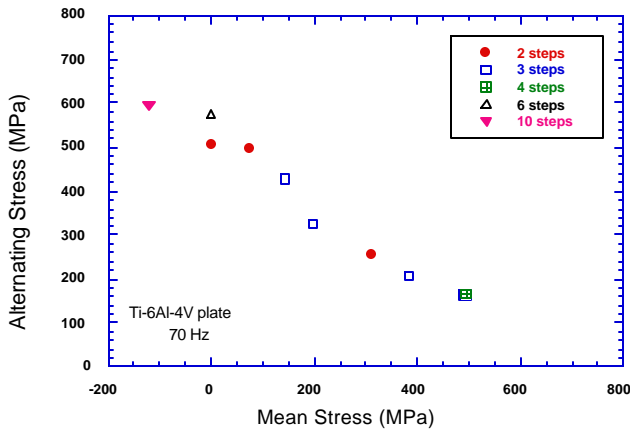


Fig. 6 Haigh diagram for plate material.

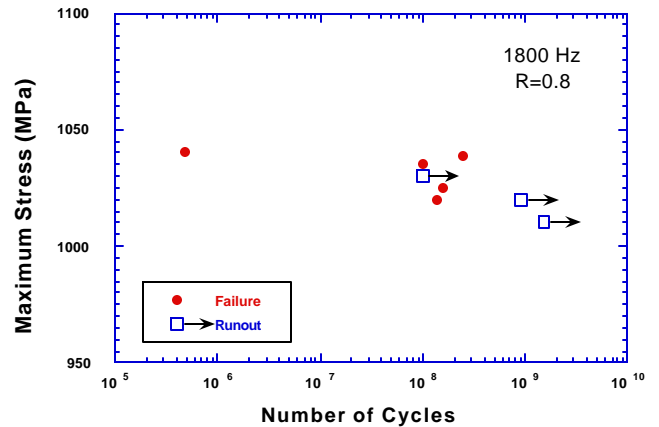


Fig. 8 S-N data for establishing  $N_f$  at  $10^9$  cycles.

Data for a Haigh diagram were obtained using the step loading procedure for both the bar and plate materials. The data are shown in Figs. 5 and 6. In each of the figures, the number of steps that were used for each specimen is indicated in the legend. All of the step loading tests were conducted at a constant value of  $R$ . Careful study of the data shows that there does not appear to be any systematic trend which would lead one to believe that the number of steps has any influence on the results. In fact, it is rather remarkable that the expected trend of higher strength versus number of steps from a purely statistical point of view is not observed. This is probably due to the choice of starting stress for each test which was very variable because each test covered a different value of  $R$  compared to the prior test.

In addition to studying the effect of prior loading history where the stresses were below the HCF fatigue limit, a brief study was made of the effect of prior LCF where stresses are above the HCF fatigue limit. It is commonly believed that cracks initiate under LCF at a smaller fraction of life than under HCF. Consequently, the subsequent HCF life may be shortened after LCF cycling because if cracks are present, the life to initiation may be drastically reduced. If, however, the LCF and HCF are conducted at different values of  $R$ , then the LCF loading may be at peak stresses below the HCF fatigue limit and any cracks may be below the fatigue crack growth threshold. The case of different values of  $R$  for LCF and HCF was investigated here. The effect of prior LCF at  $R=-1$  on the subsequent HCF fatigue limit at  $R=0.5$  was evaluated using the step loading technique. Specimens were subjected to a pre-determined number of LCF cycles and tested subsequently under HCF using the step loading

technique. The LCF life is approximately  $10^5$  cycles at  $R=-1$  and a maximum stress of 600 MPa at 1 Hz. The results showing the fatigue limit corresponding to  $10^7$  cycles as a function of prior LCF cycles are presented in Fig. 7. The data show two things. First, there does not appear to be any significant degradation of HCF fatigue limit due to prior LCF cycling, even up to 75% of life. Second, there does not appear to be a trend in the limited data obtained with the number of steps in the step loading technique as shown in Fig. 7.

Finally, we examine the results of fatigue limit testing using conventional constant stress testing. Exploring the fatigue limit corresponding to  $10^9$  cycles in a 1.8 KHz testing machine, fatigue life and runout data [12] are shown in Fig. 8. It appears that there is a small degree of scatter in the data, but the fatigue limit at  $10^9$  cycles can be established as approximately 1020 MPa. It remains to be shown if a similar number can be obtained using the step test method using fewer specimens.

### **Concluding Remarks**

The results obtained on Ti-6Al-4V do not provide any conclusive evidence of a coaxing effect. On smooth bar specimens and ones with carefully machined notches, the fatigue limit is expected to have a small amount of scatter. The experimental data show this in general, but the occasional data point which is higher than expected can either be attributed to scatter or to coaxing. We have not conducted a systematic study of coaxing, but up to this point, the step loading procedure appears to be a valid method which saves considerable testing time. For specimens which have damage from FOD or fretting fatigue, the statistical scatter is expected to be much larger. Whether or not high values of a fatigue limit stress are due to scatter or coaxing remains a question that may never be answered. Fortunately, in design, we do not have to worry too much about the occasional high value of the fatigue limit, but rather the low ones and the range of experimental scatter. For these purposes, a step loading technique appears adequate for our material. Its validity for use on other materials is yet to be established.

### **Acknowledgments**

This project was supported by the U.S. Air Force under the National Turbine Engine High Cycle Fatigue Program. The work was conducted at the Materials and Manufacturing Directorate of the Air Force Research Laboratory, partly under Contract F33615-98-C-5214 with University of Dayton Research Institute.

### **References**

1. Maxwell, D.C. and Nicholas, T., "A Rapid Method for Generation of a Haigh Diagram for High Cycle Fatigue," Fatigue and Fracture Mechanics: 29th Volume, ASTM STP 1321, T.L. Panontin and S.D. Sheppard, Eds., ASTM, 1999, (in press).
2. Bellows, R.S., Bain, K.R. and Sheldon, J.W., "Effect of Step Testing and Notches on the Endurance Limit of Ti-6Al-4V," Mechanical Behavior of Advanced Materials, MD-Vol. 84, D.C. Davis, et al., Eds., ASME, New York, 1998, 27.
3. Moore, H.F. and Wishart, H.B., "An 'Overnight' Test for Determining Endurance Limit," Proc. ASTM, Vol. 33, Part II, 1933, 334.
4. Prot, M., "Un Nouveau Type de Machine D'Essai des Metaux a la Fatigue par Flexion Rotative," Rev. Metall., Vol. 34, 1937, 440: see also: Prot, M., "Fatigue tests under progressive load. A new technique for testing materials," Rev. Metall., Vol. 45, No. 12, Dec. 1948, 481.
5. Ward, E.J., Schwartz, R.T., and Schwartz, D.C., "An Investigation of the Prot Accelerated Fatigue Test," Proc. ASTM, Vol. 53, 1953, 885.
6. Corton, H.T., Dimoff, T. and Dolan, T.J., "An Appraisal of the Prot Accelerated Fatigue Test," Proc. ASTM, Vol. 54, 1954, 875.
7. Dolan, T.J., Richart, F.E., Jr. and Work, C.E., "The Influence of Fluctuations in Stress Amplitude on the Fatigue of Metals, Proceedings ASTM, Vol. 49, 1953, 646.
8. Epremian, E. and Mehl, R.F., "A Statistical Interpretation of the Effect of Understressing on Fatigue Strength," Fatigue with Emphasis on Statistical Approach, ASTM STP 137, 1952, 58.
9. Vitovec, F.H. and Lazan, B.J., "Strength, Damping and Elasticity of Materials Under Increasing Reversed Stress with Reference to Accelerated Fatigue Testing," Proc. ASTM, Vol. 55, 1955, 844.
10. Bathias, C., "Relation Between Endurance Limits and Thresholds in the Field of Gigacycle Fatigue," Fatigue Crack Growth Thresholds, Endurance Limits, and Design, ASTM STP 1372, 1999, (in press).

11. Monty Moshier, Air Force Research Laboratory (unpublished data).
12. Alisha Hutson, University of Dayton Research Institute (unpublished data).

## ***LIST OF SYMBOLS, ABBREVIATIONS, AND ACRONYMS***

<b><u>ABBREVIATION</u></b>	<b><u>DEFINITION</u></b>
A-D	Analog-to-Digital
AFOSR	Air Force Office of Scientific Research
AFRL/MLLN	Air Force Research Laboratory/Ceramics Development and Materials
	Behavior Branch
BFS	Back Face Strain
C(T)	Compact Tension Specimen
CMC	Ceramic Matrix Composites
CMOD	Crack Mouth Opening Displacements
CPLM	Crack Propagation Load Measurement
CTE	Coefficient Thermal Expansion
DARPA	Defense Advanced Research Projects Agency
DCPD	Direct Current Potential Drop
DE(T)	Double Notched Specimen
ERLE	Engine Rotor Life Extension
FOD	Foreign Object Damage
HCF	High Cycle Fatigue
IHPTET	Integrated High Performance Turbine Engine Technology
$K_{pr}$	Crack Propagation Stress Intensity Factor
LCF	Low Cycle Fatigue
LIDG	Laser Interferometric Displacement Gage
LVDT	Linear Variable Differential Transformer
MLOC	Government Computer Support
MMC	Metal Matrix Composites
MSC/PATRAN	Software Product Name
MSE(T)	Single Notched Specimen
MTS	Material Test Systems (Brand Name)
NDE	Nondestructive Evaluation
NTED	National Turbine Engine Durability
OIM	Orientation Imaging Microscopy
SE(T)	Single Edge Notched Tension Specimen
SEM	Scanning Electron Microscope
Ti	Titanium
TiAl	Titanium Aluminide
TMC	Titanium Matrix Composites
TMCTECC	Titanium Matrix Composites Turbine Engine Component Consortium
UDRI	University of Dayton Research Institute
UMAT	User-supplied Material Model